The Dissertation Committee for Tobias Hanrath Certifies that this is the approved version of the following dissertation:

Germanium Nanowires: Synthesis, Characterization, and Utilization

Committee:

Brian A. Korgel, Supervisor

John Ekerdt

Gyeog S. Hwang

Miguel Jose Yacaman

Sanjay Banerjee

Zhen Yao

Germanium Nanowires: Synthesis, Characterization, and Utilization

by

Tobias Hanrath, M.S., B.S.

Dissertation

Presented to the Faculty of the Graduate School of
The University of Texas at Austin
in Partial Fulfillment
of the Requirements
for the Degree of

Doctor of Philosophy

The University of Texas at Austin
December 2004

Dedication

To my family and loved ones.

Acknowledgements

I would like to acknowledge all of the people who have assisted in my graduate school experience. I thank all past and present members of the Korgel group for creating an enjoyable, entertaining and supportive research environment. Special thanks to Kirk Ziegler and Lindsay Pell for getting me started on the supercritical fluid synthesis, Doh Chang Lee and Cindy Stowell for assistance with the SQUID, Aaron Saunders for seed nanocrystals, April Schricker for assistance with electrical measurements, Michael Sigman for coffee and Wendy's trips, and everyone else in the group for help, advice and friendship. Thanks to Dwight Romanovicz for help in preparing cross sectional samples.

The TEM is perhaps the most vital tool in our research, in that context I would like to thank Dr. Zhou for his assistance and training with the microscope. Outside of UT Austin, I would like to thank Dr. Mikulec at Innovalight and Dr. Stallcup for helpful discussions.

I also thank my committee members – Dr. Banerjee, Dr. Ekerdt, Dr. Hwang, Dr. Yacaman and Dr. Yao for all their advice and suggestions. Furthermore, I am indebted to Dr. Loo for helpful research discussions and career advice, and, of course, thanks to my advisor Dr. Korgel for his guidance and suggestions. All of the staff in the Department of Chemical Engineering and in the Center for Molecular Science and Nanotechnology deserve big thanks as well. Finally, I would like to thank my family and friends for their support and encouragements to pursue my dreams.

Germanium Nanowires: Synthesis, Characterization and Utilization

Publication No.____________

Tobias Hanrath, Ph.D.
The University of Texas at Austin, 2004

Supervisor: Brian A. Korgel

A supercritical fluid synthesis method was developed for the preparation of single crystal germanium (Ge) nanowires with diameters as small as 4 nanometer and several tens of micrometer in length. Alkanethiol protected gold nanocrystals were used to seed and direct nanowire growth. Nanowire processing and their implementation as building blocks in nanowire based devices requires rigorous control of nanowire surface chemistry, which differs from well-studied monolithic atomically-smooth single crystal substrate surface chemistry due to the nanowire's high surface area to volume ratio and atomically rough surface. Ge nanowire surface oxidation was studied by Ge 3d x-ray photoelectron spectroscopy. A broad range of solution-phase routes to the Ge nanowire surface passivation were explored including sulfidation, hydride and chloride termination, and organic monolayer passivation. Nanowires with covalently bonded monolayer surface terminations formed via thermally-initiated hydrogermylation reactions with alkenes, alkynes or dienes exhibited excellent chemical stability compared to untreated or etched nanowire surfaces and enabled low contact resistance ohmic electrical contacts to be made to the nanowires.

Device characteristics of single Ge nanowire devices fabricated with gold electrical contacts patterned by e-beam lithography were compared with devices prepared using focused e-beam or Ga-beam assisted Pt chemical vapor deposition. These device structures permitted direct investigation of the influence of nanowire surface chemistry, doping, and gate electrode architecture, on device operation. The impact of the surface chemistry on surface state dominated electron transport in single nanowire devices was investigated by room temperature field-effect measurements. The density and relaxation time distribution of electrically active surface states was found to be highly sensitive to the nanowire surface chemistry. Complimentary to the device measurements, fundamental electrical and optical properties were probed via electron energy loss spectroscopy on individual nanowires inside the transmission electron microscope. The volume plasmon energy increased with decreasing diameter for nanowires narrower than 24 nm. Below 24 nm, organic monolayer-coated nanowires also exhibited size-dependent Ge 3d core ionization spectra that shifted to higher energy with reduced diameter that are independent of probe position relative to the surface. In contrast, the Ge 3d edge for surface-oxidized nanowires exhibited a chemically-induced shift when positioned near the surface.

Table of Contents

List of Tables

List of Figures

Chapter 1: Introduction

1.1 BACKGROUND ON NANOWIRE SYNTHESIS

The past two decades have witnessed spectacular progress in the research of nanoscale materials. Intensive efforts in synthetic methods and characterization tools have enabled the study and utilization of a large variety of nanoscale materials. From a scientific standpoint, these materials have led to important breakthroughs in our fundamental quantum mechanical understanding of materials properties. The unique physical, electrical and optical properties have also received extensive efforts from a technological perspective and have been proposed as building blocks in future nanoscale electronic and optical devices.

In addition to size, the dimensionality of the nanostructures plays a key role in material properties and extensive experimental efforts have focused on the synthesis of one-dimensional crystals, or nanowires – also known as whiskers. Nanofibers present another interesting one dimensional material, but are distinguished from nanowires by their internal crystallography. While the earliest historical record of one dimensional structures dates back to 1574, when Lazarus Ercker noted whisker-like growths from copper and silver sulfide ores,[1] it was not until the 1950s that researchers began to understand the fundamental mechanisms responsible for their formation.

Although the characterization tools of that time limited studies to micrometer-diameter whiskers, three general approaches emerged from those studies, which apply to wires with nanometer diameters as well: (1) strain-driven wire growth from surfaces;[2] (2) whisker crystallization from the vapor or liquid phase induced by axial screw dislocations;[3,4] and (3) vapor-liquid-solid (VLS) growth in which a metal seed particle induces wire growth.[5-7]

1.2 Whisker Growth

Among the three approaches, the VLS mechanism is perhaps the best suited for rational and tunable synthesis. The VLS mechanism was first proposed by Wagner and Ellis, who conducted the seminal work on controlled whisker growth in the 1960's.[5,6] In their work silicon was deposited by chemical vapor deposition (CVD) on a substrate coated with a thin film of Au. Instead of depositing on the surface, the silicon preferentially dissolved into the Au and at temperatures above the Au:Si eutectic point formed liquid alloy droplets. Under these conditions silicon continued to dissolve in the liquid alloy droplet until reaching saturation, at which point the Si crystallized in the from the droplet in the form of a one dimensional whisker.

The key parameters necessary to induce whisker formation via the VLS mechanism are temperature, which must exceed the alloy eutectic temperature, and the concentration of crystallizing material, which must be relatively high to promote whisker growth. Inspection of binary equilibrium phase diagrams shows that the first condition is met by several metal-semiconductor systems, for example Fe-Si, Au-GaAs, Au-Ge and Al-Ge.[8] The binary equilibrium phase diagram for the Au-Ge system is shown in Figure 1.1 along with a schematic illustration of the growth of Ge nanowires from a Au seed crystal. The minimum whisker diameter achievable by this early work was limited by the minimum stable liquid drop diameter, ~100 nm. Interestingly, the VLS mechanism has also been found for whisker structure in nature[9] and even on the moon.[10]

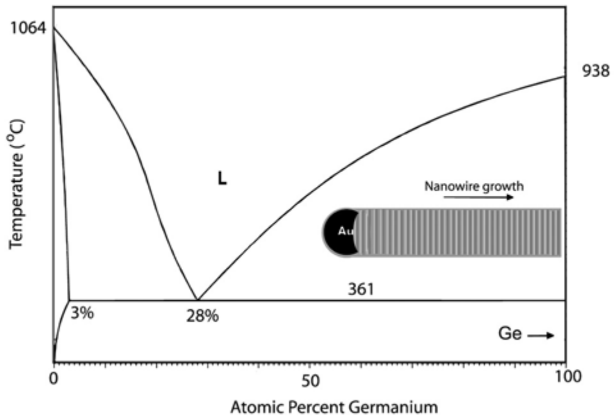

Figure 1.1: Binary equilibrium phase diagram for Au:Ge and a schematic representation of the VLS growth of single crystal nanowires.

1.1.2 Nanowire Growth

With the recent surge in interest in the synthesis of nanoscale one-dimensional materials, the VLS mechanism has regained scientific attention and serves as the foundation for the vast majority of nanowire materials synthesized today. In 1998 Morales and Lieber first combined the VLS approach with laser ablation to generate nanometer scale metal seed particles to nucleate nanowire growth.[11] This laser catalyzed growth (LCG) approach was successfully applied to a range of semiconductor materials including Si, Ge, GaN and GaAs,[11-13] however, the inherent inefficiency of the laser ablation process and the broad size distribution of the laser ablation generated seed particles presented a key limitation to the further application of this process.

The full utilization of the unique size dependent properties of the semiconductor nanowires requires synthesis methods with better control over specific nanowire diameters and monodisperse distributions than was attainable with the LCG approach. In 2000, Holmes et al.[14] reported that size selected gold nanocrystals capped with dodecanethiol could effectively be used to seed the growth of Si nanowires with diameters smaller than 10 nm micrometers in length, in supercritical hexane. As described in detail in Chapter 2, this supercritical fluid-liquid-solid (SFLS) approach has since then been extended to achieve the synthesis of milligram quantities of high-quality single crystal Ge nanowires,[15] and III-V nanowires.[16,17]

Lieber and co-workers later reported diameter control of Si and InP nanowires by combining CVD with size-monodisperse Au particles ranging in size from 5 to 30 nm attached to a surface.[18,19] Although the CVD based nanowire synthesis has been included to a range of semiconductor materials[20-26] this approach presents key limitation in the throughput of nanowire material that can be generated. Solution based syntheses on the other hand can utilize free floating seed particles enabling the synthesis of much larger quantities of nanowires than are attainable with vapor based methods. Buhro and co-workers have shown that high boiling point solutions, such as 1,3-diisopropylbenzene (T_{bp}=203°C) provide a suitable environment for the synthesis of various III-V nanowires.[27,28] Other key semiconductor materials, such as Si and Ge however require much higher synthesis and crystallization temperatures and can thus not be formed by this approach. By pressurizing and heating the solvent above it's critical pressure and temperature, solution phase reactions can be carried out it supercritical fluid environments. Heath and LeGoues reported the synthesis of Ge nanowires via the reduction of $GeCl_4$ and phenyl-$GeCl_3$ by sodium in hexane heated and pressurized (275^{o}C and 10 MPa) just above the critical point.[29] This solution synthesis provides nanowires, yet with a low yield and the nanowires were riddled with crystallographic defects.

The supercritical fluid method therefore provides an approach with superior seed crystals than are possible with CVD based system with the added advantage of being scaleable to the synthesis of technologically significant quantities of nanowires. Moreover, as is shown in Chapter 4, the SFLS approach can also be easily integrated with various surface chemistry modifications, which due to the high surface to volume ratio of the nanowires are of paramount importance for their processing and utilization.

1.2 SUPERCRITICAL FLUIDS

Supercritical fluid (SCF) conditions are observed in fluids heated and pressurized above their critical temperature and pressure, respectively. While conventional solvents provide a flexible medium for the syntheses for a variety of nanomaterials, supercritical fluids exhibit unique characteristics with significant utility when applied to these chemical systems. The generic pressure-temperature phase diagram in Figure 1.2 shows that at temperatures and pressures above the critical point the vapor-liquid coexistence curve disappears and only a single-phase fluid exists. The density, viscosity and diffusivity in the single-phase supercritical region are intermediate between those of liquids and gases and vary continuously from "gas-like" to "liquid-like" with small changes in temperature, pressure, or both. The density, which relates to solvent strength can be tuned by varying temperature and pressure as is shown in the n-hexane equilibrium phase diagram in Figure 1.3 [30,31] Additionally, the high diffusivity and low viscosity in SCFs provide an environment for fast reactions that would be transport limited in the liquid phase.[32]

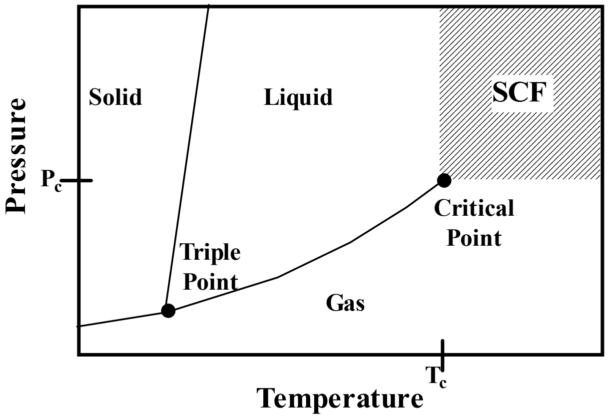

Figure 1.2: Schematic of generic equilibrium pressure-temperature phase diagram showing the triple point, the critical point and the supercritical region.

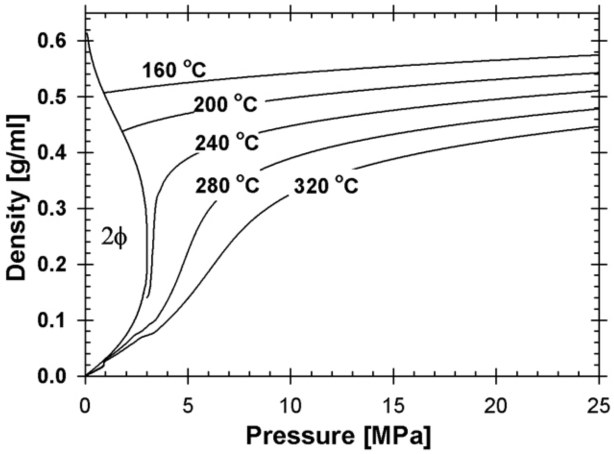

Figure 1.3: Equilibrium phase diagram of n-hexane showing density as a function of temperature and pressure.

SCFs, most commonly in the form of supercritical carbon dioxide or water, have successfully been applied in a variety of processes including extraction, chromatography, reactions, and materials processing.[33] Recently, the benefits of SCFs have also been extended toward the synthesis and processing of a variety of nanomaterials.[34] For example, Ziegler et al.[35] synthesized copper and copper oxide nanocrystals in supercritical water, while Shah et al.[36] demonstrated that synthesis and density tuned size selection of silver and gold nanocrystals in supercritical ethane. Synthesis of semiconducting nanomaterials in the Korgel group has focused on common organic supercritical solvents such as hexane, cyclohexane, or toluene. In this context, supercritical fluids are an ideal intermediate between the vapor and liquid phase synthesis and provide a superior environment for the synthesis of semiconductor nanowires for the following reasons: (1) SCF's solvent strength allows dispersion of size selected seed particles and solubilization of high precursor concentrations, (2) high synthesis temperatures required for precursor degradation and semiconductor recrystallization, (3) a scaleable continuous flow operation enabling the synthesis of technologically significant quantities of nanomaterials, and (4) integration of SCF synthesis and solution based surface chemistry modifications.

1.4 NANOWIRE PROPERTIES AND APPLICATIONS

Nanowires serve as an ideal experimental system for the experimental study of fundamental quantum mechanical concepts, however the larger impetus behind the revolutionizing research in this area is fueled by their immense technological potential. The successful implementation of nanowires and other nanoscale materials in future technologies requires the following three issues to be addressed:

(1) Consistent synthesis control over critical material aspects including the composition, dimensionality, size and surface chemistry,

(2) fundamental understanding of the unique size and shape dependent electrical, optical, mechanical and chemical properties, and

(3) controlled processing and assembly of individual and ensemble nanowires into larger functional structures.

1.4.1 Device Applications

Technological applications of nanowires will be most likely in the form of building blocks in the *bottom-up* assembly of novel devices. For example, the pioneering work by Lieber's group has shown that semiconducting nanowires can be assembled into functional electronic and optical device structures, such as logic gates,[37] memory devices,[38] photodetectors,[39] and lasers[40,41] with the potential for scaled integration over large areas using a combination of self-assembly and top-down microfabrication processes.[42] In addition to these optical and electronic applications, semiconducting nanowires have also shown tremendous promise for their application as sensors for chemical and biological species.[43,44] The small size of these nanostructures, and the associated possibilities for device miniaturization however, represents only a small part of the immense technological opportunities offered by these materials. The full realization of the potential of nanoscale materials in future technologies require the incorporation and control of their unique size-dependent electrical and optical properties dominated by quantum confinement effects.

1.4.2 Quantum Confinement Effects

The quantum confinement in these materials arise from spatial confinement of electrons and holes as independently acting 'wave-particles' or as bound excitons. As the geometric confinement approaches the bulk exciton Bohr radius, the effective bandgap of the material increases and the electronic structure of the material changes gradually from continuous bands to one characterized by discrete levels.[45] Compared to Si, Ge nanostructures are of particular interest, since the Bohr exciton radius is larger in Ge than in Si,[46] which consequently should lead to more prominent quantum confinement effects in the former. Furthermore, the dimensionality of the nanomaterials needs to be considered since the confinement effects in three-dimensional (3D) confined particles 2D confined wires and 1D confined wells evolve differently.[47,48]

1.5 DISSERTATION OVERVIEW

The synthesis of Ge and Si nanowires in supercritical fluid are discussed in Chapter 2 and 3, respectively. The effects of essential parameters such as temperature, pressure, concentration, and precursors chemistry are explored and related to the morphology of the nanowires. Like zero-dimensional nanoparticles, one-dimensional nanowires are characterized by a very surface-to-volume ratio, consequently, the detailed characterization and modification of the nanowire surface chemistry is of vital importance for their utilization in the above mentioned technological applications. These aspects are addressed in Chapter 3 which provides a detailed x-ray photoelectron spectroscopy investigation of the surface oxidation and illustrates various chemical pathways toward the passivation of the nanowire surface passivation.

Chapter 5 discusses the use of high-resolution transmission electron microscope (HRTEM) for the structural characterization of the nanowires, focusing on crystallographic aspects such as the growth direction, surface faceting, and defects. Diameter dependent electronic properties such as the volume plasmon or Ge 3d core ionization energies were investigated by STEM-

ELS and are discussed in Chapter 6. Chapter 7 discusses the fabrication of single Ge nanowire electrical devices and the electron transport through the nanowires with particular focus on the influence of surface states on the nanowire conductivity. In Chapter 8, several aspects relating ensemble nanowire processing with regards to the morphology nanowire deposits and the alignment of isolated Ge nanowires on substrates are discussed. *Top-down* and *bottom-up* fabrication routes toward Ge nanorods are discussed in Chapter 9. Finally, Chapter 10 presents recent results on preparation of Mn doped Ge nanowires.

1.6 REFERENCES

(1) Erker, L. *Treatise on Ores and Assaying*; 2nd ed.; University of Chicago, 1951.

(2) Franks, J. *Nature* **1956**, *177*, 984.

(3) Sears, G. W. *Acta Metal.* **1955**, *3*, 361-365.

(4) Brenner, S. S. *Acta Metal.* **1956**, *4*, 62-63.

(5) Wagner, R. S.; Ellis, W. C. *Appl. Phys. Lett.* **1964**, *4*, 89-90.

(6) Wagner, R. S.; Ellis, W. C.; Jackson, K. A.; Arnold, S. M. *J. Appl. Phys.* **1964**, *35*, 2993-2995.

(7) Johnson, E. R.; Amick, J. A. *J. Appl. Phys.* **1954**, *25*, 1204-1208.

(8) *Binary Alloy Phase Diagrams*; 2 ed.; ASM International: Materials Park, Ohio, 1990; Vol. 1.

(9) Finkelman, R. B.; Larson, R. R.; Dwornik, E. J. *Journal of Crystal Growth* **1974**, *22*, 159-160.

(10) Carter, J. L. *Science* **1973**, *181*, 841-842.

(11) Morales, A. M.; Lieber, C. M. *Science* **1998**, *279*, 208-211.

(12) Duan, X.; Lieber, C. M. *J. Am. Chem. Soc.* **2000**, *122*, 188-192.

(13) Hu, J.; Odom, T. W.; Lieber, C. M. *Acc. Chem. Res.* **1999**, *32*, 435-445.

(14) Holmes, J. D.; Johnston, K. P.; Doty, R. C.; Korgel, B. A. *Science* **2000**, *287*, 1471-1473.

(15) Hanrath, T.; Korgel, B. A. *J. Am. Chem. Soc.* **2002**, *124*, 1424-1429.

(16) Davidson III, F. M.; Schricker, A. D.; Wiacek, R. J.; Korgel, B. A. *Advanced Materials* **2004**, *16*, 646-649.

(17) Davidson III, F. M.; R.J., W.; Korgel Brian, A. *submitted* **2004**.

(18) Gudiksen, M. S.; Wang, J.; Lieber, C. M. *Journal of Physical Chemistry B* **2001**, *105*, 4062-4064.

(19) Cui, Y.; Lauhon, L. J.; Gudiksen, M. S.; Wang, J.; Lieber, C. M. *Applied Physics Letters* **2001**, *78*, 2214-2216.

(20) Chen, C.-C.; Yeh, C.-C.; Chen, C.-H.; Yu, M.-Y.; Liu, H.-L.; Wu, J.-J.; Chen, K.-H.; Chen, L.-C.; Peng, J.-Y.; Chen, Y.-F. *J. Am. Chem. Soc.* **2001**, *123*, 2791-2798.

(21) Kamins, T. I.; Li, X.; Williams, R. S.; Liu, X. *Nano Letters* **2004**, *4*, 503-506.

(22) Mathur, S.; Shen, H.; Sivakov, V.; Werner, U. *Chemistry of Materials* **2004**, *16*, 2449-2456.

(23) Wang, D.; Dai, H. *Angewandte Chemie, International Edition* **2002**, *41*, 4783-4786.

(24) Greytak, A. B.; Lauhon, L. J.; Gudiksen, M. S.; Lieber, C. M. *Appl. Phys. Lett.* **2004**, *84*, 4176-4179.

(25) Kuykendall, T.; Pauzauskie, P. J.; Zhang, Y.; Goldberger, J.; Sirbuly, D.; Denlinger, J.; Yang, P. *Nature Materials* **2004**, *3*, 524-528.

(26) Huang, M. H.; Wu, Y.; Feick, H.; Tran, N.; Weber, E.; Yang, P. *Advanced Materials* **2001**, *13*, 113-116.

(27) Trentler, T. J.; Hickman, K. M.; Goel, S. C.; Viano, A. M.; Gibbons, P. C.; Buhro, W. E. *Science* **1995**, *270*, 1791-1796.

(28) Yu, H.; Buhro, W. E. *Adv. Mater.* **2003**, *15*, 416-420.

(29) Heath, J. R.; LeGoues, F. K. *Chem. Phys. Lett.* **1993**, *208*, 263-266.

(30) Lemmon, E. W.; McLinden, M. O.; Friend, D. G. *NIST Chemistry WebBook, NIST Standard Reference Database Number 69* **2003**, *2004*, http://webbook.nist.gov.

(31) Span, R.; Springer: Berlin, 2000, p 367.

(32) Savage, P. E.; Goplan, S.; Mizan, T. I.; Martino, C. J.; Brock, E. E. *AIChE Journal* **1995**, *41*, 1723-1778.

(33) Dixon, D. J.; Johnston, K. P. In *Encyclopedia of Separation*; Ruthven, D. M., Ed.; John Wiley: New York, 1997, pp 1544-1569.

(34) Holmes, J. D.; Lyons, D. M.; Ziegler, K. J. *Chem. Eur. J.* **2003**, *9*, 2144-2156.

(35) Ziegler, K. J.; Doty, R. C.; Johnston, K. P.; Korgel, B. A. *J. Am. Chem. Soc.* **2001**, *123*, 7797-7803.

(36) Shah, P. S.; Holmes, J. D.; Johnston, K. P.; Korgel, B. A. *Journal of Physical Chemistry B* **2002**, *106*, 2545-2551.

(37) Huang, Y.; Duan, X.; Cui, Y.; Lauhon, L. J.; Kim, K. H.; Lieber, C. M. *Science* **2001**, *294*, 1313-1317.

(38) Duan, X.; Huang, Y.; Lieber, C. M. *Nanoletters* **2002**, *2*, 487-490.

(39) Wang, J.; Gudiksen, M. S.; Duan, X.; Cui, Y.; Lieber, C. M. *Science* **2001**, *293*, 1455-1457.

(40) Duan, X.; Huang, Y.; Agarwal, R.; Lieber, C. M. *Nature* **2003**, *421*, 241-245.

(41) Jonhson, J. C.; Yan, H.; Schaller, R. D.; Haber, L. H.; Saykally, R. J.; Yang, P. *J. Phys. Chem. B.* **2001**, *105*, 11387.

(42) Jin, S.; Whang, D.; McAlpine, M. C.; Friedman, R. S.; Wu, Y.; Lieber, C. M. *Nanoletters* **2004**, *4*, 915-919.

(43) Cui, Y.; Wei, Q.; Park, H.; Lieber, C. M. *Science* **2001**, *293*, 1289-1292.

(44) Hahm, J.-i.; Lieber, C. M. *Nano Letters* **2004**, *4*, 51-54.

(45) Alivisatos, A. P. *Science* **1996**, *271*, 933-937.

(46) Maeda, Y.; Tsukamoto, N.; Yazawa, Y.; Kanemitsu, Y.; Masumoto, Y. *Appl. Phys. Lett.* **1991**, *59*, 3168-3271.

(47) Buhro, W. E.; Colvin, V. L. *Nature Materials* **2003**, *2*, 138-139.

(48) Yu, H.; Li, J.; Looms, R. A.; Wang, L.-W.; Buhro, W. E. *Nature Materials* **2003**, *2*, 517-520.

Chapter 2: Ge Nanowire Synthesis in Supercritical Fluid

2.1 SUPERCRITICAL FLUID SYNTHESIS APPARATUSES

2.1.1 Supercritical Fluid Batch Reactor

Initial supercritical fluid reactions were carried out in a 1.0 ml stainless batch reactor steel high pressure cell (0.5 cm i.d., 2.0 cm o.d, and 7.0 cm long with a stainless LM6 HIP gland and plug, High pressure Equipment, Inc.). In a typical batch synthesis the precursor solution containing the organogermane precursor and Au nanocrystals were loaded into the cell in a nitrogen glove box (with oxygen levels typically less than 0.5 ppm). A Si (100) substrate was placed inside the reactor cell to help collect the nanowires during the reaction. The deposition substrates were cut into 4 x 20 mm sections and ultrasonically cleaned in acetone for 10 minutes followed by a rinse in isopropanol, 1:1 HCl: methanol solution, and deionized water. The cell was then inserted into cylindrical slots in a preheated brass block (7 x 25 x 17 cm) which was heated by four 300W cartridge heaters (Omega). A schematic of the reactor system is shown in Figure 2.1. The block temperature was monitored by K-type thermocouple (Omega Inc.) and controlled to within ± 1^{o}C by a digital temperature controller (Omega Inc.). Control experiments with a thermocouple inserted into an empty reactor cell showed that the inside reactor wall temperature equilibrated with the set block temperature within 2min. Once the specified reaction time had elapsed, the reactor cell was removed from the brass block and immersed in water for cooling. A polycarbonate barricade was placed in front of the apparatus for safety. After the reaction, the cell was opened to recover the deposition substrate onto which solid products were deposited. Additional solid products and liquid products were extracted from the cell by rinsing it with chloroform and hexane. The deposition substrate was stored under nitrogen prior to characterization.

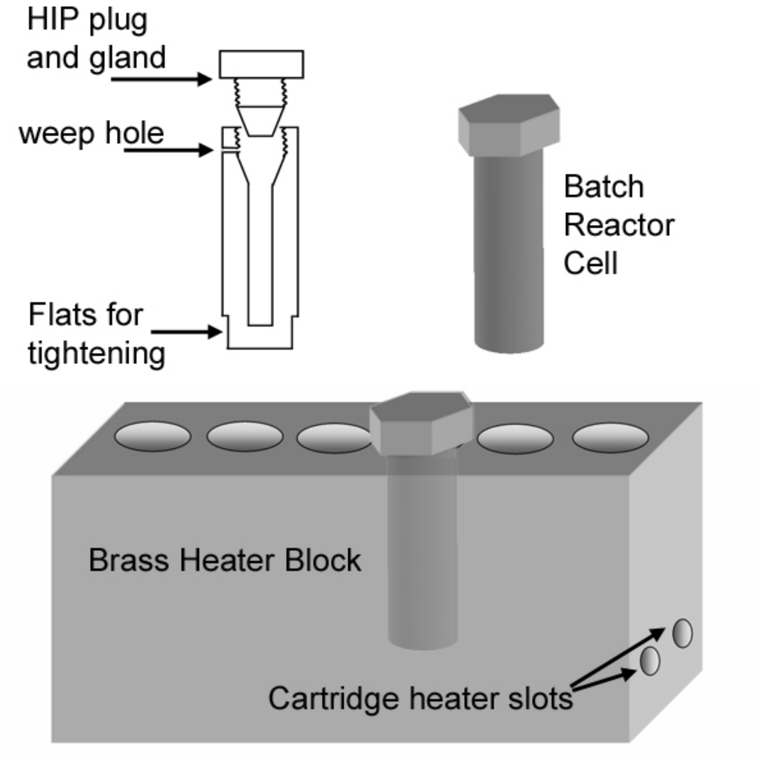

Figure 2.1: Schematic of the high-temperature multiple cell batch reactor block.

2.1.2 Supercritical Fluid Injection Apparatus

In order to permit rapid injection of the reagents and efficient post reaction product purification by rinsing with supercritical hexane, the 1.0 ml batch reactor cell described above was modified to an injection based reactor system as described below. The reactor cell material was changed from stainless steel (316) to titanium (Grade 2) in an effort to reduce the potential leaching of carbon from the reactor walls during the high synthesis temperatures. A schematic of the injection reactor system is shown in Figure 2.2A. The inlet and outlet of the 1.0 ml Ti reactor cell were connected to high-pressure (0.76 mm i.d.) tubing via LM-6 HIP (High-Pressure Equipment Co.) reducers. The reactor cell was covered with heating tape (Barnstead/Thermolyne) and insulation, allowing the reactor to be maintained to within $\pm 1^{o}$C through a temperature controller (Omega). In an effort to further reduce experiment setup time and to provide a consistent way of measuring the temperature *inside* the cell, the heating procedure was later modified replace the heating tape with a 'waffleiron-like' brass block heating element as shown in Figure 2.2B. A high-pressure liquid chromatography (HPLC) pump (Alcott) was used to pressurize a piston with doubly distilled water, which in turn pressurized the reactor with deoxygenated anhydrous cyclohexane or hexane. The Si deposition substrates used in these experiments were marked to indicate the direction from which the precursor was injected. The system pressure was monitored with a digital pressure gauge (Sensotech). In a typical synthesis, several reactor volumes of cyclohexane or n-hexane were flushed through the cell to ensure an absolutely oxygen free synthesis environment. The reactor cell was then prepressurized to 2.0 MPa and heated to the desired synthesis temperature. The precursor solution was loaded into a 350 μL injection loop connected to a 6-way valve (Valco) and subsequently injected into the supercritical environment in the reactor. The reactor was then pressurized to the desired pressure within less than 30 sec and the reaction proceeded for 8 to 20 min. After the elapsed reaction time, the heating tape and insulation were removed and the cell was slowly depressurized by ejecting the reaction mixture into a receiving vial containing cyclohexane or n-hexane. Unwanted reaction by-products in the form of polyorganogermanes were removed from the deposited material on the Si substrate by slowly flushing the reactor cell with supercritical solvent. The cell was then allowed to cool to near room temperature before it was opened to recover the nanowire material on the deposition substrate. The product solutions and the deposition substrate were stored under nitrogen prior to characterization. The achieved product yields of this approach ranged from 50-70%.

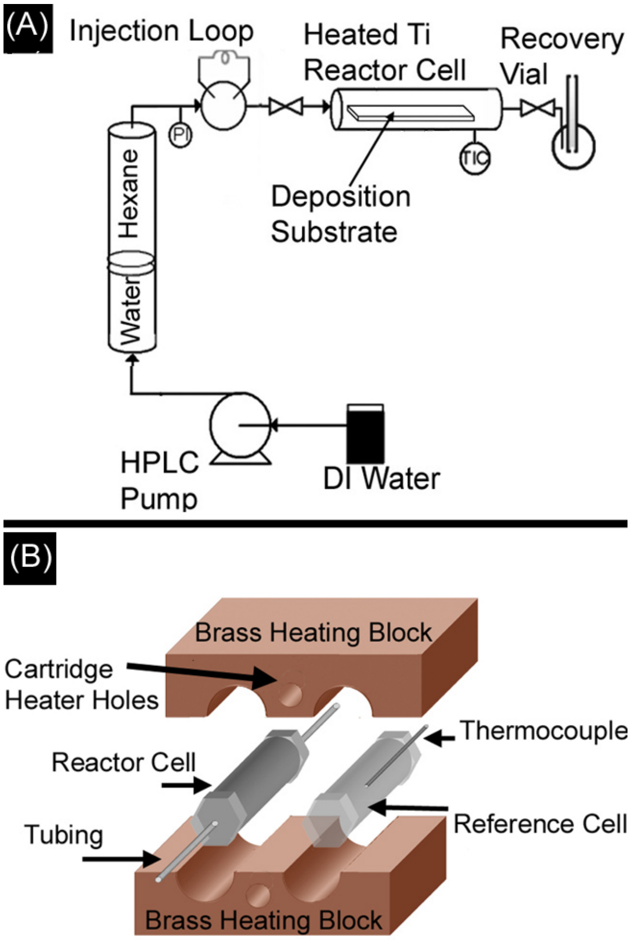

Figure 2.2: (A) Schematic of the apparatus used for nanowire synthesis in supercritical fluid via rapid injection into titanium high-pressure cell. (B) Schematic of the waffle iron heating block with auxiliary reference cell used for temperature measurement.

2.1.3 Continuous Flow reaction

In a continued effort to improve the synthesis environment and to increase the reactor throughput and yield, the injection-based system discussed above was modified to obtain a continuous flow reactor. For flow through reactions, the injection loop mentioned above was replaced with a 27 ml high-pressure piston, which was back pressured by hexane (see Figure 2.3). Additionally, the reactor effluent valve (AF-6 needle valve, HIP) was replaced by a micro control-metering valve (HF4-V, HIP) to permit precise control over the leak rate from the reactor.

Theoretical estimates for the locally varying temperature profile are provided in Appendix A and show that for moderate flowrates, the flowing solution thermally equilibrates with the reactor wall temperature after a distance of a few millimeters along the reactor cell. The calculations also show that the scale up to a large 10 ml reactor under the same residence time conditions requires a preheater to achieve similar thermal profile. The preheater used for continuous flow reactions with a 10 ml reactor cell consisted of high pressure tubing (0.76 mm i.d.) wrapped around a 300W cartridge heater. The temperature of the insulated preheater was monitored and controlled with a K-type thermocouple connected to a digital temperature controller (Omega).

In a typical flow through reaction, the reactor containing the deposition substrate was connected to the high-pressure tubing as discussed above, placed inside the ‘waffleiron’ heater block, and heated to the desired synthesis temperature. The Si deposition substrates used in these experiments were marked to indicate the direction of flow. After the cell reached the desired synthesis temperature n-hexane was flown into the reactor at a flowrate controlled by the HPLC pump. The position of the micro control-metering valve was then manually adjusted to equilibrate reactor in- and out-flow at the desired synthesis pressure. Once stable flow conditions at the desired temperature and pressure were attained, the flow solution was switched from hexane (piston A) to the precursor containing solution (piston B). Typically, the flowrate at the HPLC pump was set to 0.2 ml/min commensurate with a flowrate of ~0.5ml/min for the less dense supercritical fluid flowing through the high-pressure cell. These flow conditions correspond to an average residence time of approximately 80 s. The residence time can easily be reduced into the range of several seconds, however faster flowrates require the incorporation of a preheater to maintain the desired temperature profile (see Appendix A). Under typical conditions, a single piston provided sufficient precursor solution for 160 min of continuous reaction. Significantly, the dual piston system provides the capability for extended continuous and uninterrupted syntheses by simply switching the precursor pistons as needed. While the continuous flow reactor shown in Figure 2.3 is based on a 1.0 ml Ti reactor cell, similar continuous flow experiments with 10 ml reactor cells and commensurate temperature and residence time profiles have verified that this nanowire synthesis is scaleable to larger systems. An additional benefit of the continuous flow reactor is the ability to independently vary the residence time of the fluid flowing through the reactor. In principle, this variable should permit the controlled synthesis of nanowires with average lengths adjusted through the reactor residence time. This aspect is still under investigation and has not been experimentally realized to date; instead, nanowire length control was addressed through ultrasonic shortening as discussed in Chapter 9.

After the reaction, the nanowire deposited on the deposition substrate was rinsed with excess supercritical solvent to remove any unwanted organic byproducts and recovered as described above. Alternatively, the nanowire material could be recovered externally in a receiving vial by flowing the material out of the reactor by series short high-pressure pulses. The nanowire samples deposited on the deposition substrate were stored in nitrogen prior to characterization.

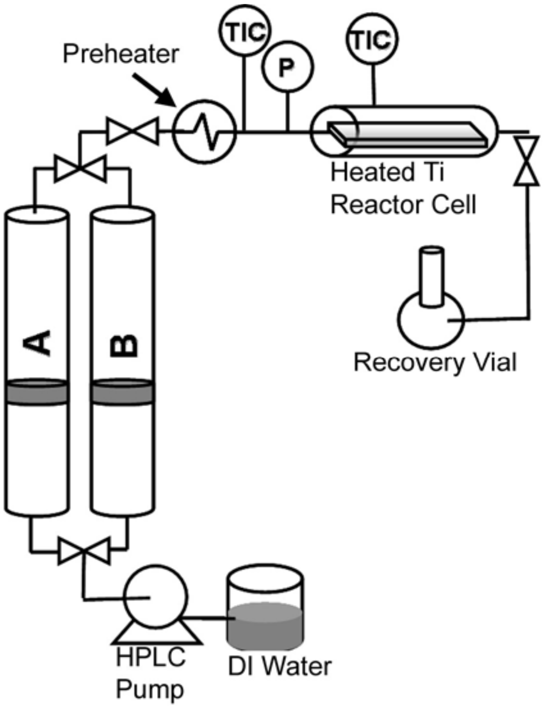

Figure 2.3: Schematic of the continuous flow reactor showing with dual piston system and preheater.

2.2 REACTION SOLUTIONS

Au nanocrystals with dodecanethiol monolayer passivation were prepared using the arrested precipitation method and size-selected according to procedures outlined in the literature.[1,2] The relative size distribution of size selected Au nanocrystals was generally less than 15%. The germanium precursors tetraethylgermane (TEG; $(CH_3CH_2)_4Ge$, Aldrich, 99%) or diphenylgermane (DPG, $(C_6H_5)_2H_2Ge$, Gelest, 95%) were used as received and stored under nitrogen atmosphere. For a typical stock solution, the organogermane was added to anhydrous hexane or cyclohexane at concentration ranging from 5 to 500mM. An Au nanocrystal stock solution in (typically at 1.0 mg/ml in hexane) was added to the precursor solution to attain the desired Au:Ge ratio. Precursor solutions with alternative seed metals such as Al, or Ag were prepared similarly. The synthesis products obtained from reactions in supercritical hexane showed no discernible difference from those in n-hexane, however, reactions carried out at temperatures above $500^{o}C$ showed a higher amount of oily solvent degradation products for cyclohexane than for similar experiments with n-hexane. Consequently, supercritical cyclohexane was only used in initial studies exploring the effects of temperature and precursor concentration with batch and injection syntheses.

2.4 NANOWIRE CHARACTERIZATION

The Ge nanowires were characterized using various techniques. High-resolution scanning electron microscopy (HRSEM) was performed using either a Hitachi S-4500 operated at 10kV or a LEO 1530 operating at 7kV for general imaging and elemental analysis and 1-3 kV for high-resolution imaging. Nanometer-scale energy dispersive X-ray energy spectral maps (EDS, iXRF Systems, Inc.) were obtained on the LEO 1530 HRSEM with 7 kV accelerating voltage. The lateral pixel resolution was 128, with a pixel dwell time of 130 μs, and a minimum of 30 overlaid frames. Ge was detected using the Ge L_α line at 1.188 keV; Au and oxygen (O) were detected using the M and K_α lines at 2.121 keV and 0.525 keV, respectively. Nanometer-resolved elemental contrast images were also obtained using a Robinson Backscattering Electron Detector (RBSD, ETP Semra Ltd.) attached to the LEO 1530 SEM. High-resolution transmission electron microscopy (HRTEM) images and selected area electron diffraction (SAED) patterns were obtained using a JEOL 2010 or a JEOL 2010F electron microscope operating at 200 kV. Elemental characterization on TEM samples was performed using electron energy loss spectroscopy (EELS, Enfina Digiscan) and EDS (Oxford INCA). HRTEM samples were prepared by drop casting a dispersion of Ge nanowires in hexane or isopropanol lacey carbon coated 200 mesh Cu grids (Electron Microscope Sciences). HRTEM was performed on nanowires removed from Si wafers by sonicating in minimal volumes of hexane after the HRSEM characterization. Alternatively, TEM samples could be prepared without intermediate solvent dispersion by directly scraping a TEM grid on the surface of a Ge nanowire containing Si substrate. X-ray photoelectron spectroscopy (XPS) was performed on a Physical Electronics XPS 5700 equipped with monochromatic a Al x-ray source (Al K_α 1.4866 keV). X-ray diffraction (XRD) spectra were obtained on quartz slides using either a Phillips vertical scanning diffractometer, with Cu K_α radiation and a scintillation detector. Thermal analysis of the nanowire ensemble samples was performed on a Perkin-Elmer Series 7 differential thermal analyzer (DTA).

2.5 RESULTS AND DISCUSSION

2.5.1 Effects of Temperature, Pressure, and Organogermane Precursor

Figure 2.4 shows HRSEM images of Ge nanowires synthesized from TEG (Figure 2.4A-C) and DPG (Figure 2.4D-F) via a single injection approach in cyclohexane at 38 MPa at temperatures varying from 300^{o}C to 500^{o}C. A similar series of experiments was carried out with both Ge precursors at a synthesis pressure of 14 MPa, but the gross morphology of the deposited material from this series of experiments did not differ significantly from the ones shown in Figure 2.4. Nanowire growth was seeded with 6.5 nm, and 2.5 nm diameter alkanethiol capped Au nanocrystals for reactions using TEG and DPG, respectively. Similar injection experiments using TEG were performed using size-monodisperse Au nanocrystals with an average diameter of 3.4 nm; however, the nanowire diameter distribution did not have significant statistical difference from that of the wires grown from the larger Au nanocrystals. Ge nanowire deposits observed on the wafers spanning the length of the "hot zone" of the reactor were homogeneous in concentration and size across the entire substrate, thus demonstrating that the reactor contents were well mixed in the cell during synthesis without appreciable temperature gradients.

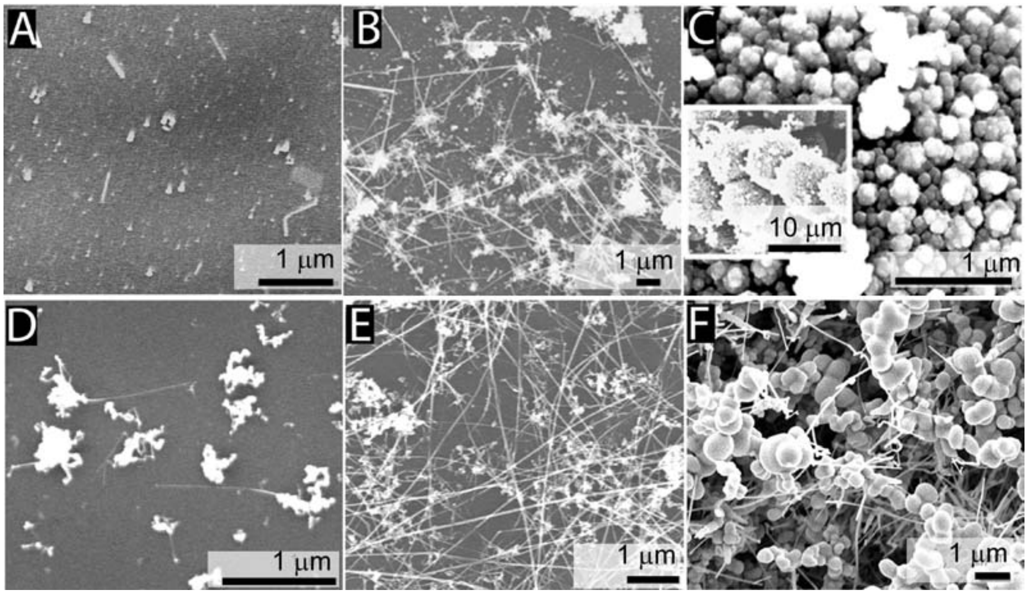

Figure 2.4: HRSEM images of Ge nanowires grown at 38 MPa for 20 minutes using TEG at (A) 300^{o}C, (B) 400^{o}C, (C) 500^{o}C. Ge nanowires grown at 38MPa for 8 min using DPG at (D) 300^{o}C, (E) 400^{o}C, and (F) 500^{o}C. The micrometer sized particles in (C) and (F) are Ge particles as confirmed by nanometer-scale EDS mapping. The morphology of wires produced from DPG with 20 minute reaction time was similar to the once shown in Figure 2d-f. The inset in (C) shows a low magnification image of micrometer spheres formed at 500^{o}C.

Injection syntheses carried out at 250^{o}C with either TEG or DPG did not yield wires. Neither precursor appeared to decompose significantly at this temperature. At 300^{o}C, limited precursor decomposition occurred (Figure 2.4A and D). A few short wires (average diameter of 45 nm and 19 nm for samples prepared from TEG and DPG, respectively) appeared, however, the majority of the product was in the form of Ge particles. Nanometer-scale EDS mapping confirmed that the particulates in Figure 2.4A consist of Ge and not Au. At 400^{o}C, wire production improved significantly. Comparison of HRSEM images of wires formed using TEG and DPG, such as those shown in Figures 2.4B and 2.4E, revealed that DPG yields much higher quality Ge nanowires than TEG. DPG produces longer wires with minimal particle formation. The lengths of the ‘raw’ nanowires was typically on the order of tens of micrometers, low-resolution TEM imaging showed some nanowires with lengths in the range of hundreds of micrometers.* The average wire diameter of the nanowires produced from TEG at 400°C was 87 nm, while DPG under the same synthesis conditions yielded nanowires with an average diameter of 17 nm. The relative standard deviations for the diameters produced from TEG and DPG were 36% and 26%, respectively. The statistical averages were based on the analysis of more than 100 wires per sample. The variation in nanowire diameter resulted in part from the nanocrystal size distribution, which commonly has relative standard deviation of less than 15%. However, microscopic fluctuations in growth conditions can also lead to broadening of the histogram. The growth kinetics also dramatically affected wire morphology and size distributions as well (see discussion below), and nanowires produced from DPG were significantly smaller and more monodisperse than those formed under identical conditions from TEG.

Two primary factors appeared to broaden the nanowire size distribution: (1) Au nanocrystal agglomeration and (2) unfavorable decomposition kinetics in the case of TEG. The extent of liquid alloy seed aggregation in the early stages of the reaction was highly dependent on the synthesis approach (i.e.: batch reaction, injection reaction, or flow reaction) as discussed in detail in section 2.5.6. The

---

* A detailed description of the initial and modified nanowire length distributions is provided in Chapter 9.

injected precursor solution contained relatively size-monodisperse sterically stabilized Au nanocrystals, however, agglomeration of nanocrystals or liquid alloy Au:Ge droplets at elevated temperatures could be expected and would subsequently lead to broad Ge nanowire diameter distributions. A control experiment in which the Au nanoparticles were subjected to the synthesis conditions in the absence of germanium precursor showed significant nanoparticle agglomeration. In fact, it is quite remarkable that the nanocrystals are sufficiently stable to yield nanowire size distributions with standard deviations about the mean diameter less than ±30% when DPG was used as a precursor. The greatest contributor to size distribution broadening appeared to be the wire growth kinetics. TEG gives rise to larger wires with very broad size distributions, while DPG produces smaller wires with relatively narrow size distributions. These differences stem from the different decomposition kinetics of each precursor. TEG appeared to be more kinetically stable, as much less Ge product resulted from the low temperature reactions than when DPG was used. DPG's congener diphenylsilane is known to thermally degrade via a bimolecular disproportionation reaction.[3,4] The first step in the degradation of DPG is presumably the homolytic cleavage of the Ge-H bond, followed by the addition of the diphenylgermyl radical to an aromatic ring in diphenylgermane. The latter reaction has been found to follow first order kinetics in the decay of the diphenylgermyl radical.[5] TEG on the other hand decomposes at a slower rate via a homogeneous unimolecular reaction.[6] Slow decomposition kinetics result in slow Ge supply to the seed particle, which is particularly crucial in the early stages of the wire formation process. Fast decomposition, such as in the case of DPG, led to efficient saturation of the Au nanocrystals to initiate nanowire crystallization. The slower decomposition kinetics of TEG, on the other hand, allowed more time to elapse before the nanocrystals are saturated enough to produce wires. Particle agglomeration can occur during this “lag time”, which could explain the production of larger average wire diameters.

Based on the VLS and SLS mechanisms, one would not expect to form wires at temperatures below the eutectic temperature. However, for the supercritical fluid synthesis Ge nanowires were observed to form at reaction temperatures as low as 300^{o}C. Recently, Wang et al.[7] have reported Ge nanowire synthesis based using germane gas precursor in a CVD system at temperatures as low as 275 ^{o}C. There are two possible explanations for this observation: either the Au:Ge eutectic temperature has been significantly reduced in the nanoscale gold droplets as recently reported by Wu and Yang,[8] or a nanometer-sized solid nucleation particle are capable of nucleating and directing wire growth. The latter possibility was suggested by Kamins et al.,[9,10] who found that Ti nucleated Si wires grew at temperatures up to 500^{o}C below the eutectic, suggesting that a solid nucleation particle has sufficiently high internal diffusion rates to permit wire growth. Similarly, Au nucleated GaAs have recently been synthesized in supercritical hexane at 500^{o}C, which is ~80^{o}C below the eutectic temperature for the pseudo binary Au:GaAs system.[11]

Nanowire synthesis was also attempted at 500^{o}C. HRSEM images of the resulting material are shown in Figure 2.4C and 2.4F for TEG and DPG, respectively. Instead of nanowires, micrometer size spherical particles formed. Nanoscale EDS mapping indicated that the particles were indeed composed of primarily Ge, and XRD revealed that the particulates consisted largely of crystalline cubic Ge. One explanation for particle formation at 500^{o}C is that Ge nanowires formed initially, but subsequently melted into particulates. This hypothesis is based on the findings of Wu and Yang[8] that the Ge melting temperature is significantly depressed in nanowires—to temperatures as low as 600^{o}C for 20 nm diameter wires. DTA scans of nanowire ensemble samples prepared from DPG at 350 ^{o}C, however, did not show any evidence of nanowire melting at temperatures up to 500^{o}C. Another explanation centers on the kinetic competition between wire growth and homogeneous Ge particle nucleation and growth. The precursor decomposed into Ge atoms that can either dissolve into the Au:Ge droplets and crystallize into nanowires, or homogeneously nucleate into spherical particles. At temperatures below 500^{o}C, Ge nucleation from the liquid Au:Ge seed particles was faster than homogeneous Ge particle nucleation. However, at 500^{o}C, nanowire growth could not be sustained because the Ge supply rate to the system overwhelmed the nanowire crystallization rate.

2.5.2 Effect of Ge:Au Ratio

By increasing the Au:Ge ratio to 1:20 instead of 1:2000, the seed particles were able to sustain nanowire growth even at synthesis temperatures as high as 500^{o}C, as shown in Figures 2.5A and 2.5B for DPG and TEG reactants, respectively. However, the inset in Figure 2.5A also shows that homogeneous nucleation of Ge on the nanowire surface remained a competing mechanism, which severely degraded the quality of the nanowires.

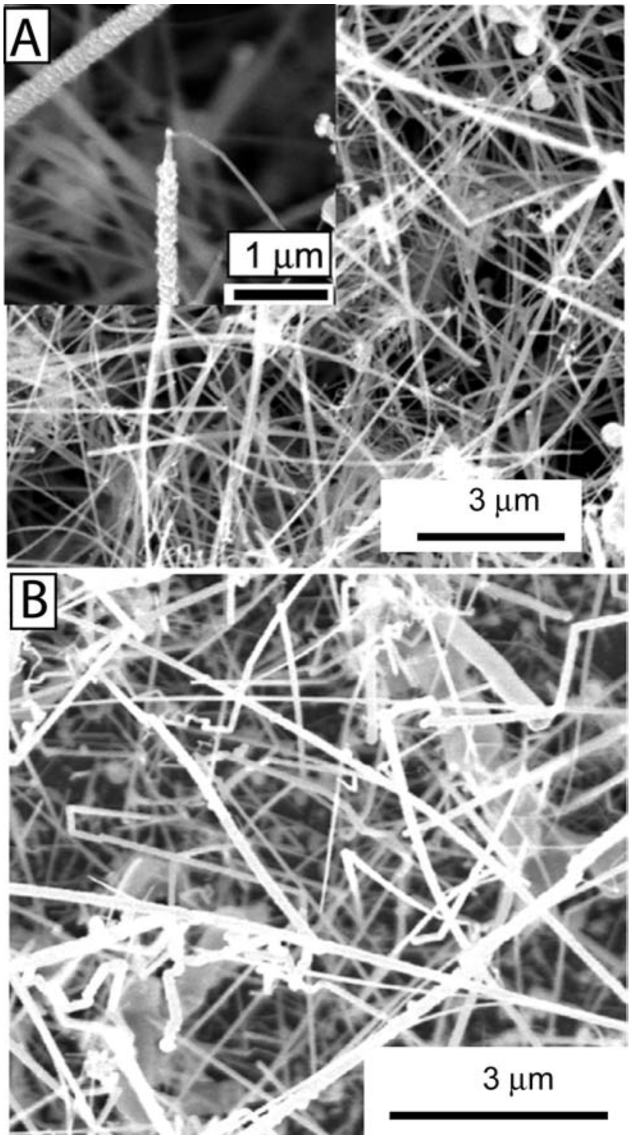

Figure 2.5: HRSEM images of Ge nanowires grown at 500°C and 38 MPa with a Au:Ge ratio of 1:20. (A) Using DPG and (B) using TEG. The inset in (a) shows the growth of excess Ge on the surface of the preexisting nanowire.

2.5.3 Crystallographic Characterization of Ge Nanowires†

The Ge nanowires synthesized in supercritical cyclohexane or hexane using gold nanocrystals as seeds exhibited defect free crystalline cores. Under optimum growth conditions, crystallographic defects were found in less than 5% of the wires investigated via HRTEM. The HRTEM image in Figure 2.6A of a Ge nanowires formed at 370°C and 10 MPa using DPG exhibit cubic diamond crystal structure with the [110] growth direction. Figure 2.6B shows an 8 nm diameter Ge nanowire grown at 400°C and 15 MPa using TEG with a crystalline $Au_{0.72}Ge_{0.28}$ tip. Based on EDS and crystallographic characterization the crystal at the tip was identified as metastable β hcp $Au_{0.72}Ge_{0.28}$ phase, which formed during the rapid quenching of the reaction after the elapsed synthesis time.[12] The abrupt crystalline interface between the tip alloy and the nanowire could prove valuable for future applications that incorporate the seed crystal into the contact design of the device.

---

† A comprehensive structural and crystallographic HRTEM analysis of the nanowires is provided in Chapter 5.

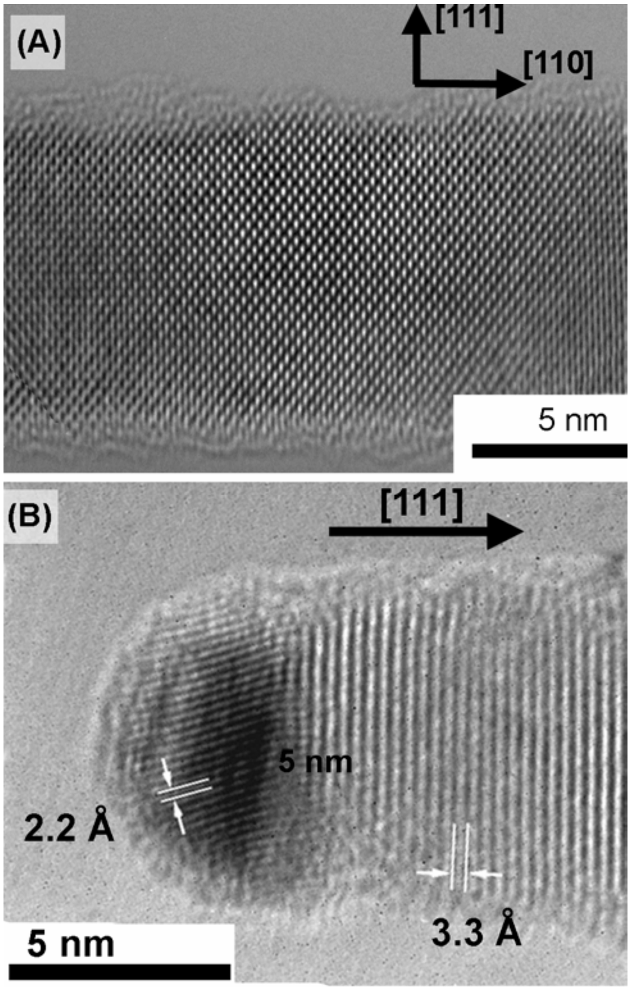

Figure 2.6: HRTEM images of single crystal nanowires; (A) 12 nm diameter Ge nanowire with [110] growth direction (B) Ge nanowire with [111] growth direction and Au seed tip. The 2.2A spacing in the tip corresponds to the (011) planes of metastable β hexagonal Au$_{0.72}$Ge$_{0.28}$

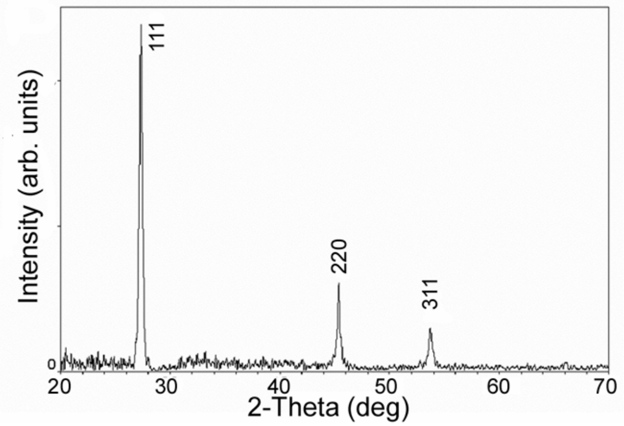

Figure 2.7: Powder XRD pattern of a bulk Ge nanowire sample.

The crystallography of ensemble nanowire samples was also verified using powder XRD as shown in Figure 2.7. The Scherrer formula was used to estimate the effective domain size based on FWHM of the diffraction peaks. The derived nanowire size produced from DPG at 400^{o}C was 20 nm, which agrees well with the 17 nm average wire diameter determined by TEM. Notably, the peak intensity ratios in the XRD pattern in Figure 2.7 differ significantly from those expected for bulk randomly oriented crystalline Ge powder. In bulk Ge, the peak intensity ratio for the (111):(220):(311) reflections is 100:57:40, whereas the ensemble Ge nanowire XRD pattern in Figure 2.7 shows an intensity ratio of 100:24:12. For randomly oriented crystals with anisotropic geometry, such as nanorods, the peak intensity of the reflection corresponding to the long axis is more intense than in the bulk powder pattern. Due to their large aspect ratio, the nanowires in this sample however are deposited in carpet like films with the predominant [110] growth axis aligned parallel to the sample surface[‡], giving rise to the observed reduction in the intensity of the (110) reflection.

2.5.4 EDS Mapping of Ge Nanowires

A further confirmation of the chemical composition of the nanowire and the presence of Au seed particles at the tops of the majority of the wires is provided by nanometer-scale EDS mapping of the Ge nanowires (Figure 2.8). The EDS map also illustrates that prior to atmospheric exposure the Ge nanowires are not significantly oxidized.[§] Despite extensive elemental characterization efforts, the extent of Au incorporation into the single crystal Ge nanowire could not be established. The largest solubility of Au in Ge is less than 0.0014 atomic % (or $6(10^{14})$ cm^{-3})[13] which is far below the detectable limit limits of spatially resolved characterization methods such as EELS or EDS.

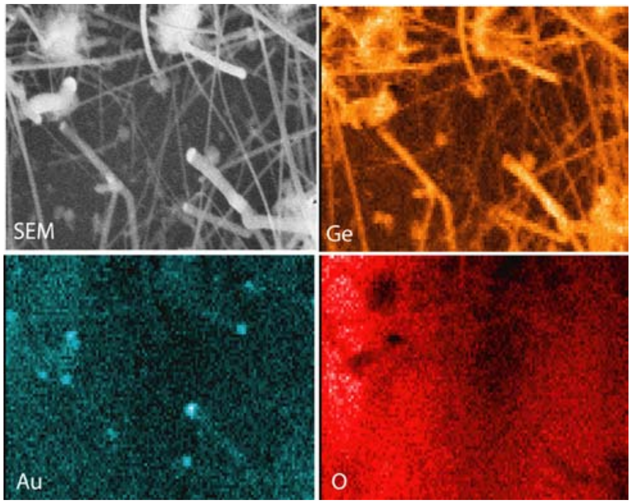

Figure 2.8: EDS map of Ge nanowires synthesized at 450°C and 10 MPa showing Ge, Au, and O atomic profiles in the nanowires. (Ge Lα 1.188 eV, Au M 2.121 eV, O Kα 0.525 eV)

[‡] The morphology of ensemble Ge nanowire deposits on substrates is discussed in Chapter 8.

[§] Chapter 4 provides a details XPS study of the oxidation of Ge nanowire surfaces exposed to wet and dry environments.

2.5.5 Effects of Precursor Concentration

While the injection solutions used for all experiments discussed above contained 200 mM, complimentary experiments with injection solutions diluted to 20 mM and concentrated to 800 mM were carried out with TEG and DPG at 450°C and 14 MPa. The results are shown in Figure 2.9. While the precursor concentration did not appear to affect the morphology of the nanowires grown with DPG, the materials obtained from the TEG experiments showed significant concentration dependence. The low TEG concentration produced very different nanowire network structures (Figure 2.9A) than those shown in Figure 2.4. The "sea urchin" structures seen in Figure 2.9A contained up to 30 nanowires with diameters ranging from 20 to 50 nm and lengths up to 1.5 μm. Nanowires grown from DPG at the same concentrations did not exhibit the sea urchin morphology (Figure 2.9B).

The sea urchin Ge nanowire structures were imaged by HRSEM (Figure 2.9A) using a Robinson backscattering detector (RBSD). Gold particles exist at many of the tips of the nanowires protruding from the central structure. Zhu and co-workers[14] have reported similar 3D structures composed of amorphous silicon oxide wires radially attached to Co catalyst particle. The mechanism proposed in Ref. 14 involves an agglomerated catalyst particle at the core and smaller catalyst particles at the tips of the wires. The "nanoflower" structures observed Ref. 14 differ in two aspects from our observed structures: (1) EDS measurements did not indicate that Au resides at the center of the structure, and (2) the wires are crystalline, as confirmed by the HRTEM. A possible mechanism for the formation of these structures begins with homogeneous nucleation of a large Ge cluster followed by Au nanocrystal adsorption. The combined effects of low precursor concentration and slower decomposition rate of TEG compared to DPG appeared to delay Ge wire nucleation for the seed particles. Therefore, increased agglomeration of non-saturated Au:Ge alloy droplets occurred in the early stage of synthesis compared to the experiments in which the precursor concentration was higher. At later stages in the reaction, Ge continued to add to the agglomerated structure, most likely through dissolution into the Au nanocrystals, which encouraged growth of the spikes from the structure.

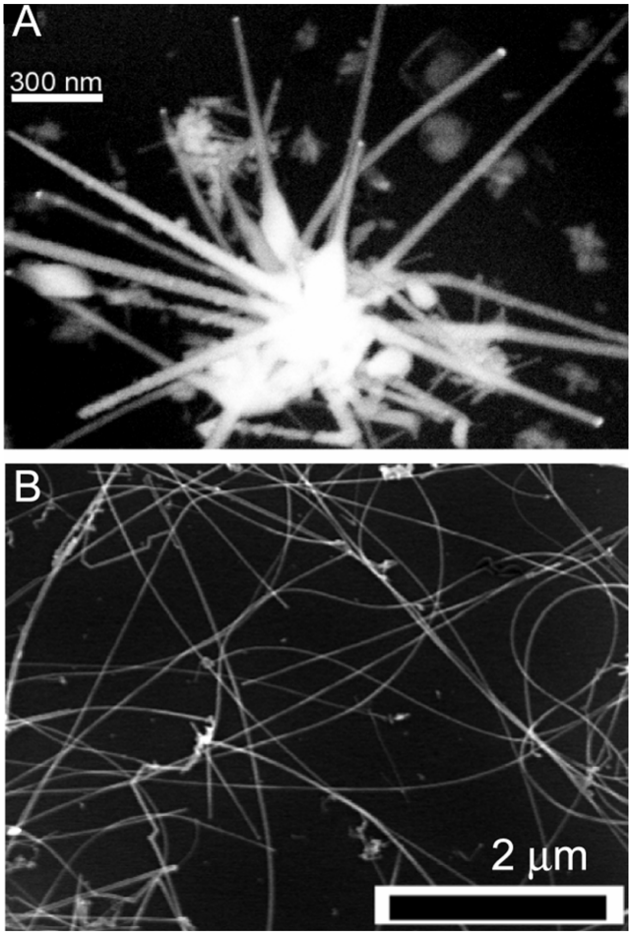

Figure 2.9: HRSEM images of Ge nanowires grown at different precursor concentrations: (A) image obtained with RBS detector of Ge nanowire structure formed by degrading TEG (20 mM) injected at 450°C, 13.8 MPa, (B) Ge nanowires formed at 450°C, 13.8 MPa with an injection solution of 20mM DPG. The Au:Ge ratio in both experiments was 1:200. In (a), backscattered electrons show the higher contrast Au particles at some of the tips of the wires protruding from the central structure.

2.5.6 Effects of Injection Method

In order to control the nanowire diameter distribution, the agglomeration of seed nanocrystals in the reactor must be limited. The initial supercritical fluid nanowire synthesis reported by Holmes et al in 2000,[15] was based on a batch reaction similar to the one described in section 2.1.1. In this approach, a solution containing monolayer stabilized Au nanocrystals and Si or Ge precursor was loaded into a batch reactor cell under inert nitrogen conditions. The reactor cell was then quickly heated to the synthesis conditions and reached the setpoint temperature within approximately 2 minutes. While the fast setup time associated with this synthesis approach permitted the rapid investigation of a broad parameter space, the materials produced had some major disadvantages as discussed below. As the reactor containing the precursor solution approached the setpoint temperature, the organogermane precursor degraded and gradually dissolved into the Au seed crystals forming liquid alloy seed crystals. During the initial nucleation stages, the liquid seed droplets were particularly susceptible towards agglomeration since the Ge supply to the droplet was limited by the decomposition rate at the instantaneous temperature during the ramp up time. The agglomeration of alloy droplets during this 'lag time' is believed to be the key factor for the broadening of the nanowire distribution encountered in nanowire samples prepared in batch reactor even when the kinetically more favorable DPG was used as the Ge precursor. The nanowire growth rate dependence on seed particle diameter is another important consideration for the broadening of the nanowire diameters encountered in these batch reactions.

Experimental work by Givargizov on Si whiskers[16] and Wu and Yang on Si/Ge heterostructure nanowires[17] showed that the nanowire growth rate is inversely proportional to the nanowire diameter which is theoretically supported by the Gibbs-Thompson effect (see Appendix B). According to the Gibbs-Thompson effects, smaller diameter seed alloys require higher supersaturation levels and are hence less likely to nucleate than larger diameter seed alloys at similar levels of supersaturation. Smaller liquid alloy droplets were consequently more likely to agglomerate into larger droplets during the nascent stages of nanowire nucleation, eventually resulting in the formation of nanowires with diameters significantly larger than the diameter of the Au seed particles.

In an effort to reduce size, broadening of the seed droplet during these initial growth stages the reactor system was modified to quickly inject the solution containing precursor and Au seed nanocrystal into a preheated and pre-pressurized reactor, as described in Section 2.1.2. The histograms in Figure 2.10A and 2.10B show the significant reduction in average nanowire diameter and polydispersity accomplished through this modification

Additional improvements toward the synthesis of technologically significant quantities of high quality, size monodisperse nanowires have been accomplished by converting the supercritical fluid method from an injection based system to a continuous flow reactor. Compared to the batch and semi-continuous processes, the flow-through reaction can be carried out with much lower precursor concentrations which minimized the agglomeration of the Au seeds during initial nucleation stages and, hence, reduced the average nanowire diameter and polydispersity.[18] This technique allows for the production of high quality Ge nanowires with a yield of approximately 80% at a rate of 10 mg/hr. A diameter histogram of nanowires grown via the continuous flow reaction is shown in Figure 2.10C which also demonstrates further improvement in diameter polydispersity compared nanowire obtained from batch or injection reactions. More importantly, the continuous nature of this approach permits scale up for the synthesis of technologically significant quantities, which cannot be met by CVD, based methods. The optical photograph in Figure 2.11A for example shows a 15 mg nanowire deposit on a 20 x 4 mm Si substrate from a single reaction and the SEM image in Figure 2.11B illustrates the high quality of nanowires synthesized under optimized growth conditions.

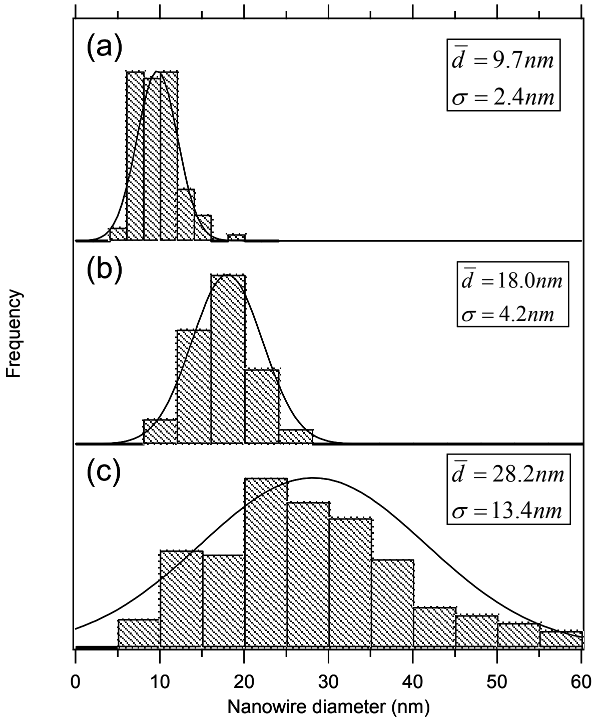

Figure 2.10: Histograms of the nanowire diameter size distributions produced by various modifications to the supercritical fluid synthesis. (A) Batch reaction with single injection followed up by pressurization (total injection time about 50 – 60 sec). (B) Semi-batch reaction with rapid injection of Au seed nanocrystals and 100mM diphenylgermane precursor solution. (C) Continuous flow reaction with a reduced diphenylgermane concentration of 10 mM to limit seed droplet aggregation prior to nanowire nucleation.

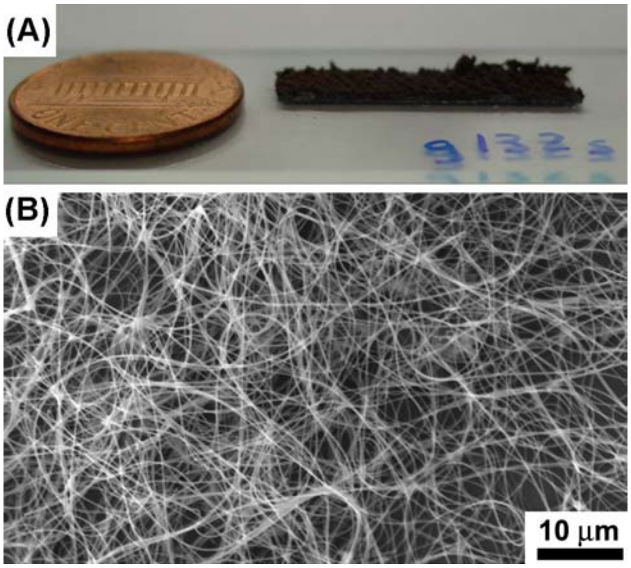

Figure 2.11 (A) Optical photograph of a 15 mg nanowire sample produced in a single continuous flow reaction and (B) SEM image of nanowires produced under optimized conditions.

2.5.7 Effects of Seed Metal Chemistry

The role of the seed particle in nanowire growth is to direct the nucleation of the nanowire material into a one-dimensional crystal and to define the diameter of the nanowire. The initial choice for a seed particle was primarily based on the presence of a low temperature liquid eutectic in the bulk equilibrium binary phase diagram. In this regard Au is a particularly attractive seed metal since it forms a simple eutectic with Si, Ge, and GaAs at 363, 361 and 630°C, respectively. Additionally, Au nanocrystals can be easily synthesized via the arrested precipitation method and refined via size selective precipitation.[1,2] The raw synthesized Au nanocrystals typically have a size polydispersity of approximately 20% relative standard deviation, which can be significantly reduced as low as 7%

through careful size selective precipitation with anti-solvent. Figure 2.12A shows a typical TEM image of size selected Au nanocrystals deposited on a carbon support film. The inset shows a high-resolution image of a 4.1 nm diameter Au nanocrystal with the (111) lattice fringes separated by 2.3Å clearly visible.[**]

In spite of these apparent benefits of Au as a seed crystal for semiconductor nanowire growth, alternative seed metals merit investigation for the following two reasons: (1) to replace Au with a seed metal that is compatible with current semiconductor processing facilities, and (2) to determine the possible catalytic effects of Au in the degradation of the organogermane or organosilane precursor.

2.5.7.1 Replacement of Au with Al nanocrystals

The compatibility of Si and Ge nanowires with current semiconductor technology is of paramount importance since future nanoelectronics are likely to consist of hybrid devices incorporating 'top-down' semiconductor architecture with nanowires as 'bottom-up' building blocks. Gold has energy levels close to the middle of the bandgap in both Si and Ge, which causes it to act as an efficient recombination center and a minority lifetime killer.[19] These characteristics are detrimental for current microelectronics research and fabrication; consequently, Au is considered as a severe contaminant and avoided for most processing steps. The presence of Au in ensemble Ge nanowire samples therefore presents a significant hurdle to be overcome before semiconductor nanowires can be integrated into current microelectronic fabrication processes. While the average

---

[**] The Au nanocrystals and TEM images were provided by the courtesy of Aaron E. Saunders.

ensemble concentration of Au in an ensemble Ge nanowires is approximately 0.05 atomic %, elemental characterizations preformed to date suggest that the Au appears to be limited to the seed end of the nanowire (see Figure 2.8). Chemical or physical methods for the removal of the seed particle in these ensemble sample are presently unavailable, although, recent work by Ng et al.[20] showed that the Au seeds on vertically aligned ZnO nanowires could be removed through chemical mechanical polishing steps.

Instead of removing Au from nanowire samples, I sought to replace Au with seed metals that are compatible with microelectronic processes. Aluminium has no near midgap energy levels in Ge or Si[19] and additionally forms a simple eutectic with Ge at with Ge at 420^{o}C.[13] However, to date efforts to synthesize Ge nanowires nucleated by Al nanoparticles have seen little success. Compared to Au, the Al nanoparticles appeared to be much less effective in nucleating wire growth and consequently only allowed Ge nanowire synthesis with a prohibitively low yield. Unlike the thiol-monolayer passivated Au nanocrystals, the commercially available Al nanocrystals (Nanotechnologies, Inc.) were surface terminated with a thin oxide layers and consequently dispersed very poorly in most organic solvents. The poor dispersibility of the Al nanoparticles led to the formation of multi-particle agglomerates (see Figure 2.12B) which readily precipitated from solution. This factor combined with the presence of a thin oxide layer on the metal particle surface are believed to be the key causes for the ineffectiveness in nucleating Ge nanowire from Al seed particles.

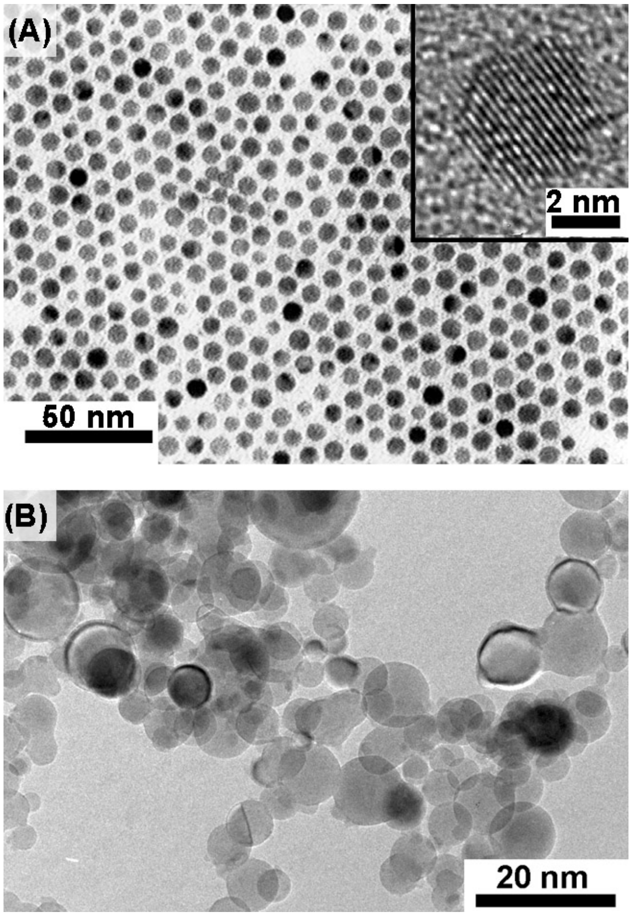

Figure 2.12: (A) Size selected Au nanoparticles with an average diameter of 5.2 nm and a relative standard deviation of 12%. Inset: A 4.1 nm Au nanocrystal with resolved 0.23 nm (111) lattice planes. (B) Polydisperse Al nanocrystals from Nanotechnologies, Inc.

2.5.7.2 Possible Catalytic Effects of Au Nanocrystals

While bulk Au as a noble metal is catalytically inert, recent studies on the formation of siloxane nanowires[21] and the Au catalyzed combustion of CO [22] have suggested that nanoscale Au may have catalytic activities. The possible catalytic activity of Au nanocrystals in the degradation of the precursor and growth of semiconductor nanowires still remains an open question. Control experiments in which diphenylgermane was injected or flown through the reactor in the absence of Au seed particles for example yielded very little product wherein only a minor fraction of the precursor degraded to form non-crystalline polyorganogermane products or malformed Ge nanocrystals. In fact, Lu et al.[23] have recently shown that the thermolytic degradation of diphenylgermane in supercritical octanol in the absence of any seed metals proceeded with a conversion of less that 7 % to yield Ge nanocrystals. Thermolytic degradation of diphenylgermane in supercritical hexane in the presence of Au seed crystals on the other hand led to a near 80% conversion toward nanowires. Similar reactions carried out in supercritical octanol or mixtures of octanol and hexane also resulted in the formation of poorly formed Ge nanowires or nanorods with a yield near 50%.[††]

To address the catalytic influence of the seed particle in the nanowire growth reactions alternative metals nanocrystals with known catalytic activity in the bulk phase were investigated. Bulk Ni metal has well known catalytic activities for a variety of reactions, however, the lowest eutectic temperature in the binary Ge:Ni equilibrium phase diagram is 762°C,[13] which is far above the highest temperature attainable in supercritical hexane. Attempts to synthesize Ge nanowires nucleated by Ni nanocrystals have not been successful to date, however recent experiments in the Korgel group by Tuan et al.[24] have shown that Ni particles can direct the growth of amorphous Si nanowires. Additionally, metal nanocrystals such as Mn and Ag - both of which were prepared by solution

---

[††] The results for Ge nanorods synthesis in a supercritical fluid mixture of hexane and octanol are discussed in Chapter 9.

methods similar to the Au synthesis - were investigated as alternative seed metals for nanowire growth. However, experiments with these seed metal did not result in the formation of Ge nanowires so that Au nanocrystals appear to remain the most effective seed metal for the synthesis high-quality single crystal Ge nanowires.

2.6 CONCLUSIONS

Sterically stabilized gold nanocrystals were used to promote the growth of milligram quantities of Ge nanowires in a supercritical fluid environment. EDS mapping confirmed the significance of Au nucleating particles to nanowire growth. Nanowire formation was observed at growth temperatures below the eutectic point of the bulk material, possibly due to reduced eutectic temperature in nanostructures or the possibility of a solid nucleation particle. The comparison of DPG and TEG as Ge precursors illustrated the importance of the precursor decomposition rate to the morphology of the synthesized nanowires. The quality of Ge nanowires formed from DPG is superior to those obtained from TEG due to the faster decomposition of the former. The optimum temperature range for Ge nanowire synthesis in supercritical hexane is between 350^{o}C and 400^{o}C, while varying the pressure between 13.8 MPa and 38 MPa did not affect the gross wire morphology. Low TEG concentrations favor the formation of aggregated sea urchin nanowire shaped structures, whereas high concentrations result in the formation of dense nanowire networks for both TEG and DPG. Agglomeration of

Au nanocrystals or the Au:Ge droplets during the initial stages of the reactions appeared to limit the diameter control of the Ge nanowires nucleated from the Au seeds. The nanowire diameter distribution was significantly reduced by reducing the synthesis approach from a batch system to an injection system. Highest quality nanowires are obtained in a continuous flow reactor, which is scaleable to provide technologically significant quantities of nanowires. Ag, Al, Mn, and Ni were investigated as potential alternative seed particles for nanowire growth, however, none matched the effectiveness of Au.

2.7 REFERENCES

(1) Brust, M.; Walker, M.; Bethell, D.; Schiffrin, D. J.; Whyman, R. *Journal of the Chemical Society, Chemical Communications* **1994**, 801-802.

(2) Korgel, B. A.; Fitzmaurice, D. *Physical Review Letters* **1998**, *80*, 3531-3534.

(3) Coutant, R. W.; Levy, A. "A kinetic study of the thermal decomposition of selected cyclohexyl and phenylsilanes," Aerospace Research Laboratories United States Air Force, 1969.

(4) Levy, A.; Coutant, R. W.; Merryman, E. L.; Trent, D. E. "The thermal stability of some arylsilanes," Aerospace Research Laboratory United States Airforce, 1965.

(5) Clark, K. B.; Griller, D. *Organometallics* **1991**, *10*, 746-750.

(6) Geddes, R. L.; Edward Mack, J. *J. Am. Chem. Soc.* **1930**, *52*, 4372-4380.

(7) Wang, D.; Dai, H. *Angewandte Chemie, International Edition* **2002**, *41*, 4783-4786.

(8) Wu, Y.; Yang, P. *Adv. Mater.* **2001**, *13*, 520.

(9) Kamins, T. I.; Williams, R. S.; Chen, Y.; Chang, Y. L.; Chang, Y. A. *Appl. Phys. Lett.* **2000**, *76*, 562.

(10) Kamins, T. I.; Williams, R. S.; Basile, D. P.; T., H.; Harris, J. S. *J. Appl. Phys.* **2001**, *89*, 1008.

(11) Davidson, F. M.; Schricker, A. D.; Wiacek, R. J.; Korgel, B. A. *Adv. Mater.* **2004**, *16*, 646-649.

(12) Schluckebier, G.; Predel, B. *Z. Metallkd.* **1980**, *71*, 535.

(13) Massalski, T. B.; Murray J.L., B. L. H., Baker H., Ed.; American Society for Metals: Metals Park ,Ohio, 1986.

(14) Zhu, Y. Q.; Hsu, W. K.; Terrones, M.; Grobert, N.; Terrones, H.; Hare, J. P.; Kroto, H. K.; Walton, D. R. M. *Adv. Mater* **1998**, *8*, 1859.

(15) Holmes, J. D.; Johnston, K. P.; Doty, R. C.; Korgel, B. A. *Science* **2000**, *287*, 1471-1473.

(16) Givargizov, E. I. *Journal of Crystal Growth* **1975**, *31*, 20-30.

(17) Wu, Y.; Fang, R.; Yang, P. *Nanoletters* **2002**, *2*, 83-86.

(18) Hanrath, T.; Lu, X.; Johnston, K. P.; Korgel, B. A., Growth of Single Crystal Nanowires, Provisional Appl. 60/485,244, **2004**, USA,

(19) Sze, S. M. *Physics of Semiconductor Devices*; 2nd ed.; Wiley: New York, 1981.

(20) Ng, H. T.; Han, J.; Yamada, T.; Nguyen, P.; Chen, Y. P.; Meyyappan, M. *Nano Letters* **2004**, *4*, 1247-1252.

(21) Prasad, B.; Stoeva, S.; Sorensen, C.; Zalkovski, V.; Klabunde, K. *J. Am. Chem. Soc.* **2003**, *125*, 10488.

(22) Sanchez, A.; Abbet, S.; Heiz, U.; Schneider, W.-D.; Häkkinen, H.; Barnett, R. N.; Landman, U. *J. Phys. Chem. A.* **1999**, *103*, 9573.

(23) Lu, X.; Ziegler, K. J.; Ghezelbash, A.; Johnston, K. P.; Korgel, B. A. *Nano Letters* **2004**, *4*, 969-974.

(24) Tuan, H. Y.; Hanrath, T.; Lee, D. C.; Korgel, B. A. *unpublished results*.

Chapter 3: Synthesis of Silicon Nanowires in supercritical fluid

3.1 INTRODUCTION

Research in metal-seeded semiconductor nanowire growth originated from whisker growth studies in the 1960s when Wagner and Ellis synthesized micrometer scale whiskers in a CVD reactor by decomposing silane in the presence of Au thin films on a substrate.[1-3] The whisker growth process from their seminal work was described by the vapor-liquid-solid (VLS) mechanism which is described in detail in Chapter 5. Lieber and co-workers later applied similar CVD growth of Si, Ge, and GaAs nanowires with nanometer sized metal seeds generated by laser ablation.[4-6] Alternative Si nanowire synthesis methods, such as the oxide assisted growth,[7] or processes based on physical evaporation of Si [8] were subsequently developed by other researchers. However, these synthesis methods generally produced low quality Si nanowires with many crystallographic defects, thick oxide coatings, and broad diameter distributions.

For full utilization of the unique electronic and optical properties of Si nanowires synthesis methods which provided controlled crystallography and diameter distributions were required. The growth of Si nanowires in supercritical fluid was first described by Holmes et al.,[9] who demonstrated that relatively size monodisperse sterically stabilized Au nanocrystals dispersed in supercritical fluid could be used to seed the growth of single crystal Si nanowires with diameters less than 10 nm. Recently, Holmes and co-workers have reported that the supercritical fluid synthesis approach can also be combined with mesoporous templates to direct the formation of high-density three-dimensional arrays of semiconductor nanowires.[10-12] In this approach, the degraded precursor material is not directed toward one-dimensional crystallization by the presence of a seed crystal; instead, the one-dimensional structures are obtained as the material fills the nanometer wide channels of the silica matrix.

In spite of the many parallels between the synthesis of Si nanowires and Ge nanowires discussed in Chapter 2, the precursor degradation chemistry and nanowire crystallization are quite different. In this work, various organosilanes were investigated for they suitability as precursors in supercritical fluid Si nanowire growth. Additionally, the growth of Si nanowires nucleated from free-floating Au seed crystals is compared to syntheses in which the seed crystal is molecularly tethered to the substrate.

3.2 EXPERIMENTAL

3.2.1 Precursor Solutions

In addition to the alkyl- and phenyl-substituted precursors considered in Chapter 2, this chapter explores a broader range of organosilanes as potential precursors for Si nanowire synthesis including the following:

1) diphenylsilane (DPS,Gelest)
2) monophenylsilane (MPS, Gelest)
3) pentamethylcyclopentadienylsilane (Cp^*SiH_3, UT-Austin[*])
4) tetraethylsilane (TES, Aldrich)

---

[*] Prepared by Rob Wiacek according to methods described in Ref. (13).

5) octylsilane (OS, Gelest)
6) trisilane (TS, Aldrich)

The molecular structures of (1), (3), and (4) are shown below in Figure 3.1. For injection and basic flow through reactions, the synthesis solutions were prepared by mixing the organosilane precursor and size selected Au nanocrystals in a N_2 glove box as described in Chapter 2.

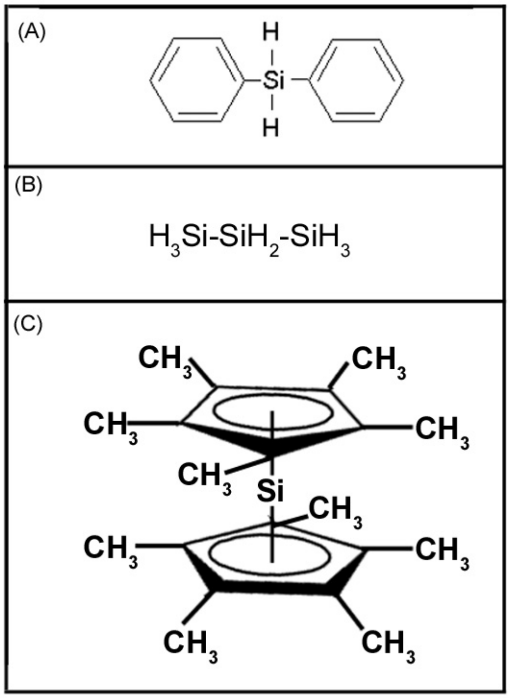

Figure 3.1: Molecular structures of organosilane precursors investigated for Si nanowire growth. (A) diphenylsilane, (B) trisilane, and (C) pentamethylcyclopentadienylsilane

3.2.1 Preparation of Au Seed Crystals Tethered to a Si Substrate

Sterically stabilized gold nanocrystals were covalently attached to a Si substrate functionalized with 3-mercapto-propyl-trimethoxysilane (MPTMS, Aldrich) as follows. A Si wafer (<100>, with ~10 nm thermal oxide, Wafer World, Inc.) was cut into 4 × 20 mm samples that were degreased with distilled deionized water (D-H_2O) and acetone in an ultrasonic bath. The Si substrates were immersed in a HCl:methanol (w:w=1:1) solution and then 98% H_2SO_4 each for 30 minutes. After rinsing with D-H_2O and drying with N_2, the substrates were immersed for one hour in a dilute aqueous solution of 1:1:40 (v:v:v) MPTMS (Gelest, Inc.):D-H_2O:isopropyl alcohol to functionalize the surface. The MPTMS-treated Si substrate was transferred to a colloidal dispersion of alkanethiol-coated Au nanocrystals in chloroform. The Au nanocrystals were synthesized according to the procedures described in the literature.[14,15] After incubating for 2 to 10 hours at room temperature, the substrate was rinsed with and stored in under nitrogen for later use.

3.2.2 Continuous Flow Reactions

Flow through reactions with Au seed particles homogeneously mixed with the precursor solution were performed under the same conditions as the continuous flow Ge nanowire reactions in Chapter as described in Chapter 2. For flow-through reactions with the Au seed crystals covalently bonded to the substrate the flow reactor was a modified 2 mL (0.5 cm I.D., 2.0 cm O.D. and 12.5 cm long) high-pressure titanium grade-2 cell with both ends connected to 1/16” O.D. and 0.03” I.D. stainless steel high-pressure tubing via titanium grade-2

LM-6 HIP reducers (High Pressure Equipment). Anhydrous cyclohexane and the modified Si substrate were loaded into the cell under an inert N_2 atmosphere in a glove box. Two stainless steel cylinders (1.7 cm I.D., 2.5 cm O.D. and 20 cm long) were equipped with stainless steel pistons and ethylene propylene O-rings. In the glove box, one of these cylinders was loaded with anhydrous cyclohexane and the other with an organosilane containing cyclohexane stock solution. The two cylinders and the reactor cell were then removed from the glove box and connected to the heater system and preheater as shown in Figure 2.3 (Chapter 2). Typical preheater temperature settings were in the range of 150-350°C and reactor cell temperatures were adjusted between 350 and 500°C. The temperature was controlled by thermocouples and temperature controllers as described previously. The flow rates of the DPS solution were controlled by the HPLC pump, which ranged from 0.1 to 3 mL/min. In contrast to the micrometering valve used in previous flow-through experiments, the reactor effluent in these experiments was controlled through an SS-4R3A back-pressure regulator (Swagelok) connected after the reaction cell and a digital pressure gauge (Stratford) between the preheater tubing and the cell maintained the pressure at 24.1±1.4 MPa. After the elapsed reaction time, solvent was flushed through the cell at 3 mL/min to remove undesired reaction byproducts and particulates from the system. The nanowire products were stored under nitrogen environment prior to characterization.

3.3 RESULTS AND DISCUSSION

3.3.1 Effect of Si Precursor

3.3.1.1. Diphenyl –and monophenylsilane

The results in Chapter 2 have demonstrated that Ge nanowires from diphenylgermane can be grown at temperatures as low as 350°C. Similar reactions with diphenylsilane at such low temperatures however did not result in the formation of appreciable quantities of solid product. Instead, the reaction products using diphenylsilane (DPS) as the precursor for synthesis temperatures up to 420 °C resulted almost exclusively in the formation of orange discolored oily products, presumably polyorganosilanes. Injection and batch reactions in supercritical hexane at temperatures as high as 500°C are complicated by the formation of oily by-products from the thermolytic degradation of the hexane solvent. Flow through reactions on the other hand are less strongly affected by the decomposition of the solvent since the exposure time to the degradative high temperature environment is limited.

Figure 3.2A shows an SEM image of the products obtained from a flow through reaction using 10 mM DPS solution with Au:Si ratio of 1:1000, at 500°C and 8 MPa with a flowrate of 0.2 ml/min commensurate with a reactor residence time of 80 sec. In contrast to reaction with diphenylgermane under similar conditions, the reaction product from DPS was mostly in the form of malformed amorphous silicon nanofibers. The raw reaction yield (conversion of injected silicon to solid products) from this reaction was only near 35% with nearly 80%

of the produced material in the form of amorphous fibers or particles and the remainder in the form of crystalline wires.

Phenylsilanes are known to degrade via a disproportionation reaction.[16] Based on the relative energies of the Si-H and Si-phenyl bonds (299 and 435 kJ/mol, respectively),[17] the limiting step in this degradation scheme is the cleavage of the Si-phenyl bond, therefore the mono-substituted aryl silane (MPS) is expected to degrade more readily than its di-substituted counterpart DPS. A flow through reaction with MPS under synthesis parameters similar to those discussed for DPS in Figure 3.2B also resulted in the formation of amorphous Si nanofibers. Compared to the DPS reaction, MPS provided slightly higher raw product yield with a lower fraction of micrometer particle byproducts.

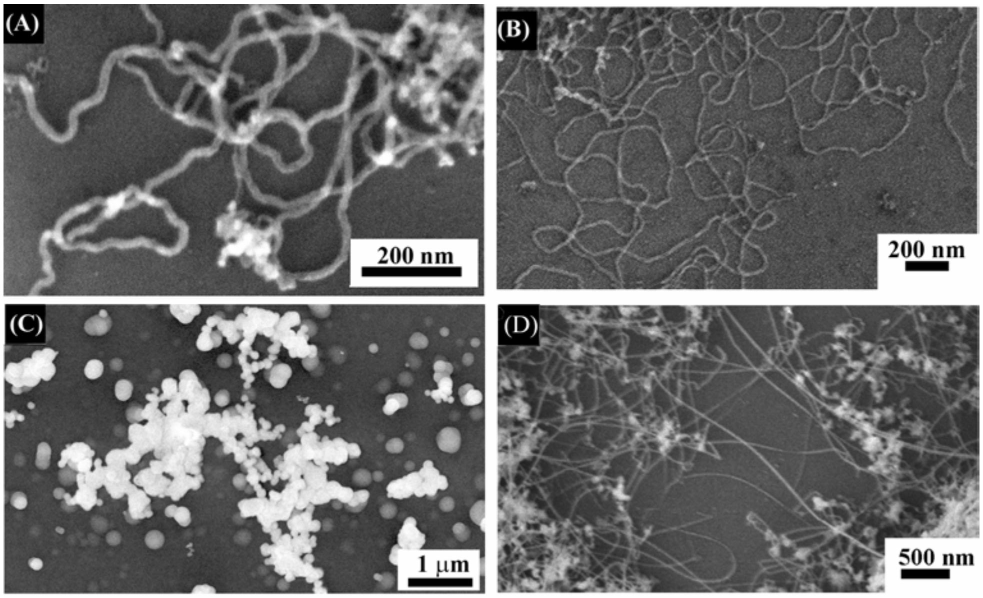

Figure 3.2: SEM images of Si nanowires synthesized in a continuous flow reactor using (A) DPS, (B) MPS, (C) trisilane, and (D) Cp*SiH_3 .

3.3.1.2 Tetraethyl and octylsilane

Tetraethylgermane has been used as a suitable, albeit not optimal, precursor for the synthesis of Ge nanowires (see Chapter 2). Experiments with the silicon congener, tetraethylsilane, under the same synthesis conditions as discussed above for DPS and MPS, on the other hand only resulted in the formation of micrometer sized spherical particles. An elemental characterization of these particles using EDS revealed their composition to be predominantly Si and C. These results illustrate the profound differences in the decomposition chemistries of alkyl substituted silanes and germanes. In fact, tetraethylsilane and tetramethylsilane have been used in the CVD for the growth of near stoichiometric silicon carbide (Si_XC_{1-x}) coatings.[18-20]

The extent of carbon incorporation into the decomposition product should significantly less for a mono-alkyl substituted precursor, like octylsilane since only one Si-C bond has to be cleaved. However, reactions using octylsilane as the Si precursor only resulted in the formation of oily organosilane films with minute amounts of nanometer-sized particles dispersed in the organic film matrix. Recent experiments in the Korgel group by Tuan however have shown that octylsilane can be used as a suitable precursor for the growth of amorphous silicon nanofibers when reacted in supercritical toluene in the presence of Ni seed particles.[21]

3.3.1.3 Trisilane

The highly reactive silanes has been the precursor of choice for many CVD based Si nanowire syntheses.[22,23] Primitive silanes like monosilane and disilane are gases at room temperature and can consequently not be used in solution-based syntheses. Trisilane, with a boiling point of 53°C however be incorporated into the solution based synthesis. The easy Si-Si bond fission in trisilane however requires extensive experimental caution since trisilane readily decomposes in the presence of traces of moisture or air. Synthesis products from the experiments using trisilane under the same parameters as for DPS and MPS above are shown in Figure 3.2C. The SEM image shows that the highly reactive trisilane reacted to form micrometer-sized particles, which consisted mostly of amorphous, and polycrystalline Si. Presumably, the rapid decomposition rate of trisilane drastically overwhelmed the rate at which Au particles were able to adsorb Si form the surrounding environment and direct crystallization towards the formation of one-dimensional nanowires. Instead, the decomposed material nucleates homogeneously to form micrometer-sized particles.

3.3.1.4 Pentamethylcyclopentadienylsilane

Pentamethylcyclopentadienylsilane (Cp^*SiH_3) is a promising alternative silicon precursor which has already been used in plasma-enhanced CVD processes.[24] The pentamethylcyclopentadienyl (Cp*) ring sterically protects the silicon and thus allows for easier handling of the precursor without the extensive precautions required for trisilane. Furthermore, in comparison to the phenyl or alkyl groups discussed above, the Cp* ring is a much better leaving group allowing selective hemolytic cleavage of the silicon carbon bond at relatively low temperatures.

Figure 3.2D shows an SEM image of the material obtained from a reaction in which Cp^*SiH_3 served as a precursor with otherwise similar synthesis parameters as described for the other silicon precursors is described above. The Cp^*SiH_3 precursor underwent near complete conversion, however the specificity of the reaction product toward crystalline nanowires was less than 30% with the majority of the product in the form of nanometer and micrometer sized silicon agglomerates. Compared to the phenyl– and alkyl substituted organosilanes discussed above the decomposition of Cp^*SiH_3 appeared to be more favorable towards the growth of Si nanowires. Further optimization of the synthesis of Si nanowires in supercritical fluid using Cp^*SiH_3 as the precursor is required to attain the similarly technologically significant quantities of high quality nanowires as are currently possible with Ge nanowires.

3.3.2 Amorphous Si Nanofibers

High-resolution transmission electron microscopy (HRTEM) characterization of the torturous Si nanofibers shown in Figure 3.3A and 3.3B confirmed the absence of a crystallographic core and illustrated the amorphous morphology of these nanofibers. Figure 3.3A, shows an amorphous Si nanofiber from the same sample as shown in Figurer 3.2A. EDS characterization confirmed the elemental composition of the wires as Si with a minor O signal, presumably due to surface oxidation. Interestingly, the amorphous wires moved much more readily under the illumination of the electron beam compared to crystalline Si or Ge nanowires, suggesting significant differences in mechanical properties of these amorphous fibers relative to their crystalline nanowire counterparts. Furthermore, beam damage in the form of burning through the specimen occurred at much lower beam dosages than are required for beam damage to be observed for crystalline wires.[†]

Closer inspection of the tip of the Si nanofiber shown in Figure 3.3A revealed the presence of a crystalline seed particle with resolved 0.23 nm lattice planes corresponding to the {111} planes of Au. Notably, the seed particle appears to be fully enclosed in the amorphous fiber material, which stands in marked contrast to the crystalline seed ends observed for Ge nanowires (see Chapter 5) where the nanowire material only protrudes from one end of the wire.

The comparison of the seed end of the amorphous fiber shown in Figure 3.3A with the seed end of crystalline Ge or Si hints at some of the important

---

[†] Electron beam induced damage to the nanowire crystal structure is discussed in Chapter 5.

differences in the underlying growth mechanisms resulting in crystalline or amorphous materials. Due to the close similarities in the synthesis conditions of the wires in Figure 3.3A and 3.3B, the differences in morphology are more likely attributable to the size of the seed end. The Gibbs-Thompson relationship (see Appendix B) suggests that the small Au seed particle shown in Figure 3.3A required high supersaturation in order to crystallize a nanowire. The Si material degraded in proximity of the Au particle materials was then presumably unable to nucleate and instead grew along the surface pushing other material along resulting in the formation of the amorphous Si nanofiber. Larger seed crystals on the other hand have a smaller contribution from the energetically unfavorable surface energy term; the Si can thus more readily alloy with the Au seed particle and subsequently crystallize in the form of a nanowire.

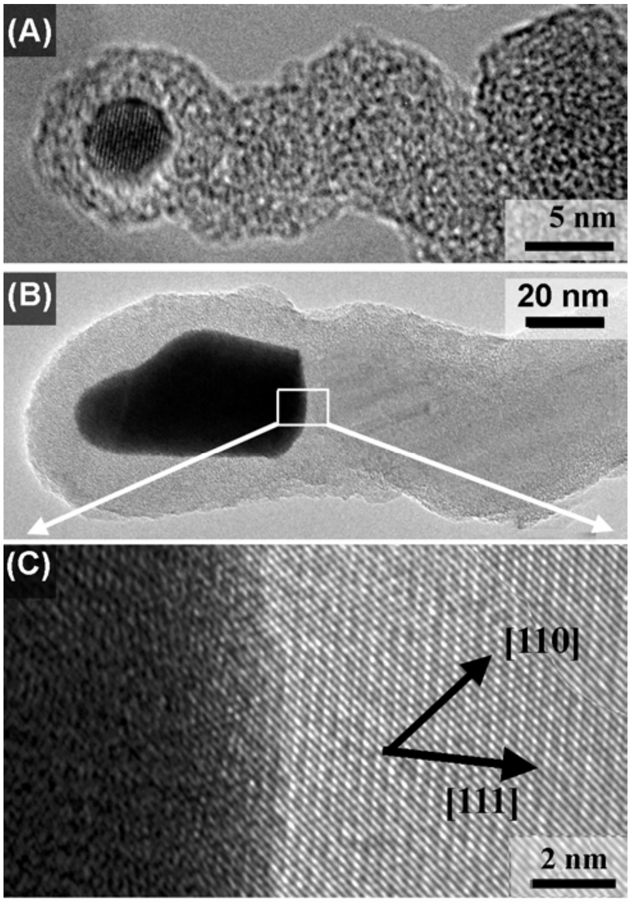

Figure 3.3: HRTEM images of Si nanowires. (A) An amorphous nanofiber with a crystalline Au particle at the tip. (B) Crystalline Si nanowire showing the {111} lattice planes with several stacking faults, and (C) slightly bent Si nanowire with [111] crystallographic growth direction.

3.3.3 Crystalline Si Nanowires

3.3.3.1 The Au:Si Interface

Figure 3.3B shows the non-spherical seed end of a torturous, yet crystalline, Si nanowire obtained from a flow through reaction using a 100 mM solution of MPS with an Au:Si ratio of 1:1000, at 450°C and 20 MPa with an average residence time of 3 min. A carbonaceous contamination layer was found to coat most of the Si nanowire and the seed end. A higher magnification HRTEM image interface region (Figure 3.3C) revealed the crystallographic structure of the Si nanowire with the long axis oriented near the [111] direction. The seed particle at the left end of the wire showed multiple crystallographic domains with the various lattice spacing measuring between 0.21 and 0.23 nm. A definite crystallographic assignment as in the case of the β hexagonal $Au_{0.72}Ge_{0.28}$ tips (see Chapter 5) was not possible in this case, although it seems reasonable to suggest that the seed particle consisted of a mixture of Au and other gold rich metastable Au-Si phases.

3.3.3.2 Nanowire Crystallographic Growth Direction and Faceting

Further HRTEM characterization of the crystalline Si nanowires revealed some interesting differences between the Si and Ge nanowire growth directions. While Ge nanowires were found to predominantly grow in the <110> crystallographic direction with minor contributions from <111> and <211> oriented wires (see Chapter 5). The silicon nanowires appears to exhibit a preferred orientation along the <111> axis.

The HRTEM images in Figure 3.4 show crystalline Si nanowires with various defect densities. Figure 3.4A shows a single crystal, 21 nm diameter Si nanowire prepared using MPS at 500^{o}C with a high density of faceting lines running along the axis of the and visible (111) and (220) lattice planes separated by 35^{o}, commensurate with the diamond cubic structure of silicon. The nanowire growth direction was measured at a 19^{o} angle relative to the [111] direction indicating that the Si nanowire grows in along the [112] crystallographic direction. As discussed in detail in Chapter 5, small diameter nanowires with the <211> growth direction exhibit rectangular cross sections faceted by {111} and {110} planes. Larger diameter nanowires such as the 20 nm diameter wire shown in Figure 3.4A, the nanowire faceting will likely deviate from the basic rectangular cross section and the cross-sectional structure becomes faceted to take on more energetically favorable near-circular geometry comprised of low energy {111} and {100} facets.

The 12nm diameter Si nanowire in Figure 3.4B was grown using DPS at 500^{o}C. The {111} lattice planes in this wire show similar faceting lines running along the axis of the wire. The 9 nm diameter nanowire shown in Figure 3.4C was obtained from a synthesis using Cp*SiH_3 as the precursor showed no visible surface facets or crystallographic defect, yet the nanowire axis appeared slightly bent and not as well defined as single crystal Ge nanowires.

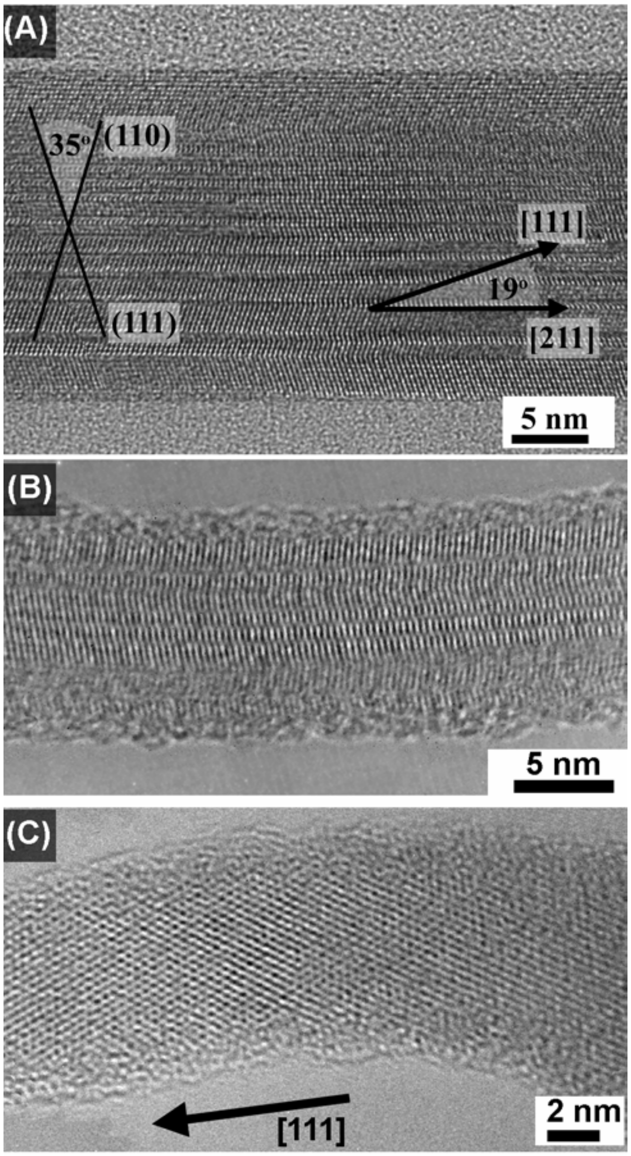

Figure 3.4: HRTEM crystalline Si nanowires (A) A 21 nm diameter Si nanowire with [211] growth direction (B) A 12 nm diameter Si nanowire {111} lattice planes. (C) A 9 nm diameter Si nanowire with [111] growth direction.

3.3.4 Si Nanowire Synthesis Nucleated by Au Seeds Molecularly Tethered to the Substrate‡

In an alternative approach aimed at reducing the agglomeration of the liquid alloy seed droplets during the initial nanowire growth stage, Au nanocrystals were tethered to the Si deposition substrate through a self-assembled monolayer. In this approach, the Au seed crystals were not free floating in solution, but rather covalently linked to the substrate as shown schematically in Figure 3.5 below.

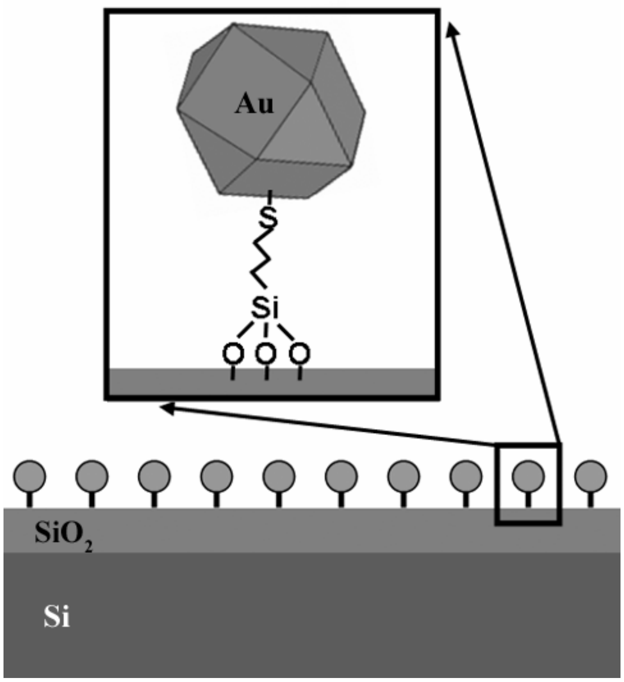

Figure 3.5: Schematic of Au nanocrystal molecularly tethered to the Si substrate through a self-assembled monolayer of MPTMS. The alkylthiol ligands stabilizing the Au nanocrystal were omitted for clarity.

---

‡ This work was conducted in collaboration with X. Lu and K.P. Johnston.

This synthesis method enabled the direct investigation of the effect of Si supply rate to the seed particle through adjustments in precursor concentration and flowrate, while maintaining a constant concentration of Au seed attached to the surface. This allowed the study of critical kinetic growth factors involved in the nanowire nucleation and growth. In addition to these experimental benefits, this approach also demonstrated an important step toward the integration of nanowire synthesis and ordered assembly, which is desirable for future technological applications. In principle, the nanowire growth could be limited to specific regions of the Si substrate by lithographically defining the areas where Au seed crystals are attached.

3.3.4.1 Effects of Precursor Flowrate and Temperature

The effect of the precursor flowrate and concentration on the morphology of the resulting nanowire materials is shown in Figure 3.6. Under conditions of limited Si supply to the seed particles, torturous nanowires with many crystallographic wires were obtained. (see Figure 3.6A). The restricted precursor supply to the reactor caused the Si absorbed into the Au particles to become the limiting step. This resulted in the intermittent growth of Si nanowires as evidenced by the frequent change in direction of the wire seen in the SEM image (Figure 3.6A). Higher precursor feed rates for the same reactor temperature however resulted in a Si supply rate exceeding the maximum rate at which Au can adsorb and direct crystal nucleation. Consequently, the reaction products for 1.0 ml/min and 3.0 ml/min (Figure 3.6B and C, respectively) were characterized by increasing amounts of homogeneously nucleated by products. Figure 3.6D shows that good quality Si nanowires were synthesized with a precursor feed rate of 1.0 ml/min and a temperature of 450°C. Similar to the flow through reactions with free-floating seed particles discussed above, further reductions in synthesis temperature below 450°C resulted in the formation of exceedingly tortuous wires.

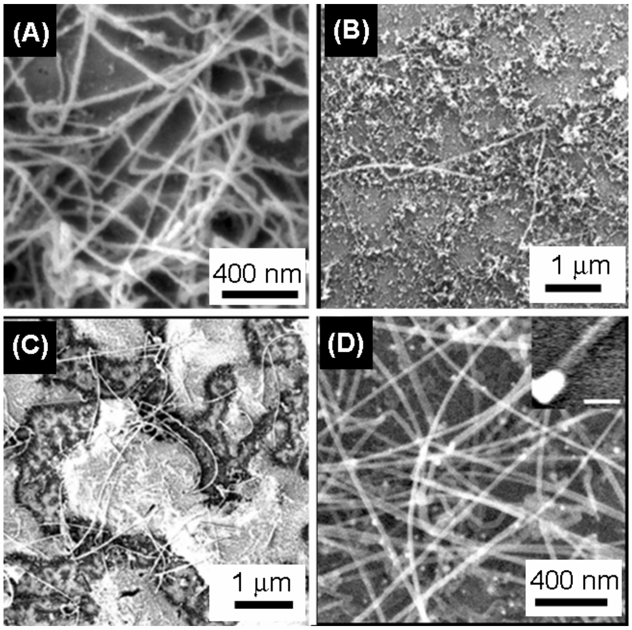

Figure 3.6: SEM images of Si nanowires grown from Au seed crystals molecularly tethered to the substrate. The nanowires were formed in the flow through reactor from a 250mM solution DPS solution. (A) 0.5 ml/min, 450°C, (B) 1.0 ml/min, 500°C, (C) 3.0 ml/min, 500°C, and (D) 0.5 ml/min, 500°C. The scale bar in the inset of (D) is 50 nm.

3.3.4.2 Growth of Helical Nanowires

A peculiar feature of Si nanowires synthesized from Au particles attached to the substrate was the occurrence of crystalline nanowires with a well-defined periodic helical morphology. Figure 3.7A shows a SEM image of a helical nanowire formed in a reaction using 250mM solution of DPS in cyclohexane at a feed rate of 1.0 ml/min and a temperature and pressure of 400°C and 22 MPa, respectively. The elemental contrast in the image revealed the presence of a large (~70nm) Au seed particle at the left end of the helical nanowire. Other helical structures from the same sample showed two helical nanowires emerging from the same Au seed particle (see Figure 3.7B). This germinate nanowire nucleation from a single particle has never been observed for straight crystalline nanowires and suggests fundamental differences in the growth mechanisms of helical and straight crystalline nanowires. A low-resolution TEM image of such helical nanowires is given in Figure 3.7C which showed the crystallinity of the wire as evidenced in the light and dark band crystal bending fringes. Higher resolution images revealed a high density of crystallographic defects, which prevented an unambiguous classification of the crystallographic growth axis along the helix. Furthermore, analysis of over 100 SEM images of helical nanowires indicated no statistically significant preferred chirality. Similar helical nanowire structure have been observed by Zhang et al.[25] in the synthesis of amorphous silicon carbide nanosprings. The formation of helical silicon carbide springs was related to the contact angle anisotropy resulting biphase (crystalline core / amorphous shell) structure of the nanospring. The helical Si nanowires in this study however did not exhibit a core/shell morphology but were instead only coated by a thin (~2-3 nm) carbonaceous and oxide surface layer. The growth mechanism responsible for the formation of these helical nanowires remains unclear, but may be related to the oscillatory movement of tethered seed particle in the laminar flow environment inside the reactor.

Recently, Wang and co-workers[26] reported the synthesis of helical ZnO nanowires, whose growth was explained via a hexagonal screw-coiling model wherein the six equivalent growth directions of the hexagonal ZnO lattice can cause a periodic 60^{o} change in growth direction. The helical Si nanowires in this work exhibit neither a core/shell morphology nor a set of six equivalent growth directions. The details of the growth mechanism responsible for the formation of these helical nanowires remains unknown, but may be related to either the oscillatory movement of tethered seed particle in the laminar flow environment inside the reactor, or due to periodic defects during the step plane growth as discussed in Chapter 5.

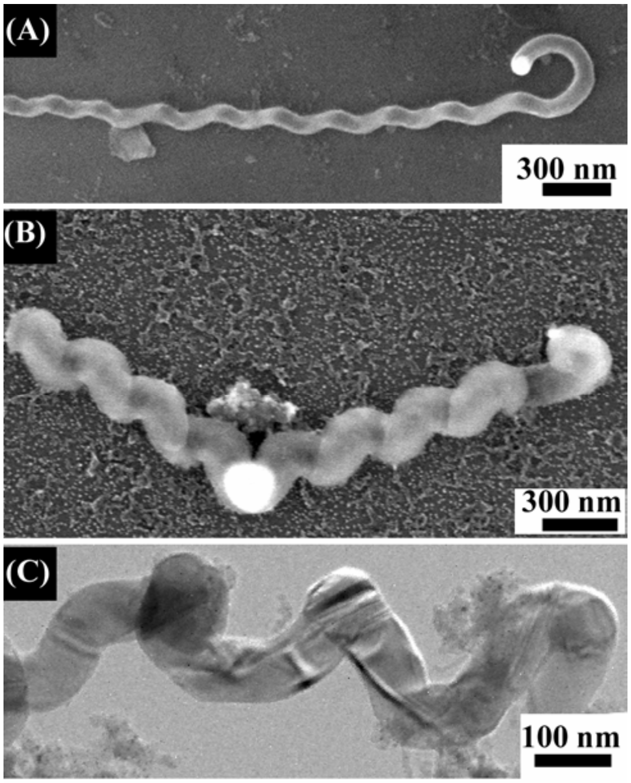

Figure 3.7: Helical Si nanowires: HRSEM images of (A) a helical nanowire grown at 400°C and (B) a helical nanowire with Au at the center germinate nucleated nanowire with more severe chirality. (C) TEM image of a helical nanowire showing the defective crystalline structure of the helical wire and dark and bright crystal bending contrast fringes.

3.4 CONCLUSIONS

In general, the reaction yield from Si nanowire syntheses was lower than the yield for Ge nanowires under comparative conditions. Since the decomposition rates for the phenyl substituted Si and Ge precursors are similar, the differences in yield appear to result primarily from the large difference in Ge-Ge and Si-Si bond energies. The differences in crystallization energies were also manifested in the observation of amorphous Si nanowires obtained from syntheses involving phenylsilanes. The survey of various organosilane precursors further illustrated the differences between Ge and Si nanowire synthesis, since neither mono- nor diphenylsilane provided satisfactory results similar to those obtained with diphenylgermane. Alkyl substituted silanes, like tetraethyl- or octylsilane and trisilane also appear to be unfeasible precursors for the synthesis of Si nanowires in supercritical fluid. Cp^*SiH_3 provided a modest yield of crystalline nanowires, although further experiments are required to determine optimized synthesis conditions for the high yield synthesis of crystalline Si nanowires. This work also demonstrated that Si nanowires could be grown from individual gold seed nanocrystals attached covalently to a Si substrate. The molecularly tethered seed particle configuration enabled the exploration of a variety of kinetic factors involved in the Si nanowire synthesis and permitted the identification of growth conditions that favored crystalline nanowires over tortuous nanofibers or Si particle byproducts.

3.5 REFERENCES

(1) Wagner, R. S. *Whisker Technology*; Wiley: New York, 1970.

(2) Wagner, R. S.; Ellis, W. C. *Appl. Phys. Lett.* **1964**, *4*, 89-90.

(3) Wagner, R. S.; Ellis, W. C.; Jackson, K. A.; Arnold, S. M. *J. Appl. Phys.* **1964**, *35*, 2993-2995.

(4) Morales, A. M.; Lieber, C. M. *Science* **1998**, *279*, 208.

(5) Duan, X.; Lieber, C. M. *J. Am. Chem. Soc.* **2000**, *122*, 188.

(6) Hu, J.; Odom, T. W.; Lieber, C. M. *Acc. Chem. Res.* **1999**, *32*, 435.

(7) Wang, N.; Zhang, Y. F.; Tang, Y. H.; Lee, C. S.; Lee, S. T. *Applied Physics Letters* **1998**, *73*, 3902-3904.

(8) Yu, D. P.; Bai, Z. G.; Ding, Y.; Hang, Q. L.; Zhang, H. Z.; Wang, J. J.; Zou, Y. H.; Qian, W.; Xiong, G. C.; Zhou, H. T.; Feng, S. Q. *Applied Physics Letters* **1998**, *72*, 3458-3460.

(9) Holmes, J. D.; Johnston, K. P.; Doty, R. C.; Korgel, B. A. *Science* **2000**, *287*, 1471-1473.

(10) Coleman, N. R. B.; O'Sullivan, N.; Ryan, K. M.; Crowley, T. A.; Morris, M. A.; Spalding, T. R.; Steytler, D. C.; Holmes, J. D. *J. Am. Chem. Soc.* **2001**, *123*, 7010.

(11) Coleman, N. R. B.; Ryan, K. M.; Spalding, T. R.; Holmes, J. D.; Morris, M. A. *Chem. Phys. Lett.* **2001**, *343*, 1.

(12) Holmes, J. D.; Lyons, D. M.; Ziegler, K. J. *Chem. Eur. J.* **2003**, *9*, 2144-2150.

(13) Klipp, A.; Petri, S. H. A.; Hammelmann, F.; Jutzi, P.; Heinzmann, U. *Organosilicon Chemistry - From Molecules to Materials*; Wiley-VCH: Weinheim, Germany, 2000.

(14) Brust, M.; Walker, M.; Bethell, D.; Schiffrin, D. J.; Whyman, R. *Journal of the Chemical Society, Chemical Communications* **1994**, 801-802.

(15) Korgel, B. A.; Fitzmaurice, D. *Physical Review Letters* **1998**, *80*, 3531-3534.

(16) Trent, D. E.; Levy, A.; Coutant, R. W.; Merryman, E. L. *Aerospace Research Laboratories* **1965**, *ARL 65-64*.

(17) Dean, J. A., Ed. *Lange's Handbook of Chemistry*; 15th ed.; McGraw-Hill: New York, 1999.

(18) Amjoud, M.; Reynes, A.; Morancho, R.; Carles, R. *Journal of Materials Chemistry* **1992**, *2*, 1205-1208.

(19) Bermudez, V. M. *Journal of Applied Physics* **1992**, *71*, 5450-5459.

(20) Maury, F.; Mestari, A.; Morancho, R. *Materials Science & Engineering, A: Structural Materials: Properties, Microstructure and Processing* **1989**, *A109*, 69-75.

(21) Tuan, H. Y.; Hanrath, T.; Lee, D. C.; Korgel, B. A. *unpublished results*.

(22) Cui, Y.; Lauhon, L. J.; Gudiksen, M. S.; Wang, J.; Lieber, C. M. *Applied Physics Letters* **2001**, *78*, 2214-2216.

(23) Westwater, J.; Gosain, D. P.; Tomiya, S.; Usui, S.; Ruda, H. *J. Vac. Sci. Tech. B* **1997**, *15*, 554.

(24) Dahlhaus, J.; Jutzi, P.; Frenck, H.-J.; Kulisch, W. *Adv. Mater.* **1993**, *5*, 377-380.

(25) Zhang, D.; Alkhateeb, A.; Han, H.; Mahmood, H.; McIlroy, D. N.; Norton, M. G. *Nanoletters* **2003**, *3*, 983-935.

(26) Zhang, H.-f.; Wang, C.-m.; Young, J. S.; Coleman, J. E.; Wang, L.-s. *Materials Research Society Symposium Proceedings* **2003**, *776*, 95-100.

Chapter 4: Chemical surface passivation of Ge nanowires

4.1 INTRODUCTION

One-dimensional (1D) nanomaterials, such as nanotubes and nanowires, have been proposed for use in numerous applications due to their unique optical, mechanical, and electrical properties.[1-4] In the context of both the processing and properties of nanowires, a detailed understanding of their surface chemistry is required to meet these technological expectations. For example, the chemical and electronic stability of nanowire surfaces is particularly important for applications such as nanowire-based computing and logic elements, as well as chemical and biological sensors, which require direct interfacing with their surrounding environment.[5-8] Nanowire dispersibility in a variety of solvents is also critical for the processing of these materials and their implementation as "building blocks" in device structures assembled using various approaches such as directed deposition from solution, spin-coating, inkjet printing, imprint lithography and stamping, as well as mechanical manipulation. While there has been significant effort focused on covalent chemical modifications of carbon nanotube surfaces[9-12] there have been very few reports on the chemical modification of semiconductor nanowire surfaces.[13-15]

Germanium (Ge) nanowires produced by gold nanocrystal-seeded SFLS synthesis discussed in Chapter 2 provided a powerful model experimental system for the study of the surface passivation chemistry of nanostructures. The nanowires were crystalline, with few dislocation defects, and their surfaces were relatively smooth with well-defined interfaces. They can be characterized using surface science techniques, such as X-ray photoelectron spectroscopy (XPS), and it is straightforward to perform high-resolution electron microscopy imaging of the semiconductor interface—a difficult and time-consuming task for monolithic substrates and porous semiconductors.

The surface chemistry of germanium's congener, silicon (Si), is *very* well studied—perhaps more than any other element in the periodic table—because of its critical importance in the microelectronics industry. Silicon forms a very stable oxide, and can be chemically passivated with a variety of organic species. The reaction mechanisms have been extensively investigated for solution-phase and vapor-phase oxidation, metallization, nitridation, and organic monolayer passivation of both the well-characterized Si surfaces of monolithic single-crystal substrates and the poorly-characterized surfaces of porous Si.[16] The situation for Ge is quite different. While many similarities exist between the surface properties of these two materials, there are some profound differences, specifically with respect to their oxide interfaces. Unlike the chemically and electronically stable Si/SiO_2 interface, the Ge/GeO_x interface is troubled with unfavorable electrical properties and poor chemical stability: for example, GeO_x dissolves in water to form $Ge(OH)_4$ and does not provide the effective electrical tunnel barrier needed for transistor applications.[17,18]

This chapter discusses a comprehensive investigation of the surface chemistry of Ge nanowires. The inherent chemical stability of "bare" nanowires, and oxidized nanowires, in the presence of ambient atmosphere and water is determined using XPS. Various pathways for chemical passivation are then developed and explored, including sulfide-, chloride-, and hydride-terminated surfaces. Finally, methods for surface passivation by the formation of covalently bonded organic monolayers are developed.

4.2 EXPERIMENTAL ASPECTS

4.2.1 Ge Nanowire Synthesis

The Ge nanowires used in this study were synthesized by an Au nanocrystal-seeded process in supercritical hexane using the diphenylgermane (DPG) as the Ge precursor, as described in detail in Chapter 2. All chemicals were used as received from Aldrich, except for diphenylgermane (DPG), which was purchased from Geleste. DPG, hexane, 1-hexene, 1-pentyne, 1,3-cyclobutadiene, 2-methyl-1,3-butadiene, 1-octene, 1-dodecene, and 1-dodecyne, methyl-MgBr and octyl-MgBr were purchased anhydrous, packaged under nitrogen, and were stored under nitrogen until use.

In order to perform an accurate comparison of different surface passivation methods, all nanowires used for the surface passivation studies were prepared under the same conditions. A precursor solution containing DPG (80mM) and Au nanocrystals in a relative ratio of Au:Ge as 1:1000 in hexane was injected into a high temperature, high pressure reactor at 385^{o}C and 8 MPa. The resulting nanowires are single-crystals with few dislocation defects. They exhibited a predominant <110> growth direction with diameters ranging from 12~24 nm.

4.2.2 Surface Passivation

4.2.2.1 Surface Passivation Outside the Supercritical Fluid Reactor

Different strategies for chemically modifying the nanowire surfaces were explored that required reactions both outside and inside the reactor. For nanowire surface chemistry modifications outside of the supercritical fluid reactor, nanowire samples were deposited onto inert Telfon© or Au-coated Si substrates. Wet and dry oxidation was investigated by submersion in deionized water or exposure to a dry air atmosphere. Sulfidation experiments were carried out using nanowires etched in 2%HF for 5min. The nanowires were submersed in a 4 vol% $(NH_4)_2S$ aqueous solution at 60^oC for 20 min, followed by a methanol rinse. Chloride- and hydride-terminated nanowires were produced by immersion in aqueous 5%HCl or 5%HF for 5 min, respectively.

4.2.2.2 Surface Passivation Inside the Supercritical Fluid Reactor

Organic monolayer passivation was achieved by exposure to alkene, alkyne or diene species at elevated temperature in the supercritical fluid reactor. In these reactions, the nanowires were first synthesized, and then the reactor was flushed with excess anhydrous supercritical hexane ($T=385^oC$ and $P=8$ MPa) to remove carbonaceous contamination and reaction byproducts. After flushing with supercritical hexane, the reactor was cooled to 220^oC before injecting the alkene, alkyne, or diene species. For *in situ* thiol passivation, the reactor was cooled to 80^oC before injecting 1-octanethiol. The surface treatment was allowed to proceed for ~2h before flushing the system once more with hexane. Prior to characterization, the nanowires were rinsed with excess hexane, chloroform, and isopropanol to remove physisorbed organic species. All samples were stored under an inert nitrogen atmosphere (<1ppm O_2).

4.2.3 Characterization

The nanowires were characterized by high-resolution transmission electron microscopy (HRTEM), scanning electron microscopy (HRSEM, LEO1530), Fourier-transform infrared (FTIR) spectroscopy, and X-ray photoelectron spectroscopy (XPS). HRTEM images were acquired from nanowires deposited over a vacuum background on lacey carbon TEM grids using a JEOL 2010F field-emission TEM operating at 200 kV. Spatially resolved elemental characterization was obtained using energy dispersive x-ray spectroscopy (EDS, Oxford INCA) and electron energy loss spectroscopy (EELS, Gatan Enfina DigiPEELS) on TEM samples. HRSEM imaging was performed using a LEO 1530 field emission gun SEM operated at 3-10 kV acceleration voltage. XPS data were acquired using a Physical Electronics XPS 5700 equipped with a monochromatic Al X-ray source (Al Kα, 1.4866 keV). Extensive efforts were taken to avoid atmospheric exposure and unintentional oxidation of the ~0 h XPS sample, and exposure of those nanowires to the atmosphere was no greater than 10 min. FTIR spectra were obtained on a Thermo Mattson Infinity Gold FTIR. FTIR spectra of nanowires with hydrogermylated surfaces were acquired in transmission mode from nanowires deposited on Si substrates. FTIR spectra reported for HF-etched nanowires were acquired in reflectance mode (54 deg) from Ge nanowires on a Au-coated Si substrate. For the electrical measurements, Pt metal electrodes were deposited by electron beam assisted metal chemical vapor deposition (CVD) on a FEI Strata DB235 dual beam SEM/FIB to contact individual nanowires drop cast from a toluene dispersion onto an oxidized Si wafer. The Pt contact lines were connected to gold contact pads patterned using electron beam lithography. The electrical measurements were performed under nitrogen using a Karl Suss PM5 electrical probe station connected to an Agilent 4145B semiconductor parameter analyzer.

4.3 RESULTS AND DISCUSSION

4.3.1 Ge Nanowire Surface Oxidation

The crude product isolated from the reactor consisted of Ge nanowires with a thin oxide layer coated by a thicker layer of carbonaceous contamination.[19] The thick carbonaceous layer was readily stripped from the surface by either flushing the reactor with supercritical hexane prior to isolating the product or by rinsing the nanowires with organic solvents such as hexane or chloroform after removal from the reactor. The remaining “native” germanium suboxide (GeO_x) layer had a typical thickness of 3~4 nm, as shown in Figure 4.1A, with a residual thin hydrocarbon film detectable by EDS under the TEM. Due to the high GeO_x solubility in aqueous solutions, it can be removed by exposure to dilute HCl or HF acid solutions, or even pure water.[18] However, acid treatment was much more effective at removing the oxide layer than submersion in pure water, as the water treatment left a residual oxide on the surface with non-uniform thickness, possibly as a result of the residual thin carbonaceous layer that could shield the etching in some places, or subtle variations in surface roughness that became exacerbated during the corrosion process.

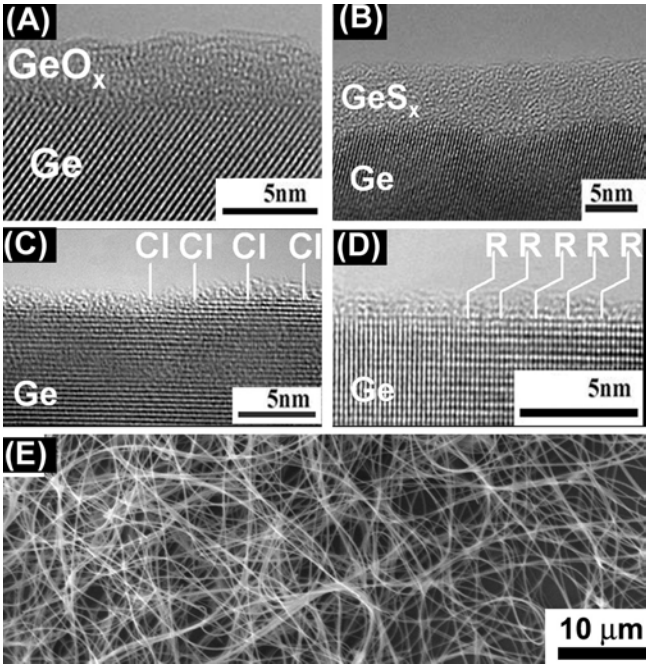

Figure 4.1: HRTEM images of (A) untreated Ge nanowire surface showing the non-uniform oxide and carbonaceous contamination coating, and Ge nanowires with (B) sulfide coating, (C) chloride termination, and (D) covalently bonded hexyl monolayer termination. (E) High-resolution SEM image of Ge nanowires.

From a device and applications standpoint, the germanium oxide that formed in the presence of water and air is not at all desirable. In addition to the poor chemical stability discussed below, the Ge/GeO_x interface is plagued by a high density of fast and slow surface states[20] and poor electronic passivation that results in large gate leakage currents. However, the oxidation chemistry that occurs on Ge nanowire surfaces deserves attention. The oxidation of the Ge surfaces is relatively complex and has been found to depend on the oxidation environment and the crystallographic orientation of the Ge surface.[21] Almost nothing is currently known about the corrosion processes that occur at the surface of single-crystal semiconductor nanowires. In the context of developing effective surface passivation strategies of semiconductor nanowires, the underlying oxidation processes must be understood in order to understand the effects of chemical treatments.

High-resolution Ge 3d photoelectron spectroscopy of Ge nanowires provided information about the oxidation states of the Ge surface after exposure to various chemical environments. Schmeisser et al.[21] studied the Ge 3d photoemission spectra of oxidized Ge(100) and Ge(111) surfaces and isolated four surface oxidation states with a core level shift of 0.85 eV per Ge-O bond, or per oxidation state (Ge is octahedrally coordinated in the +4 oxidation state, with each O shared by two Ge atoms). Figure 4.2 shows Ge 3d photoemission spectra obtained from Ge nanowires exposed to various oxidative environments. The XPS spectra were deconvoluted to determine the extent of oxidation and the Ge oxidation state. The Ge 3d peak exhibits a $3d_{3/2}$ and $3d_{5/2}$ spin-orbit splitting of 0.585 eV with an intensity ratio of 0.58. The Ge^{1+} oxidation state exhibits a peak contribution shifted by 0.85 eV.[21]

4.3.1.1 .Oxidation in Dry Ambient Atmosphere

The Ge nanowires with ~0 hours of atmospheric oxygen exposure exhibited a measurable amount of oxide on the surface with Ge in the +1 oxidation state only. Limited exposure to oxygen (in a dry atmosphere) led to surface oxidation. Prolonged exposure to oxygen increased the extent of oxidation, with the appearance of Ge^{2+} and Ge^{3+} species along with an increase in the amount of Ge^{1+} species (evident from the Ge^{1+} peak intensity relative to the $3d_{3/2}$ and $3d_{5/2}$ peaks). In contrast to Si, Ge is known to form an oxide with a stable +2 oxidation state, which corresponds to either a Ge=O double bond geometry (see Scheme 4.1) or two bridge-bonded oxygen atoms.[21] After approximately one week of exposure to a dry atmosphere environment, the oxidation of the Ge nanowire surface became self-limiting, as no noticeable changes in the oxidation states in the nanowire XPS profiles were observed with continued exposure to atmospheric oxygen. HRTEM images of nanowires subjected to dry atmosphere for one week or longer typically showed oxide thicknesses ranging from 3 to 4 nm.

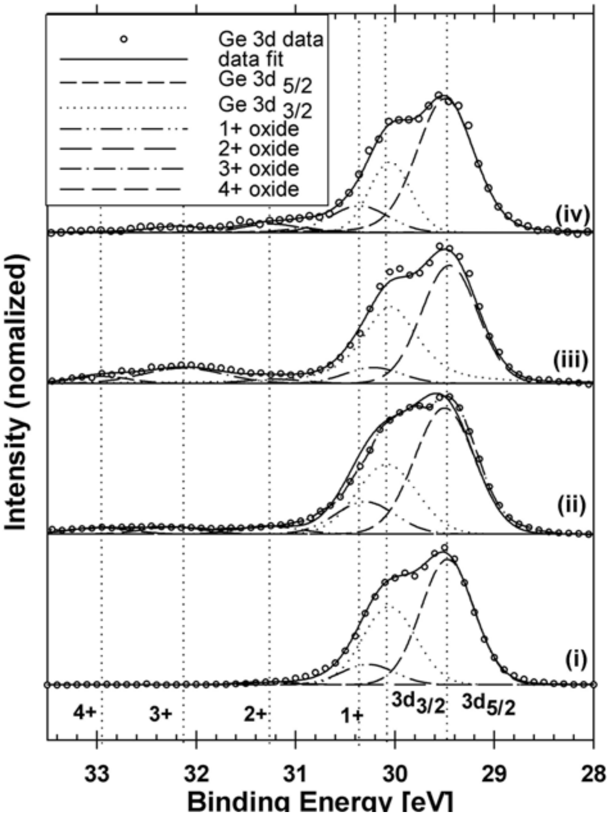

Figure 4.2: High resolution Ge 3d XPS of Ge nanowires (i) immediately after removal from reactor; (ii) after exposure to dry air for 168 h; (iii) after immersion in water for 30 min; (iv) after annealing in nitrogen at 300°C after immersion in water. Spectral deconvolution was carried out as described in Ref (22).

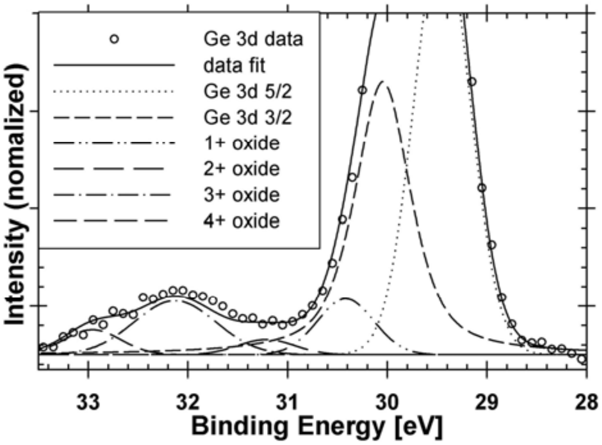

Figure 4.3: Expanded view of High resolution Ge 3d XPS of Ge nanowires after thermal annealing with a clearer view of the peak contributions from the four Ge oxidation.

4.3.1.2 Oxidation in Water

In contrast to Ge nanowires oxidized in a dry environment, nanowires immersed in deionized water showed a large amount of Ge^{3+} species in the XPS spectra—in nearly equal proportion to the Ge^{1+} peak. The relative contribution of Ge^{2+} species for nanowires oxidized in dry or wet environment appeared nearly the same, however, in HRTEM images of the interface, the overall oxide thickness of wet oxidized samples was thinner. Since GeO_x is soluble in water, one might anticipate that all of the Ge^{3+} species would be immediately etched from the surface after forming, however, this did not appear to be the case and a residual GeO_x layer remained after removing the nanowires from water. The formation of the 3+ oxidation state requires that more Ge bonds break, meaning that the oxidation process must be more extensive (see Scheme 4.1). Oxidation of

Ge nanowires to Ge^{3+} occurred readily in water, but not in dry atmosphere. Furthermore, the Ge^{2+} species observed to be on the Ge surface after dry oxidation were observed in near equal intensity on Ge nanowires after exposure to water. Theoretical work by Johnson and Panas[22] showed that the reaction between water and the two possible Ge^{2+} chemical configurations of Ge=O and the bridge-bonded Ge-O-Ge is much more thermodynamically favorable for Ge=O than for Ge-O-Ge species. The low intensity of Ge^{2+} species on nanowires exposed to water seemed to indicate that the Ge^{2+} species observed from dry-oxidized Ge nanowires were in the form of Ge=O, as opposed to two bridge-bonded oxygen atoms, since the Ge-O-Ge species exhibited some stability in water, as observed by the presence of Ge^{1+} species in XPS.

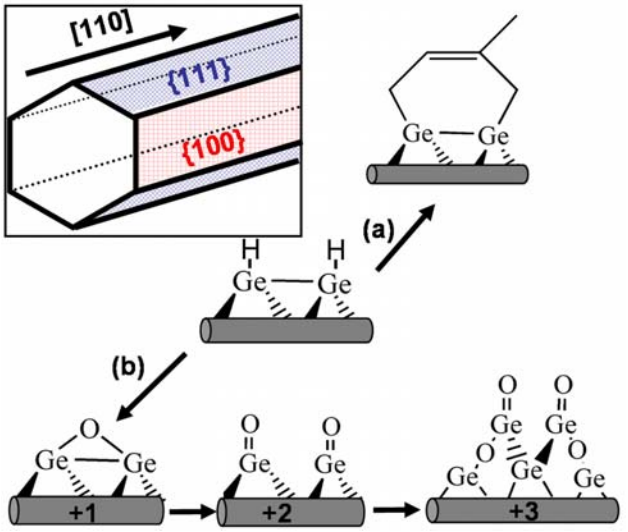

Scheme 4.1. Surface reactions at the Ge nanowire surface. (a) Thermally-initiated hydrogermylation reaction of Ge-H terminated surface with 2-methyl-1,3-butadiene. (b) Surface oxidation via either wet or dry processes resulting in 1+, 2+, and 3+ Ge oxidation states. The inset illustrates the expected {111} and {100} surface faceting for a single-crystal nanowire elongated in the <110> growth direction.

4.3.1.3 Effects of Thermal Annealing on Oxidation States

Annealing oxidized bulk Ge(111) and Ge(100) with Ge^{3+} surface-exposed species at 300°C for 15 min in ultrahigh vacuum (UHV) has been shown by Schmeisser et al.[21] to eliminate the Ge^{3+} species, with a shift in oxidation state to favor the Ge^{2+} species. A thermal anneal of the water-oxidized Ge nanowires at 300°C on a hot plate in a nitrogen glove-box (<1ppm O_2) nearly eliminated Ge^{3+} oxide species and left the Ge^{1+} species. A very small amount of Ge^{2+} species appeared in the spectra after the anneal. The predominance of Ge^{1+} species sharply contrasts the observed enrichment in Ge^{2+} on Ge (111) and Ge (100) surfaces annealed in UHV under controlled O_2 environments.[21] Furthermore, the oxidation states observed via wet and dry oxidation of the nanowires differ significantly from those observed on Ge (111) and (100) surfaces by Pabhakaran and Ogino.[23] This difference could be the result of the nanowire surface curvature favoring the formation of a single bridge bonded Ge-O-Ge at the highly curved interface of the nanowire as shown in Scheme 4.1 relative to the Ge=O species found to be favored on bulk single crystal surfaces.

The native GeO_x with octahedral coordination does not provide suitable chemical or electronic passivation. In contrast, Gregory et al.[24] reported the formation of a tetrahedrally-bonded Ge oxide, which they found to be stable in both water and HF. Attempts to form such a layer on the Ge nanowires; however, revealed that the chemical processing steps were too severe—for example, using their 40% HF and 30% H_2O_2 etching solution diluted 100 times dissolved the nanowires nearly immediately.

4.3.2 Ge-S surface termination

4.3.2.1.Sulfidation

As an alternative to oxygen, higher chalcogens such as S or Te have been proposed as surface termination candidates for Ge.[25,26] Under UHV conditions, LEED and XPS results have shown that S adsorbs to Ge(100) in a S/Ge(100)-(1x1) bridge-bonded form that saturates all dangling bonds.[25] Some literature reports have suggested that S termination of Ge (100) under UHV conditions might also be extended to the aqueous sulfidation of Ge (100) surfaces.[27] Other results by Lyman et al.,[28] however, indicated that the aqueous treatment of Ge

(001) surfaces results in a thin GeS_x layer. We explored sulfide passivation of Ge nanowires using similar reaction conditions as those reported in the literature.[27,28]

Figure 4.1B shows the surface of a sulfide-treated Ge nanowire imaged by TEM. The nanowire exhibited a 5 nm thick amorphous GeS_x coating. XPS data obtained for the sulfide-treated Ge nanowires (see Figure 4.4C) showed the S 2s and S 2p peaks as well as a splitting of the Ge 3d peak indicative of the presence of Ge-S bonds. The presence of S in the surface layer was confirmed by EDS, with the notable absence of O. In contrast to the sulfide monolayers[27] or the very thin glassy layers[28] observed to form on Ge(100) surfaces, the GeS_x layer on the nanowires was relatively thick, which is unfavorable for electrical device applications. Lyman et al.[28] attributed the formation of the amorphous GeS_x surface layer in their experiments to a high step density, or miscut Ge (100) substrates. The Ge nanowires obviously exhibit a different surface structure than the monolithic Ge(100) substrates due to their severe surface curvature, making them more susceptible to sulfidation.

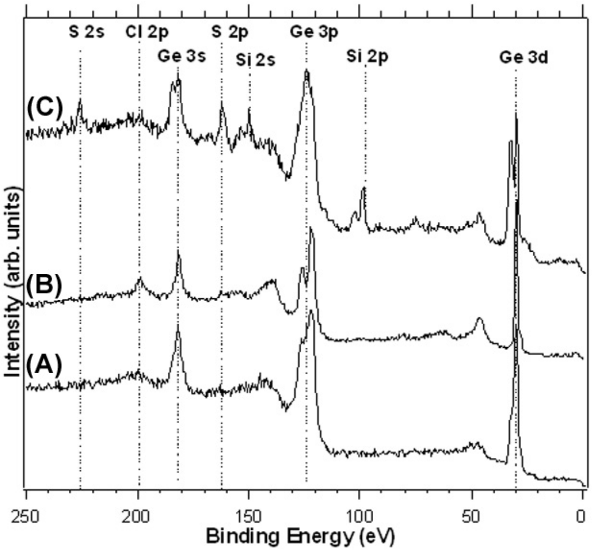

Figure 4.4: XPS of Ge nanowires: (A) before chemical surface modification, (B) after chlorination with HCl, and (C) after sulfidation with $(NH4)_2S$.

4.3.2.2 Passivation with Thiol Monolayer

To provide better chemical stability using Ge-S surface chemistry, Han and co-workers[29,30] examined the formation of alkanethiol monolayers on H-terminated Ge(111) surfaces. They formed self-assembled monolayers by exposing H-terminated Ge surfaces to alkanethiol solutions at room temperature. The monolayers were found to be stable up to 450K. Attempts to form alkanethiol monolayers on Ge nanowires by similar methods to those used by Han, et al.[29] were not successful, presumably due to the poor chemical stability of H-terminated Ge nanowires relative to H-terminated Ge substrates (see discussion below). However, using an alternate approach—exposure to octanethiol at 80°C directly in the reactor after synthesis—did successfully produce organic monolayers on the nanowires. Figure 4.5 shows an HRTEM image of the surface of a Ge nanowire that had been treated with octanethiol, along with an FTIR spectrum of the nanowires, which showed the presence of the hydrocarbon layer on the nanowires. The absorbance peaks correspond to the asymmetric and symmetric methylene stretching modes—$\nu_a(CH_2)$=2928 cm^{-1} and $\nu_s(CH_2)$=2855 cm^{-1}—and to the asymmetric in-plane and symmetric stretching modes of the terminal methyl groups—$\nu_a(CH_3$, ip)=2954.5 cm^{-1} and $\nu_s(CH_{3,}$ -FR)=2871 cm^{-1}— of the adsorbed hydrocarbon species. The peaks in the 2300 to 2400 cm^{-1} range resulted from background CO. It appears that the prevention of surface oxidation (i.e., exposure to water or oxygen) was critical to the formation of alkanethiol monolayers on the Ge nanowires.

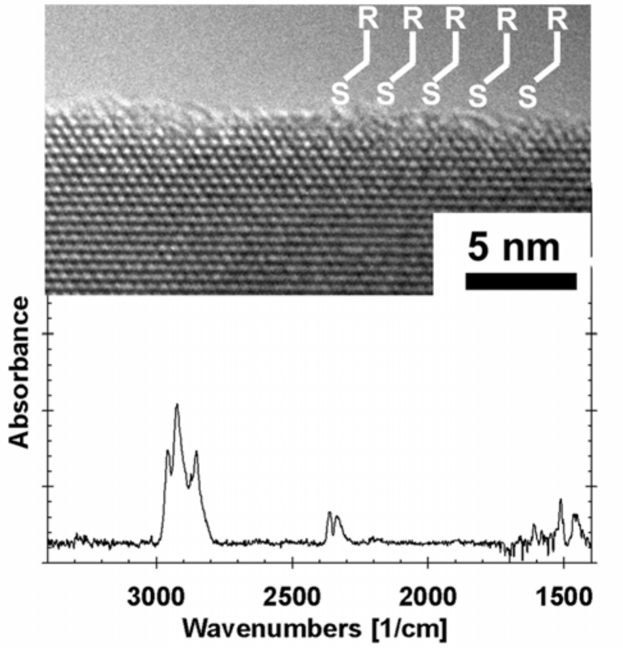

Figure 4.5. (Top) HRTEM image of a Ge nanowire treated with 1-octanethiol. Notice the absence of the surface oxide layer that is characteristic of untreated nanowires. (Bottom) FTIR spectra of octanethiol-exposed Ge nanowires.

4.3.3 HCl and HF treatment of Ge nanowire surfaces

4.3.3.1 HCl Etching and Chlorination

The chlorination of Ge(111) surfaces was first reported in 1962 by Cullen et al.[31] who exposed an oxidized Ge(111) surface to HCl gas at ~90°C. The HCl treatment results in the removal of ~200nm of Ge in the form of $GeCl_4$ gas to render a chlorinated Ge surface. Obviously, this chlorination procedure is far too aggressive to be applied to ~10 nm diameter Ge nanowires. A milder aqueous approach developed by Lu [32] that was more suitable for chlorinating Ge nanowires was applied instead. The Ge nanowires were soaked in 5% HCl for 5 min at room temperature and dried under nitrogen. TEM images of chlorinated Ge nanowire surfaces, such as that shown in Figure 4.1C, revealed clean and abrupt Ge surfaces with near complete removal of the amorphous surface oxide layer. XPS data also verified the chloride termination, with the appearance of the Cl 2p signal (Figure 4.4B) and the absence of oxide signal in the high-resolution Ge 3d spectra. (see Figure 4.7).

4.3.3.2 HF Etching and Hydride Termination

The nanowires can also be hydride-terminated by immersing Ge nanowires in 5% HF for 2 min. Based on thermodynamic considerations, exposure of a Ge surface to HF should result in F termination, since the Ge-F bond (485 kJ/mol) is stronger than the Ge-H bond (321 kJ/mol).[18] However, Choi and Buriak[33] demonstrated that kinetic factors dominate the formation of the surface species. FTIR spectra of HF-treated nanowires (Figure 4.6A) showed broad vibrations at 2010 cm^{-1}, characteristic of GeH_x. However, the stability of this hydride layer was limited to only a few minutes in the presence of oxygen, as evidenced by the absence of the ν(GeH_x) vibrational mode after 20 min of exposure to dry atmosphere. In contrast, hydride-terminated bulk Ge(100) surfaces are stable in air for up to 1 h.[33] The initial stages of wet and dry oxidation of H-terminated Si surfaces were investigated by Niwano et al.[34] who suggested that the faster oxidation in water relative to dry air is due to substitution of surface hydrogen by –OH groups, whereas the Si-H bond appeared more inert to oxygen exposure. Similar oxidation reactivities are expected for H-terminated Ge surfaces.

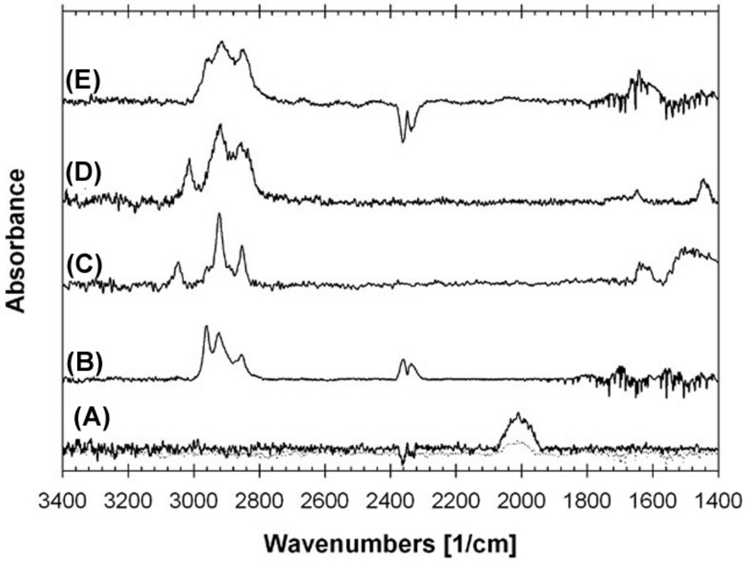

Figure 4.6: FTIR spectra of Ge nanowires (A) after immersion in 5% HF for 2 min (the dotted line shows the spectrum of the same sample after 20 min of atmospheric oxygen exposure); and after treatment in the reactor at 220°C with (B) 1-hexene, (C) 1-pentyne, (D) 1,3-cyclobutadiene, and (E) 2-methyl-1,3-butadiene as discussed in the text.

4.3.4 Ge-C Surface Termination

4.3.4.1 Alkylation via Grignard Reaction

The first attempts at surface alkylation of the Ge nanowires utilized a two-step chlorination-alkylation approach. We expected that the surface-chlorinated Ge nanowires could provide a reactive template for organic monolayer passivation using a Grignard reaction with species such as octyl-MgBr, as demonstrated by Cullen et al.[31] and more recently He et al.[35] for the alkylation of bulk Ge surfaces. While this two-step process was somewhat successful in producing monolayer passivation of the Ge nanowires, the direct thermally-initiated hydrogermylation was found to be much more efficient and effective.

4.3.4.2 Alkylation via Thermally Initiated Hydrogermylation

Halogenation/alkylation[36] and hydrosilylation reactions[37,38] on hydride-terminated Si surfaces have been well-studied for the formation of organic monolayers on Si surfaces. Buriak and co-workers[33] extended these methods to Ge, forming various organic monolayers on hydride-terminated Ge surfaces via either UV-initiated, Lewis acid mediated, or thermally initiated hydrogermylation reactions involving the insertion of unsaturated C=C bonds as the reactive species into Ge-H bonds at the surface forming Ge-C bonds as illustrated in Scheme 4.1a and Scheme 4.2. Among these three strategies, thermally-initiated hydrogermylation was most easily integrated with the supercritical fluid nanowire synthesis, since the nanowire materials could easily be subjected to the passivation reaction without intermediate oxygen exposure or HF etching.

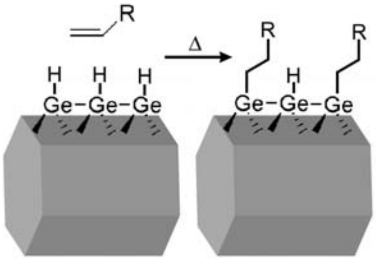

Scheme 4.2: Hydrogermylation reaction converting the surface bound Ge-H bonds into a covalently bonded monolayer terminated surface.

The Ge nanowires used in this study predominantly exhibited the <110> growth direction and are characterized by {111} and {100} faceted surfaces, as was recently experimentally verified by cross sectional HRTEM imaging of Si [39] and Ge nanowire cross-sections.* A recent STM study on Si nanowire surfaces by Lee and co-workers[40] demonstrated that these facets undergo surface reconstruction resulting in Si=Si dimer formation. Similarly, Ge=Ge dimers, which are also present in the surface reconstructions of bulk Ge {111} and {100} surfaces, may initially form on the Ge nanowire surface, but presumably quickly convert to H terminated surfaces in the supercritical fluid environment. Scheme 4.1 shows the example of the thermally initiated hydrogermylation reaction between 2-methyl-1,3-butadiene and the surface bound Ge-H bonds.

The surface passivation was carried out in the reactor after completing the nanowire synthesis. The Ge nanowires settled on a native oxide-coated Si substrate placed inside the reactor. By first flushing with excess supercritical hexane, any surface contamination of reaction byproducts that coats the

---

* Cross sectional images of <110> and <211> oriented nanowires are discussed in Chapter 5.

nanowires was removed. The reactor was cooled to ~220°C before injection of the appropriate hydrocarbon species for the thermally initiated hydrogermylation reaction. Figure 4.1D shows a TEM image of the surface of hexane-treated Ge nanowires. The nanowires exhibited clean abrupt surfaces—in sharp contrast to nanowires removed from the reactor without surface passivation. EDS and EELS (electron energy loss spectroscopy) did not show the presence of oxygen; however, these techniques were not sensitive enough to detect very small amounts of O. High-resolution Ge 3d XPS spectra revealed a weak Ge^{1+} signal, suggesting that some oxidation still occurs, either in the reactor or after removing the product from the reactor, perhaps as a result of incomplete surface termination. However, XPS (Figure 4.7) revealed that further exposure to air *and even water*, did not result in the further oxidation.

Nanowires can be surface-treated with alkene, alkyne and diene species. Figures 4.6B and 4.6C show the FTIR spectra of Ge nanowires coated with hexyl- and pentenyl-monolayers, respectively, formed by hydrogermylation reaction with hexene and pentyne. The FTIR spectra of Ge nanowires with pentenyl-monolayer termination (Figure 4.6C) showed the alkene C-H stretch at ~3050 cm^{-1}, whereas the hexyl-monolayer (Figure 4.6B) exhibited only the unsaturated $\nu(CH_x)$ stretches indicating that the reaction of Ge nanowire surfaces with pentyne involved only one double bond in the organic molecule. The FTIR spectra of the Ge nanowires reacted with 1,3 cyclobutadiene and 2-methyl-1,3-butadiene in Figures 4.6D and 4.6E showed monolayers with FTIR spectra similar to those obtained in UHV studies Diels-Alder reaction on single crystal Ge surfaces.[41,42] In UHV experiments the unsaturated bonds reacted with surface bound Ge=Ge dimers via [2+2] or [4+2] cycloaddition reactions. The similarity of the FTIR spectra of reactions involving dienes in this work to the ones reported in UHV experiments[41,42] suggest that the hydrogermylation reactions on Ge-H terminated surfaces involved similar rearrangement of the double bonds of the surface bound molecule.

4.3.5 Chemical Stability of Alkyl Passivated Ge Nanowires

The surface-coated Ge nanowires were much more chemically stable than the untreated nanowires. Figure 4.7 shows that exposure of the isoprene-passivated nanowires to oxidative conditions similar to those discussed above for the untreated nanowires did not lead to the formation GeO_x with higher oxidation states, although the presence of a small amount of Ge^{1+} could not be excluded. In comparison to isoprene passivated nanowires, octanethiol-treated nanowires exhibited even greater resistance to surface oxidation and the characteristic oxide peaks in XPS were absent after 15 h of direct submersion in water (see Figure 4.8). Bodlaki et al.[43] recently reported on the ambient stability of chemically passivated bulk Ge(111) surfaces and noted significantly more robust surface passivation to reoxidation from alkyl-terminated surfaces compared to surfaces etched with HCl or HF.

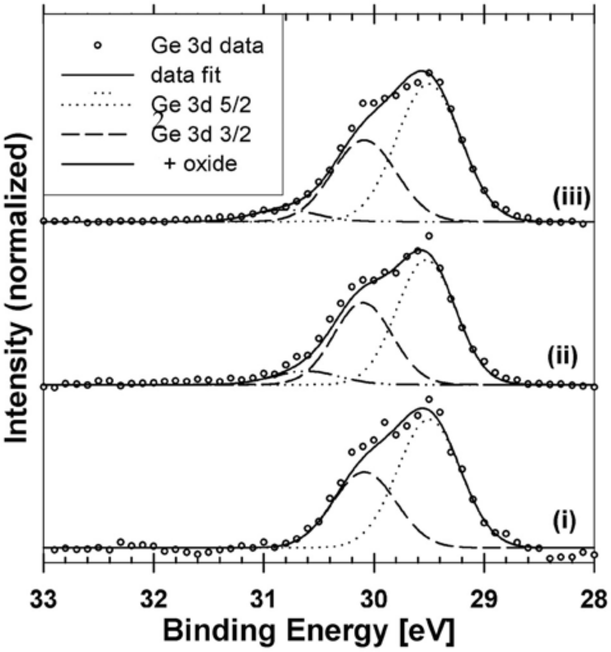

Figure 4.7: Ge 3d XPS of Ge nanowires: (i) after HCl etching and isoprene-passivated nanowires (ii) before and (iii) after 10 hr of immersion in deionized water. Note that the weak Ge^{2+} signal present in curve (ii) does not increase after water exposure (curve (iii)).

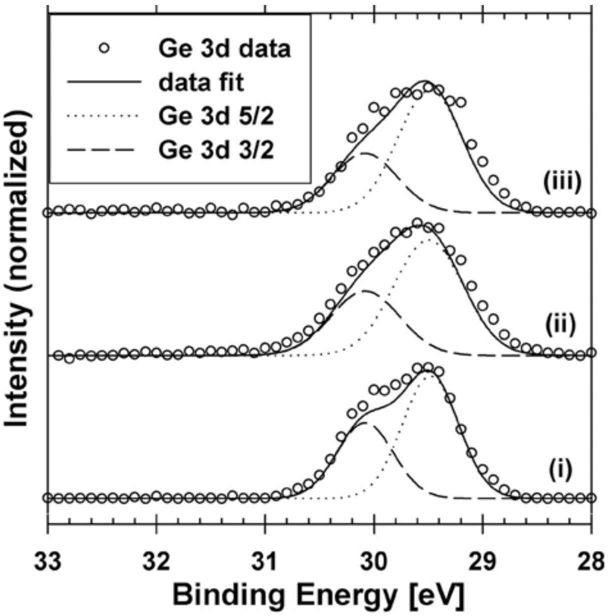

Figure 4.8: Nanowires passivated with octanethiol: (i) directly after thiol treatment (ii) after one week of dry atmosphere exposure; and (iii) after 15 h of exposure to deionized water. Note the absence of oxide characteristic peaks.

The chemical stability of the organic monolayer-coated Ge nanowires treated with 2-methyl-1,3-butadiene was also directly compared the chemical stability with untreated surface-oxidized wires by submersing them side-by-side in deionized water, as shown in the photographs in Figure 4.9. The ensemble nanowire deposits (dark brown material in the photographs) were deposited on Au coated Si substrates for enhanced visual contrast. It is noteworthy that the quality of the deposited nanowire films is much better for the hydrophobic surface-passivated nanowires than the untreated oxidized nanowires, due to their dispersibility in organic solvents.[†] The surface-oxidized Ge nanowires underwent rapid degradation in the aqueous environment, and dissolved after only 120 min (see Figures 4.9C and 4.9D). The water solubility of GeO_x in water combined with the oxidizing environment rapidly corroded the nanowires. The organic monolayer-coated Ge nanowires, however, did not visibly degrade in the aqueous environment in the same period (see Figures 4.9A and 4.9B), and appeared to be visibly stable after 10 hr. Notably, the isoprene treated samples did not show any sign of oxidation in the high resolution 3d spectra (see Figure 4.7), the satellite peak observed in spectra (ii) and (iii) could be due to a weak 2+ oxidation state, which was absent in freshly HCl etched samples shown in spectrum (i).

Figure 4.10 shows an additional example of the corrosion of untreated Ge nanowires in aqueous environments. Untreated Ge nanowires were dispersed through brief sonication in a 1 wt % aqueous solution of sodium dodecylsulfate at a concentration of 1 mg/ml. While the surfactant aided in the stabilization of the suspension (Figure 4.10A), the nanowires completely corroded to form water soluble $Ge(OH)_4$ within 24 h exposure to the aqueous environment (Figure 4.10B)

[†] The morphology of dense ensemble nanowire deposits is discussed in Chapter 8.

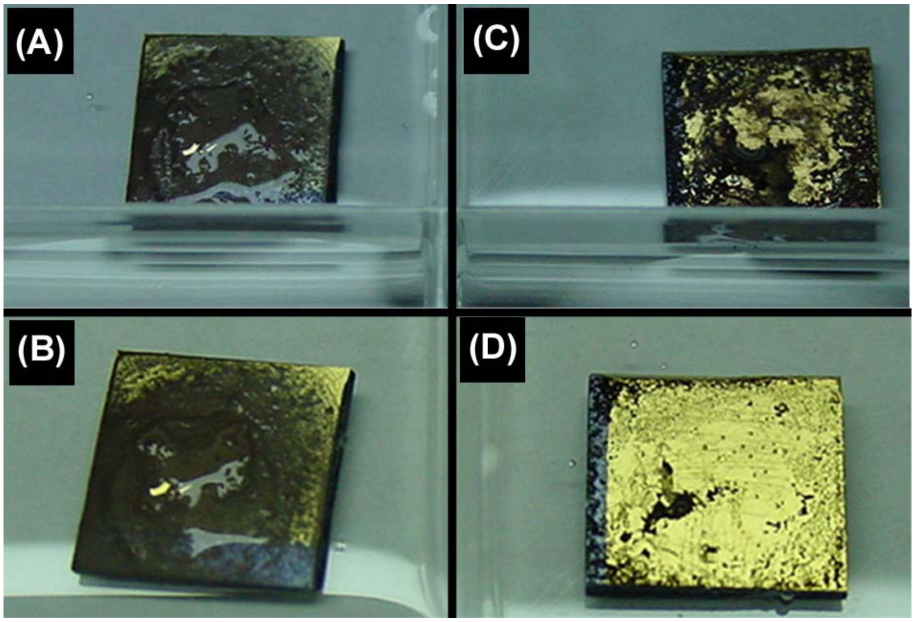

Figure 4.9: Photograph of untreated (C, D) Ge nanowires (~2 mg/cm2) and nanowires treated with (A, B) 2-methyl-1,3-butadiene before and after immersion in deionized water for 120 min. The untreated nanowires dissolve after 120 min.

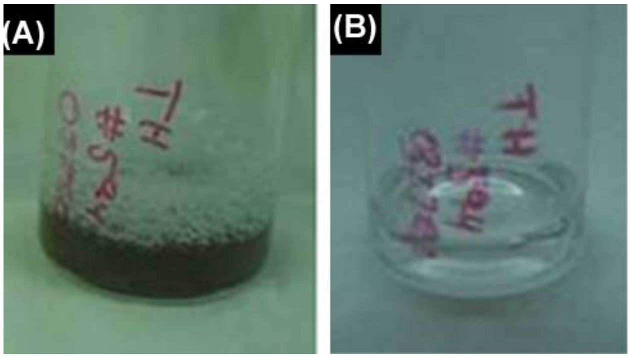

Figure 4.10: Optical photographs of an aqueous Ge nanowire suspension stabilized with sodium dodecylsulfate. (A) Initially and (B) after 24h exposure to the aqueous environment.

4.3.6 Effect of Surface Modification on Contact Resistance in Nanowire Devices

The effect of the surface modification on the ability to form low resistance electrical contacts to the Ge nanowires are discussed in detail in Chapter 7. Briefly, Ge nanowires interfaced immediately after HCl etching with Pt contacts deposited by electron beam assisted metal CVD exhibited linear current-voltage transport with a p-type gate effect (see Figure 4.11A). In contrast, HCl-etched Ge nanowires exposed to the atmosphere for ~24 h prior to contacting with e-beam lithographically defined electrodes exhibited electrical transport behavior dominated by Schottky barriers at the contacts (see Figure 4.11B). Nanowires without chemical surface treatment obtained from the crude synthetic product exhibited *massive* contact resistance, and no measurable electrical current could be passed through the nanowire.

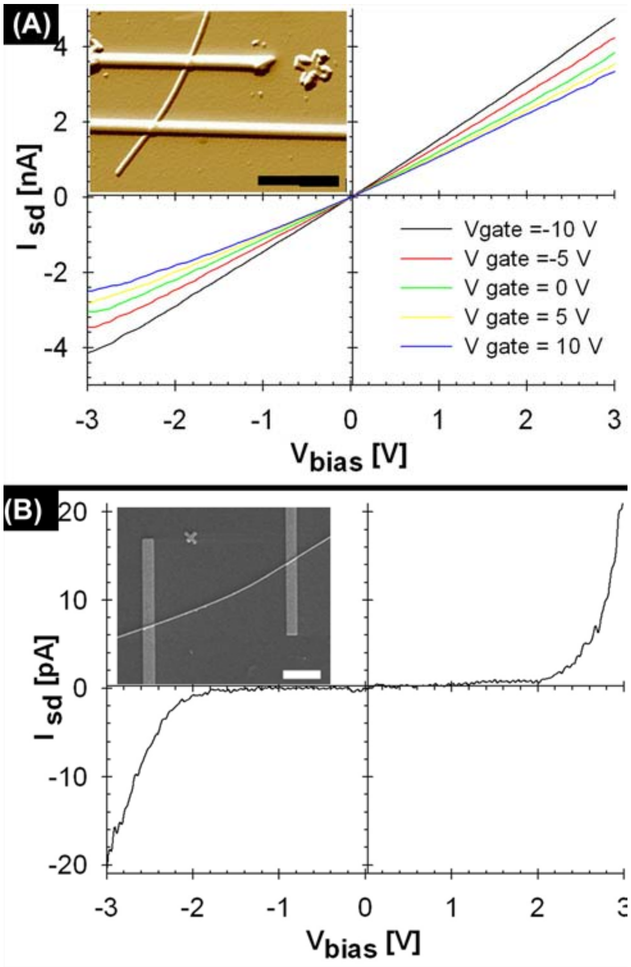

Figure 4.11: Room temperature current-voltage measurements of (A) a freshly HCl-etched Ge nanowire and (B) an HCl-etched Ge nanowire after 24 hr of exposure to dry air contacted with Pt electrodes deposited by e-beam assisted CVD. The fresh HCl-etched nanowires form ohmic Pt/nanowire contacts, whereas the oxidized nanowire exhibits significant due to the Schottky barrier at each metal contact. Insets: AFM and SEM images of devices in (A) and (B), respectively, with 2 μm scale bars.

4.4 CONCLUSIONS

Although the Ge nanowires are highly sensitive to oxidation and corrosion when exposed to oxygen and water, organic monolayers can be adsorbed to the surfaces of Ge nanowires for chemical passivation and stabilization. The thermally initiated hydrogermylation approach was found that the most effective surface treatment used in combination with the SFLS nanowire synthesis. Alkenes, alkynes, and dienes were identified as suitable monolayer precursors, thermally initiated hydrogermylation reactions. A coating of the Ge nanowires with these species left abrupt, clean nanowire interfaces. The nanowires were chemically robust and stable, even when immersed in water. Without surface passivation, the nanowires oxidized to form a suboxide, consisting mostly of Ge^{1+} and some Ge^{2+} species when exposed to air, and mostly Ge^{3+} and Ge^{1+} when immersed in water. Passivation based on S, through treatment with $(NH_4)_2S$ did not yield robust well-characterized surface layers, with S penetrating into the Ge nanowires to form a thick GeS_x layer. Thiol passivation on HF etched nanowires led to incomplete monolayer coverage, while direct post-synthesis thiol treatment in the reactor formed a well-defined monolayer terminated surface. H- and Cl-terminated Ge nanowires also exhibited sharp, clean interfaces, however, were found to be very sensitive to oxidation, making the use of these species for subsequent surface reactions (such as alkylation using Grignard reactions) impractical.

4.5 REFERENCES

(1) Hu, J.; Odom, T. W.; Lieber, C. M. *Acc. Chem. Res.* **1999**, *32*, 435-445.

(2) Prokes, S. M.; Wang, K. L. *Mater. Res. Sci. Bull.* **1999**, *24*, 13-14.

(3) Duan, X.; Huang, Y.; Cui, Y.; Wang, J.; Lieber, C. M. *Nature* **2001**, *409*, 66-69.

(4) Cui, Y.; Lieber, C. M. *Science* **2001**, *291*, 851-853.

(5) Cui, Y.; Wei, Q.; Park, H.; Lieber, C. M. *Science* **2001**, *293*, 1289-1292.

(6) Hahm, J.-i.; Lieber, C. M. *Nanoletters* **2003**, *4*, 51.

(7) Zhang, D.; Li, C.; Liu, X.; Han, S.; Tang, T.; Zhou, C. *Appl. Phys. Lett.* **2003**, *83*, 1845-1847.

(8) Kolmakov, A.; Zhang, Y.; Cheng, G.; Moskovits, M. *Adv. Mater.* **2003**, *15*, 997-1000.

(9) Chen, J.; Hamon, M. A.; Hu, H.; Chen, Y.; Rao, A. M.; Eklund, P. C.; Haddon, R. C. *Science* **1998**, *282*, 95-98.

(10) Holzinger, M.; Vostrowsky, O.; Hirsch, A.; Hennrich, F.; Kappes, M.; Weiss, R.; Jellen, F. *Angew. Chem. Int. Ed.* **2001**, *40*, 4002-4005.

(11) Georgakilas, V.; Kordatos, K.; Prato, M.; Guldi, D. M.; Holzinger, M.; Hirsch, A. *J. Am. Chem. Soc.* **2002**, *124*, 760.

(12) Bahr, J. L. Y., J.; Kosynkin, D. V.; Bronikowski, M. J.; Smalley, R. E.; Tour, J. M.; *J. Am. Chem. Soc.* **2001**, *123*, 6536-6542.

(13) Sun, X. H.; Wang, S. D.; Wong, N. B.; Ma, D. D. D.; Lee, S. T.; Teo, B. K. *Inorganic Chem.* **2003**, *42*, 2398-2404.

(14) Duan, X.; Huang, Y.; Lieber, C. M. *Nanoletters* **2002**, *2*, 487-490.

(15) Cui, Y.; Zhong, Z.; Wang, D.; Wang, W. U.; Lieber, C. M. *Nanoletters* **2002**, *3*, 149-152.

(16) Buriak, J. M. *Chemical Reviews* **2002**, *102*, 1271-1309.

(17) Pokrovski, G. S. S., Jacques *Geochimica et Cosmochimica Acta* **1998**, *62*, 1631-1633.

(18) Dean, J. A., Ed. *Lange's Handbook of Chemistry*; 15th ed.; McGraw-Hill: New York, 1999.

(19) Hanrath, T.; Korgel Brian, A. *J. Am. Chem. Soc.* **2002**, *124*, 1424-1429.

(20) Kingston, R. H. *J. Appl. Phys.* **1956**, *27*, 101-114.

(21) Schmeisser, D.; Schnell, R. D.; Bogen, A.; Himpsel, F. J.; Rieger, D.; Landgren, G.; Morar, J. F. *Surface Science* **1986**, *172*, 455-465.

(22) Johnson, J. R. T.; Panas, I. *Chem. Phys.* **1999**, *249*, 273-278.

(23) Parabhakaran, K.; Ogino, T. *Surface Science* **1995**, *325*, 263-271.

(24) Gregory, O. J.; Pruitt, L. A.; Crisman, E. E.; Roberts, C.; Stiles, P. J. *J. Electrochem. Soc.* **1988**, *135*, 923-929.

(25) Weser, T.; Bogen, A.; Konrad, B.; Schnell, R. D.; Schug, C. A.; Steinmann, W. *Phys. Rev. B* **1987**, *35*, 8184.

(26) Lyman, P. F.; Marasco, D. L.; Walko, D. A.; Bedzyk, M. J. *Phys. Rev. B.* **1999**, *60*, 8704-8712.

(27) Anderson, G. W.; Hanf, M. C.; Norton, P. R.; Lu, Z. H.; Graham, M. J. *Appl. Phys. Lett.* **1995**, *66*, 1123-1125.

(28) Lyman, P. F.; Sakata, O.; Marasco, D. L.; Lee, T. L.; Breneman, K. D.; Keane, D. T.; Bedzyk, M. J. *Surface Science* **2000**, *462*, L594-L598.

(29) Han, S. M.; Ashurst, R.; Carraro, C.; Maboudian, R. *J. Am. Chem. Soc.* **2001**, *123*, 2422-2425.

(30) Kosuri, M. R.; Cone, R.; Li, Q.; Han, S. M. *Langmuir* **2003**, *20*, 835-840.

(31) Cullen, G. W.; Amick, J. A.; Gerlich, D. J. *J. Electrochem. Soc.* **1962**, *109*, 124-138.

(32) Lu, Z. H. *Appl. Phys. Lett.* **1996**, *68*, 520-522.

(33) Choi, K.; Buriak, J. M. *Langmuir* **2000**, *16*, 7737-7741.

(34) Niwano, M.; Kageyama, J.; K.Kurita; Kinashi, K.; Takahashi, I.; Miyamoto, N. *J. Appl. Phys.* **1994**, *76*, 2157-2163.

(35) He, J.; Lu, Z. H.; Mitchell, S. A.; Wayner, D. D. M. *J. Am. Chem. Soc.* **1998**, *120*, 2660-2661.

(36) Bansal, A.; Li, X.; Lauermann, I.; Lewis, N. S. *J. Am. Chem. Soc.* **1996**, *118*, 7225-7226.

(37) Linford, M. R.; Chidsey;, C. E. D. *J. Am. Chem. Soc.* **1993**, *115*, 12631-12632.

(38) Cicero, R. L.; Linford, M. R.; Chidsey, C. E. D. *Langmuir* **2000**, *16*, 5688-5695.

(39) Li, C. P.; Lee, C. S.; Ma, X. L.; Wang, N.; Zhang, R. Q.; Lee, S. T. *Adv. Mater.* **2003**, *15*, 607-609.

(40) Ma, D. D. D.; Lee, C. S.; Au, F. C. K.; Tong, S. Y.; Lee, S. T. *Science* **2003**, *299*, 1874-1877.

(41) Teplyakov, A. V.; Lal, P.; Noah, Y. A.; Bent, S. F. *J. Am. Chem. Soc.* **1998**, *120*, 7377-7378.

(42) Lee, S. W.; Nelen, L. N.; Ihm, H.; Scoggins, T.; Greenlief, C. M. *Surface Science* **1998**, *410*, L773-778.

(43) Bodlaki, D.; Yamamoto, H.; Waldeck, D. H.; Borguet, E. *Surface Science* **2003**, *543*, 63-74.

Chapter 5: Structural and Crystallographic Characterization of Ge nanowires via High-resolution Electron microscopy

5.1 INTRODUCTION

High-resolution transmission electron microscopy (HRTEM) is arguably the most crucial and powerful characterization tool in nanomaterials research. The combination of high-resolution structural analysis and nanometer scale spatially resolved elemental and electronic characterization provides critical information about the nanomaterials that cannot be attained by any other techniques. This chapter discusses key aspects of structure analysis of single crystal Ge nanowires such as growth direction, faceting on the axial and radial surfaces, cross-sectioning, the structure at the Au-Ge interface and crystallographic defects. The results of the analysis are related to fundamental aspects of the VLS growth mechanism in an effort to elucidate growth direction determining factors. Theoretical models relating to the energy minimization of the initial Ge nucleus and the stability of the Au-Ge interface are discussed and related to the characteristics of nanowires obtained by various synthesis approaches reported in the literature. The structural analysis is also related to the unique mechanical properties of the nanowires. Finally, nanowires were intentionally destroyed by mechanical strain, intense electron beam irradiation, or electrical breakdown during electron transport measurements. The end terminals of nanowire destructed by each of these methods are compared.

5.2 EXPERIMENTAL

5.2.1 Sample Preparation

One potentially problematic aspect of materials characterization through HRTEM is that the relative amount of material analyzed in the microscope represents only a minute fraction of the overall sample, which can make it difficult to infer ensemble average quantities like nanowire diameter or growth direction. The statistical aspects of the sample analysis are akin to characterizing the population of an entire country based on the descriptions of a few people in a small village. Nevertheless, solution based sampling methods such as the ones discussed below can avoid most sample inhomogeneity problems through adequate mixing and thus still allow for a statistically significant sample analysis.

TEM samples were prepared drop casting the nanowires from a diluted isopropanol or toluene suspension onto lacey carbon films suspended over 200 mesh copper grids (EMS). Complete evaporation of the dispersion containing the nanowires commonly resulted in the co-deposition unwanted organic contamination, therefore only approximately 80% of the solvent were allowed to evaporate and the remainder of the sample was wicked away with the edge of a Kimwipe. TEM samples subjected to extended beam exposure times such as for example in STEM-ELS[*] or STEM-EDS[†] linescans, often required a brief treatment with 95/5 Ar/O_2 plasma cleaner (Fishione150) to remove unwanted carbonaceous contamination which would otherwise build up. Plasma exposure

---

[*] The results of the STEM-ELS characterization of plasmon and core loss excitations in Ge nanowires are discussed in Chapter 6.

[†] STEM-EDS results are discussed in Appendix D for the spatially resolved elemental analysis of Mn doped Ge nanowires.

times were generally limited to 20 s since longer exposure times resulted in deterioration to the lacey carbon support and consequently unfavorable specimen drift in the TEM column.

In an alternative sample preparation approach, lacey carbon TEM grids were mechanically scraped across an ensemble Ge nanowire sample deposited on a Si substrate. This method permitted the facile one-step preparation of Ge nanowire samples without any intermediate solution processing and thus avoided problems associated with organic film or solvent contamination associated with the drop casting approach.

Cross sectional samples were prepared by dispersing ensemble nanowires in epoxy (Spurr resin) and drawing the dispersion through a 0.4mm i.d. Teflon tube to aid in the alignment of the nanowires.[‡] The sample was then polymerized in a vacuum oven at 70°C for 24 - 48h. Sections with target thickness of 70 nm were then cut at -40°C using a cryo-ultramicrotome (RMC Products MT-990) and deposited on bare 300 mesh Cu TEM grids.

5.2.2 Microscope Conditions

The HRTEM characterization was performed on a JEOL 2010F equipped with a field emission gun. The vast majority of the TEM was carried out with an acceleration voltage of 200 kV, while imaging of cross sectional samples was performed at 120 kV to limit damage to the thin epoxy film. The specimens were held in either a single- or double-tilt holder allowing the proper orientation of the sample with respect to the incident beam.

[‡] The author gratefully acknowledges Dwight Romanovicz for assistance in the preparation of cross sectional samples.

Mechanical bending studies of individual Ge nanowires were carried out with a Zyvex S100 nanomanipulator placed inside a HRSEM (LEO 1550) operated at an acceleration voltage of 2 kV. Individual nanowires places on a lacey carbon grid were located with the HRSEM and manipulated with ultra-sharp tungsten probes.

5.2.3 Analysis of the Growth Direction

The classification of the nanowire growth direction was based on the combination of TEM images with corresponding electron diffraction patterns or Fourier transforms of the image. The nanowires are generally deposited flat on the support grid; however, the growth axis of the wire is not necessarily orthogonal to the axis of the incident electron beam. The accurate characterization of the growth axis therefore required tilting of the specimen to a near orthogonal alignment relative to the beam axis.

5.3 RESULTS AND DISCUSSION

5.3.1 Crystallographic Growth Direction

5.3.1.1 Comparison of Growth Directions Observed in Ge Nanowires Prepared by Various Techniques.

The classification of the nanowire crystallographic growth direction is perhaps the most important aspect of the HRTEM characterization of single crystal Ge nanowires. A detailed characterization of the metal seed-nanowire interface and the structure of the initial nanowire nucleus provide valuable insight into the fundamental processes of nanowire nucleation. A better understanding of these factors might permit synthesis control over the crystallographic growth direction of the nanowire, which is an extremely desirable goal since the anisotropic properties such as electrical conductivity, mobility, index of refraction and bandgap electronic and optical properties of the nanowires are expected to vary depending on the lattice orientation of the wire. For example, tight binding calculation on Si nanorods have predicted an anisotropy of the energy gap.[1] Control of the growth direction of Group IV semiconductors has been elusive to date, however, recent work by Yang and co-workers demonstrated the ability to control the crystallographic orientation in the growth of aligned GaN nanowire arrays.[2]

The supercritical fluid liquid solid (SLFS) synthesis described in detail in Chapter 2 provides high quality single crystal Ge nanowires which predominantly grown along the <110> axis. The HRTEM image in Figure 5.1A shows an 8.2 nm diameter nanowire with the corresponding (220) and (-111) lattice planes perpendicular and parallel, respectively, to the [110] axis of the nanowire. Figure 5.1B shows a 3.7 nm diameter nanowire from observed in the same sample. The Fourier transform in the bottom left inset indicates a crystal alignment near the [110] pole with the [-110] and [-11-1] orientations at 35^o and 90^o, respectively, relative to the [-112] growth axis. Based on the crystallographic characterization of hundreds of nanowires prepared under various synthesis conditions the <110> growth axis was observed in nearly 90% of all cases. With approximately 5% of the nanowires oriented along the <211> axis and the remaining fraction with either <111> or an unidentifiable growth axis. The correlation between the relative occurrence of non-<110> oriented nanowires and synthesis conditions is discussed below.

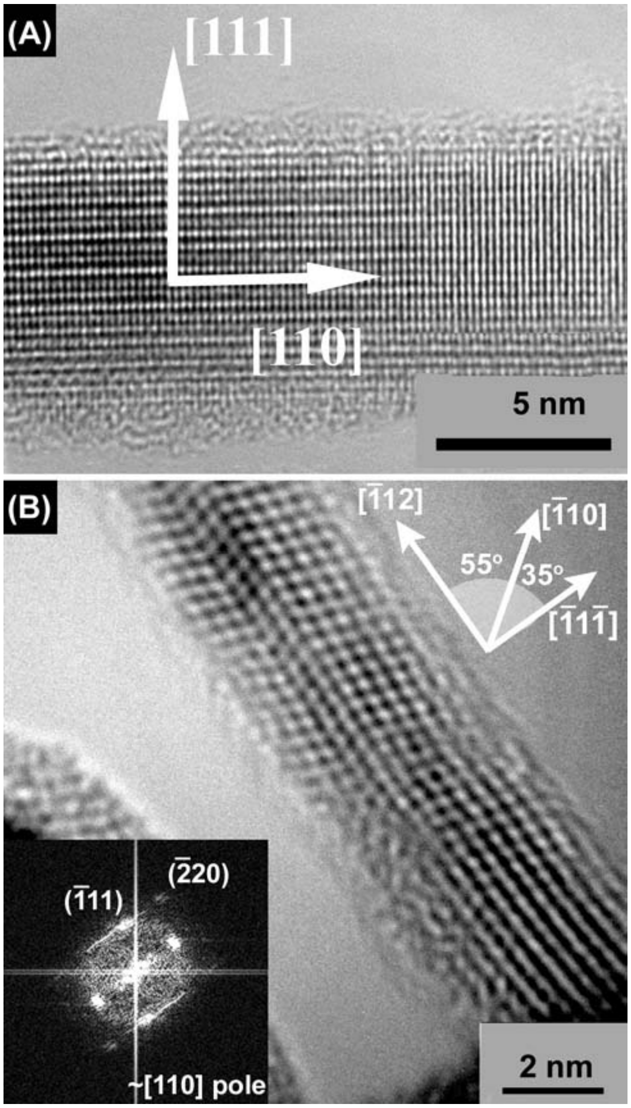

Figure 5.1: HRTEM images of Ge nanowires: (A) An 8.6 nm diameter nanowire oriented along the [110] axis and (B) a 3.7 nm diameter nanowire with the less common [-112] growth axis.

The predominant single crystal growth direction distinguishes between various synthesis approaches reported for Ge nanowires as outlines in Table 5.1. High temperature methods such as the laser catalyzed growth (LCG)[3], and physical vapor transport (PVT)[4-6] result in the formation of wires oriented predominantly along the <111> axis. For synthesis temperatures in the range of 320-380°C chemical vapor deposition (CVD) approaches using $(Cp^*)_2Ge$ and GeH_4 precursors in combination with Fe and Au, respectively, as nucleation Ge nanowires exhibit <111> oriented growth.[7,8] Similar CVD methods at lower temperatures (275-320°C) on the other hand favor the <110> growth axis.[9,10] Similarly, Ge nanowires prepared via solution based methods in the temperature range of 270-400°C also exhibit <110> growth.[11,12]

The oxide assisted growth (OAG) [13,14] synthesis, which involves the high temperature laser ablation of a mixture of Ge and GeO_2 in the absence of a metal seed particle results almost exclusively in <211> oriented nanowires. These results suggest that a variety of thermodynamic and kinetic factors are involved in the processes determining the crystallographic orientation of Ge nanowires. The general trend however appears to be that nanowires prepared under high temperature and high supersaturation conditions commensurate with fast nanowire growth favor the <111> orientation.

Based on the supersaturation criterion, a shift in the predominant growth direction from <110> to <111> is therefore expected if the SLFS synthesis parameters are modified to more closely resemble the high temperature high supersaturation conditions encountered in PVT and LCG. In fact, we have observed a higher relative occurrences of <111> oriented growth in near 20% of the analyzed nanowires from samples prepared using tetraethylgermane as the precursor at 400°C—conditions expected to provide greater seed droplet supersaturation. Similar synthesis temperature influence on nanowire growth direction has recently been shown for hot filament CVD grown GaN nanowires. [15]

Growth Axis	Method	Temp. [°C]	Precursor	Seed Metal	Reference
<111>	PVT	950	Ge powder	Au	4
	PVT	1010	Ge, GeI_4	Au	5
	PVT	800	Ge particles	Au	6
	LCG	820	$Ge_{0.9}Fe_{0.1}$ target	Fe	3
	CVD	320-380	GeH_4	Au	8
	CVD	325	$(Cp^*)_2Ge$	Fe	7
<110>	SFLS	370-400	DPG,TEG	Au	11
	Soln.	275	$GeCl_4$,Ph-$GeCl_4$	Na	12
	CVD	320-285*	GeH_4	Au	10
	CVD	275	GeH_4	Au	9
<211>	OAG	700	Ge,GeO_2	none	13,14

Table 5.1: Summary of the growth directions and key synthesis parameters for Ge nanowires prepared by various techniques, such as physical vapor transport (PVT), laser catalyzed growth (LCG), chemical vapor deposition (CVD), supercritical fluid liquid solid (SFLS) and oxide assisted growth (OAG). *The Ge nanowire synthesis by Greytak et al.[10] was initiated at 320°C and then maintained at 285°C.

5.3.1.2 Stability of the Initial Ge Nucleus

The apparent correlation between supersaturation conditions and crystallographic growth axis warrants a closer inspection of the fundamental aspects of the VLS growth. Figure 5.2A shows the bulk equilibrium binary phase diagram for Au-Ge and a schematic representation of the three critical stages of nanowire nucleation. First Ge, generated by the thermolytic degradation of the organogermane precursor, adsorbs and dissolves into the crystalline Au seed particle (Figure 5.2B).

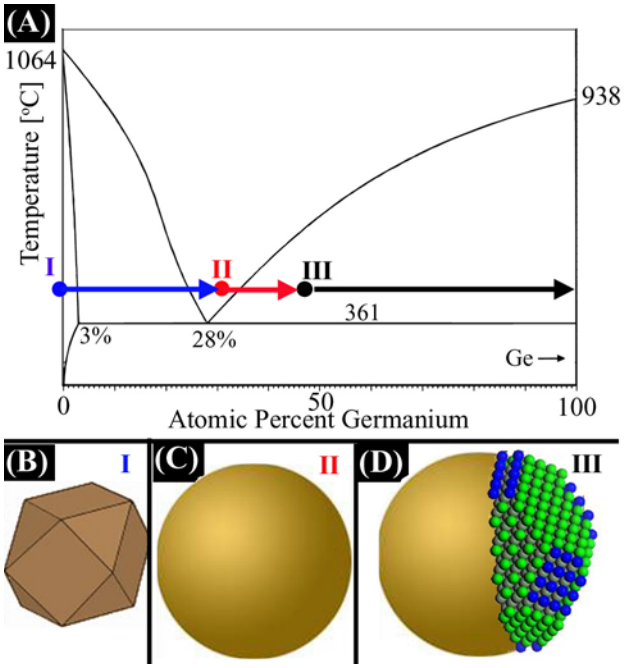

Figure 5.2- Detailed Schematic of the VLS nanowire growth mechanism. (A) Binary equilibrium phase diagram for bulk Au-Ge, (B) crystalline Au seed particle, (C) liquefied AuGe alloy droplet, and (D) liquid alloy droplet with initial Ge nucleus. {111} surface atoms are shown in bright green, Ge atoms in {100} planes are shown in light blue and non-surface atoms are shown in dark green.

With continued adsorption of Ge from the surrounding supercritical fluid environment, the Ge concentration in the seed particle increased until the alloy particle undergoes a phase change and liquefies (Figure 5.2C). While the covalently bonded dodecanethiol sterically stabilizes the Au seed nanocrystals, the ligand coverage and corresponding stabilization effects on the liquid alloy appear to be much weaker as evidenced by the undesirable agglomeration of liquid seed alloys discussed in Chapter 2. Further adsorption of Ge eventually leads to supersaturation of the liquid AuGe alloy droplet and result in the formation of an initial Ge nucleus crystal (Figure 5.2D). The structural properties of this nucleus appear to be a decisive factor in the crystallographic orientation of the nanowire that ultimately grows from it. Wu and Yang[6] reported an in-situ observation wherein Ge nanowires were grown from au crystal at 850°C inside a TEM, however, the image resolution of their experiment did not permit a detailed analysis of the crystal structure.

5.3.1.3 Faceting at the Nascent Nanowire Terminal

The structure of the initial Ge nucleus is governed by energy minimization, which requires consideration of the surface energies of various crystallographic facets and the curvature at the liquid-crystal interface. For bulk Ge, the surface energies of low-index facets decrease in the order of $\gamma_{\{111\}} < \gamma_{\{100\}} < \gamma_{\{110\}}$, suggesting that the initial nucleus should be dominated by {111} surface facets. However, the extreme curvature at the liquid-crystal interface and its small size prohibits the formation of a reconstructed a single {111} facet. Instead, a nucleus structure that more closely adapts to the curvature of the interface should be favored. The series of bulk surface energies listed above can serve as a general guide, but their applicability for predicting the surface energy of for the nucleus structure is questionable due to the extensive rearrangement expected to occur on nanoscale curved structures. The combined considerations of curvature, low surface energy, and symmetry suggest a faceting composed of {111} (green) and {100} (blue) surfaces as shown in Figure 5.2D.

The HRTEM image in Figure 5.3 illustrates the terminal end of a 9.6 nm diameter Ge nanowire with [-110] growth direction. The Fourier transform in the top left inset confirms the crystallographic orientation as viewed from the [110] pole axis. Notably, the nascent end of the nanowire is tapered by two {111} facets at a 55^{o} angle relative to the [-110] growth axis. The model shown in the bottom right is aligned to near the same pole axis as the TEM image and shows similar {111} (shown in green) faceting at the nascent end. The faceting of the side surfaces is discussed in detail below. The good agreement between the crystallographic model and the HRTEM image confirms the significance of the formation of an energy-minimized nucleus during the initial stage of the nanowire growth.

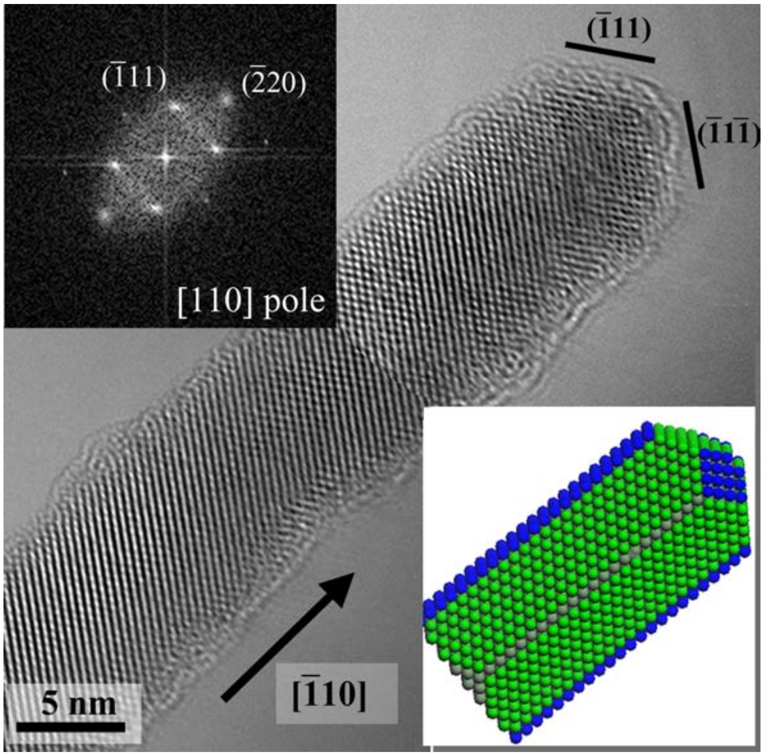

Figure 5.3: HRTEM image of the terminal end of a 9.6 nm Ge diameter with [-110] growth direction. Top left inset: Fourier transform of the image indicating the [110] pole axis of the wire. Bottom right inset: crystallographic model of a nanowire oriented along the sample pole as the nanowire in the image. Note the {111} facets at the nascent end of the nanowire.

The influence of the curvature on the structure of the seed crystal suggests the presence of a critical seed particle diameter above which the nucleation of a single {111} facet becomes energetically permissible, akin to the early growth of Si whiskers orthogonal to the lowest energy {111} liquid-crystal interface.[16] This trend has in fact been observed by Lieber and co-workers who noted a preferred nanowire orientation along the <110> and <211> axes for small diameter nanowires, whereas nanowires with diameters larger than 20 nm strongly favored the <111> growth direction. The analysis of the crystallographic orientation in hundreds of nanowires in this work has not verified this trend for the solution grown Ge nanowires. Instead, the growth direction appears to be more influenced by the extent of supersaturation prevailing during synthesis as discussed above.

5.3.1.4 Interface Structure of the Metal Seed - Nanowire Terminal

Wu et al.[17] have ascribed the preference of <110> orientation in small diameter Si nanowires to the presence of a V-shaped interface comprised of two {111} facets at the metal-nanowire terminal. The Analysis of various Au-Ge nanowire interfaces observed in this work are shown in Figure 5.4. Significantly, in contrast to the interfaces reported by Lieber and co-workers[17] the seed terminals of nanowires with <110>, <211>, and <111> growth axes are almost exclusively crystalline. Furthermore, the Au-Ge interfaces shown in Figures 4A-C are essentially flat and well defined reminiscent to the quality of MBE grown interfaces. As the seed particles changes from liquid to solid at the end of the nanowire growth, one might expect the crystallographic orientation of the Au_xGe_{1-x} alloy to be defined by the attached Ge crystals. However, the orientation of the alloy crystal relative to the direction of the Ge nanowire emanating from it did not show any consistent trends.

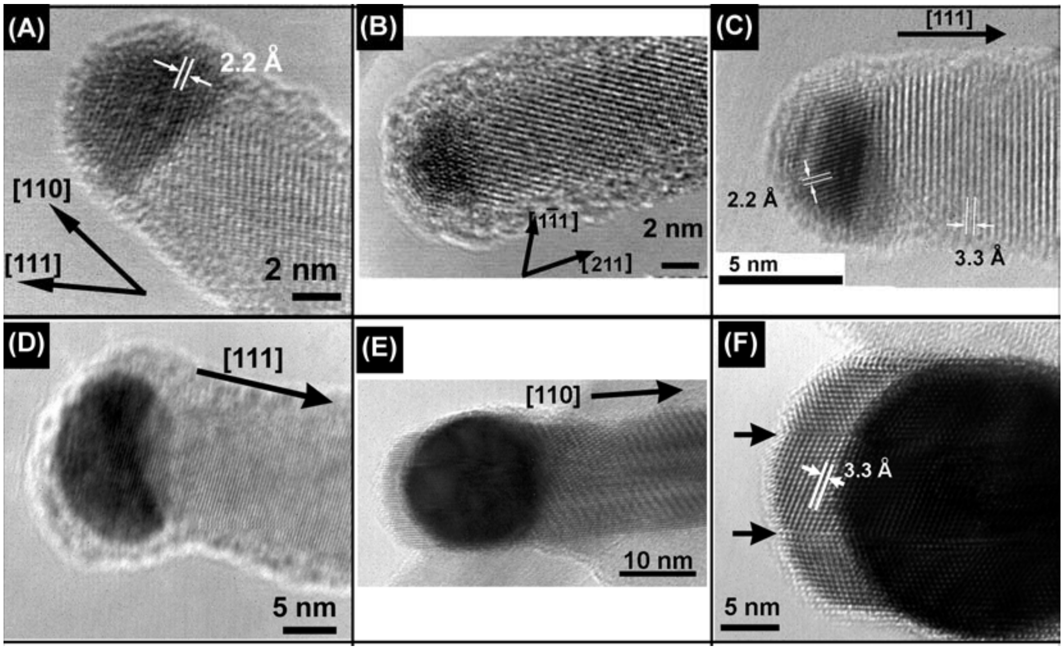

Figure 5.4: Au-Ge interface structure at the seed end of nanowires oriented along the (A) [111], (B) [211], (C) [111] axes. (D) [111] oriented Ge nanowire with non-crystalline Au seed particle. (E) Au seed particle with Ge emanating from two opposite sides and (F) higher resolution image of the left Au-Ge interface shown in (E). The arrows indicate two crystallographic defects.

Figure 5.4D shows the rare occurrence of an apparently non-crystalline seed crystal at the end of a [111] oriented Ge nanowire. The slight curvature of the Au-Ge interface is different from the more common flat interfaces (Figures 5.4A-C), although a similarity to the V-shaped interface presented by Wu et al.[17] is not apparent. A very rare occurrence of an apparently double nucleation arising from a single seed particle is shown in Figure 5.4E. The high-resolution image reveals a high number of two crystalline defects extending from both directions of the seed particle. The arrows indicate the presence of a twinning-type defect observed at the right end of the seed particle.

5.3.2 Crystallographic Defects

The dominance of <211> oriented Ge nanowires prepared by the OAG method[13,14] was explained with a model based on stability criteria of atoms added to specific crystal planes of the growing crystal and the presence of a crystallographic defect (such as a low energy screw dislocation). This model predicts that only <110> and <211> oriented nanowires should be observed. <111> oriented growth on the other hand should be forbidden due to the absence of a perpetuating {111} surface step. Apparently the high levels of supersaturation present during LCG and PVT syntheses eliminate the need for a crystal defect to sustain growth and atoms can attach directly to the {111} surface allowing growth sustained growth in the <111> direction.

5.3.2.1 Defects Resulting in Change of the Direction of the Nanowire

While the OAG model may not accurately describe the nanowire growth under supersaturation conditions, it provides some useful insights into underlying processes responsible for the formation of crystallographic defects in nanowires. Figure 5.5 shows an SEM image of Si nanowires formed under conditions of low supersaturation (450°C and 6MPa).[§] The image shows several large diameter (50-80 nm) nanowires with a high number of defects predominantly in the form of a 60° changes in direction of the nanowire. The schematics in Figure 5.5B and C show the growth by {111} steps along the [110] direction as suggested by the OAG model discussed above. Presumably, the low supersaturation conditions can

---

[§] Germanium nanowire synthesis under these temperature and pressure conditions would be characteristic of high Ge supersaturation growth. However, as discussed in Chapter 3 the conditions for Si nanowire growth are significantly different so that 450°C and 6 MPa is characterized by low Si supersaturation.

lead to a disturbance at the liquid-crystal interface (Figure 5.5C) resulting in temporary asymmetric growth which eventually reverts to the growth along a favored [101] direction oriented at 60^o to the initial wire axis. The inset of Figure 5.5A shows a 60 nm diameter Si nanowire, which undergoes at least eight well-defined successive 60^o changes in nanowire orientation along the length of just a few micrometers.

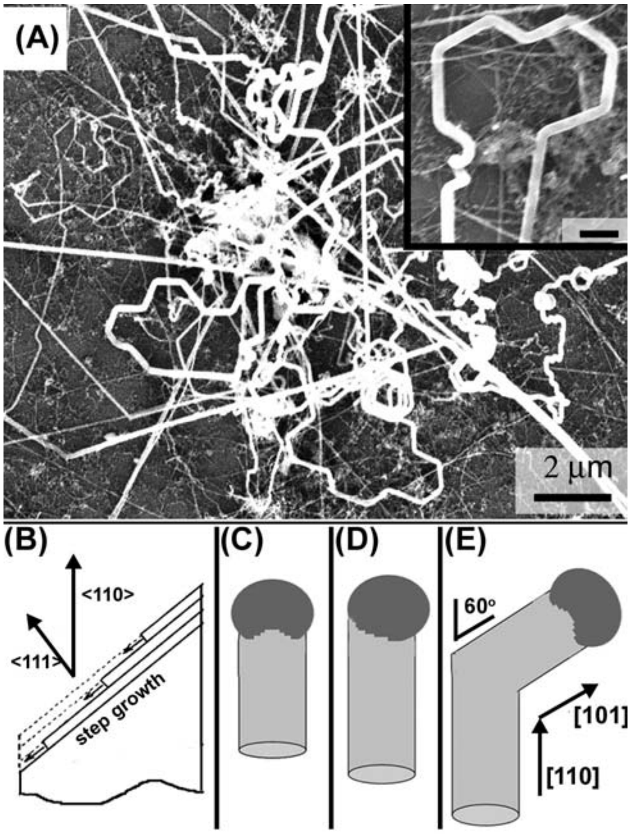

Figure 5.5: SEM image of Si nanowires with many defects inset scale bar 400 nm. (B) Schematic of nanowire growth via {111} step plane growth. (C) Initial nanowire growth (D) interface disturbance resulting in a 60^0 change in nanowire orientation.

5.3.2.2 Defects Resulting in Change of the Crystallographic Orientation and Direction of the Nanowire

Figure 5.6 shows Ge nanowire with a rare and intriguing crystallographic defect. The bottom segment of the structure shows a defect-free 6 nm diameter with oriented along the [-1-10] growth axis. The nanowire then appears to encounter a disturbance during growth resulting in the formation of the kinked defect structure (see high-resolution image in the inset). The nanowire emerging from the defect site at a 73^{o} angle relative to the incident wire maintains a 6 nm diameter yet undergoes a change in crystallographic growth axis and grows along the [21-1] axis. The inset on the right illustrates the single crystal character of the kinked site and shows a defect running along the axis of the [21-1] segment of the nanowire. In contrast to the common {111} twinning defect observed in GaAs nanowires grown via the SFLS approach,[18] crystallographic defects in Ge nanowires grown by the same method are very rare and observed in less than 5% of the analyzed samples.

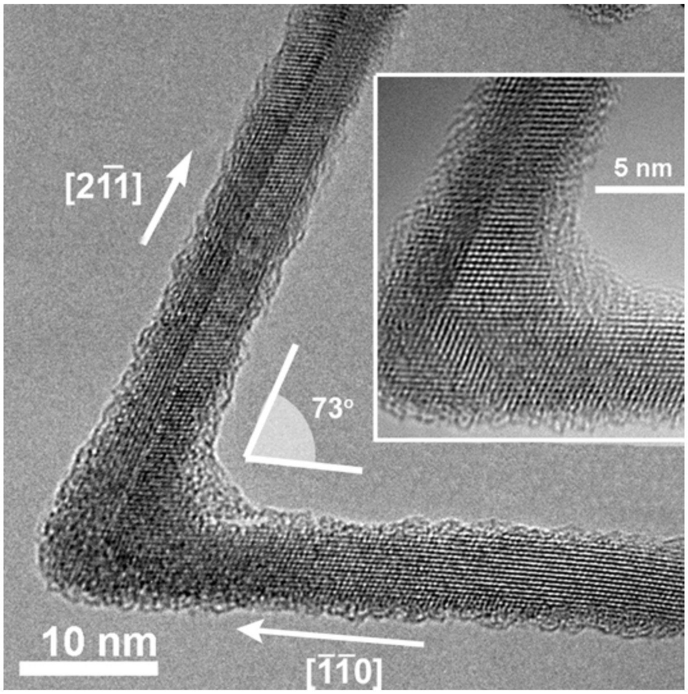

Figure 5.6: Ge nanowire with peculiar crystallographic defect. The nanowire undergoes a 73o change concomitant with a growth axis change from [-1-10] to [21-1]. The higher magnification image in the inset illustrates the single crystal at the kink site and a defect running along the [21-1] segment of the wire that the kink site is a single crystal.

5.3.3 Side Surface Faceting

5.3.3.1 Cross Sectional Imaging

The structure of the side surfaces of Ge nanowire was analyzed from cross sectional samples. Previous HRTEM[19] and STM[20] studies on Si nanowires obtained by the OAG synthesis have revealed the cross-sectional surface to be faceted by low energy {111} and {100} surfaces. HRTEM cross-sectional images of Ge nanowires with <110> and <211> growth axis are shown in Figure

5.7. The 22 nm (Figure 5.7A) and 35 nm (Figure 5.7C) diameter nanowires grown along the <110> axis exhibit a hexagonal shape faceted by {111} and {100} surfaces angled at 55^0 (Figure 5.7C). Cross sectional images with diameters less than 20 nm have not been acquired to date but are expected to exhibit similar cross-sectional geometry. Nanowires oriented along the <211> axis exhibit a rectangular cross-sectional structure faceted by {111} and {110} surfaces. The small diameter <211> nanowire with a 9x14 nm cross –section (Figure 5.7D) exhibits a slightly oblique geometry a {110}/{111} surface facet ratio of 0.64. The 27x33 nm cross-section of the larger [211] oriented nanowire shown in Figure 5.7F exhibits a more square-like geometry with a {110}/{111} surface facet ratio of 0.82.

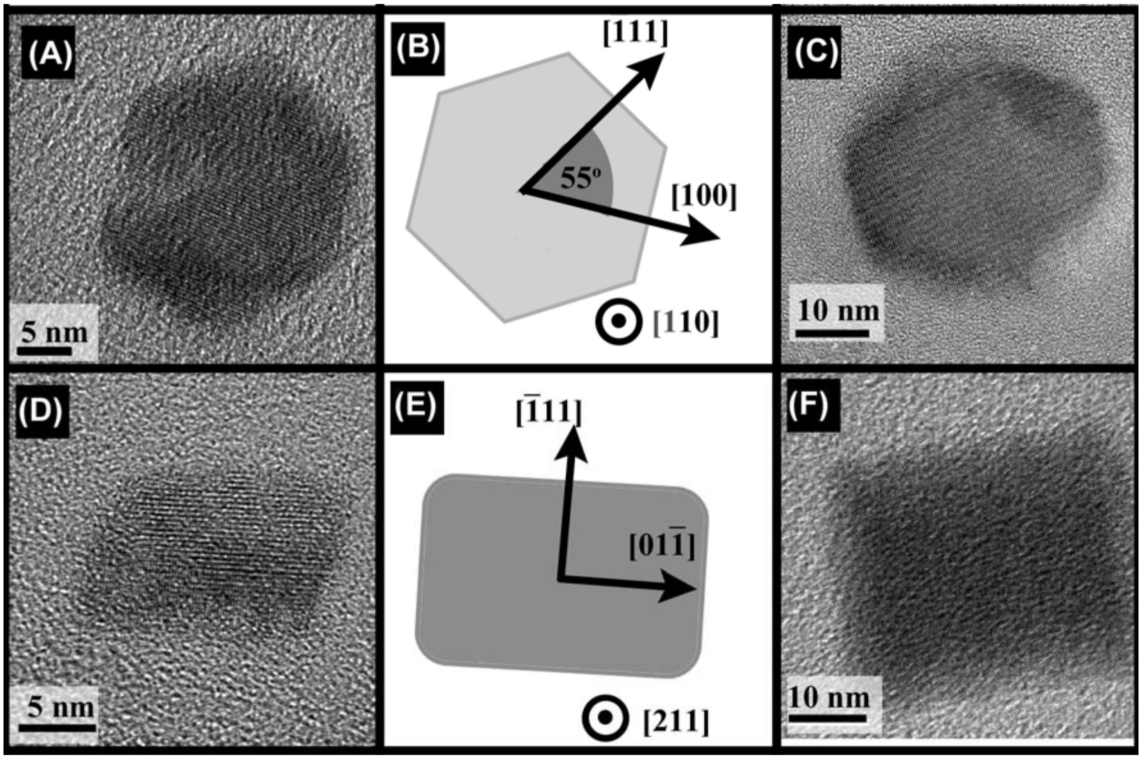

Figure 5.7: Cross sectional HRTEM images of Ge nanowires with <110> growth axis and (A) 22 nm and (C) 35 nm diameter. <211> oriented nanowires with a (D) 9x14 nm slightly oblique cross section and (F) 27x33 nm rectangular cross section.

5.3.3.2 Side Surface Faceting Analyzed through Sample Tilting

The cross-sectional faceting of the nanowires is observed in HRTEM imaging of nanowires aligned perpendicular to the incident beam and appears to be more pronounced in nanowires with <211> orientations. Figure 5.8A shows a HRTEM image of a single crystal Ge nanowire grown along the [211] axis and imaged near the [-315] pole. The feature observed to run along the axis could easily be misinterpreted as a stacking default, but is in fact an imaging artifact due to the faceting of the nanowire cross-section. Careful tilting of the nanowire to align the [-111] axis of the wire with the incident beam axis (Figure 5.8B) confirms the defect free crystal structure of the nanowire. The change in the apparent nanowire diameter as viewed from the [-315] and [-111] pole axis (i.e.: 13.8 and 13.2 nm, respectively) is another, albeit more indirect, indication of the cross- sectional structure of the nanowire. A schematic representation nanowire imaged from the [-315] and [-111] pole axis is given in Figure 5.8C.

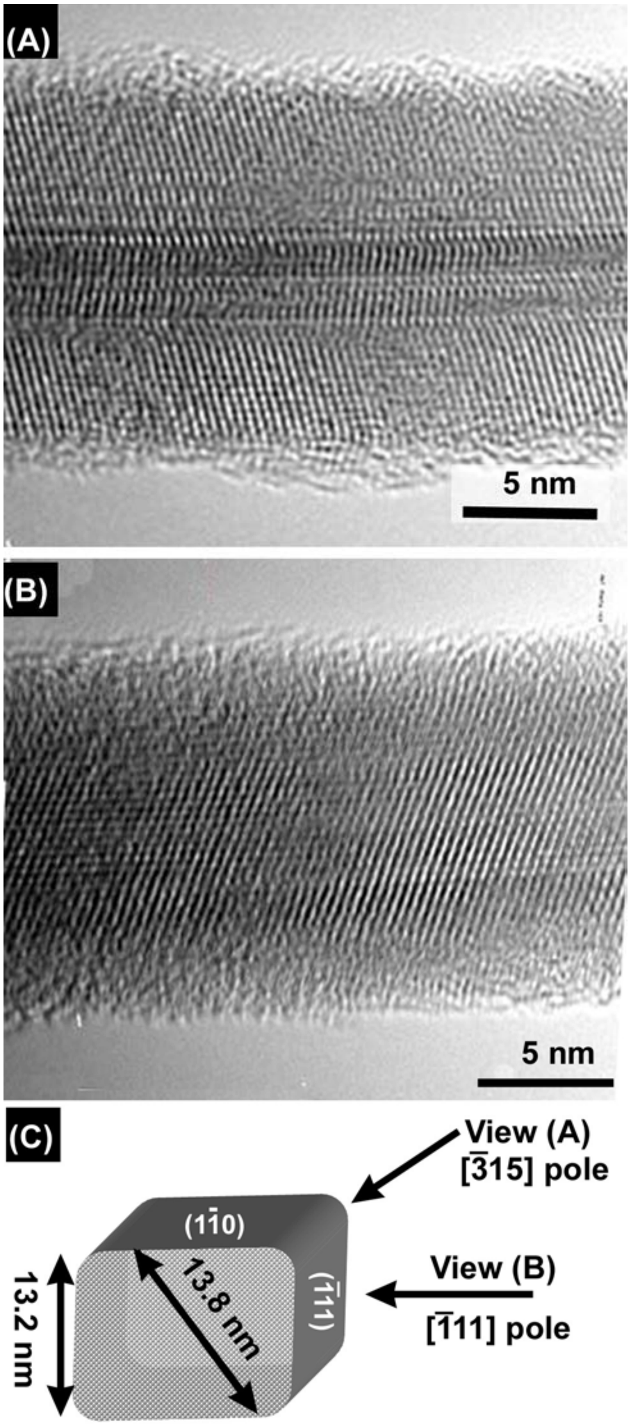

Figure 5.8: HRTEM images of a Ge nanowire with [211] growth axis imaged from the (A) [-315] and (B) [-111] pole axis. (C) Schematic representation of the nanowire viewed from the different perspectives and change in apparent nanowire diameter.

5.3.3.3 Forbidden Diffraction Spots Resulting from Incomplete Surface Layers

Electron diffraction (ED) patterns are not only important in the characterization of the nanowire growth axis, but can also provide information about the crystallographic structure of the nanowire surface. The [111] pole axis ED pattern of a 27 nm diameter Ge nanowire with <110> growth axis in Figure 5.9A shows the {220} reflections in the typical hexagonal arrangement. In addition to the normal {220}, (422}, and (440} reflections, a closer inspection of the diffraction pattern reveals reflections commensurate with a spacing of 1/3 {422}. These reflections are forbidden for a diamond cubic and face centered cubic lattice structures, but have previously been observed for incomplete surface faceting on Au nanocrystals.[21] In the case of Ge nanowires, these reflections are thus ascribed to incomplete {111} surface layers as schematically illustrated Figure 5.9B.

Similar forbidden Bragg reflections in thin film Ge specimens have been attributed to the presence Ge crystal with the hexagonal (lonsdaleite) crystal structure.[22,23] The hexagonal Ge phase has been predicted to have some intriguing electrical properties, such as low-temperature superconductivity.[24] The presence of this phase in synthesized Ge nanowires however, can be ruled out by absence of perfect diamagnetism in SQUID measurements[**] and the extensive crystallographic characterization discussed above. The possible formation of hexagonal Ge during the amorphization and recrystallization during intense electron beam irradiation is discussed in Section 5.3.5.3 below.

[**] SQUID measurements of ensemble Ge nanowire samples are discussed in Chapter 10.

Convergent beam electron diffraction patterns (CBED) contain additional information about the crystal structure not available from ED. As part of the completed structural characterization of Ge nanowires, CBED patterns were acquired to investigate the presence of chirality in the nanowire crystal. Figure 5.9C shows a CBED pattern of a 17 nm diameter nanowire viewed from the [101] showing the characteristic ±020, ±202, and ±111 Kikuchi lines. The appearance of the CBED pattern is more diffuse and the examination of the ±111 Kikuchi lines reveals a shift off the [101] pole as indicated by the direction of the arrow. The comparison of these CBED pattern reveal a slight change in crystal orientation along the length of the wire. Although extra care was taken in isolating a Ge nanowire with no apparent bending in the horizontal or vertical planes of the sample, the possibility of bending effects could not be ruled out. The observed change in crystal orientation can therefore not unambiguously be ascribed to possible nanowire chirality and bending effects (as discussed below) have to be taken into consideration.

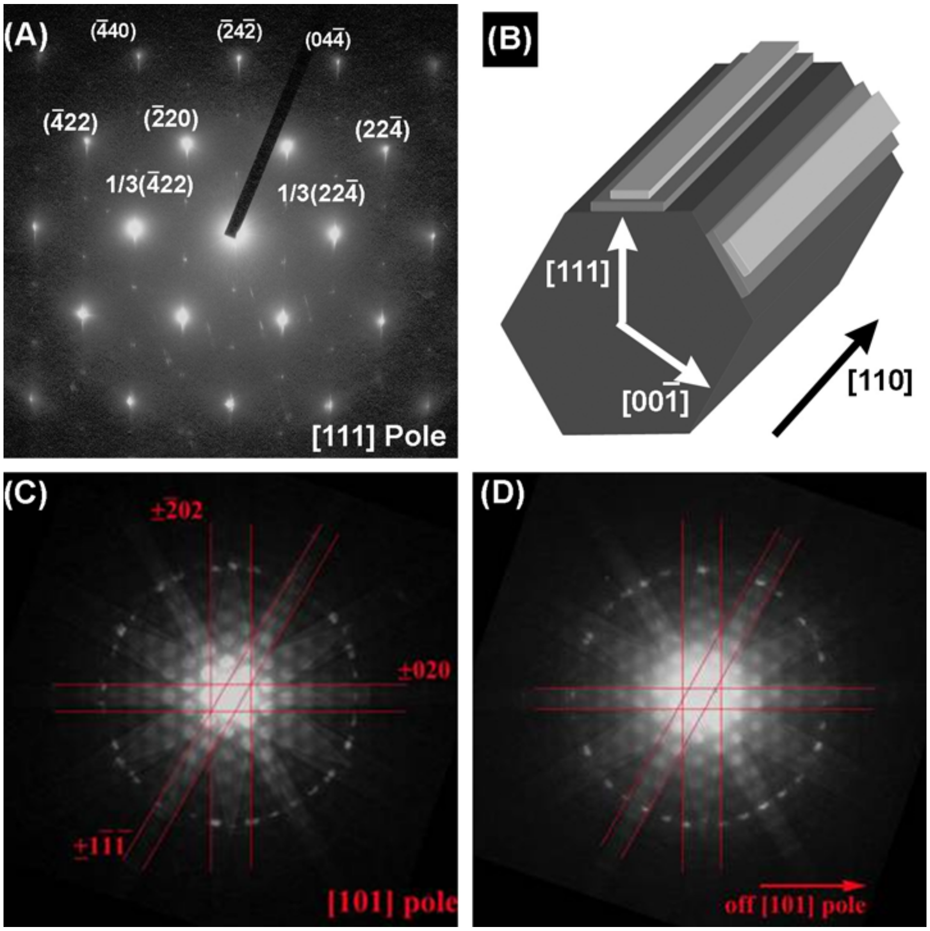

Figure 5.9: Electron diffraction patterns of Ge nanowires. (A) ED pattern acquired along the [111] pole axis showing typical {221}, {422}, and {400} reflections and forbidden reflections with 1/3{422} spacing. (B) Schematic of a nanowire with [110] growth axis and incomplete surface facets believed responsible for the forbidden reflections in (A). (C) CBED pattern of a nanowire aligned along the [101] pole and similar pattern acquired nearby (D) showing the twisting and or bending from the [101] pole axis.

5.3.3.4 Changes in Surface Structure along the Length of the Nanowire

The HRTEM images of the surfaces discussed above exhibited relatively smooth well-defined surfaces characterized by low index facets such as {111} and {110}. While the vast majority of the analyzed nanowires exhibited smooth surfaces, isolated samples with rougher surface morphology, such as the [110] oriented nanowire with a 4nm thick oxide layer in Figure 5.10 revealed reconstruction into (001) and (112) facets. While the reconstruction of the crystal at the surface is interesting and important to understand in the context of the surface chemistry of the nanowire, the occurrence of surface faceting steps as shown in Figure 5.10 are too rare to warrant a statistically accurate analysis.

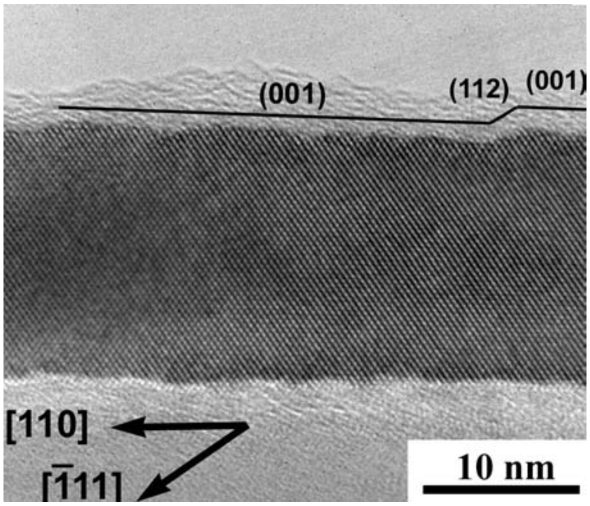

Figure 5.10: HRTEM image of a [110] oriented Ge nanowire with an oxide surface layer and surface faceting by (001) and (112) planes.

5.3.4 Bending of the Nanowire and Mechanical Properties

5.3.4.1 Bending Contrast Fringes

Low-resolution SEM and TEM images as well as the CBED patterns discussed above reveal that the single crystal nanowire exhibit an amazing flexibility that profoundly differs extremely brittle mechanical characteristics of bulk Ge single crystals. TEM images reveal the bending of the single crystals in the form of contrast bending fringes as shown in Figure 5.11. The low-resolution image in Figure 5.11A reveals contrast fringes along the length of several wires deposited along the length of the wires. Such contrast features are common in the imaging of crystalline structures. The large 60 nm diameter nanowire shown in Figure 5.11A shows thickness fringes –resulting from differences in the projected thickness of the nanowire across its diameter – and bending contrast fringes. The former contrast feature is only observed in large diameter nanowires, while bending contrast is observed in all nanowires and appears to be more pronounced in small diameter nanowires. The HRTEM image in Figure 5.11B shows that the nanowire maintains single crystal character in the bend regions.

Bending contrast fringes result from a change in the lattice orientation relative to the incident beam (see schematic in Figure 5.11D). Certain atomic planes are bent to satisfy the Bragg diffraction and hence diffract stronger than neighboring crystal sections. These areas appear as dark bands in bright field images (Figure 5.11A) or light bands in dark field STEM images (Figure 5.11C). The shape of the bending fringes contain some interesting information about the cross section of the crystal an possible chirality, yet its analysis is much less quantitative than the approaches discussed above.

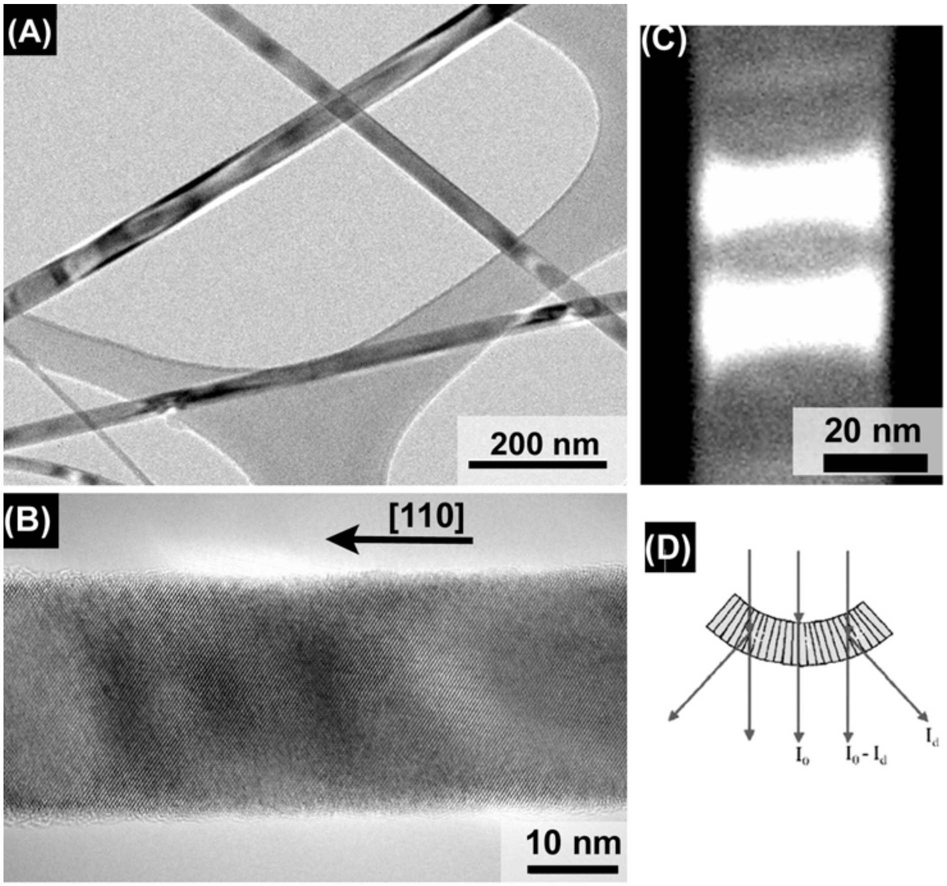

Figure 5.11: Bending contrast fringes in Ge nanowires. (A) Low-resolution TEM image showing bending and thickness fringes. (B) HTEM image confirming the absence of defects in the bend regions. (C) dark-field STEM image showing bending fringes in a 22 nm diameter nanowire. (D) Schematic model about the formation of bending contour (adapted from Ding and Wang.[25])

5.3.4.2 Mechanical Properties of Single Crystal Nanowires

The mechanical properties of the single crystal nanowires are fascinating, yet remain relatively unexplored to date. For example, the low-resolution image of a 12 nm diameter Ge nanowire shown in Figure 5.12A undergoes a 270^{o} bend resulting in the formation a complete loop. The corresponding HRTEM image of this wire in Figure 5.12B confirms the single crystal character of the nanowire and importantly shows the complete absence of crystallographic defects. This remarkable flexibility is simply unimaginable for bulk Ge single crystals which have a Young's and Shear modulus of 102 GPa and 67 GPa, respectively,[26] and undergo brittle fracture under the application small stresses.

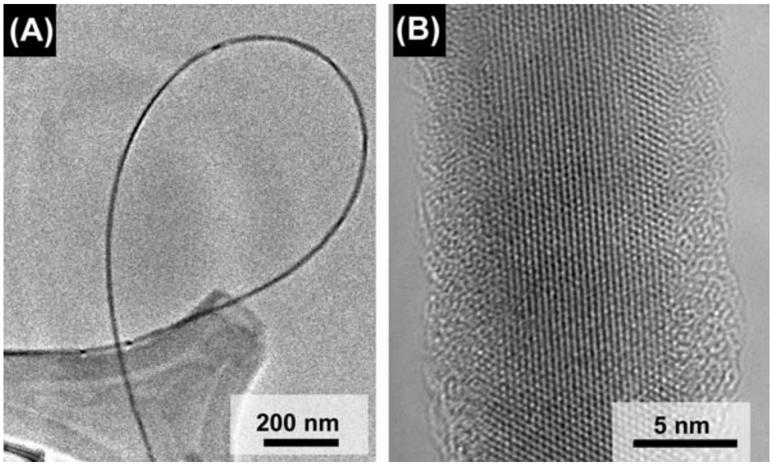

Figure 5.12: Low-resolution image (A) of a single crystal Ge nanowire undergoing a 270^{o} bend and forming a complete loop. (B) HRTEM image of the same wire showing the defect-free [110] oriented crystal structure.

5.3.4.3 Qualitative Testing of Mechanical Properties through Bending of a Nanowire with a Nanomanipulator

A quantitative analysis of mechanical properties of the nanowire such as the determination of the Young's or Shear modulus of the nanowire has not been performed largely due to the extremely difficulties associated with the handling of isolated nanowires. Recent experiments on Ge nanowires using a nanomanipulator placed inside a HRSEM however have shown promising progress toward the mechanical characterization of these structures. These early experiments are purely qualitative, yet confirm the nanowires remarkable mechanical properties. Figures 13A-C show a single crystal Ge nanowire manipulated by two tungsten probes connected to the nanomanipulator. The images confirm the amazing flexural strength of the nanowire under the application of significant compressive stresses. Removal of the applied stress resulted in the nanowire to spring back to its original configuration without exhibiting any discernable memory effects.

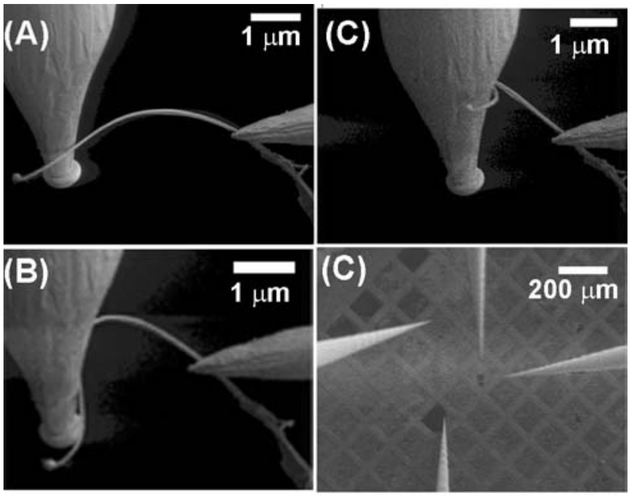

Figure 5.13: SEM images of a nanowire probed with a nanomanipulator (A)-(C) and (D) low magnification image showing the four tungsten manipulator probes.

5.3.5 Characterization of Fractured and Melted nanowires

5.3.5.1 Characterization of Nanowires Melted via Electrical Breakdown in Electron Transport Measurements.

The TEM image in Figure 5.14A was acquired from the same nanowire shown in the SEM images of the bending experiment in Figure 5.13. The crystallinity of the nanowire is confirmed by the visible bending fringes. The spherical particle at the end of the wire is not an Au seed droplet, but rather a single Ge crystal that melted and recrystallized during the electrical testing of the nanowire with the nanomanipulator. The inset of Figure 5.14A confirms the diamond cubic crystal structure of the particle at the tip. The current-voltage sweep applied through the nanomanipulators (Figure 5.14B) shows that the nanowire undergoes sudden failure at near 70 nA current corresponding to a maximum current density of near 2400A/cm^2.

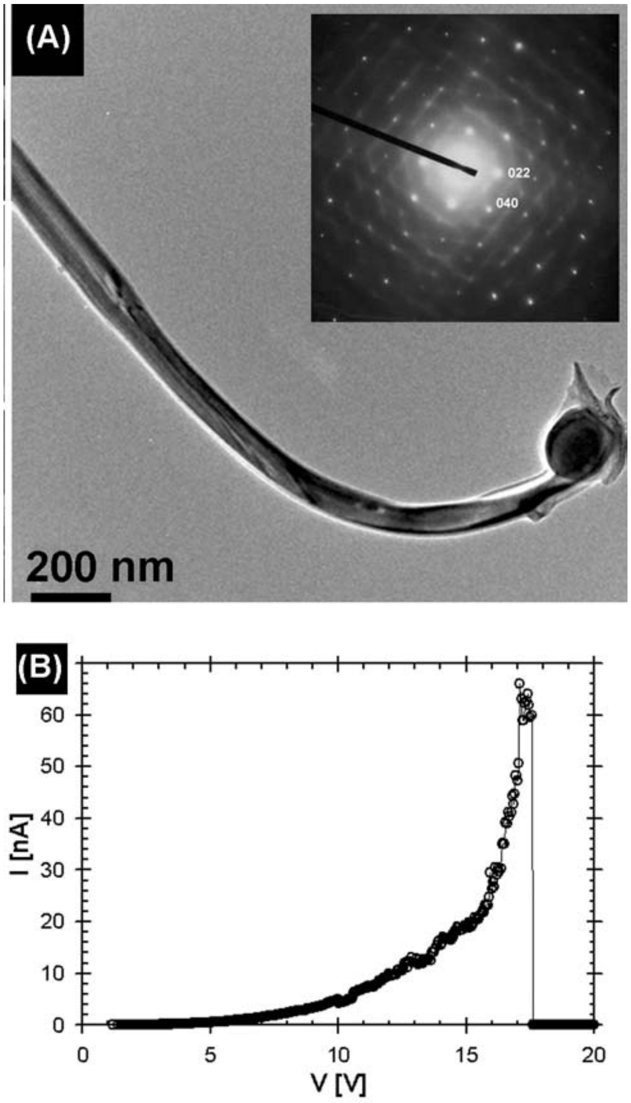

Figure 5.14: HRTEM image of a nanowire that melted during electrical testing (A). The inset shows an ED pattern confirming that the tip of the spherical particle is crystalline. (B) Corresponding current-voltage plot of the nanowire showing failure current density of approximately 2400A/cm^2.

5.3.5.2 Crystallographic Characterization of Mechanically Fractured Surfaces

Despite the remarkable mechanical properties of the nanowires, the application of sufficient stress or strain to the nanowire will ultimately result in the fracture of the crystal. Ultrasonication of a nanowire containing suspension results in the shortening of the average length of the nanowires.†† Nanowire samples prepared with extensive Ultrasonication commonly exhibited flat fracture surfaces. Alternatively, fractured nanowire surfaces can be analyzed in cross sectional samples of nanowires aligned parallel to the direction of microtome cut. The application of shear stress to nanowires embedded in a solid polymer matrix results in the brittle fracture of the nanowires bending of the nanowire is not free as shown in Figure 5.15, but constrained by the surrounding polymer. Figure 5.15A shows the fracture of a nanowire embedded in Parr resin under the application of strain in the apparent direction indicated in the direction of the arrows. Higher resolution images of the fracture surface reveal that the nanowires undergo brittle fraction along the {110} planes, in contrast to the {111} fracture plane encountered in bulk Ge. Presumably, the nanowires fracture along the {110} planes since the lower energy {111} are not accessible in a favorable orientation near perpendicular to the nanowire axis.

[††] Ultrasonication experiments aimed at the formation of Ge nanorods via the fracture of Ge nanowires are discussed in Chapter 9.

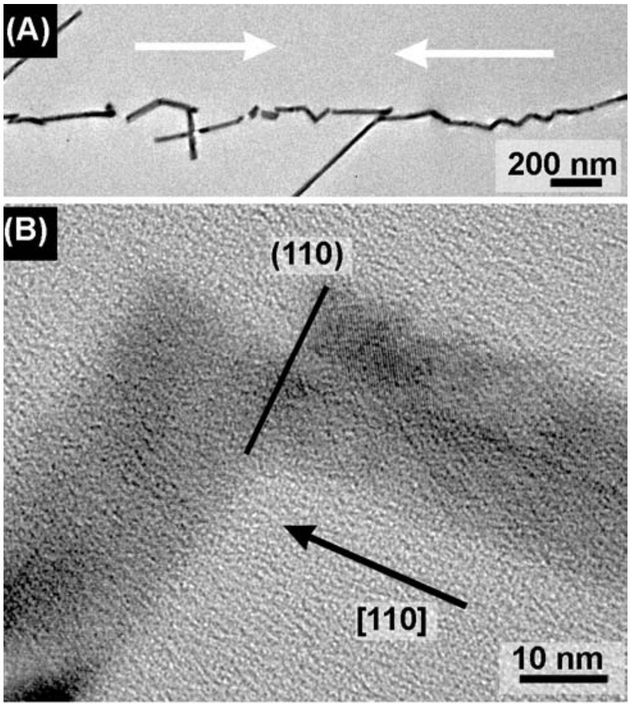

Figure 5.15: Fractured nanowires embedded in a polymer matrix. (A) Low-resolution image shows the fracture of the nanowires under the application of stress applied in the direction of the arrows. (B) HRTEM image of fracture surface in the same sample showing fracture in the along the {110] planes perpendicular to the nanowire axis.

5.3.5.3 Characterization of Nanowires Melted under Intense Electron Beam Irradiation

In 1983 Parson and Hoelke reported that the amorphous Ge thin films irradiated with an intense electron beam recrystallized in a hexagonal lattice.[27,28] Motivated by this work, similar recrystallization on Ge nanowires inside the HRTEM column were performed. Nanowires were first carefully amorphized under intense electron beam irradiation without breaking the wire. Additional exposure to less intense beam illumination then resulted in the recrystallization of the nanowire. Figure 5.16 shows a series of HRTEM images of a 6 nm diameter Ge nanowire after successive cross-over irradiation of the 200 kV electron beam with a beam current density near 500 pA/cm^2. Initially the nanowire shows defect free diamond cubic crystal structure with the [110] growth directions and lattice spacing 0.329 nm {111} and 0.201 nm {220} and interplanar angles of 55^o, 55^o, and 70^o.

After four ‘cross-over’ irradiation cycles, the nanowire shows clear damage to the crystal structure (Figure 5.16B). Additional ‘cross-over’ cycles result in the compete amorphization of the nanowire crystal and thinning of the cross section (Figure 5.16C). Figure 5.16D shows first signs of recrystallization of the nanowire and further thinning of the nanowire cross-section after further electron beam illumination. The small nanowire eventually breaks and forms a well-defined crystalline tip (Figure 5.16E). The high-resolution TEM image in Figure 5.16F and the corresponding FFT in the inset reveal interplanar angles of 57^o,57^o, and 67^o and 0.334 nm lattice spacings. For comparison, Parson and Hoelke observed interplanar angles of 56^o, 62^o, 62^o with lattice spacings of 0.343 nm and 0.324 nm.[27,28] The crystallographic properties of the recrystallized tip do not fully agree with either the diamond cubic, nor the hexagonal crystal structure, but more closely resemble the former. However, a conclusive crystal structure assignment cannot be made given the error associated with the measurement, the high similarities between the diamond cubic and hexagonal lattices, and the reconstruction effects due to the small size of the tip at the crystal. Similar experiments on larger nanowires wherein the nanowire did not break during the recrystallization process also failed to show unambiguous proof for the formation of hexagonal Ge.

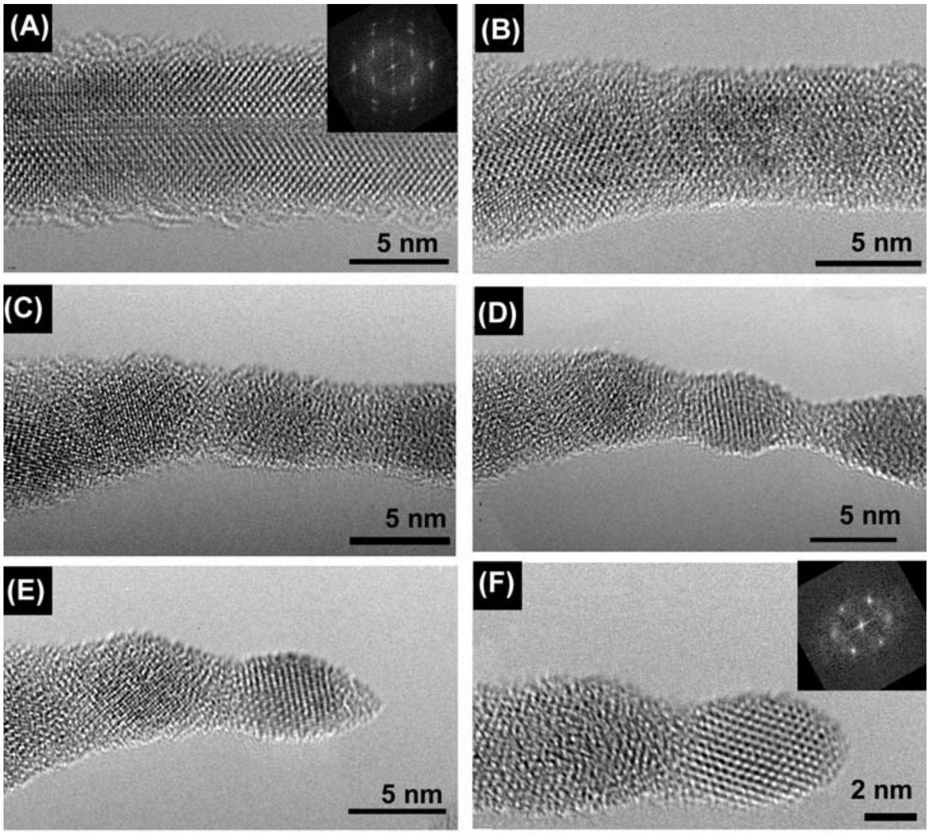

Figure 5.16: HRTEM images of a single crystal Ge nanowire after successive electron beam 'cross-over' irradiation. (A-F). The Fourier transform in the inset of (A) shows that the nanowire is a single crystal with [110] growth axis. The Fourier transform in the inset of (F) did not allow unambiguous crystal characterization as either diamond cubic or hexagonal Ge.

5.4 OUTLOOK AND CONCLUSIONS

Ge nanowires synthesized in supercritical fluid predominantly exhibited the <110> growth direction with minor contributions from <211> and <111> oriented nanowires. The comparison of the crystallographic growth directions observed in Ge nanowires prepared by various techniques is influenced by a range of kinetic and thermodynamic factors. The growth direction of Ge nanowires grown in supercritical fluid is predominantly determined by the structure and faceting of initial nucleus formed at the AuGe liquid alloy:crystal interface.

Cross-sectional imaging showed that the <110> oriented nanowires are characterized by a hexagonal cross-section low energy {111} and {100} facets. Nanowires with the <211> growth axis exhibited rectangular cross-sections with {111} and {110} surface facets. Additional cross sectional imaging experiments are currently under way to determine the diameter dependent evolution of the cross sectional faceting. Forbidden reflections observed in electron diffraction patterns were attributed to surface structures with fractional units cells terminating the {111} facets.

Preliminary mechanical property characterization revealed that the nanowires exhibit remarkable flexural strength while maintaining their single crystal structure. Additional in-situ mechanical experiments testing are required to better understand the correlation of the mechanical properties an crystallography in these nanostructures. Ge nanowires embedded in a polymer resign did not exhibit such flexibility and fractured with {110} fracture facets orthogonal to the growth direction. Intense electron beam irradiation resulted in the amorphization and subsequent recrystallization of the nanowires.

5.5 REFERENCES

(1) Yorikawa, H.; Uchida, H.; Muramatsu, S. *J. Appl. Phys.* **1996**, *79 (7)*, 3619-3621.

(2) Kuykendall, T.; Pauzauskie, P. J.; Zhang, Y.; Goldberger, J.; Sirbuly, D.; Denlinger, J.; Yang, P. *Nature Materials* **2004**, *3*, 524-528.

(3) Morales, A. M.; Lieber, C. M. *Science* **1998**, *279*, 208-211.

(4) Gu, G.; Burghard, M.; Kim, G. T.; Duesberg, G. S.; Chiu, P. W.; Krstic, V.; Han, W. Q. *J. Appl. Phys.* **2001**, *90*, 5747-5750.

(5) Wu, Y.; Yang, P. *Chemistry of Materials* **2000**, *12*, 605-607.

(6) Wu, Y.; Yang, P. *Journal of the American Chemical Society* **2001**, *123*, 3165-3166.

(7) Mathur, S.; Shen, H.; Sivakov, V.; Werner, U. *Chemistry of Materials* **2004**, *16*, 2449-2456.

(8) Kamins, T. I.; Li, X.; Williams, R. S.; Liu, X. *Nano Letters* **2004**, *4*, 503-506.

(9) Wang, D.; Dai, H. *Angewandte Chemie, International Edition* **2002**, *41*, 4783-4786.

(10) Greytak, A. B.; Lauhon, L. J.; Gudiksen, M. S.; Lieber, C. M. *Appl. Phys. Lett.* **2004**, *84*, 4176-4179.

(11) Hanrath, T.; Korgel Brian, A. *J. Am. Chem. Soc.* **2002**, *124*, 1424-1429.

(12) Heath, J. R.; LeGoues, F. K. *Chem. Phys. Lett.* **1993**, *208*, 263-266.

(13) Zhang, Y. F.; Tang, Y. H.; Lam, C.; Wang, N.; Lee, C. S.; Bello, I.; Lee, S. T. *J. Cryst. Growth* **2000**, *212*, 115.

(14) Zhang, Y. F.; Tang, Y. H.; Wang, N.; Lee, C. S.; Bello, I.; Lee, S. T. *Phys. Rev. B* **2000**, *61*, 4518-4521.

(15) Peng, H. Y.; Wang, N.; Zhou, X. T.; Zheng, Y. F.; Lee, C. S.; Lee, S. T. *Chem. Phys. Lett.* **2002**, *359*, 241-245.

(16) Wagner, R. S. *Whisker Technology*; Wiley: New York, 1970.

(17) Wu, Y.; Cui, Y.; Huynh, L.; Barrelet, C. J.; Bell, D. C.; Lieber, C. M. *Nano Letters* **2004**, *4*, 433-436.

(18) Davidson, F. M., III; Schricker, A. D.; Wiacek, R. J.; Korgel, B. A. *Advanced Materials* **2004**, *16*, 646-649.

(19) Li, C. P.; Lee, C. S.; Ma, X. L.; Wang, N.; Zhang, R. Q.; Lee, S. T. *Adv. Mater.* **2003**, *15*, 607-609.

(20) Ma, D. D. D.; Lee, C. S.; Au, F. C. K.; Tong, S. Y.; Lee, S. T. *Science* **2003**, *299*, 1874-1877.

(21) Lynch, D. F. *Acta Crystal.* **1971**, *27*, 399-407.

(22) Zhang, Y.; Iqbal, Z.; Vijayalakshmi, S.; Qadri, S.; Grebel, H. *Solid State Communications* **2000**, *115*, 657-660.

(23) Parsons, J. R.; Hoelke, C. W. *Philosophical Magazine A: Physics of Condensed Matter: Structure, Defects and Mechanical Properties* **1984**, *50*, 329-337.

(24) Martins, J. L.; Cohen, M. L. *Phys. Rev. B* **1988**, *37*, 3304-3307.

(25) Ding, Y.; Wang, Z. L. *J. Phys. Chem. B* **2004**, *108*, 12280-12291.

(26) Linde, D. R., Ed. *CRC Handbook of Chemistry and Physics*; 81st ed.; CRC Press: Boca Raton, Fl, 2000.

(27) Parsons, J. R.; Hoelke, C. W. *Nature* **1983**, *301*, 591-592.

(28) Parsons, J. R.; Hoelke, C. W. *Nature* **1983**, *301*, 591-592.

Chapter 6: Comprehensive study of electron energy losses in Ge nanowires

6.1 INTRODUCTION

Due to their ease of fabrication and unique physical properties, semiconductor nanowires have been proposed as building blocks for a variety of nanoelectronic and photonic devices. However, significant uncertainty exists about their fundamental properties, largely due to the lack of data correlating optical and electronic properties with microscopic details like crystallinity and surface chemistry. Combined scanning transmission electron microscopy and energy loss spectroscopy (STEM-ELS) provides a means to access this kind of information. In STEM-ELS, a relatively high-energy electron beam (200 keV) is focused to subnanometer-size and positioned on the nanostructure. Figure 6.1 illustrates how momentum transfer from the fast probing incident electrons (E_i) results in energy losses (E_L) due to low energy (generally less than 25 eV) interband transitions and plasmon excitations, and higher energy (tens to hundreds of eV) ionization of core electrons to the conduction band. Plasmons are high frequency collective excitations of valence electrons, with energy $E_{p,0}$, that depends approximately only on the electron charge e, mass m_e, and density n_e, when the plasmon energy greatly exceeds the single particle (electron) energy: $E_{p,0} = \hbar\omega_p = \hbar\left(4\pi n_e e^2/m_e\right)^{1/2}$. In Ge, the plasmon energy (~16 eV) is much larger than the band gap (~0.7 eV), hence plasmons can be treated accurately as free electrons.[1]

By collecting the inelastically scattered electrons, spectroscopic data is obtained—similar to what can be measured using X-ray techniques at a synchrotron, but with structural information and spatial resolution at the individual nanostructure level. This chapter discusses how STEM-ELS was applied to measure the diameter-dependent volume plasmon, 2p and 3d ionization edge energies of Ge nanowires ranging from 7 to 50 nm in diameter, and demonstrates chemically shifted Ge 3d core levels near the oxidized nanowire surface.

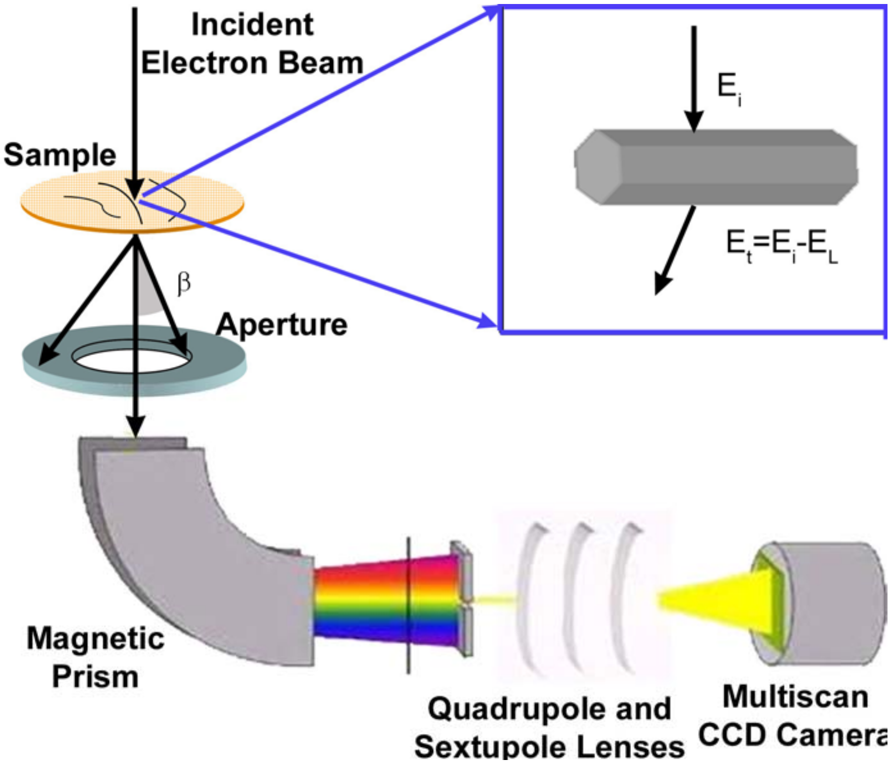

Figure 6.1: Schematic representation of STEM-ELS measurement. The inset shows the energy losses of fast probing incident electron interacting with the nanowire sample.

Since the seminal work on STEM-ELS by Batson[2] in the early 1990's this technique has seen impressive progress allowing the acquisition of atomic spatial resolution spectra with energy resolutions as low at 0.5 eV.[3,4] Despite the immense potential of this technique, only a limited number of studies have been published on the electronic properties of individual zero-dimensional[4-8] and one-dimensional (1D)[9,10] nanoscale semiconductors. Common to these studies is a significant uncertainty in discerning the fundamental effect of size-dependent factors, like quantum and plasmon confinement, from other factors that affect the spectra, including changes in crystallographic direction, local strain, and interface states in the nanostructure. One prerequisite for decoupling size effects from those related to defects and chemical fluctuations is the availability of high quality materials with well-behaved crystal structure and surface chemistry. In this context, the free-floating Ge nanowires synthesized by supercritical fluid-liquid-solid (SFLS) growth are well-suited for STEM-ELS measurements for the following reasons:

1. The nanowires exhibit smooth surfaces with few dislocation defects.
2. The relatively large Bohr diameter of Ge (~24 nm) makes it possible to probe a wide range of nanowire diameters for quantum confinement effects.
3. Their micrometer length allows them to be suspended over a vacuum background on lacey carbon substrates.

(4) Standard chemical recipes for the cleaning and passivation of the nanowire surfaces are available as was discussed in Chapter 4.

Precise control of the materials chemistry, combined with accurate analysis of the STEM-ELS data therefore enables the size-dependent effects to be decoupled from other factors. .

6.2 EXPERIMENTAL

6.2.1 Sample Preparation

For the studies reported in this chapter, Ge nanowires were prepared by the SFLS method, as described in detail in Chapter 2. For the work described in this chapter the nanowire surfaces were chemically modified by either a post-reaction HCl etch to remove the oxide and render a Cl terminated surface[11] or by thermally initiated hydrogermylation with hexene to render an alkyl terminated nanowire surface (see Chapter 4). Samples were prepared for TEM and STEM-ELS by drop casting the nanowires from an isopropanol suspension onto lacey carbon films suspended over 200 mesh copper grids.

6.2.2 Acquisition of Images and Electron Energy Loss Spectra

6.2.2.1 Microscope and Spectrometer Settings

TEM images and ELS were acquired using a JEOL 2010F equipped with a field emission gun operating at 200 kV accelerating voltage. ELS with high spatial and energy resolution were collected with the microscope operating in scanning mode with a probe size of 0.5 nm and a beam current of ~0.2 nA to prevent damage to the nanowire sample. The full width at half maximum

(FWHM) of the zero-loss peak was typically 1.0 eV. The convergence and collection semiangles were 3 and 11 mrad, respectively. The electron ELS were collected with a Gatan DigiPEELS at 0.05 eV/channel energy dispersion for plasmon and 3d core losses and at a dispersion of 0.3 eV/channel for Ge 2p core losses. Since the DigiPEELS spectrometer design provides inadequate shielding from stray external magnetic field, extraordinary precautions had to be taken to limit the disturbing influence of environmental factors. For example, the simple act of moving the microscope operator chair a few feet shifted the zero-loss peak in the live-spectrum by as much as 2 eV. Consequently, all mobile metallic objects had to be avoided and the vast majority of the spectra were acquired at night with the microscope operator sitting on an inverted plastic trashcan as an improvised chair.

6.2.2.2 Parameters for Acquisition of Spatially Resolved Spectra

Plasmon and Ge3d core ionizations were probed with linescan spectra acquired from averaging 4 spectra per pixel each with an acquisition time of 2 seconds per spectrum. The JEOL 2010F/Gatan DigiPEELS system does not have sufficient energy resolution in the low loss region near the zero-loss peak to resolve the band gap energy, but the bulk E_2 transition[12] at ~4 eV and the volume and surface plasmon energies of Ge (~16 and ~11 eV) are easily resolvable. All spectra were aligned with respect to the zero-loss peak (ZLP). Removal of the ZLP from low loss spectra was performed by a technique similar to the one described by Reed et al.[10] as described below.

The acquisition of high-resolution Ge 2p core loss spectra was complicated by experimental limitations posed by the energy range accessible with the Gatan DigiPEELS detector. Since the CCD detector contains 1340 channels, the Ge 2p edge near 1220 eV edge can be acquired with a spectrometer dispersion of 1.0 eV/channel. However, under these conditions the obtained energy resolution was prohibitively poor prohibiting the analysis of small (up to 1.5 eV) shifts in the edge position. Limited improvement in the spectrum quality was achieved by first acquiring a spectrum at 0.3 eV/channel dispersion and using the C 2s edge at 284 eV for calibration. Immediately afterward, another spectrum was acquired with the same dispersion and a detector offset of 1000 eV, using remnant charging effects in the CCD array from the zero-loss channel and the calibrated dispersion to acquire the Ge 2p edge near 1220 eV.

6.2.2.3 Spectra Analysis: Background Subtraction and Deconvolution

In order to obtain accurate Ge 3d ionization profiles allowing the precise determination of size and probe position dependent shifts, the raw spectra (as shown in Figure 6.2) were processed as follows. The possible superposition of the two-plasmon signal near 32 eV was removed from the raw data (triangles) using Fourier-log deconvolution. Artifacts introduced during in the deconvoluted data (dashed lines) were then removed with a 0.2 eV low pass filter. Finally, the background was removed using the power law form as described by Egerton.[1]

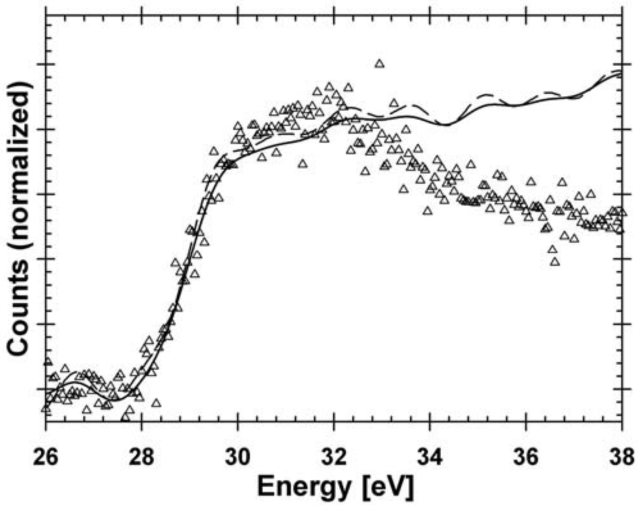

Figure 6.2: Ge 3d core loss spectrum. The superimposed secondary plasmon was removed from the raw data (triangles) through Fourier-log deconvolution (dashed lines). The background was subtracted using a power-law form.

6.3 RESULTS AND DISCUSSION

Since the measured plasmon losses in nanostructures are a function of the surface chemistry, sample crystallography and the probe position, the accurate elucidation of diameter dependent plasmon energies required these factors to be decoupled as discussed below.

6.3.1 Low Loss Spectrum Peak Assignment

ELS can be measured as a function of probe position by scanning from the central axis radially to the surface and taking spectra. Figure 6.3A shows an ELS linescan for a 10 nm diameter Ge nanowire. Zalabda et al.[13] recently used a dielectric formalism to predict surface and volume plasmon responses in nanowires. Based on their theoretical work, the features at ~4 eV and ~11 eV are attributed to monopolar (m=0) and multipolar (m>0) surface oscillations, as depicted shown in the diagram in Figure 6.4B. The volume and weak two-plasmon scattering peaks emerge at ~16 and ~32 eV. Additional superimposed peaks are discernible at ~4 eV due to the Ge E2 interband transition[12], and ~30 eV from Ge 3d electron ionization to the conduction band.

6.3.2 Probe Position Dependent Plasmon Losses

The peak intensities in the spectra vary with probe position, depending on the relative contributions of each mode of electronic excitation. The maximum scattering intensity from the volume plasmon occurs when the electron probe is positioned on-axis. In their dielectric formalism for plasmon responses in nanowires, Zabalda et al.[13] provide a detailed theoretical description for the correction to the volume plasmon excitation probability resulting from increased interactions between volume and surface plasmons when the probe is positioned near the surface, known as the *Begrenzungs* effect. In agreement with their model, the relative contributions of surface plasmons (~11eV) and interband transitions (~4eV) were found to be more pronounced when the probe is positioned away from the central axis of the nanowire. As the probe is positioned outside of the nanowire, surface plasmons are still observed due to so-called "aloof excitations". The monopolar (m=0) surface oscillation near 4 eV is still observable for a fast electron passing as far as 15 nm from the nanowire surface. This far aloof excitation has been attributed to the azimuthally symmetric nature of the charge oscillation[13] and has previously been observed in Si nanofilaments.[10]

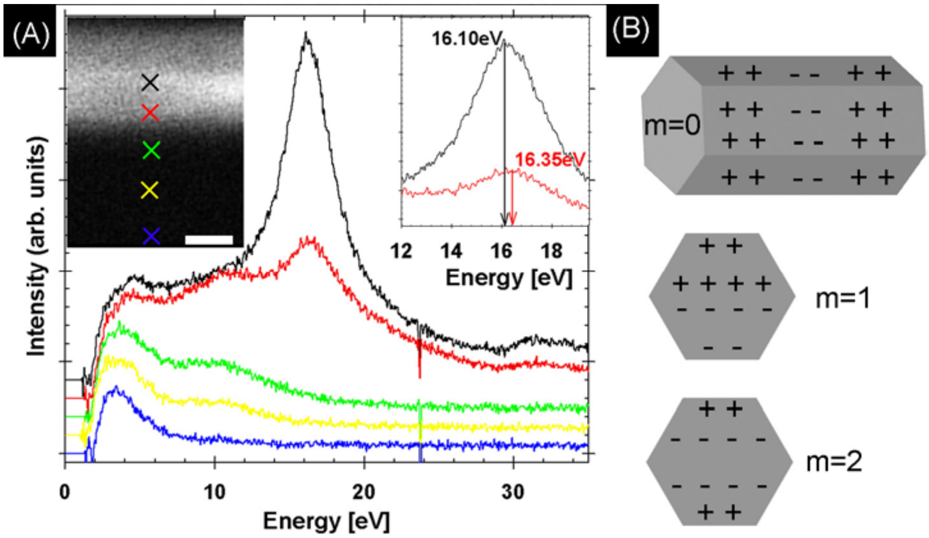

Figure 6.3: Probe position dependent plasmon energy losses. (A) ELS linescan across a Ge nanowire. The color-coordinated "X"s in the STEM image in the inset (scale bar=5 nm) correspond to the probe position where the spectra were obtained. The top right inset shows an expanded view of the volume plasmon peak as a function of probe position**.** (B) Schematic representation of monopolar (m=0) and multipolar (m>0) surface plasmon modes.

6.3.3 Effects of Surfaces on Plasmon Losses

6.3.3.1 The Begrenzungs Effect

The preliminary measurements of the volume plasmon energy clearly indicated a size-dependent shift. However, in order to quantitatively extract the size dependence of the volume plasmon energy from the ELS data, the effects of the surfaces on the plasmon response must be accounted for.

As a first approximation, the plasmon response in a nanowire can be estimated using a Drude free electron model with a modified composite dielectric function [1,14] $\varepsilon(\omega) = \frac{\omega_p^2}{\omega^2 + i\Gamma\omega} + \sum_j \frac{\omega_{pj}^2}{\omega_{pj}^2 - \omega^2 - i\Gamma_j\omega}$, where the first term includes the participation of unbound electrons and the second term includes the effect of bound surface charges. The shifted volume plasmon occurs at $\varepsilon(\omega) = 0$, where ω_j and Γ_j are the frequency and damping constant of the contributing bound oscillators, respectively. The loss function $\mathrm{Im}\left[-\varepsilon(\omega)^{-1}\right]$, describes the volume plasmon peak shape and the plasmon resonance occurs at the frequency where the dielectric function equals zero.[15,16]

The inset in Figure 6.3A confirms the characteristic blue-shift in the volume plasmon peak at non-zero impact parameter (the impact parameter is defined as the radial probe position divided by the nanowire radius) that results from the influence of bound surface charges and other sources of surface oscillations. The contributions of oscillators with $\omega < \omega_p$ is a convolution of the multipolar surface plasmons at ~11eV, the longitudinal surface plasmon and interband transitions at ~4eV observed in this case consequently shift the observed volume plasmon to slightly higher energies. Unfortunately, the convolution of surface plasmons and interband transitions in this low loss region presently does not permit a more detailed study of the evolution of these signals with decreased nanowire diameter.

6.3.3.2 Effect of Surface Contamination

Nanowires with surface layers of oxide or carbonaceous contamination were found to give rise to more significant surface-dependent shifts in the volume plasmon peak energy. For example, the untreated nanowire in Figure 6.4A shows the strong signal contribution near the surface due to the carbonaceous contamination layer indicated by the dotted circle in Figure 6.4B. The hexyl-passivated nanowire shown in Figure 6.4C on the other hand shows a clean well defined surface and the absence of undesired contamination responses near the nanowire surface (Figure 6.4D). Therefore, the volume plasmon energies reported here were obtained with zero impact parameter on nanowires with Cl or organic monolayer surface termination.

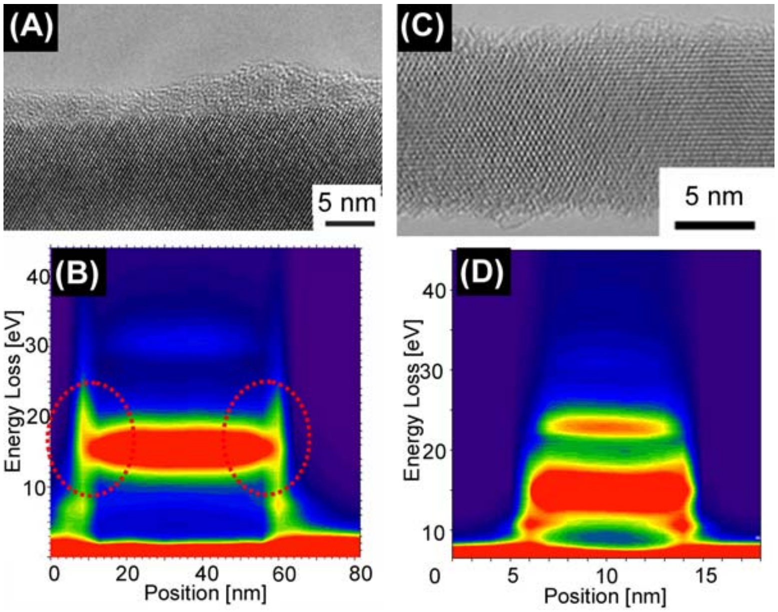

Figure 6.4: Effects of surface contamination on energy loss spectra measured near the surface. (A) HRTEM image of untreated Ge nanowire with carbonaceous surface contamination and corresponding cross-diameter ELS linescan (B) showing the undesired surface signals outlined by dotted circles. (C) HRTEM image of hexyl-monolayer terminated Ge nanowire showing no undesired surface signals in corresponding ELS linescan (D)

6.3.4 Crystallographic Effects on Measured Plasmon Energy

6.3.4.1 Effects of Crystal Bending

The effects of nanowire strain and changes in crystallographic orientation in the wire must also be decoupled from the measurements. Local strained regions along the length of the nanowire appear as dark bands in HRTEM images (see Chapter 5) or bright bands in dark-field STEM images (see Figure 6.5) due to bending in the wire. The bending leads to slight changes in crystallographic orientation with respect to the probing electrons, which gives rise to fluctuations in scattering intensity. For example, within the region of the nanowire that exhibits the near two-beam diffraction condition, the energy loss signal is attenuated by about a factor of 2. The bending does not affect the peak energy or width and is therefore trivially accounted for in the ELS data, provided the wire is dislocation-free.[17]

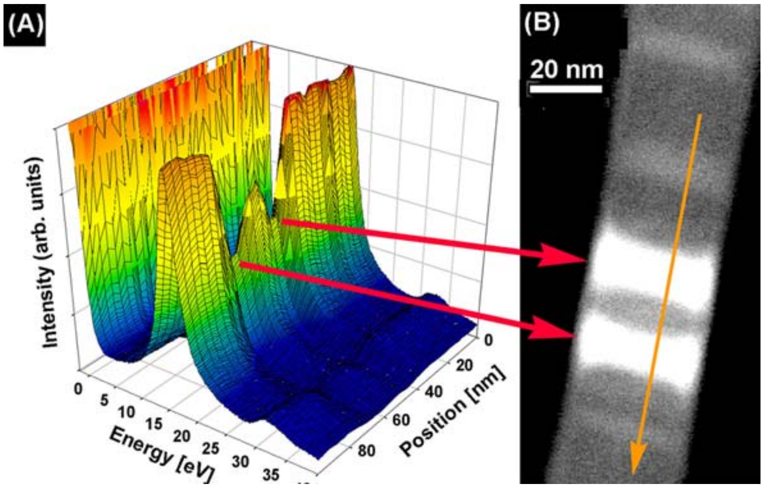

Figure 6.5: Linescan STEM-ELS plot and corresponding dark-field STEM image showing the effects of bending contours on the measured plasmon intensity

6.3.4.2 Effects of Crystallographic Defects

In addition to the effects of crystal bending in defect free crystal discussed above, the spatially resolved plasmon signal was also found to be sensitive to crystallographic defects in the nanowire. A stacking fault, such as the one shown in the dark-field STEM image in Figure 6.6A, strongly attenuates the plasmon signal. The HRTEM image in Figure 6.6B shows a similar twinning-type defect confined to a single plane running along the axis of the nanowire. Unwanted crystallographic artifacts in the data were therefore avoided by confining the diameter dependent analysis discussed below to plasmon spectra acquired from single-crystal defect-free nanowires in unstrained regions.

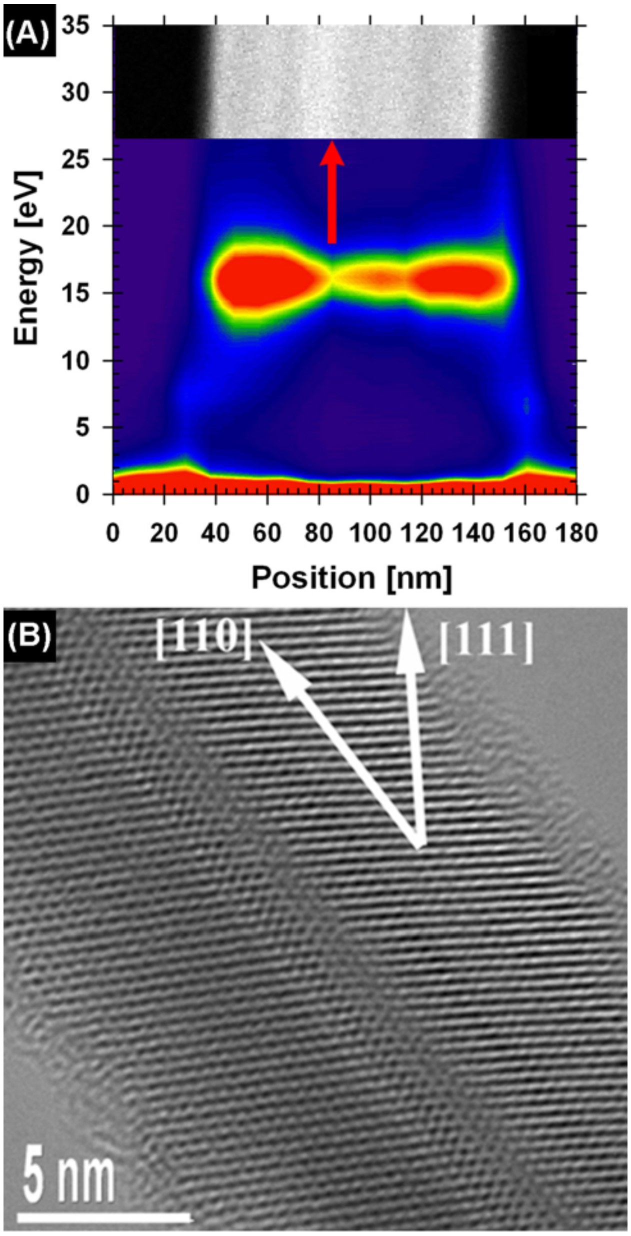

Figure 6.6: Effect of crystallographic defects on the measured plasmon energy. (A) STEM-ELS across a nanowire with a defect along the axis of the wire and (B) HRTEM or a nanowire with a similar twinning defect.

6.3.5 Diameter Dependent Volume Plasmon Energy

Figure 6.7 shows volume plasmon energies measured at zero impact parameter for Ge nanowires of different diameter after accounting appropriately for the effects of strain and crystallographic variations, and surface effects. The graph shows that the peak energy increases significantly when the diameter is less than ~25 nm. The increase in volume plasmon energy indicates that the plasmons are confined in this size range. When the nanowire diameter approaches the plasmon wavelength, the plasmons form standing waves bound in the confined direction—in this case, the radial dimension. A naïve expectation is that the peak energy will shift with nanowire diameter according to the plasmon dispersion relation in the long wavelength limit: $E_p = E_{p,0} + \left(\hbar^2/m_e\right)\alpha q^2$, where the dispersion coefficient α, relates to the Fermi energy as $\alpha = 3E_F/5E_{p,0}$, and the wavevector q, can only take on half-integer multiples of the wire diameter, $q = \pi/d$.[18] The predicted free electron value of α for bulk Ge is 0.43 and has been measured to be 0.83±0.15.[19] The value of $E_{p,0}$ varies in the literature from 15.5 eV to 16.5 eV [20-22] and has been predicted to be as low as 14.8 eV.[21] $E_{p,0}$ measured here for Ge nanowires is 15.45 eV. A fit of the plasmon dispersion relation to the data however reveals that the experimentally observed shift in plasmon energy is an order of magnitude higher than the shift expected from dispersion effects. Furthermore, a best fit of the diameter dependence of the volume plasmon energy gives $E_p \propto \frac{1}{d^{1.21}}$ as opposed to the $\frac{1}{d^2}$ dependence given by the dispersion relation.

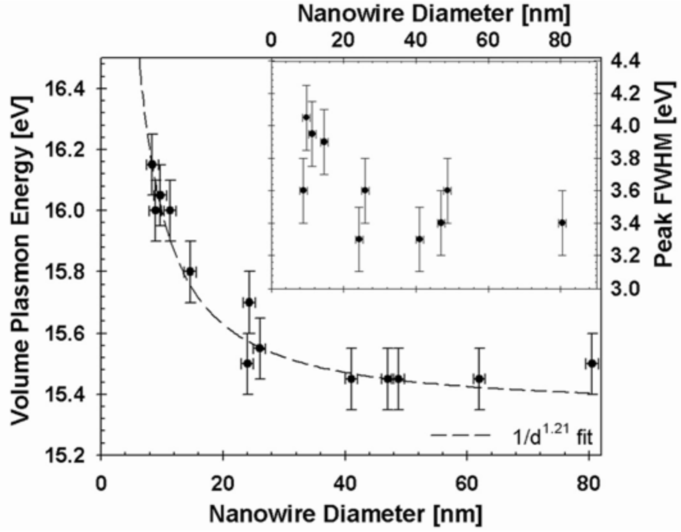

Figure 6.7: Volume plasmon energy measured from Ge nanowires of varying diameter. Surface and crystallographic effects were subtracted from the measured spectrum as detailed in the text. The dashed curve represents the best fit of the scaling relationship $E_p \propto 1/d^n$, where n=1.2. Inset: The plasmon pea FWHM as a function of nanowire diameter.

While an increase in α is consistent with expectations based on enhanced electron-electron interactions and/or size-dependent changes in the electronic structure,[23] it appears unlikely that dispersion effects alone can account for the observed diameter-dependent shift in plasmon energy. The relationship between plasmon confinement in these nanostructures and quantum confinement is not straightforward, despite efforts by several research groups to directly attribute size-dependent shifts in volume plasmon energies to quantum confinement effects by using a widely cited "effective mass model." This model, developed by Mitome et al.,[6] relates the plasmon energy shift directly to size-dependent changes in the band gap. Measurements of Si,[6] Ge,[7] and CdS[8] nanocrystals have followed the expected trend of $E_p \propto 1/d^2$. Nonetheless, the derivation of the model violates the *f*-sum rule, which calls it into question, and effects such as increased electron-electron interactions that are expected to be significant are not accounted for.

While dispersion and quantum confinement effects cannot be neglected in the interpretation of the low loss data, the main contributor to the observed shift in volume plasmon energy appears to be the Begrenzungs effect. As noted above, the Begrenzungs effect is one factor that leads to the shift in the volume plasmon peak to slightly higher energy when the probe approaches the nanowire surface. The Begrenzungs effect can also lead to a blue-shift in the volume plasmon energy measured at zero impact parameter for nanowires with decreasing diameter. The fast electron penetrating the nanostructure generates a wake potential as illustrated in the wake potential surface plot in Figure 6.8. The fast probing electron moving along the z direction is trailed by an oscillating potential with the plasmon frequency ω_p and corresponding wavelength of $\lambda_w = 2\pi \, {}^{\upsilon}\!/_{\omega_p}$, where υ is the relativistic velocity of the probing electron.

Garcia De Abjao and Echenique[24] calculated that the wake trailing the fast electron is destructed within distances of approximately $\lambda_w/4$ from the exit or entrance surface of the material. For a cylindrical geometry[*], the *Begrenzungs* effect should thus be observable in nanowire specimen with diameters less than $\lambda_w/2$, which corresponds to a diameter of 27 nm for the 200 keV electrons used

---

[*] The cylindrical geometry is a simplification of the actual hexagonal cross-section discussed in Chapter 4.

in this study. The observed onset diameter for increasing volume plasmon energy agrees well with predictions from this model.

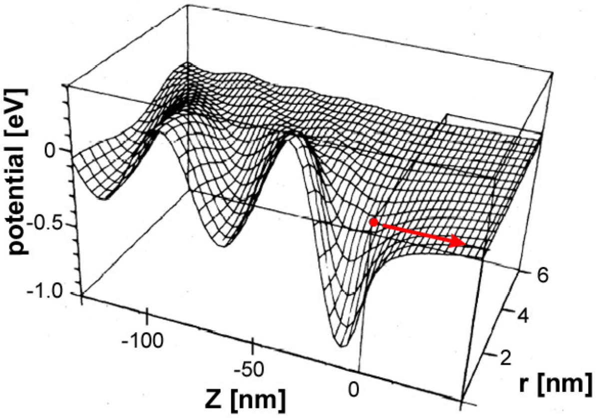

Figure 6.8: Wake potential surface† illustrating the response of the Ge to the fast moving electron (red dot) moving in the direction indicated by the arrow.

The plasmon peak width also increases with decreasing nanowire diameter (see inset of Figure 6.7). The peak broadening is associated with decreased plasmon lifetime, due to enhanced plasmon absorption by electrons[23] and increased surface scattering,[26] and is consistent with plasmon energies that are shifting from the free electron value with decreased diameter.[19] Since the plasmon excitations are collective in nature, even at the smallest diameters studied here, effects such as increased electron-electron interactions and the details of the changing band structure with even smaller nanowire sizes are most likely needed

---

† The potential surface is adopted from Echenique et al. *Phys. Rev. B.* **1979**, *20*, 2567-2580. with the axis relabeled to correspond to a 200 keV electron moving through a medium with a 16 eV plasmon energy.

to fully understand the nature of the size-dependent volume plasmon energy in the Ge nanowires. Unfortunately, a comprehensive theoretical model providing a quantitative relationship between nanowire diameter and shift is presently not available and requires additional study. Delerue et al.[27] have reported related calculations, however their work was based on very small Si cluster, <160 SI atoms, which gave spectra that were "molecular-like" in nature.

6.3.6 Core Loss Ionizations

STEM-ELS was also used to examine the size-dependence of the Ge 3d and 2p core electron ionization edges to determine changes in the conduction band edge and band structure. While the relationship between the size-dependent volume plasmon energy and electronic quantum confinement effects is not obvious—due to the fact that plasmon excitations are the result of collective many-body electron-electron interactions—core loss excitations result from electronic transitions of single electrons that directly reflect the electronic structure of the nanowires. For example, EELS measurements on individual Si nanocrystals less than 5 nm in diameter by Batson and Heath[5] revealed significant changes in the core 2p ionization edge position, shape and intensity. Based on the selection rules $(\Delta l = \pm 1)$ governing the core ionizations, investigation of the Ge 2p edge provides information about changes in the s and d projected density of states (DOS) in the valence band, whereas changes in the 3d edge reveal changes in the p projected DOS. Changes in the spectra of both the Ge 2p and 3d ionization edges (~1220 and ~30 eV, respectively) can thus provide a complete picture of the quantum confinement related changes in the s, p, and d hybridized valence band structure. Both edges were probed by STEM-ELS, although the above mentioned experimental limitations associated with spectra of high energy loss edges (Ge 2p near 12120 eV) severely the quality and resolution of Ge 2p core loss spectra.

6.3.6.1 Ge 3d Core Ionization - Effect of Probe Position on Ge 3d Ionization Energy

First of all, the possible influence of surface chemistry on the measured Ge 3d edge must be considered. Figure 6.9 shows the Ge 3d absorption edge obtained for Ge nanowires with different surface chemistry‡. An oxide layer on the nanowire surface significantly affects the Ge 3d core ionization spectra, shifting the edge inflection point by ~0.3 eV when acquired at the nanowire surface. In contrast, nanowires treated with hexene provide a clean organic monolayer-terminated surface that does not influence the 3d core ionization spectra—the spectra do not exhibit an energy shift with probe position in the nanowire. Batson reported a similar absence of chemically-induced core loss shifts near the surfaces of thin Si samples, and attributed the presence or absence of these shifts to the nature of local electric fields generated at the surface.[28] More recently, Muller et al.[3] probed energy shifts in the more localized oxygen K edge across ultrathin Si-SiO_2-Si gate oxide interfaces and observed changes in the edge structure attributed to additional electronic states below the SiO_2 conduction band due to induced gap states. Chemically-passivated surfaces presumably exhibit long-range weak fields that shift the valence and conduction bands by the

---

‡ Superimposed secondary plasmon and background signals were removed from Ge 3d core loss spectra as described in the experimental section above.

same amount, and therefore do not shift the ionization spectra; whereas, strong localized fields, such as those expected to occur on samples with poorly terminated surfaces—such as the suboxide-coated Ge nanowires—will shift the ionization edge measured in the spectra. For example, chemical shifts in the Ge 3d core ionization edge were reported by Surnev from high-resolution reflectance EELS (HREELS) experiments.[29,30] While the resolution of our measured shifts by STEM-ELS is less than those possible using HREELS, the chemically-induced shifts in Ge 3d edge we observe follow the expected trend.

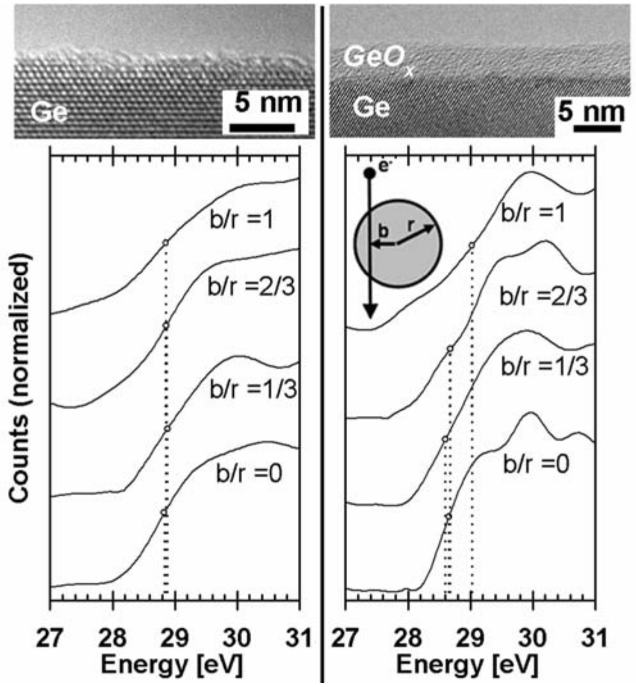

Figure 6.9: Normalized Ge 3d core loss spectra obtained for a hexyl-terminated (left) and oxide terminated (right) Ge nanowire at different probe positions relative to the nanowire axis. The chemical shift of the Ge 3d signal in the oxidized surface measures approximately 0.3 eV.

6.3.6.2 Diameter Dependent Ge 3d core ionization

Figure 6.10 shows a series of normalized Ge 3d core loss spectra obtained from organic monolayer-coated Ge nanowires with different diameters. The inflection point in the band edge increases in energy with decreasing diameter, along with an associated change in peak structure suggesting that the projected DOS in the conduction band is changing. This finding is qualitatively similar to the findings of Batson and Heath on Si nanocrystals[5] and Bostedt,[31] who observed size-dependent changes in the Ge 3d ionization edge for films of polydisperse Ge nanocrystals (1.4 to 3.4 nm in diameter) using X-ray absorption spectroscopy (XAS).

The onset of the size-dependent shift in the Ge 3d ionization edge occurs at a nanowire diameter close to the Bohr exciton diameter for Ge (24 nm) (see Figure 6.10). Notably, the observed shifts occur at significantly larger diameters than has been in XAS studies of Ge nanocrystal ensembles.[31] This suggests that the p-like projected DOS probed here may be subject to more pronounced quantum confinement effects than the s- and d-like states probed in Bostedt's XAS study of size dependent Ge 2p ionization edges.[31] An inspection of the Ge band diagram reveals three closely spaced energy minima with the absolute minimum at the L point and other local minima within 0.05 to 0.12 eV at the X and Γ point. Empirical pseudopotential calculations by Reboredo and Zunger [32] have shown that the quantum confinement effects are more pronounced at the L and Γ point than at the X point. This suggests that the finals conduction band states accessed through Ge 3d core ionization may correspond to points in the

Brillouin zone that are subject to stronger confinement effects than the absolute band minimum at the L point. Based on effective mass model, involving solutions of the Schrödinger equation[§] for the electron kinetic energy, the shift in conduction band energy relates to the size dependent shift in the electron kinetic energy, $E_k = \left(\frac{\hbar^2}{2m^*}\right)\left(\frac{2S_{nm}}{d}\right)^2$, where S_{nm} is the nth zero of the mth order Bessel function. This effective mass model therefore predicts a shift that scales as $1/d^2$. Although the shift in ionization edge energy agrees well with this prediction, a slightly better fit gives $\Delta E_{Ge3d \to CB} \propto 1/d^{1.49}$.

[§] The solution to the Schrödinger equation for electron confinement in the radial direction is shown in Appendix C.

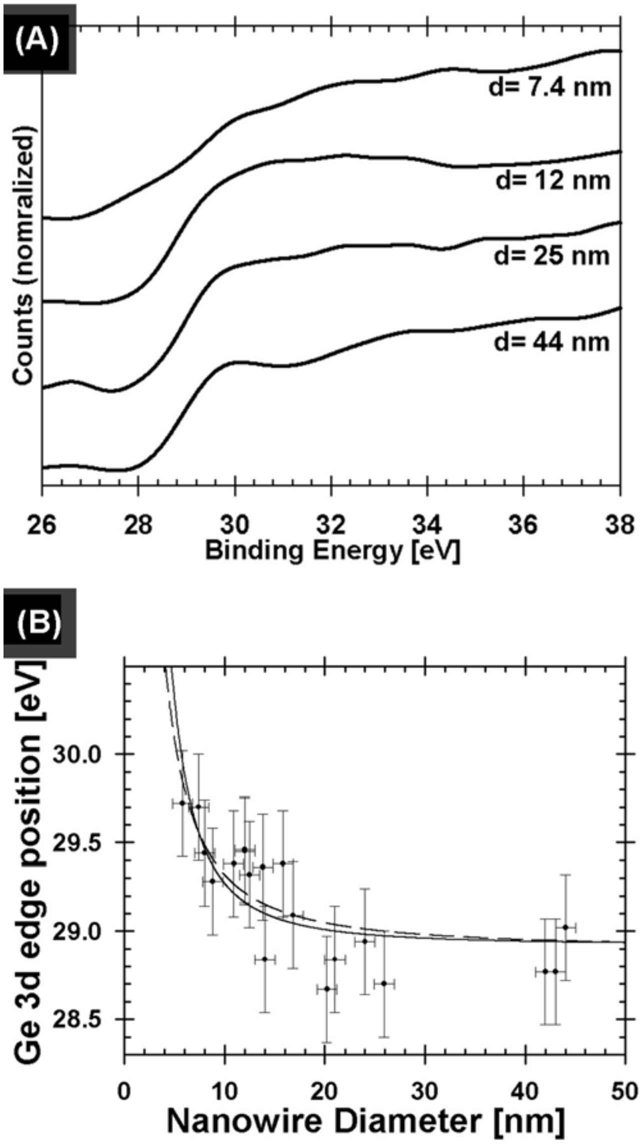

Figure 6.10: (A) Normalized Ge 3d core loss spectra obtained for Ge nanowires of different diameter: the peak onset shifts and the peak fine structure changes with decreasing nanowire diameter. (B) Ge 3d ionization edge inflection point versus nanowire diameter. The solid line is the $1/d^2$ fit expected from an effective mass model of an electron confined to a cylinder. The dashed line shows the best fit of $1/d^n$ to the data, showing a $1/d^{1.49}$ diameter dependence.

6.3.6.3 Ge 2p Core Ionization

Figure 6.11A shows several Ge 2p core loss spectra of nanowires with diameters ranging from 4.5 to 54 nm. Compared to the Ge 3d spectra discussed above, the Ge 2p ionizations with energy near 1220 eV are characterized by unfavorably poor signal-to-noise ratio. While the inflection point analysis (see Figure 6.11B) suggests similar changes in Ge 2p core ionizations, the limited consistency and quality of this data prohibited a reliable determination of diameter dependent edge positions. Nevertheless, a slight blue shift in the Ge 2p edge onset is perceptible from the data presented in Figure 6.12.

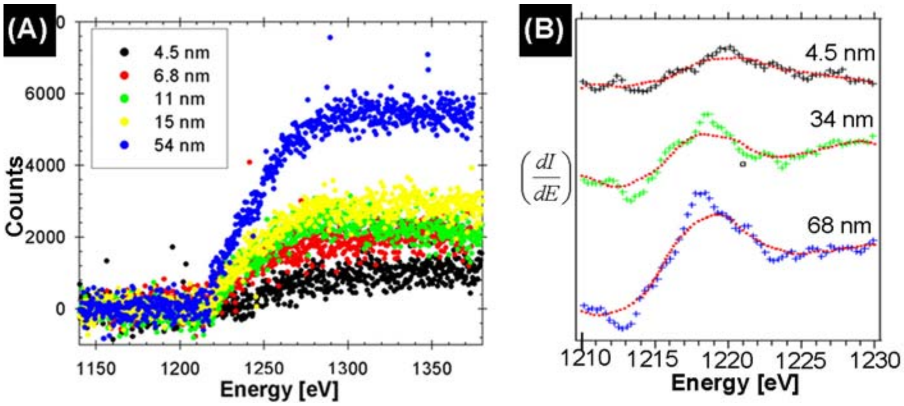

Figure 6.11: (A) Ge 2p core loss spectra of Ge nanowires with diameters ranging from 4.5 to 54 nm. (B) Differential spectra reveal a slight shift in the edge inflection point.

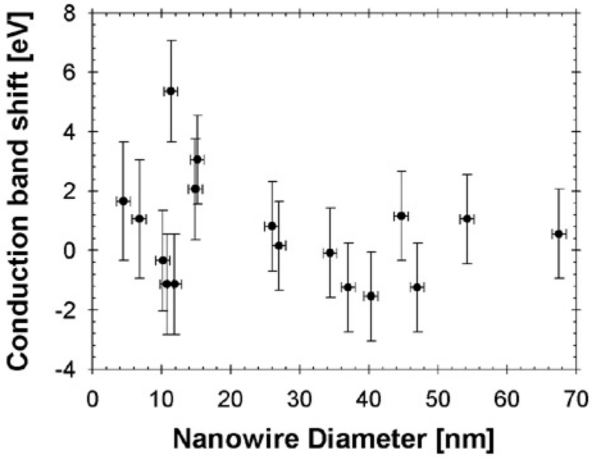

Figure 6.12: Ge 2p ionization edge inflection point versus nanowire diameter.

6.4 CONCLUSIONS

In order to unravel the detailed relationship between microscopic properties, such as crystallinity and surface chemistry, and size-dependent optical and electronic properties of nanostructures, measurements at the single nanostructure level that correlate these properties are needed. STEM-ELS provides one tool available for obtaining these kinds of measurements, provided the quality of the nanomaterials is very high, and uncertainty due to poor crystallinity, poorly defined interfaces, or strongly fluctuating diameter along individual nanowires can be eliminated. Here, we have presented accurate measurements of the size-dependent volume plasmon energy and Ge 3d photoemission spectra. The size-dependence of the volume plasmon energy was obtained using STEM-ELS by decoupling the influence of strain and surface effects. The volume plasmon energy becomes a strong function of size, increasing by ~0.8 eV with a diameter decrease from ~25 nm to ~8 nm. At diameters smaller than ~25 nm, the Ge 3d ionization edge also shifts to higher energy with significant changes in the peak fine structure. A similar analysis for diameter dependent Ge 2p ionization energies was overwhelmed by unfavorably low signal-to-noise ratio in the high-energy energy loss spectra large The Ge 3d ionization edges is also very sensitive to surface chemistry, and oxidized nanowires with poor electrical passivation exhibit up to a ~0.3 eV shift in edge inflection point when the probe is positioned near the surface.

6.5 REFERENCES

(1) Egerton, R. F. *Electron Energy-Loss Spectroscopy in Electron Microscope*; 2nd ed.; Plenum Press: New York, 1996.

(2) Batson, P. E. *Rev. of Sci. Instr.* **1986**, *57*, 43-48.

(3) Muller, D. A.; Sorsch, T.; Moccio, S.; F. H. Baumann; Evans-Lutterodt, K.; Timp, G. *Nature* **1999**, *399*, 758-761.

(4) Scheu, C.; Gao, M.; Benthem, K. V.; Tsukimoto, S.; Schmidt, S.; Sigle, W.; Richter, G.; Thomas, J. *J. Microscopy* **2003**, *210*, 16-24.

(5) Batson, P. E.; Heath, J. R. *Phys. Rev. Lett.* **1993**, *71*, 911-914.

(6) Mitome, M.; Yamazaki, Y.; Takagi, H.; Nakagiri, T. *J. Appl. Phys.* **1992**, *72*, 812-814.

(7) Maeda, Y. *Phys. Low-Dim. Struct.* **1997**, *10*, 23-25.

(8) Nakashime, P. N. H.; Tsuzuki, T.; Johnson, A. W. S. *J. Appl. Phys.* **1999**, *85*, 1556-1559.

(9) Sander, M. S.; Gronsky, G.; Lin, Y. M.; Dresselhaus, M. S. *J. Appl. Phys.* **2001**, *89*, 2733-2736.

(10) Reed, B. W.; Chen, J. M.; MacDonald, N. C.; Silcox, J.; Bertsch, G. F. *Phys. Rev. B* **1999**, *60*, 5641-5652.

(11) Lu, Z. H. *Appl. Phys. Lett.* **1996**, *68*, 520-522.

(12) Melnikov, D. V.; Chelikowsky, J. R. *Solid State Commun.* **2003**, *127*, 361-365.

(13) Zabala, N.; Ogando, E.; Rivacoba, A.; Abajo, F. J. G. d. *Phys. Rev. B* **2001**, *64*, 205410.

(14) Raether, H. *Springer Tracts in Modern Physics*; Springer Verlag: New York, New York; Vol. 88.

(15) Hinz, H. J.; Raether, H. *Thin Solid Films* **1979**, *58*, 281-284.

(16) Sturm, K. *Phys. Rev. Lett.* **1978**, *40*, 1599-1602.

(17) Hinz, H. J. *Zeitschift fuer Physik* **1980**, *38*, 111.

(18) Schaich, W. L.; MacDonald, A. H. *Solid State Commun.* **1992**, *83*, 779.

(19) Pines, D. *Rev. Mod. Phys.* **1956**, *28*, 184-198.

(20) Richter, H.; Rukwied, A. *Zeitschift fuer Physik* **1960**, *160*, 473-480.

(21) Sueoka, O. *J. Phys. Soc. of Japan* **1965**, *20*, 2203.

(22) Zeppenfeld, K.; Raether, H. *Zeitschift fuer Physik* **1966**, *193*, 471-477.

(23) Raether, H. *Springer Tracts in Modern Physics*; Springer Verlag: New York, 1980; Vol. 88.

(24) García de Abajo, F. J.; Echenique, P. M. *Phys. Rev. B* **1992**, *45*, 8771-8774.

(25) Echenique, P. M.; Ritchie, R. H.; Brandt, W. *Phys. Rev. B.* **1979**, *20*, 2567-2580.

(26) Batson, P. E. *Solid State Commun.* **1980**, *34*, 477-480.

(27) Delerue, C.; Lannoo, M.; Allan, G. *Phys. Rev. B* **1997**, *56*, 15306-15313.

(28) Batson, P. E. *Ultramicroscopy* **1993**, *50*, 1.

(29) Surnev, L. *Surface Science* **1981**, *110*, 439-457.

(30) Surnev, L.; Tikhov, M. *Surface Science* **1982**, *123*, 505-518.

(31) Bostedt, C., Electronic Structure of germanium Nanocrystal Films probed with Synchrotron Radiation (Thesis) University of Hamburg, 2002.

(32) Reboredo, F. A.; Zunger, A. *Phys. Rev. B* **2001**, *63*, 235314.

Chapter 7: Electron transport in single Ge nanowire devices

7.1 INTRODUCTION

Pioneering work by Lieber and coworkers showed that chemically-grown semiconducting nanowires can be assembled into functional electronic and optical device structures, such as logic gates,[1] memory devices,[2] photodetectors,[3] and lasers[4,5] with the potential for scaled integration over large areas using a combination of self-assembly and top-down microfabrication processes.[6] Each of these new device technologies requires conductive electrical contacts to the nanowires; however, little information exists in the literature about how to best make contacts to nanowire with chemically sensitive surfaces.[7] For nanowires with small diameters (i.e., <~10 nm), the strategy of heavily doping the semiconductor at the metal contact to create low resistance connections may not be a viable approach due to the large statistical fluctuations in dopant level likely to occur from wire to wire. For example, at a doping level of 10^{19}~10^{20} cm^{-3}, which is a typical value needed to reduce the depletion width at the metal/semiconductor interface to enable efficient carrier tunneling,[8] a 10 nm long segment of a 10 nm diameter Ge nanowire of ~10^4 Ge atoms would have ~10 dopant atoms. A variation in dopant concentration of only a few atoms would significantly alter the contact resistance (and the resistance in the nanowire itself!), leading to unreliability in device performance and manufacturability. Furthermore, the fabrication method must be "responsive" to the variable position of the nanowires deposited on the chip, which of course varies from device to device. In this context, how will low resistance electrical contacts be made to the nanowires? To address this issue, the first part of this chapter provides a systematic study of the electrical resistance and chemical integrity of metal/germanium (Ge) nanowire contacts in transistor device structures contacted with metal source/drain electrodes using three different techniques: a nanoscale patterning technique, electron beam lithography (EBL), and two “direct-write” nanodeposition methods, focused ion- and electron-beam (FIB and FEB) assisted chemical vapor deposition.

Although certainly not optimized, the overall performance of these devices has so far not been good with respect to the current state of the art in Si CMOS. Regardless, the chemical synthesis of semiconductor nanowires described in Chapter 2 has the potential to be scaled up with relatively low cost. Since solution-processable nanowires are compatible with plastic electronics technology platforms (see Chapter 8), they introduce the potential for cheap, disposable electronics, which would not necessarily require high performance. Nonetheless, low resistance electrical contacts would be almost certainly necessary, even for these kinds of applications.

Germanium (Ge) nanowires are particularly exciting materials for nanowire-based electronics due to Ge’s intrinsically higher electron and hole mobility compared to silicon,[9] which make it a prime candidate for future high performance nanostructured electronics. Of course, the primary technical hurdle that has prevented the widespread use of Ge in electronics has been the lack of a good insulating dielectric layer, such as SiO2 on Si. As a proof of concept, electrical devices have been fabricated by several groups from doped Ge nanowires synthesized by vapor-liquid-solid (VLS) methods.[10-12] However, these studies contain little detail about the properties of the nanowire/metal contact or the effects of surface chemistry on the transport behavior, despite the importance to the device and future improvements in performance.

Ge was in fact the semiconductor that was studied in detail by Shockley and Pearson[13] in 1948 that ultimately led to the field effect transistor (FET). Although Shockley and Pearson observed a change in conductance with an applied external field, the effect was less than expected based on the amount of induced charge generated and the free carrier mobility. This discrepancy was ascribed to surface states located within the band gap that resulted in trapped and immobilized carriers. Further research on Ge slabs and junction transistors showed that two classes of surface states were present, each associated with a different relative time scale for electron or hole capture. “Fast” surface states are characterized by capture times shorter than a microsecond, are primarily responsible for recombination processes, and have been chemically identified as localized species near the Ge/GeO$_x$ interface. Slow surface states exhibit capture times ranging from a few seconds to several minutes, and are believed to be associated with imperfections in the oxide layer or surface adsorbates. Extensive studies of the slow surface states (which can have densities as high as 10^{15} cm^{-2}) in the 1950s demonstrated how the influence of surface structure and the ambient environment on the surface state properties. A comprehensive review of early work on Ge surface states is given by Kingston.[14]

The first part of this chapter discussed measurements of the electrical properties of Ge nanowires synthesized by SFLS and electrically connected using fabrication methods based on either EBL, FIB or FEB. Device fabrication methods that minimized the unintentional modification of the nanowire surface chemistry were identified and used to subsequently study the impact of surface chemistry on electron transport. In the second part of the chapter the time dependent field effect response of nanowire devices fabricated from Ge nanowires with different surface terminations are compared. Using a non-linear decay model, the characteristics relaxation times are related to the slow surface state density and their position within the Ge band gap. Finally, the nanowire surface chemistry and the corresponding slow surface states are investigated via sinusoidal gate voltage measurements at variable frequencies.

7.2 EXPERIMENTAL

7.2.1 Fabrication

Nanowire devices were fabricated on p-type Si substrates (1-10 Ωcm) coated with 100 nm SiO$_2$. Au contact pads and alignment marks were fabricated by electron beam lithography (EBL) patterning (Raith 50) of PMMA photoresist (developed in a 1:3 solution of methyl-isobutylketone:isopropanol), followed by thermal evaporation of 3 nm Cr and 40 nm Au (Denton Thermal Evaporator), and a lift-off procedure in boiling acetone. Figure 7.1A shows a typical 10x10 mm substrate with eight arrays of the contact pad structures shown in Figure 7.1B. Within each contact pad array, several nanowire devices with local interconnects spanning from the nanowire to the pad structures, such as the one shown in Figure 7.1C, can be electrically connected. The nanowires were deposited within the contact pad array by immersing the substrate in a dilute (~10μg/ml) isopropanol suspension of Ge nanowires for 10 to 15 min. These deposition conditions yielded a nanowire surface density of ~500 mm^{-2}. For nanowires not treated with an organic monolayer, the device substrate was subjected to a 30 sec etch in 5% HCl to remove the surface oxide layer on the nanowires prior to depositing the local interconnects. Devices with nanowires coated with hydrocarbon monolayers were not chemically etched prior to depositing the local contacts.

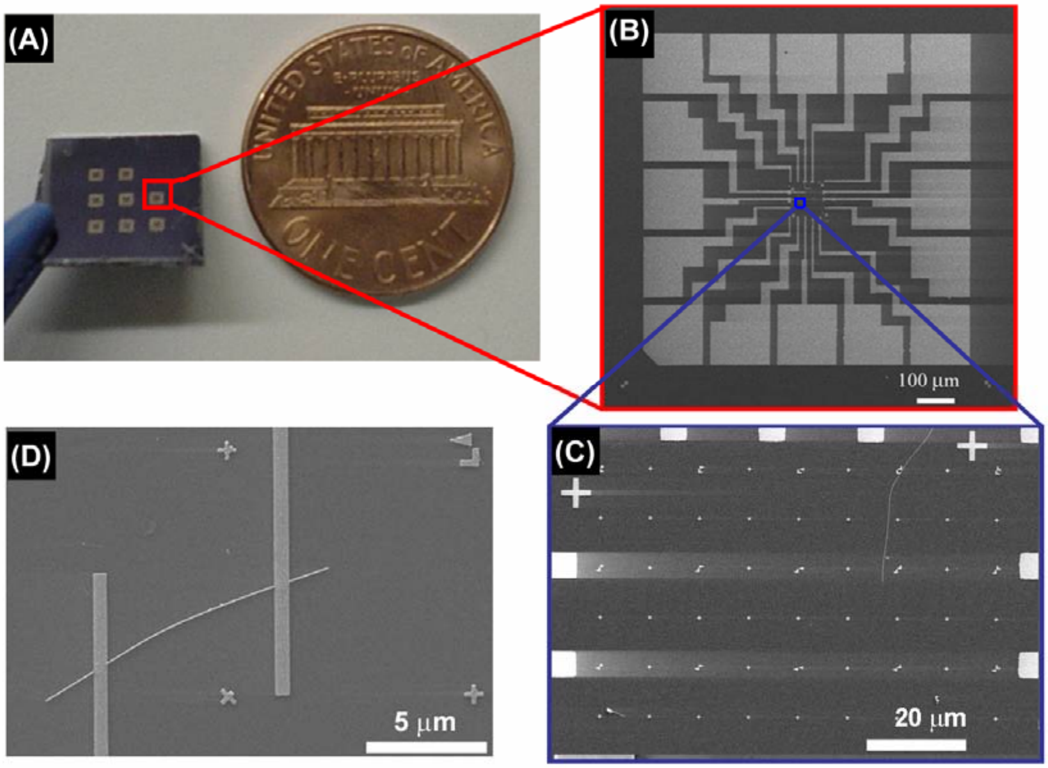

Figure 7.1: Overview of the nanowire device fabrication process: (A) Silicon substrate onto which contact electrode pads and reference markers are defined using e-beam lithography. (B) each device area consist of 16 contact electrodes and a 100x100 µm area for nanowires at its center. (C) Higher magnification SEM image showing single nanowire deposited in an array of markers. (D) Individual nanowires are located relative to the reference marks and contacted by electrodes.

The nanowires were located on the substrate with either atomic force microscopy (AFM) (Digital Instruments Dimension 3100) or high-resolution scanning electron microscopy (HRSEM) (LEO 1530) using the prefabricated alignment marks (shown in Figure 7.1C) as reference points. Then the local electrical interconnects between individual nanowires and the Au contact pad structures were fabricated using either EBL, FIB or FEB. For the EBL approach, the local interconnects consisted of vapor-deposited 40 nm Au layer on a 3 nm Cr adhesion layer using the EBL procedure described above. With PMMA as the e-beam photoresist, electrode lines as narrow as 100 nm were easily fabricated using this approach.

As an alternative to the multi step EBL approach, nanowire contacts were fabricated using the single-step “direct write” processes based on Ga-ion-beam or electron-beam assisted Pt chemical vapor deposition (IA-CVD and EA-CVD) in a dual-beam FIB/SEM (FEI Strata DB235). In EA-CVD or IA-CVD, a focused electron or ion beam assisted the decomposition of a Pt-containing gas (trimethyl-methylclyclopentadienyl-platinum), to directly deposit metal lines with approximately 250 or 150 nm height, respectively. IA-CVD was performed with a 30 keV Ga^+-beam at 10 pA beam current and EA-CVD was performed at 5 keV and 300 μA. The IA-CVD Pt electrodes had a cross sectional area of ~0.35 μm^2 with line resistance <~5 kΩ. Pt lines deposited by EA-CVD exhibited higher resistivity, and were therefore limited in use to only the immediate vicinity of the nanowire. IA-CVD was used to extend EA-CVD deposited Pt lines to reach the Au pad structures. The total resistance of the Pt electrodes written using this combined EA-CVD and IA-CVD approach was <~10 kΩ. In some cases, devices were annealed after EA-CVD or IA-CVD at 250°C or 400°C for 30min in vacuum (~1 mTorr) or under nitrogen. The resistance changes for devices annealed at 400°C did not differ significantly from those annealed at 250°C. Similarly, the results of the annealing step did not show significant differences for devices annealed in vacuum compared to those annealed in nitrogen.

Ion implantation of the Ge nanowires by Ga^+ was studied on the dual-beam FIB/SEM instrument. The nanowires were deposited from an isopropanol dispersion onto a lacey carbon-coated copper TEM grid and exposed to the Ga^+-beam with an implantation dose of $\sim 10^{12}$ cm^{-2}. The nanowires were then imaged by TEM on a JEOL 2010F HRTEM operating at 200kV to observe crystallographic changes resulting from the ion implantation.

7.2.2 Electrical Measurements

Room temperature current-voltage (IV) measurements were performed using a Karl Suss PM5 probe station connected to a Keithley 4200 parameter analyzer with the device placed in a home-built nitrogen chamber. Prior to electrical characterization, intermediate air exposure was limited to less than 30 min for devices fabricated by EBL, while devices prepared with EA- or IA-CVD were exposed to ambient air for less than 5 min. The gate voltage for nanowire field effect transistor (FET) measurements was supplied by either a “global” back gate with the highly doped substrate serving as the gate electrode, or by a local gate electrode written on the substrate near the wire, positioned between the source and drain electrodes.

7.3 DEVICE FABRICATION

Electron beam lithography requires a serial process of resist deposition, e-beam exposure and patterning, developing, metal deposition and then lift-off. It is a time-consuming process, yet high quality metal electrodes can be fabricated routinely using this approach. However, these multiple processing steps invariably modify the surface chemistry of the nanowires, and since one of the focal points of this work was to investigate the effect of surface termination on slow states, isolated Ge nanowires had to be contacted in a manner that did not unintentionally alter the surface termination of the nanowire.

FIB and FEB are both “direct write” nanofabrication methods, for depositing metal contacts directly to the nanowire in a single step without requiring the use of photoresist and thus enables the preservation of the nanowire surface chemistry. Both FIB and FEB are certainly more convenient; however, the nanowires are exposed to either an ion beam or an electron beam, which could potentially affect the nanowire electrical properties. The contact resistance of local interconnects fabricated using each of these approaches was measured and compared.

7.3.1 Electron-Beam Lithography defined Au/Cr electrodes.

Figure 7.2A shows an SEM image of a four-probe Ge nanowire device made with 3nm/40 nm Cr/Au contact electrodes defined by EBL. Devices fabricated by this approach exhibited non-linear IV curves with picoamp currents as shown in Figure 7.2B. The symmetric IV curves with a large gap of zero conductance are characteristic of two back-to-back Schottky diodes, similar to those observed in Si nanowire devices studied by Heath and coworkers.[15,16] The high contact resistance of these devices presumably resulted from a poor nanowire/metal interface, as one would not expect a Schottky barrier between the Ge nanowire and the Cr buffer layer. Early work on Ge transistors in the 1950s revealed many practical problems during device fabrication related to the chemically and electrically defective oxide that forms on Ge surfaces.[14] Similarly, the Ge nanowire surface was highly reactive to environmental oxygen (and water) and despite extensive efforts, such as an additional HCl-etching step and brief exposure to Ar/O_2 plasma after developing the EBL pattern prior to metal deposition, surface oxidation could not be eliminated completely. While Heath and coworkers[16] decreased the contact resistance between Au electrodes and Si nanowires by thermal annealing, this approach did not work for Ge nanowires as annealing at 250^{o}C in nitrogen destroyed most of the devices, as shown in Figure 7.3A.

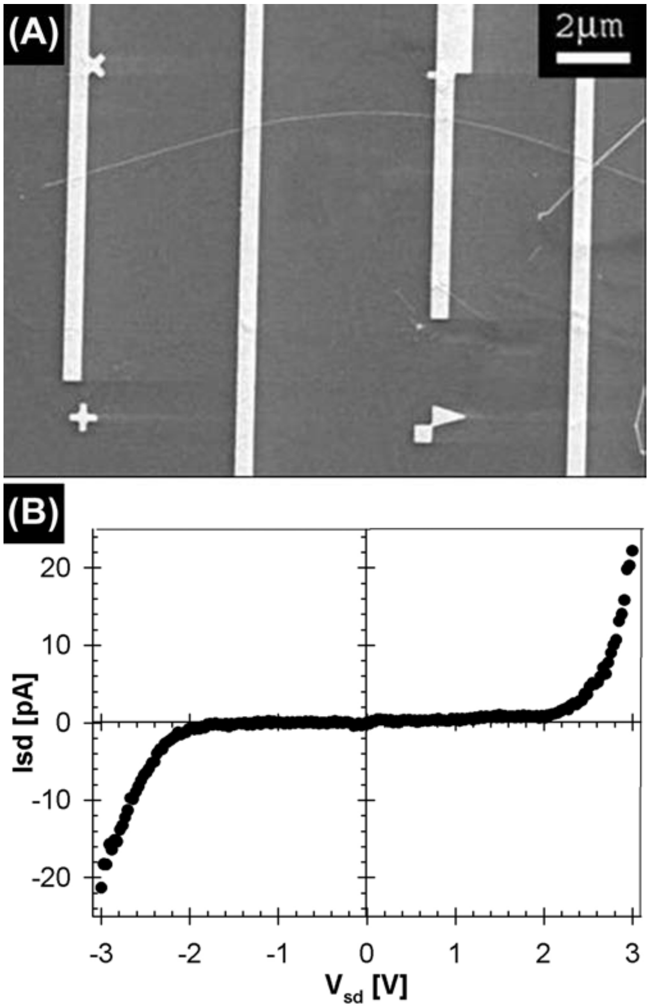

Figure 7.2: (A) HRSEM image of a four-probe nanowire device fabricated with EBL. Prefabricated alignment marks are visible in the bottom of the image. (B) IV plot of an EBL fabricated device.

In addition to the high contact resistances between EBL-defined Au/Cr electrodes and Ge nanowires, the time-consuming multiple processing steps—PMMA spin coating, PMMA prebaking, EBL exposure, MIBK developing, IPA rinse, metal vapor deposition and lift-off in boiling acetone, among which the developing and lift-off steps are likely the most harmful—make it very difficult to control the nanowire surface chemistry. Since control and characterization of the nanowire surfaces in these devices is of paramount importance in the study of their electron transport properties, a contacting method that does not perturb the surface chemistry was desired. Furthermore, EBL fabricated devices were plagued by a high failure rate, with close to 60% of all devices failing either due to complete nanowire degradation (see Figure 7.3B) or mechanical disintegration (see Figure 7.3C) prior to annealing and electrical measurement. The direct-write focused beam-assisted CVD of Pt electrodes has the potential to overcome both the inefficiency of the EBL process and the difficulties encountered in controlling the surface chemistry. For example, Cronin et al.[7] demonstrated how the combined milling and deposition capabilities in a dual beam FIB system can conveniently be used to form ohmic contacts to oxide-coated nanowires.

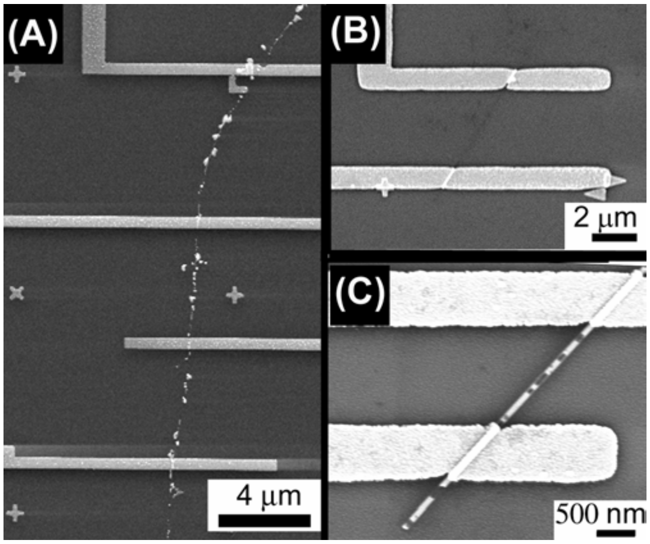

Figure 7.3: Typical defects encountered in EBL fabricated nanowire devices. (A) Destruction of the nanowire during thermal annealing at 250°C. (B) Complete dissolution of the nanowire, and (C) mechanical and chemical damage to a Ge nanowire prior to thermal annealing.

7.3.2 Beam-Assisted Chemical Vapor Deposition of Pt Electrodes

7.3.2.1 Electrical Characteristics of Pt electrodes

The electronic properties of Pt lines deposited by IA- and EA-CVD are characteristic of dirty metals with resistivities of ~10 μΩcm and 0.1~10 mΩcm for each method, respectively, compared to 10 nΩcm for pure Pt metal. Both IA- and EA-CVD incorporated significant amounts of impurities, such as C, Ga, and O that reduced the conductive properties of the metal. For example, Telari et al.[17] showed that the resistivity of Pt films deposited by IA-CVD decreased proportionally with increasing carbon content. Since the electron beam used in EA-CVD Pt deposition was less efficient than the ion beam in fully degrading the Pt precursor, higher amounts of C were incorporated in Pt films deposited by EA-CVD resulting in significantly higher resistivity. A structural and electronic investigation of EA-CVD deposited Pt nanowires by Rotkina et al. [18] revealed that their deposited material consisted of Pt nanocrystals embedded in an amorphous matrix composed primarily of C and Ga, which exhibited slightly non-linear transport at room-temperature. In comparison, the C and Ga contamination in the Pt lines deposited by EA-CVD in our laboratory was lower, and the metal lines always exhibited linear current-voltage characteristics with sufficiently low resistivity for potential use as Ohmic metal contacts for the Ge nanowires.

7.3.2.2 Electrical Characteristics of IA-CVD Contacted Ge Nanowire Devices

Ge nanowires contacted with Pt electrodes deposited by IA-CVD exhibited linear IV curves at room temperature with currents in the nanoamp range as shown in Figure 7.4A. A local electric field applied from a proximity probe placed at the top surface of the device (see SEM image in the inset of Figure 7.4A) affected the current through the nanowire, exhibiting decreased conductivity with positive applied gate voltage. This suggests that electron transport through the nanowire occurs via p-type carriers. The p-type field effect response was also illustrated in the gate sweep in Figure 7.4B. Notably, the gate sweep plot exhibited significant hysteresis, which is typically an indication of trapped charge at the nanowire surface or the nanowire/contact electrode interface. The hysteresis effects and the origin of p-type electron transport in these Ge nanowires is discussed in detail in Section 7.4.2.2 below.

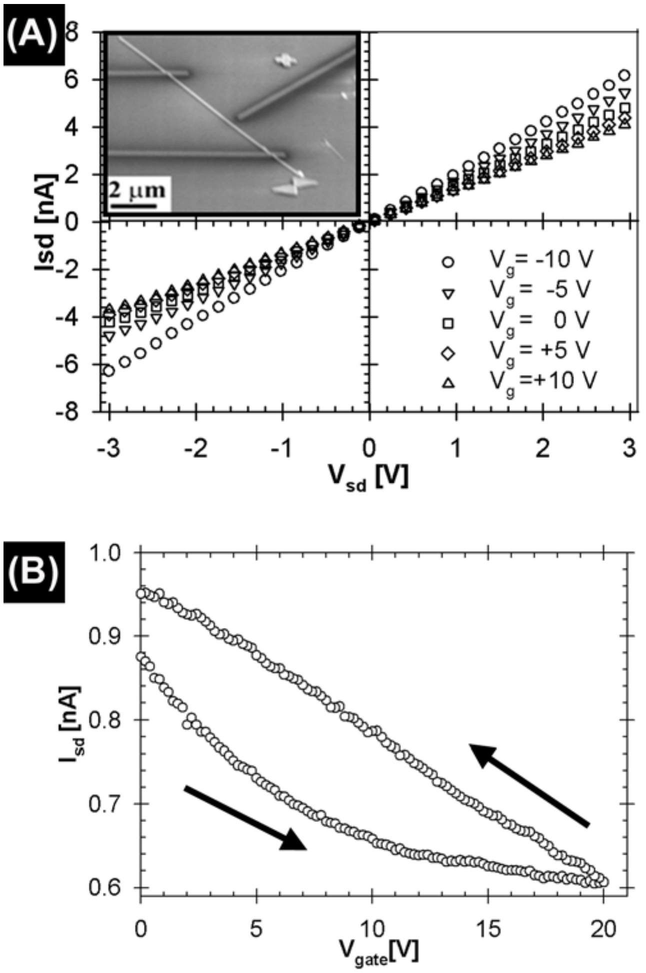

Figure 7.4: (A) IV plot of a Ge nanowire device fabricated Pt metal electrodes deposited using IA-CVD. Nanowire conductivity decreases with increasing gate voltage, indicating p-type transport. The inset shows a nanowire gated through a proximity electrode. (B) Current vs. gate voltage for a device biased at +1.0 V showing counterclockwise hysteresis during the gate voltage sweep. The arrows indicate the direction of voltage sweep.

7.3.2.3 Four-Point Probe Measurements of IA-CVD Contacted Ge Nanowire Devices

While two-probe measurements are very important from the standpoint of practical device measurements, the transport properties of the nanowires are lumped together with the transport properties of the metal/semiconductor contact and cannot be differentiated. Four-probe measurements provide a convenient way to deconvolute the measured device resistance into its component nanowire and contact resistances. In a typical four-probe measurement, a known current is passed between two outer electrodes, while the potential drop across an inner set of electrodes is monitored. Since there is no current flowing through the inner electrodes, the potential drop across the inner probes is due to the intrinsic nanowire resistance. The intrinsic nanowire resistance is then scaled to the length between the outer pair of electrodes and subtracted from the total device resistance to obtain the contact resistance. The contact resistance in this case represents the sum of all resistances between the probe station and the nanowire, but is dominated by several orders of magnitude by the metal/nanowire contact resistance. In contrast to work by Yu et al.[16] on Si nanowires, the SFLS-grown Ge nanowires did not show any evidence of conductivity variations along the length of the wire, making four-probe measurements a reliable approach for differentiating nanowire and contact resistances.

A four-probe measurement of resistance versus applied voltage from a Ge nanowire device with metal contacts fabricated by IA-CVD is shown in Figure 7.5A. The device resistance (49 MΩ) resulted from the serial resistances of the nanowire (31 MΩ) and the contacts (18 MΩ). Although the contact resistance was certainly significant, it did not dominate the device properties, as in the case of the EBL-defined Au electrodes. The IV curves were Ohmic; however, the contact resistance exhibited a slight variation with applied voltage and a perceptible hysteresis at negative applied voltage, which may have been due to charge trapping at the metal/nanowire interface. Annealing this four-probe device for 30 min in nitrogen at 250^{o}C decreased the overall resistance by ~12 MΩ. As shown in Figure 7.5B, the nanowire resistance decreased by ~2 MΩ; whereas, the contact resistance decreased by ~10 MΩ. The observed hysteresis in contact resistance disappeared after the thermal anneal and the dependence of the contact resistance was reduced from an initial slope of 2.3 MΩ/V to 0.14 MΩ/V over the range of applied voltage. After accounting for the contact resistance, the Ge nanowire resistivity can be determined, exhibiting values ranging between 10^{1}~10^{-1} Ω cm for all wires measured to date.

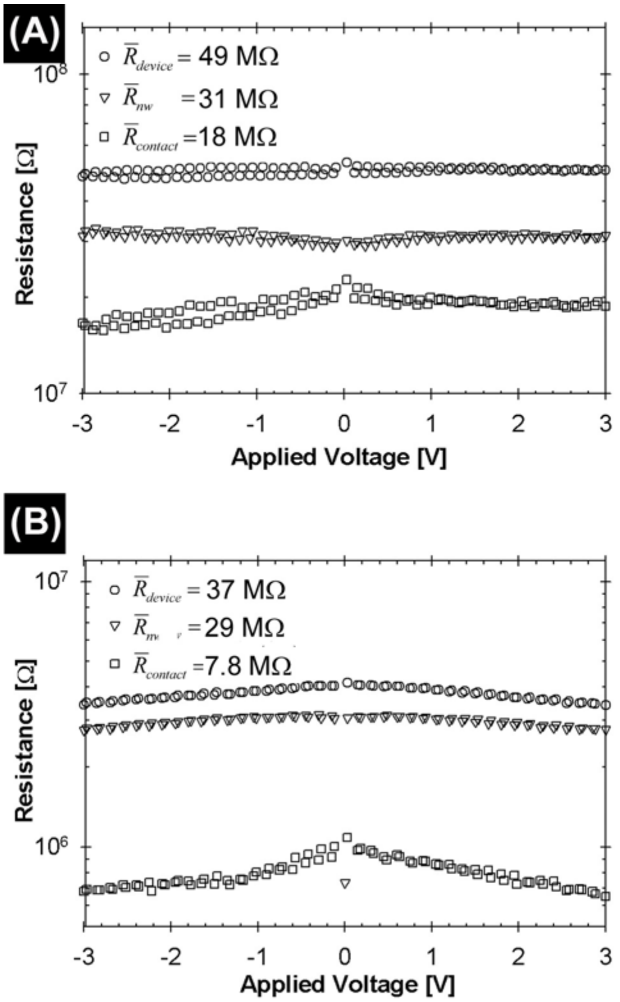

Figure 7.5: Four probe electrical measurements of IA-CVD contacted devices (A) before and (B) after annealing at 250°C in nitrogen. The average device, nanowire, and contact resistances are shown in the top-left inset.

Electrical experiments on the Pt lines themselves revealed an *increase* in resistivity of ~30% for Pt deposited by IA-CVD and ~50% when deposited by EA-CVD. Since the contact resistance of the Ge nanowire devices decreased upon annealing, the reduction in contact resistance that occurred due to chemical changes at the metal/nanowire interface upon annealing were most likely even larger than what was suggested by the four-probe results. For most nanowires, thermal annealing did not change the nanowire resistance.

7.3.2.4 Intentional Ge Nanowire Exposure to Ga^+ Beam – Doping via Ion Implantation

There was initial concern about unintentional p-doping of the nanowires by Ga^+ from the ion beam used during IA-CVD. If the nanowires were unintentionally doped, annealing was expected to thermally activate these carriers and significantly decrease the nanowire resistance. Devices prepared by IA-CVD and annealed at higher temperatures (400^oC) also did not show increased nanowire conductivity. These results were encouraging; nevertheless, difficult processing challenges were associated with using the IA-CVD process for metallization of the nanowires. Although significant changes in nanowire conductivity were not observed by unintentional Ga^+ ion doping, HRTEM images of nanowires intentionally exposed to the Ga^+ beam for ion implantation studies showed significant amorphization even for modest implantation dosages on the order of 10^{11} cm^{-2}. Figure 7.6A shows the initial single-crystal Ge nanowire before Ga^+ implantation and Figures 7.6B and 7.6C showing nanowires after implantation reveal partial or complete amorphization. Attempts to expose isolated areas of a multiprobe nanowire device to ion implantation failed due to significant morphological degradation of the nanowire during ion beam exposure. Even the use of a protective masking layer of PMMA (500 nm) over the nanowires to prevent milling damage and control ion dosage, did not lead to increased carrier concentrations and enhanced conductivities after thermal annealing at 400°C, suggesting that crystallographic changes to the nanowire shown in Figure 7.6 are irreversible and implanted Ga^+ is not thermally activated. While ion implanted bulk substrates can tolerate high annealing temperatures and even brief local melting, high temperature annealing conditions are not feasible for nanowires as local melting disintegrates the nanowire into droplets.

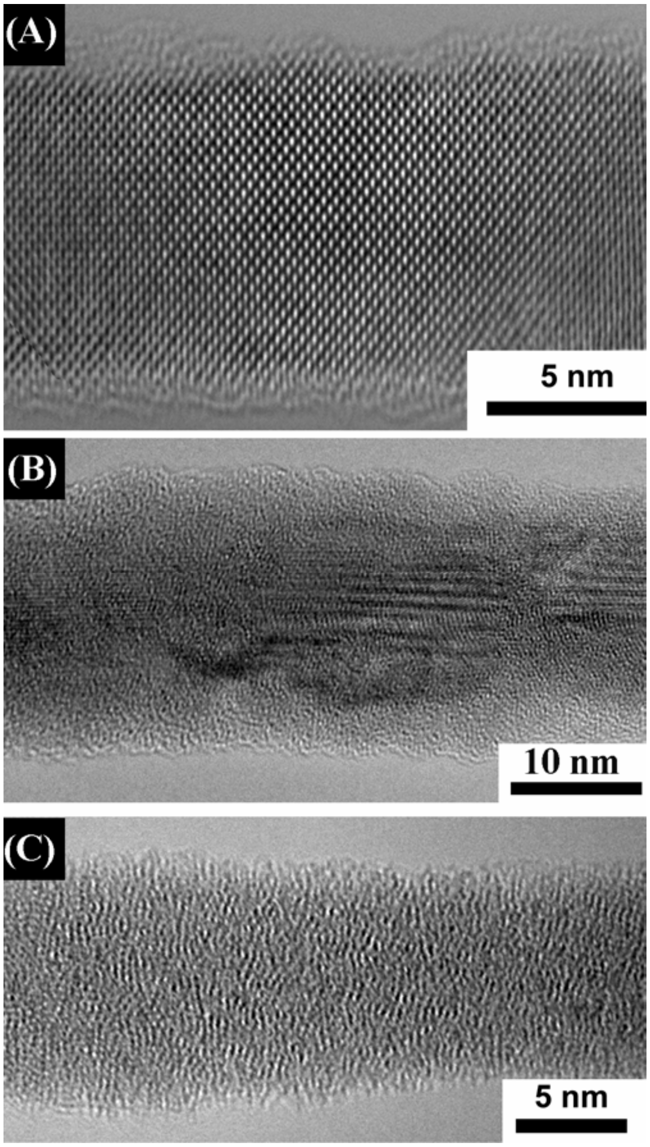

Figure 7.6: HRTEM of individual nanowires. (A) Typical single crystal defect free nanowire with the [110] crystallographic growth direction, (B) partially and (C) fully amorphized Ge nanowires during focused ion beam implantation.

7.3.2.5 Contact Structure at the Electrode/Nanowire Interface

The mild ion milling that occurred during the IA-CVD process had one other important consequence. The nanowire actually eroded as metal deposition occurred. Figure 7.7A shows an AFM image of a Pt/Ge nanowire junction deposited by IA-CVD and removed from the FIB chamber prior to completing the deposition process. It is clear from the image that the Pt electrode in fact penetrated to the nanowire core. This may potentially not present a problem for source/drain electrodes, however, a single nanowire device with sequential positioning of nanowires may not be able to be fabricated using IA-CVD. Figure 7.7B shows an AFM image of a Ge nanowire contacted by EA-CVD as discussed in the following section. The schematic in Figure 7.7C shows a single nanowire contacted by two different electrode configurations. The left contact is typical for IA-CVD, penetrating into the interior of the nanowire, while the electrode on the right coats the nanowire, as is typical of Pt or Au deposited by EA-CVD or a EBL approach. A proximity gate electrode is shown. The gate could also be applied globally using the underlying Si substrate as a back gate.

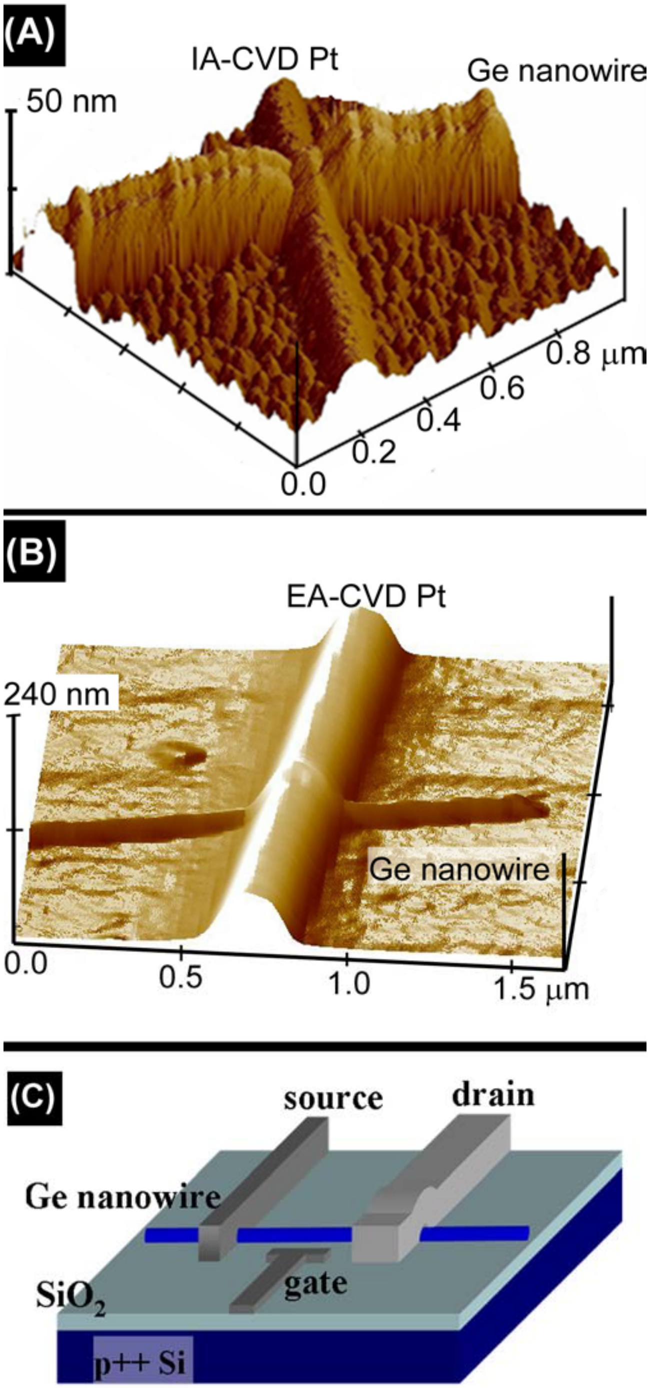

Figure 7.7: (A) AFM image of Ge nanowire/Pt contact formed by IA-CVD. The device was removed from the FIB for imaging before the deposition of the metal was completed (The final height of IA-CVD written electrodes is typically around 150 nm). (B) AFM image of a Ge nanowire contacted by EA-CVD written Pt electrode. (C) Schematic representation of a single Ge nanowire device with two different source/drain electrode configurations.

7.3.2.6 Four-Point Probe Measurements of EA-CVD Contacted Ge Nanowire Devices

In contrast to IA-CVD, EA-CVD was a milder process that did not erode the nanowire during deposition and posed no risk unintentional ion implantation. For example, Figure 7.7B shows an AFM image of a Pt/Ge nanowire junction deposited by EA-CVD. The schematic in Figure 7.7C illustrates the difference between metal electrodes deposited by EA-CVD and IA-CVD. The metal electrode wrapped around the nanowire surface and did not dig into the nanowire core. However, nanowires contacted with Pt lines deposited by EA-CVD showed markedly different transport characteristics than devices fabricated using IA-CVD. For example, as shown in the four-probe measurements in Figure 7.8A, the IV curves were non-linear similar to those observed in EBL fabricated devices and the contact resistance is 4.3 GΩ— two orders of magnitude higher than the IA-CVD Pt contacts. The resistance versus voltage (RV) plot also revealed that the majority of the non-linear IV behavior and hysteresis occurred at the contact. Thermal annealing in nitrogen at 250^{o}C for 30 min resulted in several pronounced changes in device characteristics (see Figure 7.8B): the contact resistance decreased by two orders of magnitude, the hysteresis in the contact resistance disappeared, and the IV curves became linear. Nonetheless, the contact resistance in the annealed device was still ~4 times larger than the nanowire resistance. Although one would not expect a Schottky barrier at the Pt/Ge interface, the Pt electrode was really composed of a significant quantity of C, which would impose a Schottky barrier. Also note that annealing decreased the nanowire resistance by a factor of 3, which is believed to have resulted from a reduction in effective electrode spacing due to a spread in electrical contact during the thermal anneal—sputter from the metal deposition process that did not conduct very well before anneal became incorporated into the contact electrode after annealing.

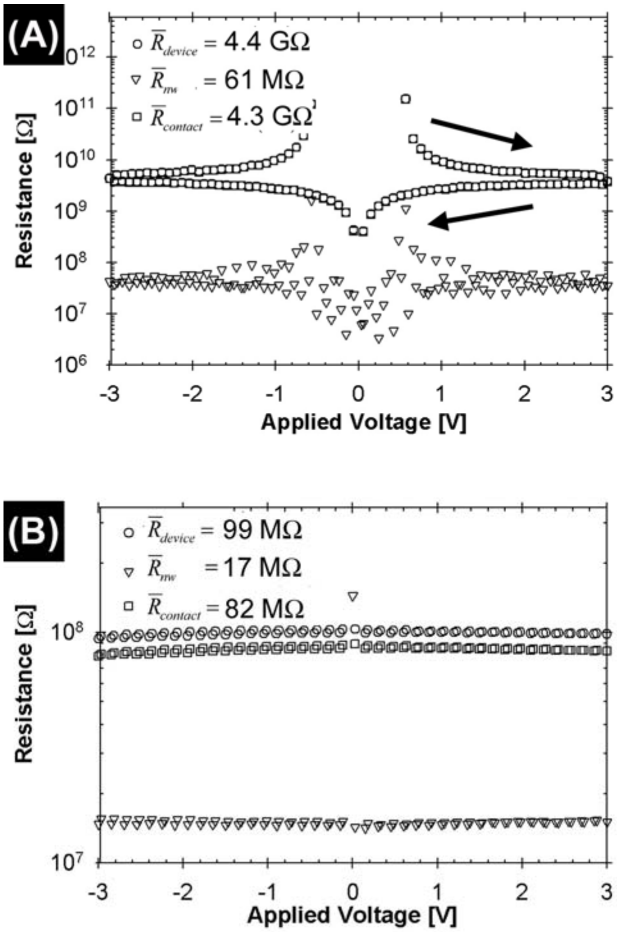

Figure 7.8: Four probe electrical measurements of EA-CVD contacted devices (A) before and (B) after annealing at 250^{o}C in nitrogen. The average resistances are shown in the inset.

7.3.3 Dependence of Contact Resistance on Nanowire Surface Chemistry

The contact resistance of IA-CVD fabricated electrodes did not depend on the nanowire surface chemistry since metallization was accompanied by mild ion milling into the wire core (see AFM image in Figure 7.7A and the schematic representation in the left hand side electrode in Figure 7.7C). On the other hand, EBL and EA-CVD fabricated electrodes wrapped around the nanowire surface and the metal/nanowire interface fabricated using these two techniques were consequently expected to be very sensitive to the surface chemistry of the nanowire before metallization. It turned out that careful surface treatment of the Ge nanowires prior to metallization significantly decreased the contact resistance.

In Figure 7.9A, a Ge nanowire with an organic monolayer-passivated surface was contacted by four Pt lines using EA-CVD. The nanowire was passivated by a solution-phase hydrogermylation reaction with isoprene (see Chapter 4) to terminate the surface as shown schematically in the inset of Figure 7.9A. The results presented in Chapter 4 have shown that isoprene surface passivation rendered the nanowire chemically robust and resistant to oxidation, in contrast to the “bare” nanowires that rapidly oxidized to electrically unfavorable GeO_{2-x} species that created slow surface states and charge traps. Figure 7.9B shows room temperature RV curves obtained for an isoprene-passivated Ge nanowire contacted with Pt electrodes deposited by EA-CVD. Without annealing, the contact resistance was only ~0.8 MΩ, four orders of magnitude lower than EA-CVD contacts deposited on untreated nanowires (Figure 7.9B), and one-to-two orders of magnitude lower than IA-CVD contacts and annealed EA-CVD contacts. The IV behavior was linear and the resistance did not depend on the applied voltage. Thermal annealing of the isoprene passivated nanowire device in Figure 7.9B did not change the device resistance. The nanowire resistance itself was also lower, by nearly an order of magnitude, in comparison to Ge nanowires with untreated surfaces. The surface chemistry was critically important for both the nanowire and the nanowire contact transport properties.

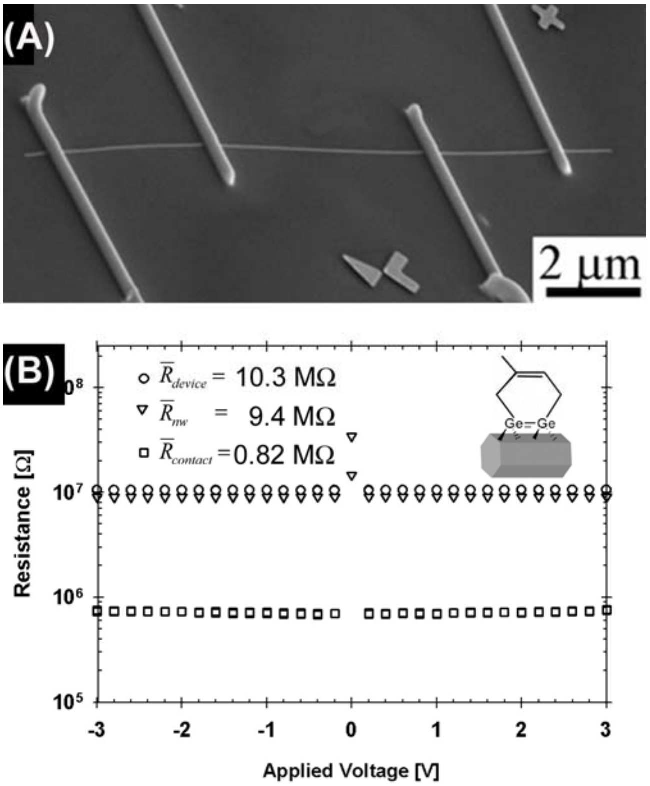

Figure 7.9: (A) HRSEM image of an isoprene passivated Ge nanowire contacted by four electrodes written with EA-CVD. (B) Four probe electrical measurements show significantly lower contact resistance than for unpassivated Ge nanowires. (Inset) Schematic showing covalent isoprene termination of the Ge nanowire surface.

7.3.4 Effect of Surface Chemistry on Electron Transport Through Nanowire Cross-Junctions

A perhaps more explicit example of the importance of surface chemistry in the electron transport through nanowires is given in the nanowire cross junction device shown in the SEM image in Figure 7.10A. Earlier reports on similar measurements of Si nanowire cross junctions by Heath and co-workers,[16] showed that cross junction currents could only be measured for devices after a 800°C thermal anneal in 95/5 Ar/H_2. In agreement with their reports no measurable cross-junction currents for similar devices fabricated from untreated Ge nanowires were detected. Similar measurement on cross-junction devices prepared from isoprene passivated Ge nanowire devise however exhibited markedly different characteristics. Electrical measurements of one of the wires making up the cross-junction device shown in the HRSEM image in Figure 7.10A showed linear I-V behavior with a p-type field effect (see Figure 7.10B). Significantly, electrical measurements across the nanowire junction[22] showed non-linear I-V characteristics in the near microampere range with a threshold voltage of approximately 1.1 V (see Figure 7.10C). This result clearly demonstrates that the isoprene passivation of Ge nanowire surface not only renders a chemically robust surface termination as was demonstrated in Chapter 4, but also enables the formation of low resistance, electrically favorable nanowire-to-nanowire interfaces that do not require extensive annealing steps as in Ref. 17.

---

[22] Cross-junction measurement were accomplished by applying the *source* and *drain* contacts to different wires, for example by measuring transport from terminal (1) to (a) or (2) to (b) as shown in Figure 7.10A.

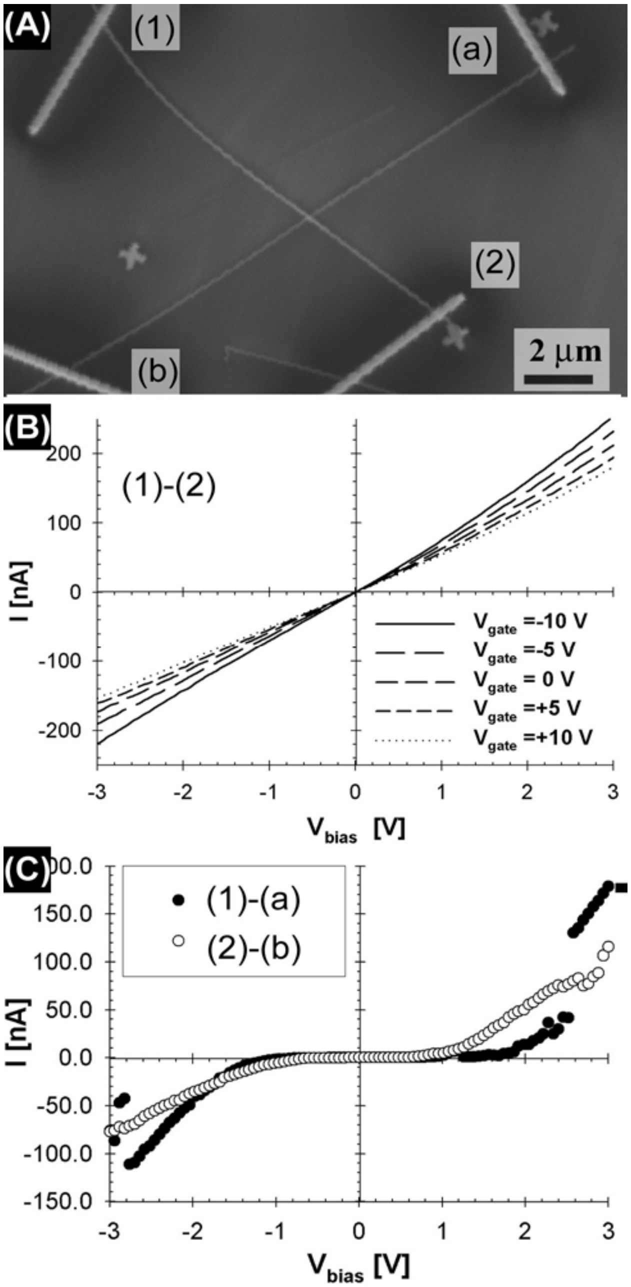

Figure 7.10: (A)HRSEM image of a nanowire cross-junction device prepared from isoprene passivated Ge nanowires. (B) I-V characteristics of one of the nanowires measured by connecting terminals (1) and (2). (B) Cross-junction IV characteristics measured by across terminals (1)-(a) and (2)-(b).

7.4 SURFACE EFFECTS ON NANOWIRE TRANSPORT

7.4.1 Field Effect Response due to Unintentional Au Doping

The typical room-temperature field current-voltage (I-V) measurements of a Ge nanowire contacted by IA-CVD defined Pt electrodes shown in Figure 7.11A exhibited linear transport characteristics and p-type field effect response. AFM imaged permitted the precise determination of the nanowire diameter (d) and the length of the nanowire segment between electrodes (L). Measurement of the resistance (R) or the nanowire device then allowed the resistivity (ρ) to be calculated from:

$$\rho = R\left(\frac{\pi d^2}{4L}\right) \qquad (1)$$

The Ge nanowire devices measured to date exhibited resistivities ranging from 10^1 to 10^{-1} Ωcm, which is far lower than the resistivity expected for intrinsic Ge. Gu et al.[10] have reported even lower resistivities (10^{-2} Ωcm) for *undoped* Ge,[23] which exhibited no discernible field effect response. The high conductivity in their measurements was attributed to the presence Au contamination. A similar interpretation for the nanowires investigated in this work would suggest an extrinsic carrier concentration with approximate concentration ranging from 10^{14} to 10^{16} cm^{-3}.[9] Au has four energy levels within the Ge bandgap (three acceptor levels at 0.04, 0.2 and 0.51 eV below the bottom of the conduction band and one donor level 0.04 eV above the top of the valence band).[9] These energy levels render Au a p-type (hole) dopant, however, since two of the four energy levels are

---

[23] The nanowires measured by Gu et al. were prepared by physical vapor transport at 950°C and exhibited the <111> growth axis.

close to middle of the energy gap Au acts as an efficient recombination center and is hence considered a carrier trap.

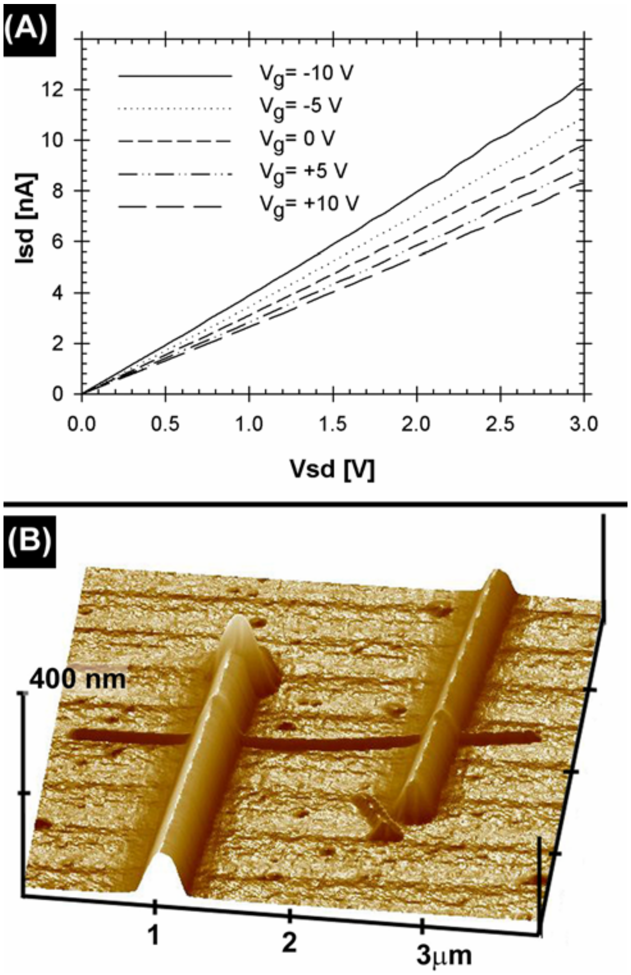

Figure 7.11: (A) Typical IV curve of a Ge nanowire device showing reduced conductivity with more positive gate voltage. (B) Corresponding AFM image of the device measured in (A) showing the 24 nm diameter Ge nanowire contacted by two Pt electrodes.

To date, the extensive elemental characterization efforts discussed in Chapter 5 have not allowed a conclusive determination of possible Au contamination in the Ge nanowires. The largest solubility of Au in Ge is less than $1.4(10^{-3})$ atomic%,[19] which is below the detectable limit of EDS or EELS characterization methods. Multiprobe measurements on Si nanowires by Yu et al.[16] showed variations in nanowire conductivity along the length of the nanowire, which they attributed to systematic local variations of seed metal contamination levels. As discussed above, similar multiprobe measurements on Ge nanowires used in this study did not show any conductivity variations along the length of the nanowire, suggesting either the absence of Au contamination, or small Au contamination levels with no local variations.

7.4.2 Field Effect Response due Surface States

7.4.2.1 Theoretical Investigations of the Effect of Finite Surfaces

An alternative and more plausible explanation for the observed p-type field effect response in the Ge nanowires is based on considerations of the finite size effects. Sundaram and Mitzel[20] reported a semi-classical theoretical investigation of surface effects in nanowire transport using the steady state Boltzmann equation. Their model treated surface effects with a finite width model, and showed significant departure form bulk values for nanowires with diameters in the range of 100 to 300 nm – an order of magnitude larger than the average nanowire diameter of the Ge nanowires investigated in this work.

Recently, Kobayashi[21] presented a more explicit illustration of the significance of surface effects in theoretical treatment[24] of conductance in Si nanowires with diameters ranging from 3-4 nm. The nanowire model in his work was based on a hexagonal nanowire cross section (as experimentally confirmed in Chapter 4) which exhibited highly inhomogeneous current distributions with localized conductance channels at the edges of the nanowire cross section. Figure 7.12 illustrates the theoretical current densities with closed and open circles show the current flowing in the positive and reverse direction along the wire axis, respectively, and the radius of the circles proportional to the absolute value of the current. For an energy potential of -0.5 eV along the long axis the nanowire exhibits a nearly homogeneous current distribution carried mostly by bulk states (see Figure 7.12A). However, at other potentials, the current distribution is carried mostly b {100}, {111}, or edge states (see Figures 7.12B,C, and D, respectively)

Although the nanowires used to fabricate field effect devices studied in this work have slightly larger diameters than the dimensions considered by Kobayashi, his theoretical work nevertheless underlines the importance of consideration of finite size effects in the analysis of electron transport through nanowires.

---

[24] In Kobayashi's work the electronic states of the faceted Si nanowire were expressed by a tight-binding method and the conductance was calculated by the Landauer formalism.

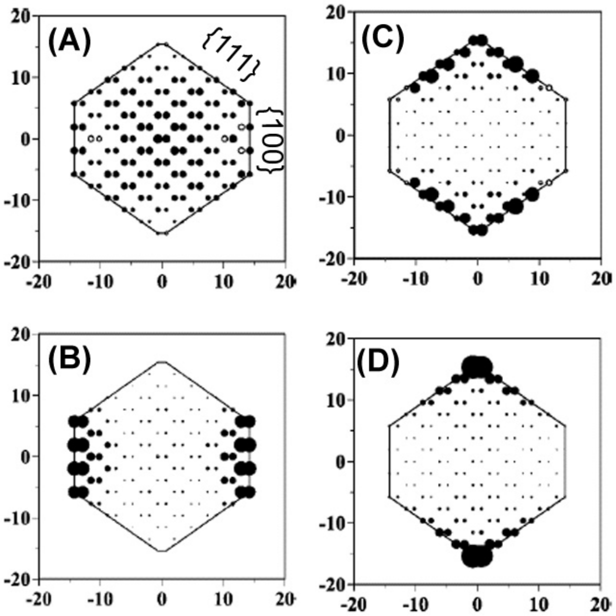

Figure 7.12: Theoretical current distribution in Si nanowires adopted from Kobayashi.[21] Energy potential along the length of the wire is (A)-0.5 eV, (B)-0.1 eV, (C)+0.6 eV, and (D)+1.0 eV. Units of the length scale are Å.

7.4.2.2 Gate Hysteresis Effects

Field effect measurements on Ge nanowire devices investigated in this work exhibited significant hysteresis effects. Such hysteresis effects cannot be explained by Au contamination but are instead commonly related to charged surfaces and have been observed in previous nanowire device measurements.[22,23] Figure 7.13A shows the hysteresis effects in a device prepared from untreated Ge nanowires. The gate voltage in these measurements was swept in the direction indicated by the arrows at a rate of ~0.5V/s. The figure clearly shows a reduction in hysteresis for gate voltages swept at the same rate over a smaller range suggesting that more charged states responsible for the observed hysteresis effects were populated at higher applied voltages. A similar current vs. gate voltage plot from a device fabricated from hexyl-monolayer terminated Ge nanowires is shown in Figure 7.13B. Hysteresis effects were still clearly visible in this device; however, the reduced hysteresis compared to the untreated nanowire device in Figure 7.13A suggested a lower density of charged states on the nanowire surface. The relation between surface chemistry and density of electrically active surface states was more is more clearly illustrated in time dependent field effect measurements discussed in the next section.

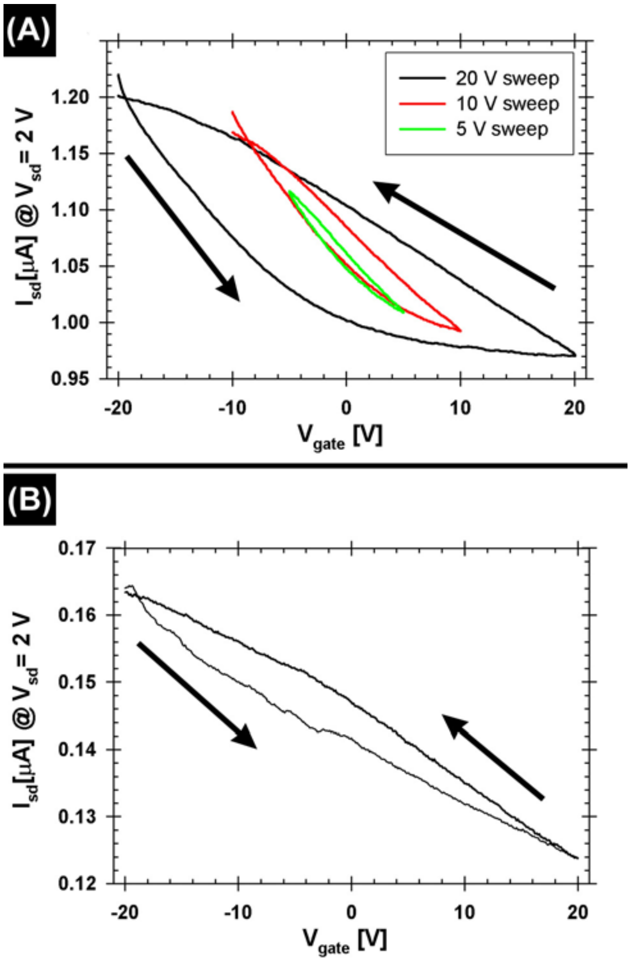

Figure 7.13: Current vs. gate voltage plots for (A) an untreated Ge nanowire device and (B) a device build from hexyl-monolayer terminated Ge nanowires.

7.4.3 Time Dependent Field Effect – Slow Surface States

7.4.3.1 The Multiple Relaxation Time Model

Closer inspection of the field effect response of Ge nanowire devices revealed transition phenomena wherein the gate voltage induced change in conductance decays over the course of seconds or minutes. Kingston and McWhorter have interpreted these slow surface relaxations based on a model in which mobile carriers tunnel through a barrier into non conducting surface states.[24] The relaxation times observed in their experiments were explained as a measure of the rate at which electrons are transferred from the bulk to surface states. While the surface relaxations measured by Kingston et al.[24,25] were invariable with temperature, similar experiments by Morrison[26] claimed an exponential temperature dependence and influence of other external factors such as illumination and oxygen partial pressure. According to Morrison's model, the rate-determining process is the transfer of free carriers over a surface potential barrier whose height is determined by the charge on the surface. Later work by Koc[27] attempted to explain slow surface relaxations based on diffusion of induced charges into trapping levels in the surface oxide. Based on this assumption Koc reported an empirical formula, which provided good agreement with the non-exponential relaxation processes. Koc's empirical model described the time dependent change in conductance as

$$\Delta\sigma = \Delta\sigma_0 \exp(-t/\tau)^{0.6} \tag{2}$$

where $\Delta\sigma$ and $\Delta\sigma_0$ are the instantaneous and initial change in surface conductivity, t is the elapsed time after application of the field effect and τ is a characteristic relaxation time. The experimental data discussed below were analyzed in a theoretical framework combining Koc's empirical model with Kingston and McWhorter's multiple relaxation time interpretation. Specifically, the slow relaxation processes discussed below were fitted to a model in which multiple relaxation times were convoluted in the form:

$$\Delta\sigma = \sum_{\tau} \left(\Delta\sigma_0 \exp\left(-t/\tau\right)^{0.6} \right) \tag{3}$$

7.4.3.2 Slow Surface States on Untreated Ge Nanowire Surfaces

The slow surface relaxation in a device fabricated from a Ge nanowire with an untreated (i.e.: oxidized) surface is shown in Figure 7.14. The gate voltage was applied as a step function with a delay time of 0.5 s to account for possible displacement currents and the resulting source drain current at a bias of 2 V was monitored as shown in Figure 7.14A. When a +20 V field effect was applied, the current through the nanowire returned to its initial value within approximately 500 s. A much more rapid field effect relaxation was observed when -20V gate voltage was applied and the source drain current decayed to near its initial value within approximately 120 s. Similar relaxation profiles were observed in experiments in which the step gate voltages were applied in opposite order (i.e.: -20 V followed by +20 V). Figure 7.14B and 7.14C show the slow surface relaxation for positive and negative applied gate voltages, respectively. The insets illustrate the good fit to the experimental data provided by equation (3). The respective relaxation time distributions differed significantly for the polarity of the applied field effect, suggesting that the density of surface states was unevenly distributed across the Ge bandgap as in the diagram in Figure 7.15.

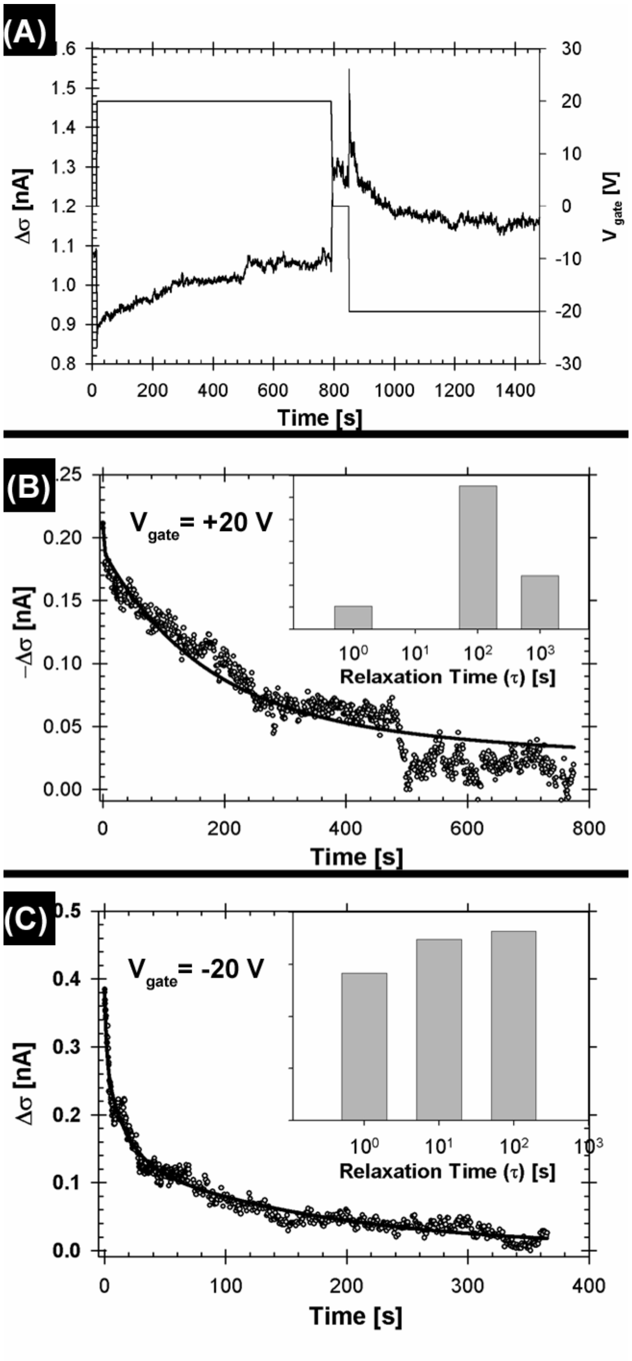

Figure 7.14: (A)Conductance (left axis) vs. time plots for step changes in applied gate voltage (right axis) measured on a device prepared from oxidized Ge nanowires. Detailed view of the field effect decay during positive (B) and negative (C) applied gate voltage. The histograms in the inset show the relaxation time distributions obtained from a fit to the experimental data.

The energy level diagram shown in Figure 7.15A shows the corresponding distribution of surface trapping levels expected on the oxide surface layer. For negatively charged surface states, the energy bands near the surface bend upward creating a p-type inversion layer within the bulk. With knowledge of the surface charge and the excess carrier concentration in the bulk, the penetration depth of this inversion layer may be calculated, which is approximately 10^2 nm, far exceeding the dimensions of the nanowire diameters considered in this study. The holes induced near the surface of the oxide layer therefore appeared to dominate the electron transport through the intrinsic nanowires.

Since the untreated Ge nanowire exhibited pronounced relaxation effects for positive and negative applied gate voltages, the energy levels of the capturing surface states appeared to be spread across with entire Ge band gap. More drastic relaxation for positive applied gate voltages could be interpreted in the context of shorter characteristic relaxation times or higher relative concentration of surface traps near the bottom of the energy gap. In contrast, Figure 7.15B shows the energy diagram for a nanowire surface without a charged oxide layer. The inset of the figure shows a HRTEM image of a nanowire with an isoprene passivate surface illustrating the absence of the thick charged oxide layer such as the one shown of an untreated surface in the inset of Figure 7.15A. An electrically perfect surface termination without any surface charges is physically not feasible for these nanowire surfaces, however, the removal of the thick surface oxide or a covalently bonded monolayer termination should allow significant reduction in the number of surface traps.

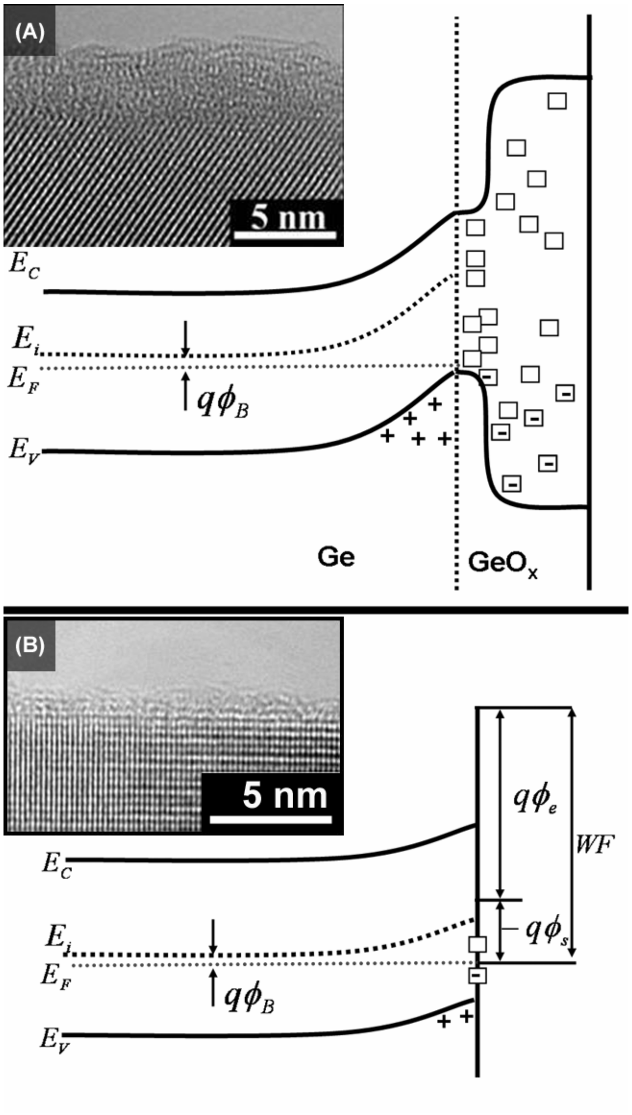

Figure 7.15: Schematic representations of the energy diagram near (A) an oxidized and (B) well passivated Ge nanowire surface. The insets show HRTEM images of oxidized and isoprene passivated surfaces, respectively.

7.4.3.3 Slow Surface States on Etched Ge Nanowire Surfaces

Field effect relaxation measurements on Ge nanowire specimens with etched surfaces showed less rapid decay of the field effect (see Figure 7.16). As in the case for untreated surfaces, the relaxation behavior was well described by the empirical model in equation (3), however the capture of induced carriers for positive applied gate voltages appeared much slower with characteristic relaxation times on the order of 10^3 s (Figure 7.16B). Interestingly, the field effect decay during -20V gate voltage was well represented by a single relaxation time (58 s). Carriers induced for negative gate voltages on the other hand appeared to be trapped more quickly resulting in near complete reduction toward the no field conductivity within approximately 200 s. These results suggest that the density of surface states in an etched nanowire sample was than in an untreated surface, while at the same time the relative distribution of capture states appeared to be localized near the top of the Ge valence band.

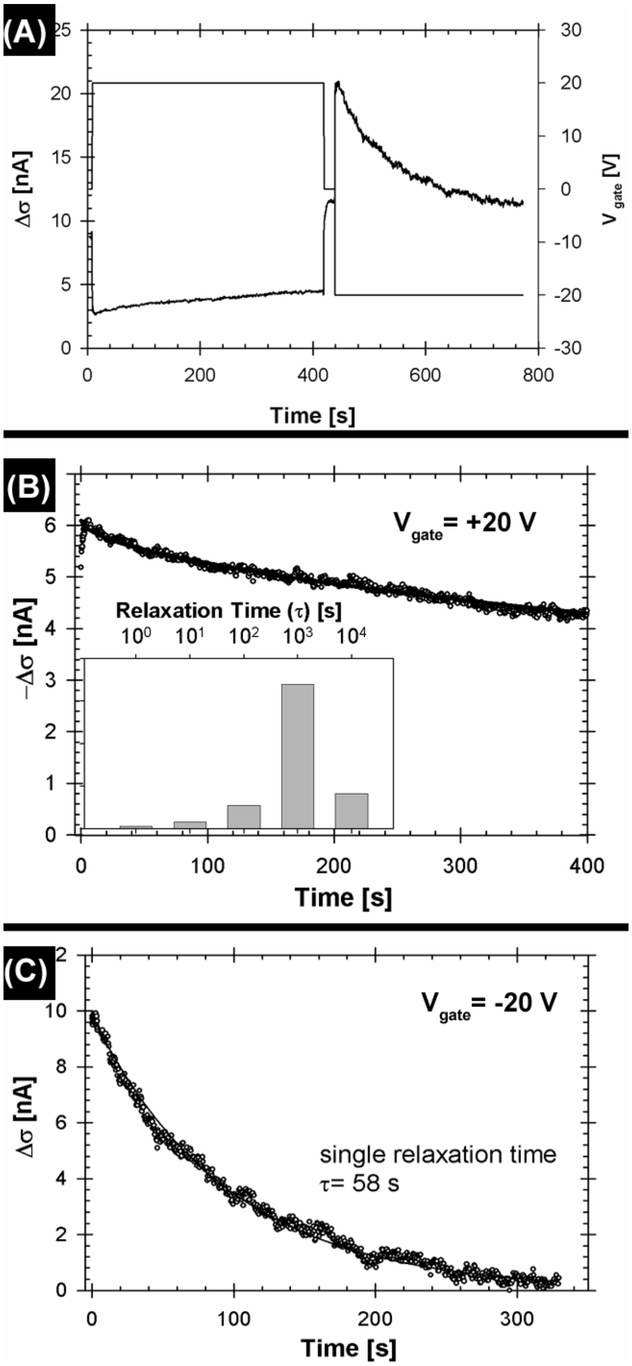

Figure 7.16: (A)Conductance (left axis) vs. time plots for step changes in applied gate voltage (right axis) measured on a device prepared from freshly etched Ge nanowires. Detailed view of the field effect decay during positive (B) and negative (C) applied gate voltage. The histograms in the inset show the relaxation time distributions obtained from a fit to the experimental data.

7.4.3.4 Slow Surface States on Isoprene-Passivated Ge Nanowire Surfaces

Figure 7.17 shows the relaxation of the field effect for a typical device fabricated from isoprene passivated Ge nanowires. The observed relaxation under positive applied gate voltages seemed negligible (Figure 7.17B), although a good fit with equation (2) was obtained for long characteristic relaxation times on the order of 10^4 s. The negative gate voltage induced change in conductivity appeared to decay to near half of its no-field value where it then tangentially equilibrated. The empirical fit to this relaxation behavior (Figure 7.17C) was consequently characterized by relaxation times about 10^4 s with a notable contribution of capture states with relaxation times near 10^2 s. Based on the work by Dinger,[28] the carrier mobility in the surface inversion layer was calculated from

$$\mu_s = \left(\frac{\delta I_{sd}}{\delta V_G}\right)\left(\frac{L^2}{C}\right)\left(\frac{1}{V_{sd}}\right) \tag{4}$$

where μ_s is the surface mobility, δV_G is the voltage step change and δI_{sd} the corresponding change in source-drain current, C is the device capacitance and L the interelectrode spacing. The calculated surface mobilities were on the order of 10^2 cm^2/V, which stands in reasonable agreement with the mobilities measured by Dinger[28] and theoretical predictions of mobility reduction do to diffuse scattering the surface by Schrieffer.[29]

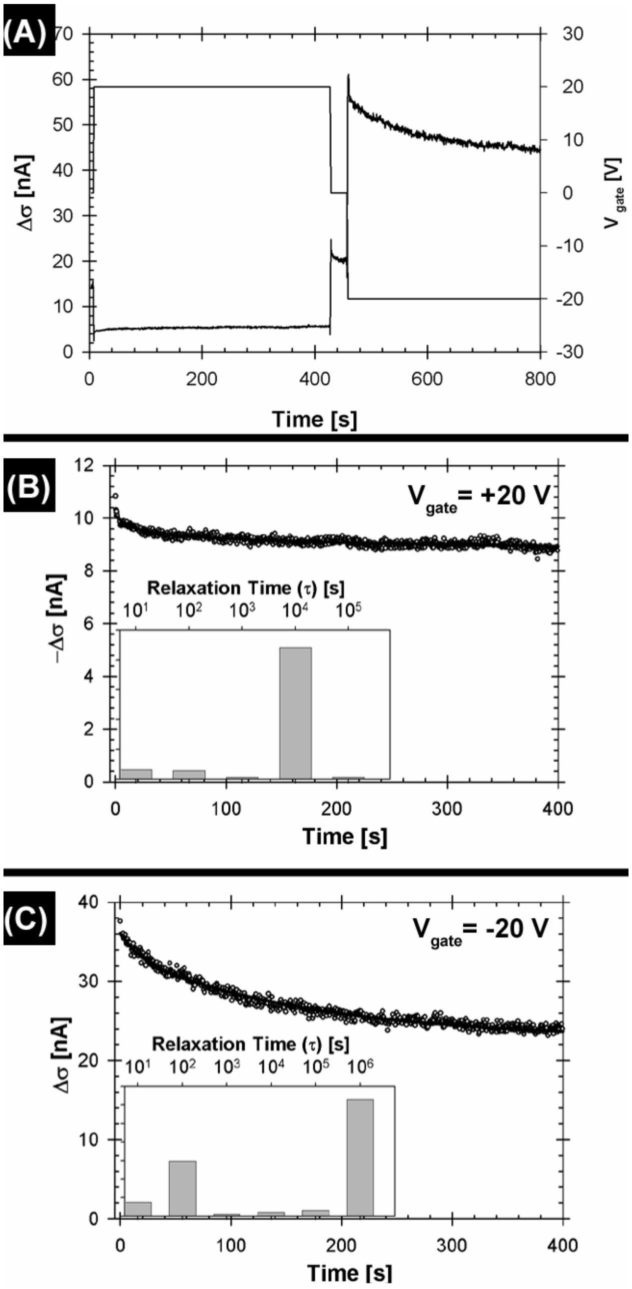

Figure 7.17: (A)Conductance (left axis) vs. time plots for step changes in applied gate voltage (right axis) measured on a device prepared from isoprene passivated Ge nanowires. Detailed view of the field effect decay during positive (B) and negative (C) applied gate voltage. The histograms in the inset show the relaxation time distributions obtained from a fit to the experimental data.

7.4.3.4 Slow Surface States Measured via Sinusoidal Applied Gate Voltage

Kingston and McWhorter[24] introduced an alternative approach for characterizing the relaxation time distributions for slow surface reactions on germanium wherein the gate voltage was not applied as a step function, but rather as a sinus wave with variable frequency. In this situation, surface traps with slow capture times are unable to respond to the applied sinusoidal field effect at high frequency. The response of a hexyl-monolayer terminated Ge nanowire to a sinusoidal gate voltage at a frequency of ω= 25 mHz is shown in Figure 7.18A. A sweep of different frequencies therefore provided a more direct measure of the relative response of the surface states quantified by the peak-to-peak change in conductance. The frequency dependent data can then be mathematically transformed to obtain a response function, which provides the number of states per unit trapping time. Figure 7.18B shows the normalized relative response of several Ge nanowire devices with different surface terminations.* The observed trend stands in good agreement with measurements by Kingston and McWhorter on bulk Ge samples.[24] Furthermore, the graph illustrates the reproducibility among different nanowire devices with the same surface termination and demonstrates the more pronounced gate effect relaxation for nanowires with untreated oxide surfaces. Experimental limitations associated with the sinusoidal gate voltage measurements precluded a broader and more detailed survey of

---

* The experimental data was fitted to the form $R(\omega) = a(\ln(\omega))^b + c$

different frequencies. A detailed mathematical analysis of the presented data as was reported by Kingston and McWhorter[24] was therefore not warranted.

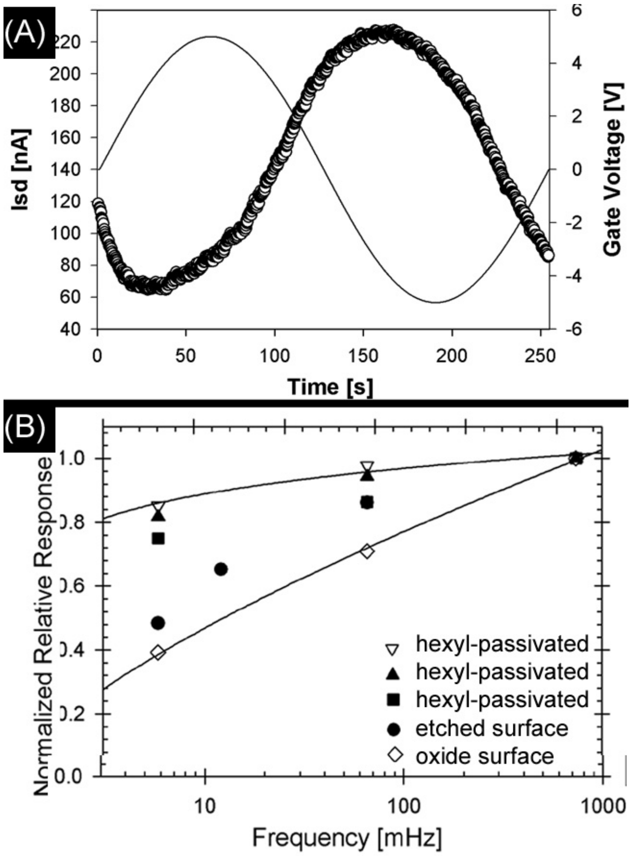

Figure 7.18: (A) Conductance vs. time for a sinusoidal applied gate voltage. (B) Normalized relative response of Ge nanowire devices with various surface terminations as a function of frequency (ω).

7.5 CONCLUSIONS

This chapter compared the electrical transport properties of individual Ge nanowires with Au/Cr contacts fabricated using electron-beam lithography methods and Pt contacts deposited by direct-write EA-CVD or IA-CVD methods. The EBL-fabricated devices exhibited non-linear Schottky diode behavior and unacceptably high contact resistances. The process reliability was also poor, with a 60% failure rate due to the poor stability of the Au/Ge nanowire contact. Devices prepared with Pt EA-CVD and IA-CVD exhibited lower contact resistances and could be fabricated with nearly 100% success rate within a timeframe of only a few hours. The IA-CVD devices exhibited the lowest contact resistance for Ge nanowires with untreated surfaces, in the range of 1~10MΩ. In fact, pre-annealed Ge nanowire devices with EA-CVD Pt metal contacts exhibited GΩ contact resistance with nonlinear IV behavior. Annealing the EA-CVD contacts brought the contact resistance down to the range of tens of MΩ. The most effective metal/nanowire electrical contacts were made by EA-CVD Pt deposition on organic monolayer-passivated Ge nanowires, which exhibited reasonably low contact resistance of ~0.8MΩ without the need for thermal annealing. FEB deposited Pt source/drain electrodes on nanowires with organic monolayer surface treatment were found to offer the lowest contact resistance and least amount of nanowire damage in comparison to FIB and EBL.

The electron transport properties of single crystal intrinsic Ge nanowires were measured at room temperature. The intrinsic nanowires exhibit p-type field effect due to an inversion layer formed at the negatively charged nanowire surface. Electron transport through the intrinsic nanowires was found to be dominated by surface states. The charged nanowire surface was also manifested in the hysteresis observed in gate voltage measurements. Untreated nanowires with an oxide termination exhibited more pronounced hysteresis than nanowires with a hexyl monolayer surface termination. Tunneling currents across a nanowire cross-junction was demonstrated without the need for a high temperature anneal in a device fabricated from isoprene passivated Ge nanowires. Transient behavior observed in field effect measurements were ascribed to the presence of slow surface states on the nanowire surfaces. The density, relative position within the Ge band gap, and the characteristic relaxation times were found to be highly sensitive to the nanowire surface chemistry. Field effect polarization in oxidized nanowire surfaces occurred over the course of hundred of seconds, whereas monolayer passivated surface exhibited much longer recombination times on the order of 10^4 s. Oxidized surfaces Gate voltage measurements exhibited hysteresis effects attributable to a charged surface. Relaxation time distributions were confirmed with sinusoidal applied gate voltage measurements.

7.6 REFERENCES

(1) Huang, Y.; Duan, X.; Cui, Y.; Lauhon, L. J.; Kim, K. H.; Lieber, C. M. *Science* **2001**, *294*, 1313-1317.

(2) Duan, X.; Huang, Y.; Lieber, C. M. *Nanoletters* **2002**, *2*, 487-490.

(3) Wang, J.; Gudiksen, M. S.; Duan, X.; Cui, Y.; Lieber, C. M. *Science* **2001**, *293*, 1455-1457.

(4) Duan, X.; Huang, Y.; Agarwal, R.; Lieber, C. M. *Nature* **2003**, *421*, 241-245.

(5) Johnson, J. C.; Yan, H.; Schaller, R. D.; Haber, L. H.; Saykally, R. J.; Yang, P. *J. Phys. Chem. B.* **2001**, *105*, 11387-11390.

(6) Jin, S.; Whang, D.; McAlpine, M. C.; Friedman, R. S.; Wu, Y.; Lieber, C. M. *NanoLetters* **2004**, *4*, 915-919.

(7) Cronin, S. B.; Lin, Y.-L.; Rabin, O.; Black, M. R.; Ying, J. Y.; Dresselhaus, M. S.; Gai, P. L.; Minet, J.-P.; Issi, J.-P. *Nanotechnology* **2002**, *13*, 653-658.

(8) Streetman, B. G.; Banerjee, S. *Solid State Electronic Devices*; 5th ed.; Prentice Hall: Upper Saddle River, 2000.

(9) Sze, S. M. *Physics of Semiconductor Devices*; 2nd ed.; Wiley: New York, 1981.

(10) Gu, G.; Burghard, M.; Kim, G. T.; Duesberg, G. S.; Chiu, P. W.; Krstic, V.; Han, W. Q. *J. Appl. Phys.* **2001**, *90*, 5747-5750.

(11) Wang, D.; Wang, Q.; Javey, A.; Tu, R.; Dai, H.; Kim, H.; McIntyre, P. C.; Krishnamohan, T.; Saraswat, K. C. *Appl. Phys. Lett.* **2003**, *82*, 232-2434.

(12) Greytak, A. B.; Lauhon, L. J.; Gudiksen, M. S.; Lieber, C. M. *Appl. Phys. Lett.* **2004**, *84*, 4176-4179.

(13) Shockley, W.; Pearson, G. L. *Phys. Rev.* **1948**, *74*, 232-233.

(14) Kingston, R. H. *J. Appl. Phys.* **1956**, *27*, 101-114.

(15) Chung, S.-W.; J-Y., Y.; Heath, J. R. *Appl. Phys. Lett.* **2000**, *76*, 2068.

(16) Yu, J.-Y.; Chung, S.-W.; Heath, J. R. *J. Phys. Chem. B.* **2000**, *104*, 11864-11870.

(17) Telari, K. A.; Rogers, B. R.; Fang, H.; Shen, L.; Weller, R. A.; Baski, D. N. *J. Vac. Sci. Technol. B* **2002**, *20*, 590-595.

(18) Rotkina, L.; Lin, J.-F.; Bird, J. P. *Appl. Phys. Lett.* **2003**, *83*, 4426-4428.

(19) Massalski, T. B.; Murray J.L., B. L. H., Baker H., Ed.; American Society for Metals: Metals Park ,Ohio, 1986.

(20) Sundarram, V. S.; Mitzel, A. *Jounral of Physics: Condensed Matter* **2004**, *16*, 4697-4709.

(21) Kobayashi, K. *Phys. Rev. B* **2004**, *69*, 115338-118345.

(22) Wang, D.; Chang, Y.-L.; Wang, Q.; Cao, J.; Farmer, D.; Gordon, R.; Dai, H. *Condensed Matter - preprints* **2004**.

(23) Duan, X.; Huang, Y.; Lieber, C. M. *Nano Letters* **2002**, *2*, 487-490.

(24) Kingston, R. H.; McWhorter, A. L. *Phys. Rev.* **1956**, *103*, 534-540.

(25) Kingston, R. H. *Phys. Rev.* **1955**, *98*, 1766-1775.

(26) Morrison, S. R. *Phys. Rev.* **1956**, *102*, 1297-1301.

(27) Koc, S. *Phys. Stat. Sol.* **1962**, *2*, 1304-1311.

(28) Dinger, R. *Thin Solid Films* **1977**, *43*, 311-318.

(29) Schrieffer, J. R. *Phys. Rev.* **1955**, *97*, 641-646.

Chapter 8: Morphology and Alignment of Ensemble and Isolated Ge nanowires

8.1 INTRODUCTION

The successful implementation of semiconducting nanowires into large-scale device configurations requires the controlled and precise deposition and alignment of isolated as well as ensemble nanowires. This aspect has long been considered a limiting factor for the broad technological utilization of nanowires and nanotubes and has consequently been under investigation by many researchers. Vertical alignment has been reported for carbon nanotubes[1-4] and ZnO nanowires,[5] however, the lateral alignment of nanowires and nanotubes has broader technological applicability. Initial attempts for the controlled lateral deposition of carbon nanotubes to specific areas on a substrate were based on the chemical interactions between the nanotube and surface bound self-assembled monolayers. Burghard et al.[6] and later Liu et al.[7] reported the successful implementation of this approach in the alignment of carbon nanotubes in parallel arrays defined by chemically functionalized nanolithographic substrates.

By combining the surface patterning technique with microfluidic channels, Huang et al.[8] have successfully demonstrated the alignment of nanowires into more complex network structures through sequential processing steps. This process however required multiple processing steps to define the microfluidic channels and more importantly only allowed for the deposition of nanowires in very limited regions. In their studies on pressure-induces changes of inorganic nanorods assemblies from isotropic to nematic or smectic liquid crystal phases, Yang and co-workers[9] demonstrated that Langmuir-Blodgett (LB) film techniques could successfully be employed in the large area deposition of aligned one-dimensional nanostructures. Later, Lieber and co-workers implemented the same technique for the large scale hierarchical assembly of semiconductor nanowires.[10]

Although the LB approach offers the possibility for large scale parallel arrays of nanowires, its principal limitation is the lack specificity and precision in the area in which the nanowires are deposited. Alternative methods, such as the electric field assisted assembly[11] or alignment through standing surface acoustic waves[12] could overcome these limitations. This chapter discusses the morphologies of ensemble and isolated Ge nanowire deposits formed onto various substrates. The microscale structure of these deposits is investigated with regards to the surface chemistry of the nanowires and the physical parameters during the deposition.

8.2 EXPERIMENTAL

Ge nanowires were prepared via the SFLS method as discussed in Chapter 2. Two general surface chemistries were investigated: (1) nanowires with clear yet otherwise unpassivated surfaces, and (2) nanowires whose surfaces were isoprene passivated via thermally initiated hydrogermylation as described in Chapter 4.

Bare Si (100) wafers were cut into ~1x1 cm sections for deposition experiments and sonically cleaned in acetone for 10 minutes followed by a rinse in isopropanol, and a 15 min rinse in a 1:1 HCl:methanol solution. Isolated Ge nanowire deposits were prepared as discussed in Chapter 7 whereas ensemble deposits were obtained from the deposition of high concentration (~10mg/ml) nanowire dispersions in toluene. The nanowires were dispersed with the aid of a sonic bath prior to drop casting the suspension onto a Si substrate heated placed on top of a hot plate heated to 60°C.[*] In a typical experiment approximately 300 μL of the suspension evaporated within 30 sec. SEM characterization was performed on a LEO 1530 operating at 3 kV acceleration voltage.

Electric field alignment experiments were performed by similar drop casting of a concentrated nanowire containing toluene suspension onto a borosilicate glass slide with

---

[*] The deposition experiments were carried out on a slightly heated surface to accelerate toluene solvent evaporation rate.

a predefined interdigitated electrode array structure. Details of the array interdigitated electrode array fabrication have been published by Doty et al.[13], briefly, arrays with 20μm spacing were photolithographically defined followed by thermal evaporation of Cr/Au (5nm/1000nm). The array structure was placed under an optical microscope (Carl Zeiss Axioskop 2 MAT) for in-situ observation. A 20V, 60Hz alternating potential (corresponding to a field strength of 10,000 V/cm) was applied across the two terminals of the array and the solvent was allowed to flash.

In collaboration with Kwangseok Lee (Loo's group) chemically functionalized Si substrates were prepared via micocontact transfer printing (μCP) as described in detail elsewhere.[14] Briefly, parallel 20 μm wide lines with alternating hydrophilic domains (surface hydroxyl –OH) and hydrophobic (– OC_nH_{2n+1}) were formed by first hydroxylating the surface followed by microcontact stamping with a high-resolution poly(dimethylsiloxane) stamp coated with n-octadecyltrichlorosilane.

8.3 RESULTS AND DISCUSSION

8.3.1 Ensemble Nanowire Deposits

8.3.1.1 Ensemble Deposits of Unpassivated Ge Nanowires

The poor dispersibility of unpassivated Ge nanowire samples was briefly discussed in Chapter 4. Ge nanowires with cleaned, yet oxidized surfaces can be temporarily dispersed in variety of aqueous and organic solvents with a brief treatment in a sonic bath. However, within minutes after sonication, the suspensions typically became unstable, began to flocculate and ultimately precipitated from the suspension. The morphology of ensemble Ge nanowire deposited from unpassivated samples was consequently characterized by clustered deposits of randomly oriented nanowires. An SEM image of such a deposit cluster is shown in Figure 8.1A and a higher magnification image of the cluster showing the randomly oriented flexible entanglement of nanowires See Figure 8.1B).

The optical properties of the nanowire suspensions were also investigated by polarized optical microscopy. Figure 8.2A shows a nearly cross-polarized and fully cross-polarized (Figure 8.2B) image of unstable nanowire suspensions in isopropanol. The bright spots correspond to aggregates, which appeared to contain small locally oriented nanowire segments that were able to polarize the light.

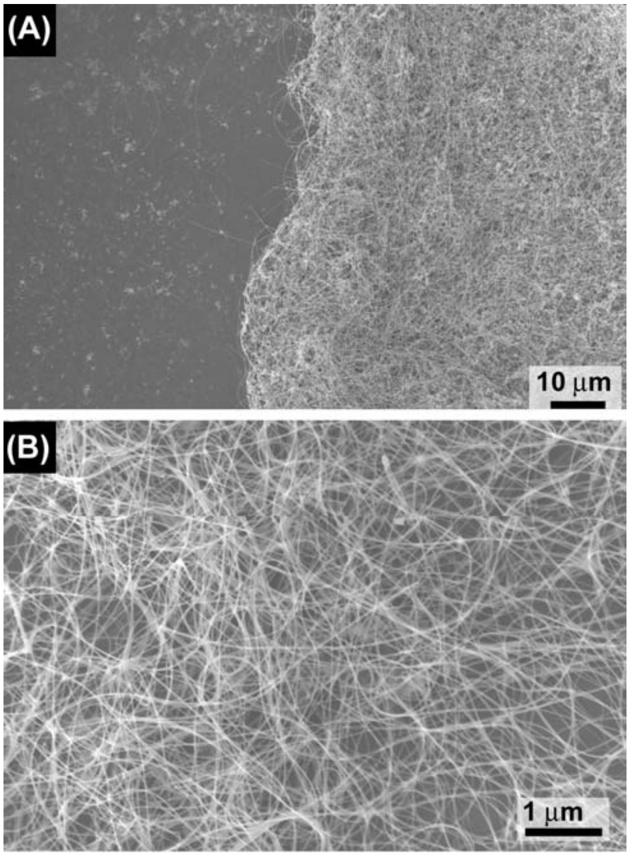

Figure 8.1: (A) low-resolution SEM image of an ensemble Ge nanowire deposit formed from unpassivated Ge nanowires. (B) High-resolution SEM image of the same deposit showing the random orientation of nanowires within the entanglement.

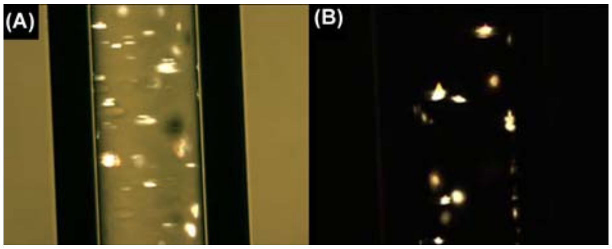

Figure 8.2: Optical micrographs of unpassivated nanowire suspension inside a 0.5mm i.d. glass capillary tube imaged under (A) partial and (B) full cross-polarization.

8.3.1.2 Ensemble Deposits of Isoprene Surface- Passivated Ge Nanowires

The morphology of Ge ensemble deposits prepared from isoprene passivated Ge nanowires differed significantly from those of unpassivated Ge nanowires discussed above. The low- and high-resolution SEM images in Figure 8.3A and 3B, respectively, show an ensemble deposit in which the nanowires were parallel aligned into a near continuous film. Instead of the local clusters seen in Figure 8.1A, the isoprene passivated Ge nanowires generally formed a smooth film with a nematic-like phase morphology. The parallel alignment persisted over length scales as large as 100μm and gradually changed from one domain to another. The local ordering was probed by laser diffraction using a red (632.8 nm) laser transmitted through an ensemble Ge nanowire film deposited on a transparent Kapton© window. Figure 8.4A shows a laser diffraction pattern of an unpassivated Ge nanowire sample showing angular symmetric laser scattering around the central spot (blocked by a beam blocker). The corresponding laser diffraction pattern of an isoprene passivated Ge nanowire deposited on the other had shows a diffraction pattern with clear angular scattering anisotropy along the direction indicated by the arrow. A more quantitative analysis of the short and long range ordering of the nanowires deposits via SAXS[†] has not been possible to date since the relatively large x-

---

[†] Small-angle x-ray scattering (SAXS) experiments were performed in collaboration with Aaron E. Saunders.

ray spot size samples appears to probe several domains resulting in an angle averaged isotropic scattering signal.

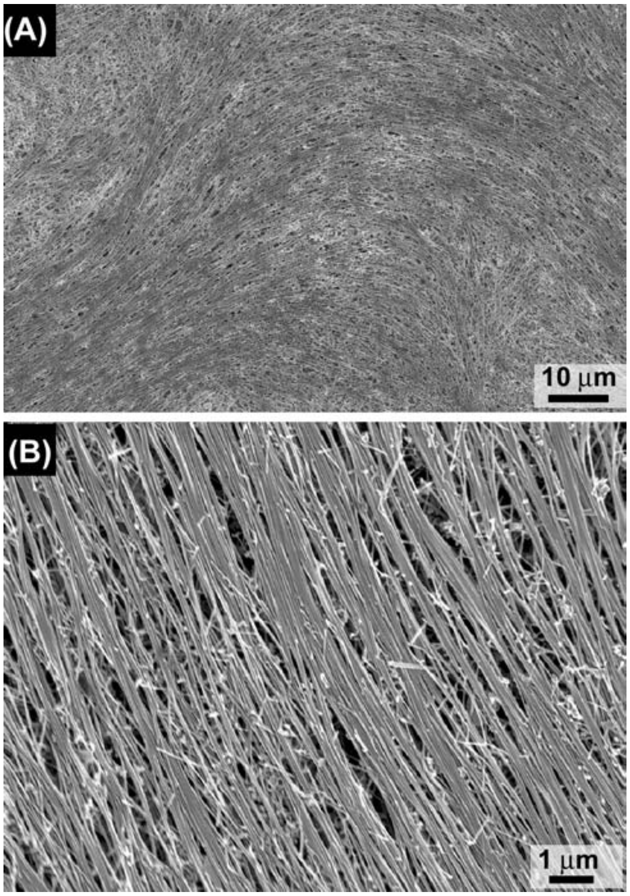

Figure 8.3: (A) Low-resolution SEM image showing nematic phase like domains of aligned isoprene passivated Ge nanowires and (B) high-resolution SEM image of the same deposit showing parallel aligned Ge nanowires.

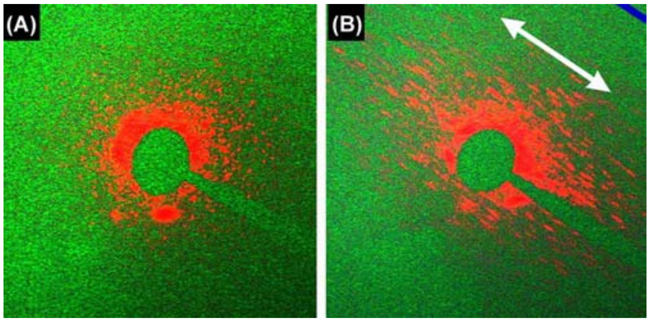

Figure 8.4: Laser diffraction images of Ge nanowires deposited on a Kapton© window (A) isotropic nanowire deposit and (B) anisotropic nanowire deposit showing preferential diffraction in the direction indicated by the arrow.

The nematic alignment of nanowires into birefringent domains was further confirmed by the polarized optical micrographs shown in Figure 8.4. Similar birefringence behavior was noted by Smalley and co-workers[15] in carbon nanotubes solubilized via polymer wrapping. Owing to their high aspect ratio, the organization of nanotubes and nanowires into nematic-like phases requires a much higher solubility and mobility in the host solvent. Inorganic, metallic, and semiconductor nanorods have much smaller aspect ratios than the nanowires considered in this work and hence appear to more readily undergo phase transitions into smectic and nematic phases.[9,16-19] Unpassivated Ge nanowires discussed had poor solubility and hence lacked the required mobility to rearrange into ordered structures. The isoprene-passivated nanowires on the other hand did not precipitate from the suspension prior to solvent evaporation; instead, the suspension underwent a phase change and formed the thermodynamically favored nematic-like phase. The final orientation of the nanowire liquid crystal was then determined by the direction of the retracting liquid-vapor interface.

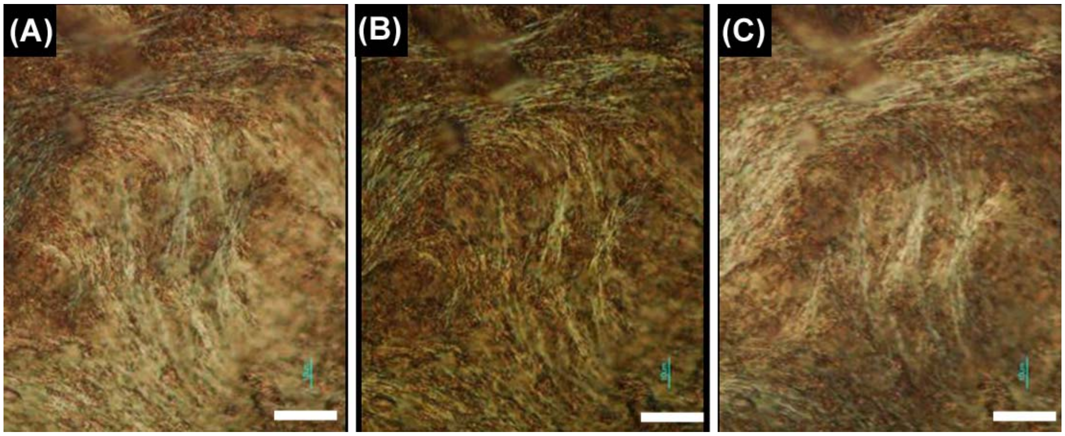

Figure 8.5: Optical micrographs of the same deposit as shown in Figure 8.3. (A), (B), and (C) have been acquired with different polarizations to illustrate the optical response of the birefringent domains. The scale bar is 20 μm.

8.3.1.3 Ensemble Deposits Formed During Slow Depressurization and Cooling of Nanowires in Supercritical Fluid

In contrast to the two ensemble deposit morphologies discussed above, nanowires deposits obtained in the slow depressurization and cooling[*] from the supercritical hexane suspension exhibited a three-dimensional structure as shown in Figure 8.7. The low-resolution image (Figure 8.7A) shows a microscopic cellular structure reminiscent to those observed by Chakrepani et al.[20] in the capillary-driven assembly of two-dimensional cellular carbon nanotube foams. Similar structures, although with different and better defined ordering have been observed in the evaporation of nanoparticle suspensions.[21,22] In those cases, the formation of the three-dimensional structure was attributed to Marangoni convection and the nucleation and growth of holes. The Marangoni convection alignment requires a temperature or pressure gradient from the substrate surface to the surrounding medium and a two-phase interface. While both of these requirements may be met during the slow cooling and depressurization of the reactor, the exact mechanism responsible for the formation of the deposit structure shown in Figure 8.7 is currently still unknown.

---

[*] After a regular Ge nanowire synthesis without subsequent passivation reactions, the supercritical fluid suspension was first slowly cooled at near constant pressure (6 MPa) from 380°C to 200°C within approximately 30 min. The fluid was then gradually depressurized and cooled to a final state of 0.7 MPa and 60°C at which point the substrate was removed from the supercritical fluid cell.

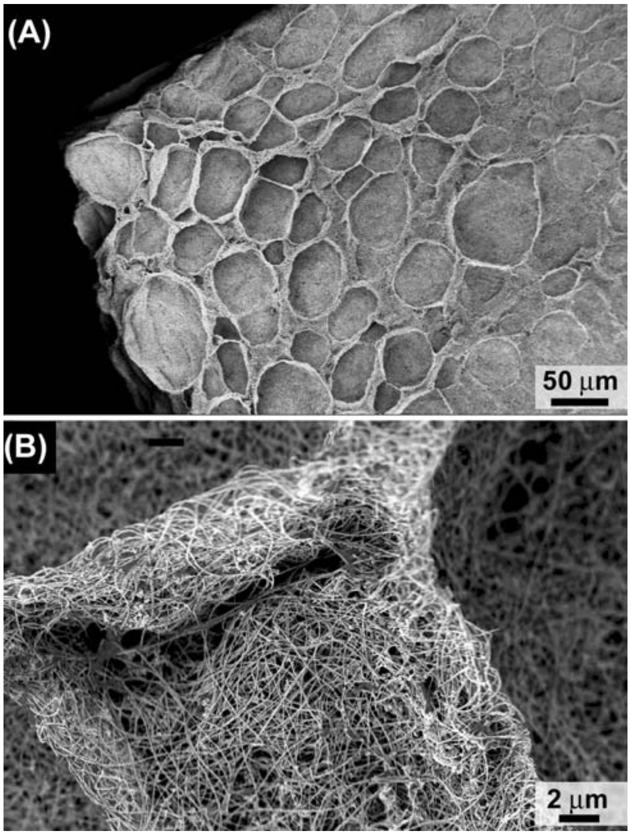

Figure 8.7: SEM image of Ge nanowire deposit obtained during the slow depressurization and cooling showing (A) the three dimensional cellular structure composed of a dense matrix (B) of randomly entangled Ge nanowires.

8.3.2 Aligned Deposition of Isolated Ge Nanowires

The nanowire deposits discussed in the previous section were formed in the absence of external influences. This section discusses depositions that involved intentional external factors in an effort to form isolated and aligned Ge nanowire deposits.

8.3.2.1 Fluidic Alignment

Initial attempts in the preparation of aligned isolated Ge nanowire deposits focused on the utilization of mild shear associated with fluidic motion of the dilute suspension across the device substrate. Nanowire entanglement and subsequent cluster formation were avoided by using nanowire suspensions with typical concentrations in the range of 10 – 50 μg/ml. Instead of using complex poly(dimethylsiloxane) PDMS microfluidic channels to guide the flow direction, a modified compressed air system was used to provide a uniform air flow field across the 1x1 cm Si deposition substrate. The SEM image in Figure 8.8A shows isolated Ge nanowires[†] partially aligned in the direction of the flow field (indicated by the arrow). Similar experiments involving nanowires with substantially longer average lengths commonly resulted in deposits with less alignment due to the more pronounced entanglement and cluster formation. For example, Figure 8.8B shows the results of a fluidic alignment of a nanowire sample onto a carbon coated TEM grid, while a general alignment trend is still discernible, the overall quality of the nanowire placement is less than that for the shorter wires in Figure 8.8A. Although the simplified fluidic alignment method

---

[†] The short average length of this nanowire sample is the result of extensive sonication as discussed in detail in Chapter 9.

was suitable for the alignment of short nanowires, this approach was relatively ineffective for the alignment of nanowires with length scale required for the fabrication of electronic devices such as the ones discussed in Chapter 7.

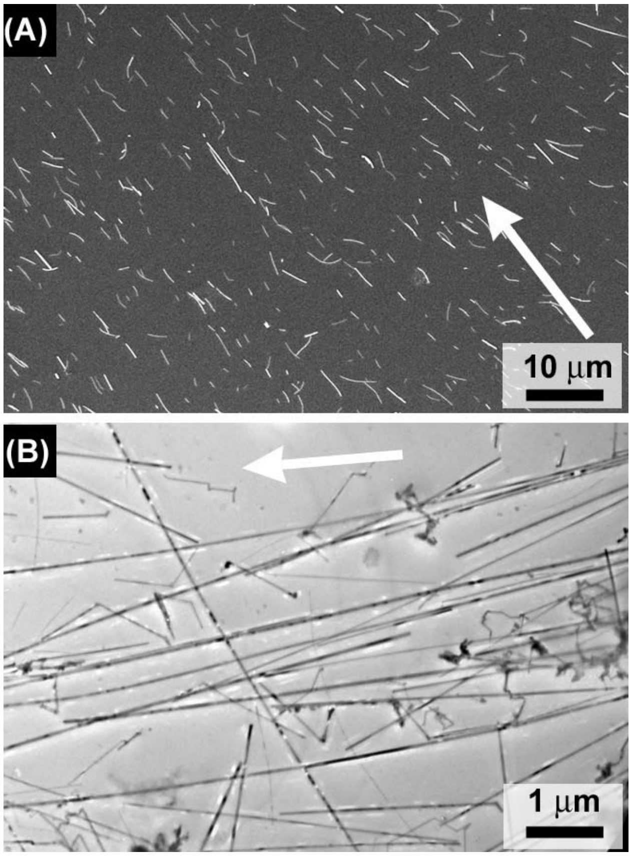

Figure 8.8: SEM images of partially aligned nanowires (A) SEM images of sonically shortened nanowires deposited on a Si substrate in a flow field directed by an air stream and (B) TEM image of similarly aligned nanowires on a carbon coated TEM grid.

8.3.2.2 Fluidic Alignment on a Chemically Functionalized Si Substrate

The alignment of nanowires during synthesis is highly desirable and the presence of the flow field during continuous flow nanowire syntheses in supercritical fluid presented another opportunity for the alignment of nanowires. The fluidic nanowire alignment in PDMS molds reported by Huang et al.[23] was performed with a linear flow velocity of ~ 6.4mm/s and in room temperature ethanol suspensions with have a viscosity of approximately 1.1 cP.[24] Their work revealed a direct correlation between the shear rate and the extent of alignment (quantified by the angular spread of aligned nanowires) suggesting that relatively high shear rates are required for efficient alignment. In comparison, a typical continuous flow reaction was performed with a linear flow velocity near 0.8 mm/s and the viscosity of supercritical hexane at the synthesis conditions (390^{o}C, 6 MPa) is approximately 0.012 cP.[25] The shear rate encountered in the supercritical fluid reactor was therefore several orders of magnitude less than for the ethanol flow in PDMS molds. Consequently, the prevailing shear rate alone should not be sufficient for effective nanowire alignment during reaction in the supercritical flow-through reactor; this was verified in numerous continuous flow experiments. Utilization of significantly higher flowrates to improve the prevailing fluid shear was not viable, since higher flowrates cannot ensure thermodynamic equilibrium of the fluid and the surrounding reactor wall.[‡]

In an effort to compensate for the limiting available shear flow during the supercritical flow-through reaction, the synthesis was combined with a substrate

---

[‡] The temperature profile in the continuous flow reactor under typical conditions is calculated in Appendix A.

whose surface had been prepatterned with a parallel array of chemically functionalized domains. The Si surface was modified with an array of 20 μm wide parallel lines with hydrophobic and hydrophilic surface functionalization. The substrate was placed in the reactors cell with the array lines oriented parallel to the direction of flow. The SEM image in Figure 8.9A shows that nanowires aligned in nearly the same direction as the prepatterned array. The surface patterning, visible as disconnected lines of dark areas on the substrate surface, appeared to be marginally stable during the supercritical flow conditions and in many areas appears to have degraded to the point beyond which the surface pattern can no longer support the alignment of nanowires. Figure 8.9B, for example, shows domains on the same sample surface where nanowire alignment was not accomplished due to pronounced entanglement of nanowires, severely limiting the extent of nanowire alignment. The presence of a chemically functionalized substrate therefore does not appear to be sufficient to overcome the unfavorably low shear rate present during continuous flow reactions. Similar experiments directed at the controlled deposition of nanowires onto substrates with various chemical functionalization are presently still under investigation in collaboration with the Loo group.

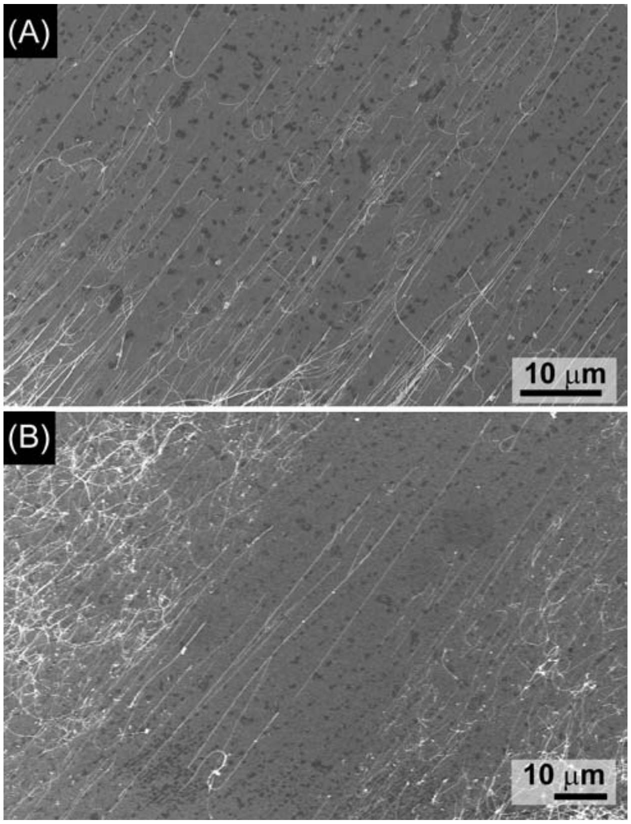

Figure 8.9: Ge nanowires deposited onto a chemically functionalized Si substrate during a continuous flow reaction showing (A) adequate alignment of isolated nanowires and (B) unfavorable effects of nanowire entanglement.

8.3.2.3 Electric Field Assisted Alignment

The electrical field assisted alignment of Au nanorods reported by Smith et al.[11] was limited to small areas defined by the interdigitated electrode array structure buried underneath a silicon nitride dielectric layer. The array structure used in their work was rather complex and involved the multistep processing, including the array metallization, the deposition of a dielectric layer, etching of a channel orthogonal to the array structure and finally a second metallization on top of the insulating later. This section described the electric field assisted alignment of nanowires using a simple Au electrode structure on top op borosilicate glass.

Figure 8.10A shows a transmitted-light, non-polarized optical micrograph or the interdigitated array structure after the deposition and alignment of nanowires as described in the experimental section. The cross-polarized image of the same device region (see Figure 8.10B) shows bright birefringence in the array interstitial regions due to the parallel-aligned Ge nanowires in this region. The higher magnification image (Figure 8.10C) acquired in incident total interference contrast mode shows nanowires aligned orthogonal to the array orientation. Significantly, the nanowires deposited neat the edge of the active region of the array structure align in the direction of the electric field lines emanating from the tip of the electrode line. This represents a significant advantage over the unidirectional nanowire alignment associated with the LB technique and therefore offers far greater flexibility in the nanowire device architectures that can be constructed from these assemblies. The high-resolution SEM image in Figure

8.10D provides further evidence for the high degree of parallel alignment of isolated Ge nanowires spanning the two array electrodes.

Smith et al.[11] have attributed the electric field assisted alignment to the polarization of the nanowires. While their work was performed with alternating voltages at frequencies ranging from 1 to 20 kHz our preliminary investigation showed surprisingly good alignment with the common frequency of only 60 Hz. The large area electric field assisted nanowire alignment illustrated in Figure 8.10, appeared to depend on two critical factors. The nanowire suspension needed to exhibit sufficient stability and mobility to permit the electrically polarized nanowires to orient themselves in the thermodynamically lowest energy configuration (aligned along the electric field lines). As illustrated in the case of isoprene passivated ensemble Ge nanowire deposits above, this requirement was satisfactorily met in toluene suspensions of organic monolayer passivated Ge nanowires. Secondly, the electrostatic forces aligning the nanowires appeared to be weaker than the shear forces associated with the retreating liquid-vapor interface during solvent evaporation, which required a quick and non-interruptive evaporation of the solvent. In fact, similar experiments in which the solvent was not flashed but instead slowly evaporated showed very little alignment relative to the electrode array. In that case, the shear forces of the retreating liquid-vapor interface appeared to have rearranged and randomized the nanowire alignment.

Alternative approaches for the stabilization of the electrostatic alignment of the nanowires are currently under investigation. Similar electric field assisted nanowire alignment should for example be possible in or on top of thin polymer films providing exciting new opportunities in the fabrication of polymer/nanowire composite flexible electronics.

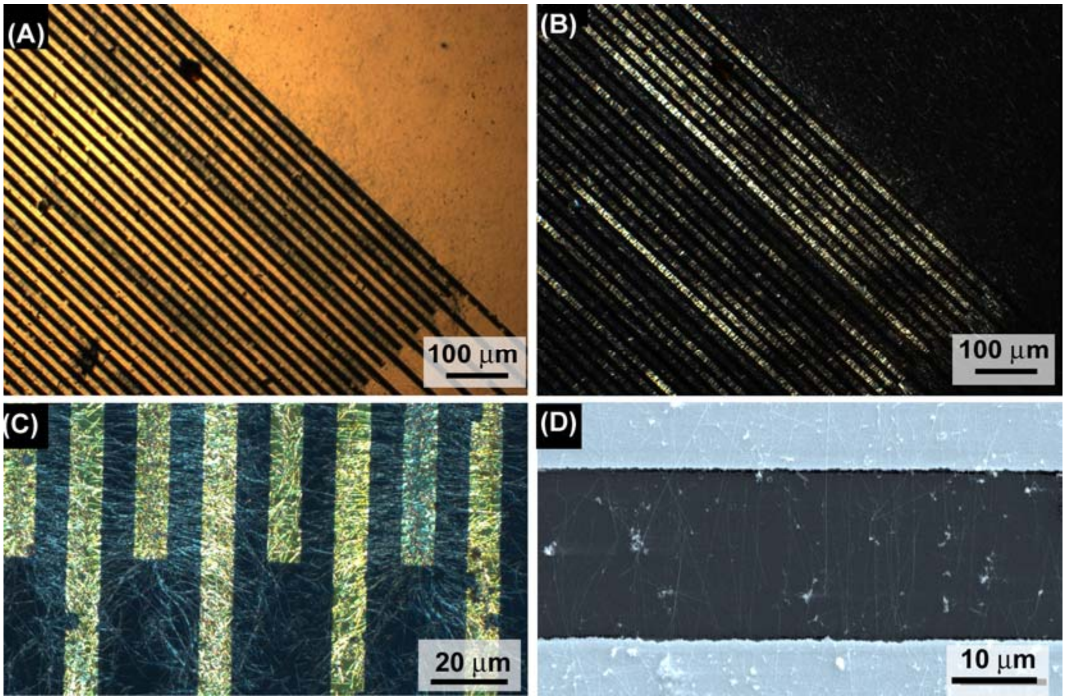

Figure 8.10: Ge nanowires aligned in the presence of an electric Field (A) Non-polarized optical micrograph of the interdigitated array structure. (B) Polarized image (C) higher magnification image near the end of the interdigitated array showing nanowires aligned with the electric field lines. (D) HRSEM image showing the alignment of individual Ge nanowires between the two electrodes.

8.4 OUTLOOK AND CONCLUSION

The morphology of ensemble Ge nanowire deposits is shaped by multiple factors including the temperature, solubility and mobility in the suspension solvent. Nanowires with chemically passivated surfaces exhibited significantly enhanced solubility permitting the ensemble samples to undergo phase change into thermodynamically favored nematic-like phases. Unpassivated nanowires on the other had precipitated from the suspension forming randomly oriented agglomerates. Various external factors were explored for the alignment of isolated Ge nanowire deposits, while alignment in flow fields and on chemically functionalized substrates showed moderate success, the electric field assisted nanowire assembly showed broadest applicability for technological applications. This approach enables the same large-scale alignment capability as the Langmuir-Blodgett film technique, while at the same time providing greater flexibility in the local multidirectional alignment of isolated nanowires.

8.5 REFERENCES

(1) Terrones, M.; Grobert, N.; Olivares, J.; Zhang, J. P.; Terrones, H.; Kordatos, K.; Hsu, W. K.; Hare, J. P.; Townsend, P. D.; Prassides, K.; Cheetham, A. K.; Kroto, H. W.; Walton, D. R. M. *Nature* **1997**, *388*, 52-55.

(2) Li, W. Z.; Xie, S. S.; Qian, L. X.; Chang, B. H.; Zou, B. S.; Zhou, W. Y.; Zhao, R. A.; Wang, G. *Science* **1996**, *274*, 1701-1703.

(3) Ren, Z. F.; Huang, Z. P.; Xu, J. W.; Wang, J. H.; Bush, P.; Siegal, M. P.; Provencio, P. N. *Science* **1998**, *282*, 1105-1107.

(4) Schlittler, R. R.; Seo, J. W.; Gimzewski, J. K.; Durkan, C.; Saifullah, M. S. M.; Welland, M. E. *Science* **2001**, *292*, 1136-1139.

(5) Kuykendall, T.; Pauzauskie, P. J.; Zhang, Y.; Goldberger, J.; Sirbuly, D.; Denlinger, J.; Yang, P. *Nature Materials* **2004**, *3*, 524-528.

(6) Burghard, M.; Duesberg, G.; Philipp, G.; Muster, J.; Roth, S. *Adv. Mater.* **1998**, *10*, 584-589.

(7) Liu, J.; Casavant, J.; Cox, M.; Walters, D. A.; Boul, P.; Lu, W.; Rimberg, A. J.; Smith, K. A.; Colbert, D. T.; Smalley, R. E. *Chem. Phys. Lett.* **1999**, *303*, 125-129.

(8) Huang, Y.; Duan, X.; Wei, Q.; Lieber, C. M. *Science* **2001**, *291*, 630-633.

(9) Kim, F.; Kwan, S.; Akana, J.; Yang, P. *Journal of the American Chemical Society* **2001**, *123*, 4360-4361.

(10) Whang, D.; Jin, S.; Wu, Y.; Lieber, C. M. *Nano Letters* **2003**, *3*, 1255-1259.

(11) Smith, P. A.; Nordquist, C. D.; Jackson, T. N.; Mayer, T. S.; Martin, B. R.; Mbindyo, J.; Mallouk, T. E. *Appl. Phys. Lett.* **2000**, *77*, 1399-1401.

(12) Strobl, C. J.; Schaflein, C.; Beierlein, U.; Ebbecke, J.; Wixforth, A. *Applied Physics Letters* **2004**, *85*, 1427-1429.

(13) Doty, R. C.; Yu, H.; Shih, C. K.; Korgel, B. A. *Journal of Physical Chemistry B* **2001**, *105*, 8291-8296.

(14) Loo, Y.-L. W., R. L.; Baldwin, K. W.; Rogers, J. A.; *J. Am. Chem. Soc.* **2002**, *124*, 7654-7755.

(15) O'Connell, M. J.; Boul, P.; Ericson, L. M.; Huffman, C.; Wang, Y.; Haroz, E.; Kuper, C.; Tour, J.; Ausman, K. D.; Smalley, R. E. *Chem. Phys. Lett.* **2001**, *342*, 265-271.

(16) Li, L. S.; Walda, J.; Manna, L.; Alivisatos, A. P. *Nanoletters* **2002**, *2*, 557-560.

(17) Li, L.-S.; Alivisatos, A. P. *Adv. Mater.* **2003**, *15*, 408-411.

(18) Li, L.-s.; Marjanska, M.; Park, G. H. J.; Pines, A.; Alivisatos, A. P. *J. Chem. Phys.* **2004**, *120*, 1149-1152.

(19) Jana, N. R.; Gearheart, L. A.; Obare, S. O.; Johnson, C. J.; Edler, K. J.; Mann, S.; Murphy, C. J. *J. Mater. Chem* **2002**, *12*, 2909-2912.

(20) Chakrapani, N.; Wei, B.; Carrillo, A.; Ajayan Pulickel, M.; Kane Ravi, S. *Proc. Nat. Acad. of Sciences* **2004**, *101*, 4009-4012.

(21) Stowell, C.; Korgel, B. A. *Nano Letters* **2001**, *1*, 595-600.

(22) Moriarty, P.; Taylor, M. D. R.; Brust, M. *Phys. Rev. Lett.* **2002**, *89*, 248303.

(23) Huang, Y.; Duan, X.; Wei, Q.; Lieber, C. M. *Science* **2001**, *291*, 630-633.

(24) Dean, J. A., Ed. *Lange's Handbook of Chemistry*; 15th ed.; McGraw-Hill: New York, 1999.

(25) Lemmon, E. W.; McLinden, M. O.; Friend, D. G. *NIST Chemistry WebBook, NIST Standard Reference Database Number 69* **2003**, http://webbook.nist.gov.

Chapter 9: Preparation of Ge nanorods

9.1 INTRODUCTION

As intermediate between zero-dimensional quantum dots and one-dimensional nanowires, nanorods, which typically have aspect ratios[31] between 1.5 and 50, have garnered significant research attention. The electrical and optical properties of these materials are size tunable and dimensionally dependent, making them ideal candidates for the study of fundamental quantum confinement concepts[1,2] and as components for future nanoscale electronic and optoelectronic devices.[3,4]

The pioneering work on the synthesis of II-VI semiconductor nanowire was performed by Alivisatos and co-workers, who carried out the pyrolytic degradation of precursors in hot surfactant mixtures typically consisting of trioctylphosphine (TOP) and trioctylphosphineoxide (TOPO).[1,5] In their approach width and length control was achieved by varying the composition of the surfactants, which adjusts the growth kinetics along specific directions of the anisotropic crystal structure.[32] The solution-liquid-solid (SLS) synthesis of III-V nanorods, such as InAs was later reported by Banin and co-workers who combined the hot surfactant medium containing TOP and TOPO with Au seed nanocrystals to grow single crystal InAs nanorods.[6,7]

Despite the significant progress in the synthesis of II-VI and III-V semiconductor nanorods, reports on similar group IV semiconductor nanorods have been scarce. Group IV semiconductor nanorods synthesis has been attempted via DC sputtering[8], electron UHV electron beam evaporation,[9] and physical vapor transport,[10] however, low quality, lack of crystallinity and ill- controlled dimensionality of these materials has limited their applicability in fundamental studies or technological applications. The combined benefits of a high temperature reaction environment and the controlled interactions of

---

[31] The aspect ratio of these nanostructures is defined as the length ratio of the long axis to the short axis.

[32] II-VI nanorods are typically elongated along the c-axis of the hexagonal crystal structure.

organic ligands with the surfaces of Si and Ge nanostructures presents a unique opportunity for the SFLS approach to be extended to include the synthesis of group IV semiconductor nanorods.

This chapter discusses two general approaches for the preparation of Ge nanorods. First, the *top-down* approach involving the length shortening of solution grown Ge nanowires via various mechanical means including shear flow fracture and sonication is discussed. Secondly, preliminary results from the *bottom-up* synthetic approach which combines the SFLS nanowire synthesis described in Chapter 2 and surface ligand dominated arrested precipitation principles are illustrated.

9.2 TOP-DOWN APPROACH: NANOWIRE LENGTH SHORTENING

The initial approach for the preparation of nanorods with specific aspect ratios was based on the destructive shortening of previously synthesized Ge nanowires. Ge nanowires prepared via the SFLS method discussed in Chapter 2 have very high aspect ratios and initial length ranging up to hundred of micrometers. A precise determination of the initial length distribution of the nanowire samples is complicated by the extensive entanglement of the nanowires in the ensemble deposits (see Chapter 8).

9.2.1 Nanowire Length Reduction via Shear Flow Induced Fracture

Early work in the processing of nanowire suspensions assumed the single crystal nanowires to exhibit brittle mechanical properties[33], consequently a nanowire sample exposed to high shear flow conditions was expected to undergo extensive fracture resulting in the reduction of the average nanowire length. In a modification of the supercritical reactor setup described in Chapter 2, a dilute suspension of Ge nanowires in toluene was loaded into a high-pressure piston as shown in the inset of Figure 9.1A and passed through a 2 μm stainless steel frit (Valco). The shear flow through the frit was

---

[33] A preliminary investigation of the remarkable mechanical properties, particularly its extraordinary flexural strength, was discussed in Chapter 5.

achieved through the application of pressure pulses from the pump to the piston containing the nanowire suspension. However, despite the use of a relatively dilute nanowire suspension, extensive clogging occurred at the frit, so that the nanowire throughput was prohibitively low even in the case of 50 MPa pressure pulses.[34]

The clear solution obtained at the effluent side of the frit was analyzed by HRTEM. Figure 9.1A, shows a low-resolution TEM image of a short Ge nanowire with extensive crystallographic damage. The higher resolution image in Figure 9.1B further illustrates extensive crystallographic damage to the nanowire incurred during the shear flow experiment. Entanglement and the unexpected flexibility of the nanowires precluded the shear flow technique as an efficient means for reducing the average nanowire length.

---

[34] 50 MPa is the maximum pressure attainable with the Alcott HPLC pump used in this system.

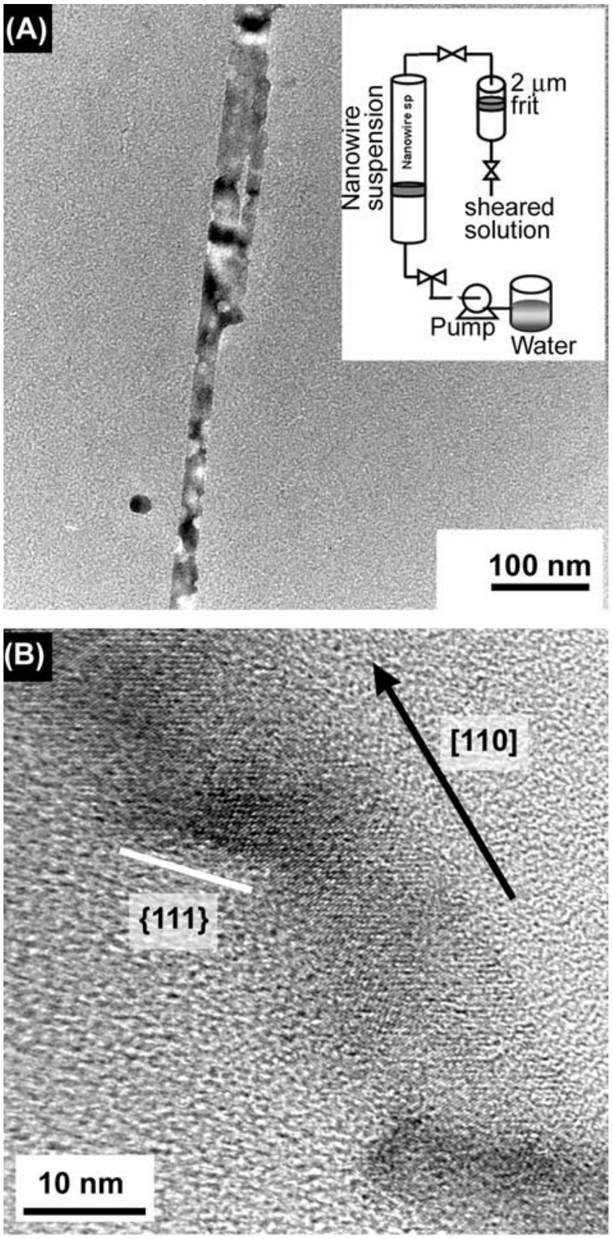

Figure 9.1: TEM images of nanowire segments obtained from shear flow shortening experiments (A) low-resolution image showing multiple fracture and damage points in the nanowire crystal segment. The inset shows the experimental setup used for the shear flow experiment. (B) HRTEM image illustrating the crystallographic damage to the sample and an apparent {111} fracture facet.

9.2.2 Nanowire Length Reduction via Ultrasonication

9.2.2.1 Sonication in a Water Bath

Early nanowire device fabrication experiments required the preparation of dilute nanowire suspensions, which allowed the deposition of isolated nanowire onto specific areas of the device substrate. These processing steps also showed that extensive sonication lead to a gradual decrease in the average length of the nanowires in the suspension. Sonication was consequently explored as an alternative route to controlled *top-down* fracture of Ge nanowire samples resulting in the formation of Ge nanorods with controlled aspect ratios.

Ge nanowire suspensions[35] at a concentration of 0.5 mg/ml in toluene were placed into a sonic water bath (Cole-Palmer, 100W 42kHz) and sonicated at room temperature for up to 12 h. Sample aliquots were taken at specific time intervals and analyzed by HRTEM. Figure 9.2 shows a low-resolution TEM image of a Ge nanorods sample with an average length of 690 nm and a relative standard deviation of 80% obtained after 300 min of sonication in the water bath. The histogram of the nanowire length distribution in the inset of the figure shows that the nanowire lengths were well represented by a log-normal distribution.

Despite the initial promising results of the top-down sonic shortening, later experiments showed that this approach suffered from poor repeatability. For example, the histograms shown in Figure 9.3 show the results of sonication of the same sample and at the same concentration (0.5 mg/ml) as shown in Figure 9.2 above. While the series of histograms clearly show the gradual reduction of the average nanorod length and concomitant reduction in length polydispersity, the histogram for the sample sonicated for 700 min still exhibits an average nanorods length exceeding 2 μm. The results contrasts the 690 nm average length obtained after 300 min from the same sample as

---

[35] The nanowire samples subjected to Ultrasonication experiments were surface passivated with a hexyl-monolayer to aid in the formation of stable suspensions in organic solvents.

discussed above. The discrepancy could be an artifact of the sampling and analysis procedure; however, since the histograms of both samples are based on the analysis of over 300 nanowires, such statistical error seems unlikely. A more plausible explanation for the observed discrepancy appears to be the variations of sonic power in specific locations of the sonic bath. The Cole-Parmer sonic bath used in these experiments utilized small frequency sweeps around the central 42 kHz operating frequency to reduce local variations in sonic power. However, local variations in sonic field strength were still discernible from visible inspection of the bath.

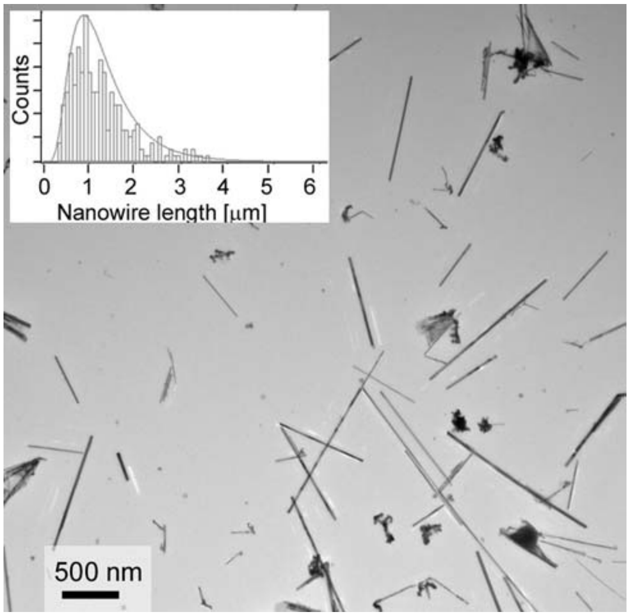

Figure 9.2: Low-resolution TEM image of a Ge nanorods sample obtained from 300 min water bath sonication of a Ge nanowire sample. The inset shows the nanorods length distribution fitted to a log-normal distribution.

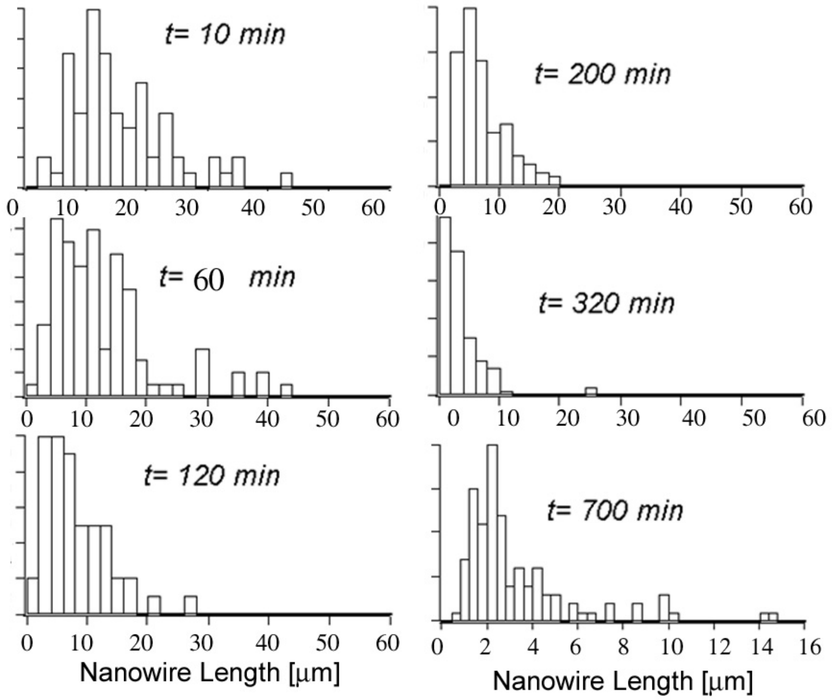

Figure 9.3: Histograms of nanorods length distributions in aliquots samples obtained after various sonication times.

9.2.2.2 Ultrasonic Probe

In an effort to reduce the above mentioned unfavorable variability complications associated with the sonic bath and to reduce the extensive sonication times, the ultrasonic bath was replaced with a more powerful sonic horn. Ultrasonic horns permit the sonic power to be focused to a much smaller volume compared to the liter-sized sonic water bath discussed above. The tip of the horn was submersed into a 2 ml conical vial containing a nanowire suspension (0.5 mg/ml in toluene in toluene) and ultrasonication was applied at a peak power of 120 W at a frequency of 20 kHz. During ultrasonication microscopic bubbles are known to form in the liquid; the growth and collapse of these cavities occurs within microseconds and causes local hot spots with temperatures and pressures reaching 5000°C and 50 MPa, respectively.[11] The intensive sonication provided by the probe required the sample to be submersed in ice water to prevent the toluene suspension from being heated above its boiling point. Aliquots were taken at specific times and analyzed as described above.

Figure 9.4 shows the histograms of nanowire samples obtained after 3 and 15 min of ultrasonication, respectively. Notably, the reduction of nanowire length was achieved in significantly less time than was required with the sonic bath. However, the nanorod dispersions obtained from horn-ultrasonication were significantly less stable than those obtained from the ultrasonic bath. While nanorod suspensions prepared with the sonic bath generally remained stable for up to 12 h, sample with similar length distributions obtained from horn-ultrasonication typically precipitated from the solution within tens of minutes after the sonication. The instability of these nanorod suspensions is attributed to the destruction of the organic monolayer surface passivation during the local heating associated with the ultrasonication. Process modifications that limit the extent of damage to the surface passivation monolayers are presently still under investigation.

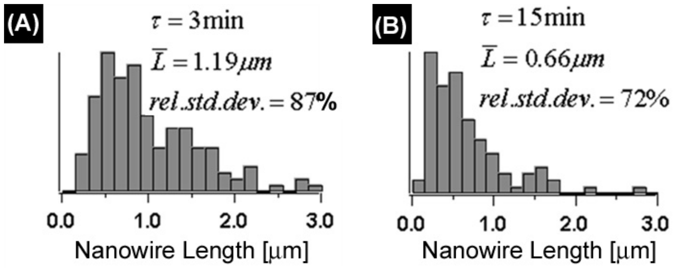

Figure 9.4: Length histograms of Ge nanorods prepared from horn-ultrasonication for (A) 3 min and (B) 15 min.

9.3 BOTTOM-UP APPROACH: SYNTHESIS OF GE NANORODS IN SUPERCRITICAL FLUID

As an alternative to the destructive *top-down* nanorod fabrication processes discussed above, a *bottom-up* synthesis combining synthesis principles of solution growth of anisotropic II-VI and III-V nanorods with the SFLS method discussed in Chapter 2 was developed. Ge nanorods were prepared by degrading tetraethylgermane (TEG) in the presence of sterically stabilized Au seed particles in a supercritical fluid environment heated and pressurized above its critical point. In contrast to the SLFS nanowire syntheses described in Chapter 2, these syntheses were carried out in a supercritical fluid environment consisting of a mixture of octanol and hexane.

Figures 9.5A and 9.5B show SEM images of Ge nanorod samples prepared via an injection of a solution containing TEG at concentration of 500 mM, a 500:1 Au:Ge molar ratio and a 1:3 (Figure 9.5A) or 1:1 (Figure 9.5B) octanol:hexane ratio into a supercritical hexane environment at 450^{o}C and 25 MPa. Syntheses under similar conditions in the absence of octanol led to the formation of large quantities of high aspect ratio Ge nanowires as discussed in Chapter 2. The octanol appeared to act as a surface capping ligand similar to the function of long chain thiols in the steric stabilization of Au and Ag nanocrystals. The octanol therefore stabilized the surface of the Ge nucleus and reduced the chemical potential differences for nucleation which ultimately drastically reduced the one-dimensional growth rate.[*]

The presence of octanol in the reaction environment also appeared to reduce the overall yield of nanorod material to approximately 30% compared to the near 80% yield obtained under similar conditions in pure supercritical hexane. Recent work by Lu et al.[12] has shown that similar reaction conditions in the absence of Au seed crystals lead to the formation of octanol-capped Ge nanocrystals. The preliminary results discussed in this chapter do not correspond to the optimized growth parameters for the supercritical fluid synthesis of Ge nanorods, but rather illustrate the potential for future syntheses in this area. Current research in the Korgel group led by Lee and Huang focuses on the improved synthesis methods for Si and Ge nanorods utilizing a variety of surface ligands and the benefits of tunable residence time offered by the continuous flow reactor.

---

[*] The relation between chemical potential difference and nanowire or nanorods growth rate based on the Gibbs- Thompson effect is discussed in Appendix B.

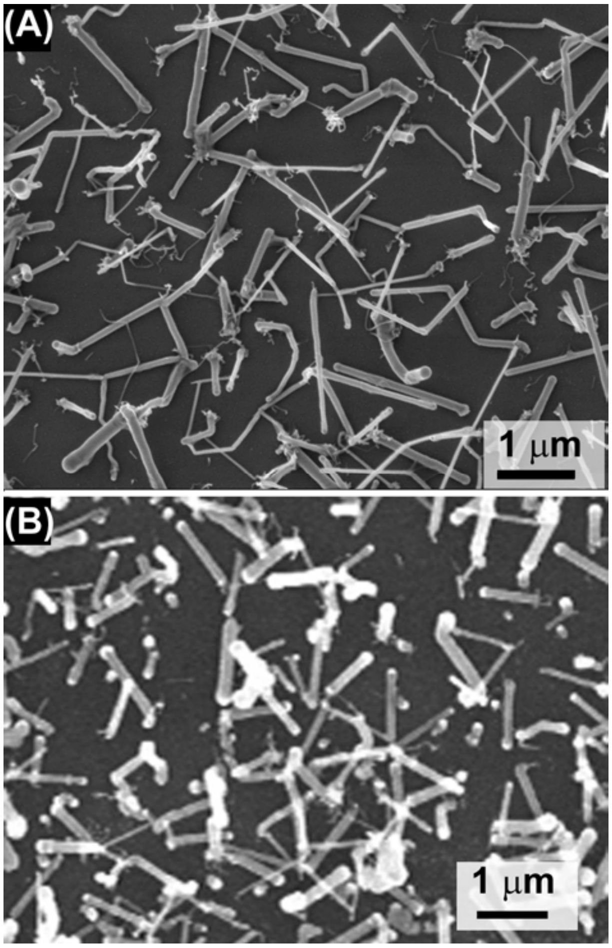

Figure 9.5: SEM image of Ge nanorods synthesized in supercritical fluid hexane from an injection solution composed of (A) 25% v/v octanol and (B) 50% v/v octanol in hexane. Both reactions were carried out at 450°C and 25MPa using TEG as a precursor.

9.4 OUTLOOK AND CONCLUSION

Ge nanorod formation was attempted via two general approaches. The *top-down* approach involved the destructive sonication of Ge nanowires via ultrasonication. This approach benefits from the existing knowledge base for Ge nanowires synthesis and provides a general route for the formation of Ge nanorods. However, current variations in the sonically induced fracture of the nanowires do not provide adequate control over the nanowire length. Furthermore, the ultrasonication appeared to incur significant damage to the nanowire surface passivation resulting in Ge nanorods with limited dispersibility in organic solvents.

The general feasibility of the *bottom-up* approach has been demonstrated in preliminary measurements. The combination of metal particle nucleated nanowire growth (see Chapter 2) with in-situ surface passivations (see Chapter 4) and the benefits of the highly tunable continuous flow reactor present broad opportunities for the synthesis of group IV semiconductor nanorods. The synthesis and processing of these materials is currently actively pursued by various members in the Korgel group.

9.5 REFERENCES

(1) Peng, X.; Manna, L.; Yang, W.; Wickham, J.; Scher, E.; Kadavanich, A.; Alivisatos, A. P. *Nature* **2000**, *404*, 59-61.

(2) Steiner, D.; Katz, D.; Millo, O.; Aharoni, A.; Kan, S.; Mokari, T.; Banin, U. *Nano Letters* **2004**, *4*, 1073-1077.

(3) Goldberger, J.; He, R.; Zhang, Y.; Lee, S.; Yan, H.; Choi, H.-J.; Yang, P. *Nature* **2003**, *422*, 599-602.

(4) Tesster, N.; Medvedev, V.; Kazes, M.; Kan, S.; Banin, U. *Science* **2002**, *295*, 1506-1508.

(5) Hu, J.; Li, L. S.; Yang, W.; Manna, L.; Wang, L. W.; Alivisatos, A. P. *Science* **2001**, *292*, 2060.

(6) Kan, S.; Aharoni, A.; Mokari, T.; Banin, U. *Faraday Discussions* **2003**, *125*, 23-38.

(7) Kan, S.; Mokari, T.; Rothenberg, E.; Banin, U. *Nature Materials* **2003**, *2*, 155-158.

(8) Zhu, Y.; Cheng, G. S.; Zhang, L. D. *Journal of Materials Science Letters* **1998**, *17*, 1897-1898.

(9) Xie, X.; Wan, Q.; Liu, W.; Men, C.; Lin, Q.; Lin, C. *Applied Surface Science* **2003**, *217*, 39-42.

(10) Wu, X.; Tao, Y. *Mater. Res. Bull.* **2002**, *37*, 2179-2183.

(11) *Sonics & Materials*; Ultrasonic Equipment for Sonochemistry: http://www.sonicsandmateials.com, 2004.

(12) Lu, X.; Ziegler, K. J.; Ghezelbash, A.; Johnston, K. P.; Korgel, B. A. *Nano Letters* **2004**, *4*, 969-974.

Chapter 10: Synthesis and Characterization of Mn doped Ge nanowires

10.1 INTRODUCTION

The coexistence of semiconducting behavior and spin in dilute magnetic semiconductors has attracted great interest for studying the fundamental origins of ferromagnetic order and due to their potential application in spin-dependent electronics. Control of the spin state in ferromagnetic semiconductors offers exiting technological possibilities enabling the operation of quantum bits required for quantum computing.[1] Technological applications leading to potential spintronic devices require materials that exhibit a Curie temperature (T_C) above room temperature and can be easily integrated with current semiconductor processing technology. The most promising route towards spin injection into nonmagnetic semiconductors is the preparation of dilute magnetic semiconductors through the introduction of magnetic ions such as Mn^{2+}, Cr^{2+} or Ni^{2+} into substitutional sites of the semiconductor matrix. Ferromagnetic semiconductors were first realized in III-V semiconductors like $In_{1-x}Mn_xAs$ or $Ga_{1-x}Mn_xAs$ with Mn concentrations (x) near 0.05 and Curie temperatures up to 110K.[2-5]

In 2001, Jonker and co-workers first reported attempts to prepare the dilute magnetic semiconductor Mn_xGe_{1-x} via molecular beam epitaxy (MBE).[6] Their initial synthesis products at growth temperatures near 300°C were characterized by ~100 nm sized of $Mn_{11}Ge_8$ clusters embedded in a ferromagnetic Mn_xGe_{1-x} , whose magnetic properties were dominated by the clusters. In more recent work, the same researchers have reported the formation of ferromagnetic

Mn_xGe_{1-x} with Curie temperatures ranging from 25 to 116K linearly proportional to the Mn concentration.[7] The formation of $Mn_{11}Ge_8$ nanoclusters was avoided by reducing the non-equilibrium MBE growth temperature 70°C. Furthermore, Jonker and co-workers illustrated the potential technological applications of Mn_xGe_{1-x} and demonstrated control of the ferromagnetic order in the Mn_xGe_{1-x} through the application of a ± 0.5 V gate voltage. Choi et al.[8] later reported an alternative fabrication route for Mn doped Ge via simple melting and recrystallization of Ge power in the presence of Mn impurities. Their work reported Mn concentrations as high as 6% and Curie temperature near 285K. The reported magnetic properties changed from paramagnetic to ferromagnetic to antiferromagnetic with a reduction in temperature from 400K to 5K. This appendix discusses recent results of the synthesis Mn_xGe_{1-x} nanowires as well as their elemental and magnetic characterization.

10.2 FABRICATION OF MN DOPED GE NANOWIRES

Ge nanowires were prepared via the SFLS methods as described in Chapter 2. Previous work in the Korgel group by Stowell et al.[9] has demonstrated the inclusion of Mn into InAs nanocrystals. Based on their work, initial experiments directed at the Mn doping of the Ge nanowires involved the addition of a manganese precursor to the injection or flow through solution containing diphenylgermane and Au seed nanocrystals. Various manganese precursors including $Mn(II)Cl_2$, Mn(II)acac, $[Mn(CO)_5]_2$ and $Cp^*{}_2Mn$[*] were explored. The

---

[*] Mn(II)acac = manganese acetylacetonate; $[Mn(CO)_5]_2$ = bis(pentacarbonylmanganese); $Cp^*{}_2Mn$ = bis(pentamethylcyclopentadienyl)manganese ;manganocene

co-injection of the Mn precursor however adversely influenced the SFLS nanowire synthesis resulting in the formation of large (~80-100nm), malformed nanowires with unusually high crystallographic defect densities suggesting that the presence of Mn during nanowire synthesis somehow poisoned the catalytic processes underlying nanowire growth. Recent *ab initio* density functional calculations by Singh el al.[10] have predicted that hexagonal Ge nanotubes could be stabilized by doping with Mn atoms, however to date no such structures have been observed in the reaction products.

Similar to the in-situ surface passivation experiments discussed in Chapter 4, Mn doping of Ge nanowires was pursued in an approach involving the introduction of the Mn dopant after the completion of the nanowire synthesis. All post-reaction doping experiments discussed below were performed with Cp^*_2Mn since this precursor had most favorable solubility characteristics and showed the least pronounced poisoning effects among the various manganese precursors explored above. In a typical experiment, Ge nanowires were prepared via continuous flow reactions at 390^{o}C and 7 MPa. The nanowire product was rinsed with supercritical hexane to clean the surface and remove byproducts while the reactor system was slowly cooled and depressurized to 110^{o}C and 1.5 MPa. The Mn precursor solution (Cp^*_2Mn in anhydrous hexane) was then injected in amount proportional to a Mn:Ge ratio of 5:95. Decomposition of Cp^*_2Mn and subsequent diffusion of Mn into Ge nanowires was allowed to proceed under these conditions (110^{o}C, 10MPa) for 2 h. The doping temperature was limited to 110^{o}C to avoid the formation of bulk phase materials such as Mn_3Ge or Mn_5Ge_3.[11]

The doped nanowire material was then removed from the reactor and cleaned by brief sonication in toluene, hexane, and isopropanol and centrifuged to remove soluble byproducts in the supernatant solution. These additional cleaning procedures were required since previous experiments showed unusual carbonaceous contamination on surfaces of Mn doped Ge nanowires cleaned by conventional supercritical hexane flushing. The Mn doped nanowires were stored in a N_2 glove box prior to characterization.

10.3 STRUCTURAL AND ELEMENTAL CHARACTERIZATION OF $\mathrm{MN_XGE_{1-X}}$ NANOWIRES

10.3.1 STEM-EDS Mapping

Structural and elemental characterization of the Mn doped Ge nanowires was performed with HRTEM and STEM-EDS.† Figure 10.1A shows a dark field STEM image of an isolated Mn_xGe_{1-x} nanowire. EDS linescans were performed for spatially resolved elemental analysis as shown in the right of Figure 10.1A and the spectra superimposed on the STEM image. The Ge linescan showed a symmetric profile with the maximum located at the nanowire axis. The O profile on the other hand showed two maxima located near the surface of the nanowire indicative of a core shell Ge/GeO_x structure. Due to the relatively low Mn concentration (x=0.02) in this Mn_xGe_{1-x} nanowire, the analysis of the Mn profile is limited by the low signal counts, although the profile in Figure 10.1A suggests Mn signal maxima near the nanowire surface. The oxidation, which presumably

---

† TEM sample preparation and microscope conditions were identical to those discussed in Chapter 5.

resulted from the extensive cleaning procedures, was also confirmed by HRTEM images such as the one shown in Figure 10.1B. Significantly, the HRTEM image of the nanowire surface confirmed the absence of $Mn_{11}Ge_8$ clusters as the ones observed by park et al.[6]

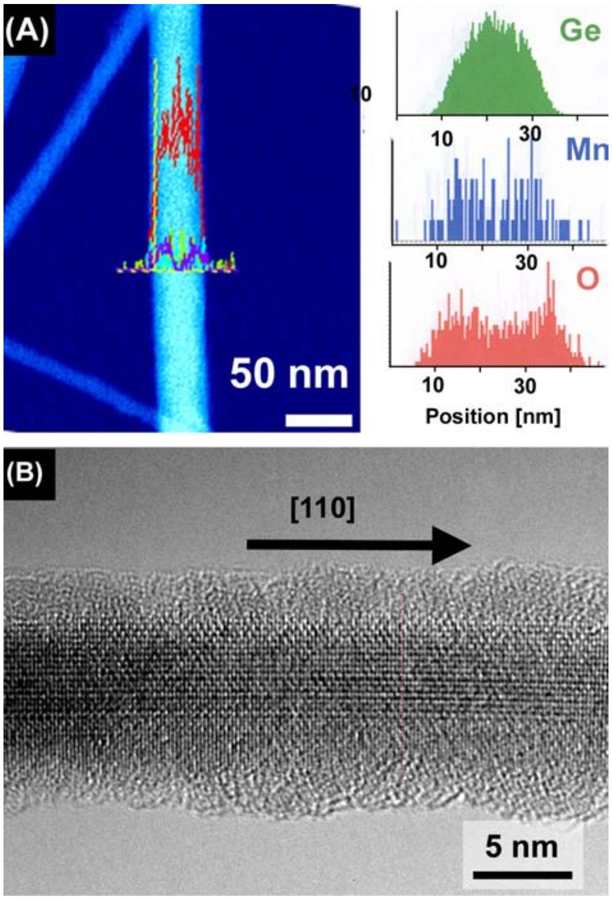

Figure 10.1: (A) Dark-field STEM image of Mn doped Ge nanowire and corresponding cross-diameter STEM-EDS linescan. The spectra on the right show the Ge, Mn and O profiles. (B) HRTEM image of a single crystal Ge nanowire from the same sample showing the thin surface oxide layer and [110] growth direction.

10.3.2 Diameter Dependent Mn concentration

Figure 10.2A shows an EDS spectrum acquired on the central axis of a 20 nm diameter Ge nanowire. The Cu and Si signals are artifacts due to the TEM support grid and the EDS detector, respectively. Elemental characterization of a large number of nanowires revealed that the Mn concentration was not constant, but instead varied as a function of nanowire diameter as shown in Figure 10.2B The diameter dependent Mn concentration in the sample prepared with a Mn:Ge ratio of 5:95 was found to vary from 1% to 5% and exhibited good agreement with the 1/d fit given by the dashed line. The 1/d proportionality suggests that the distribution of Mn dopants throughout the host crystal was limited by Mn diffusion from the surface to the core of the nanowire. In the Mn doping process described above, the Cp^*_2Mn precursors first underwent thermolytic degradation and then adsorbed onto the exposed clean Ge nanowire surfaces. Limiting diffusion of Mn into the Ge nanowire crystal host lattice would consequently result in a radially varying Mn concentration profile as suggested by the Mn profile in the EDS linescan in Figure 10.1A. These results illustrate the need for additional annealing experiments in order to minimize the radial Mn concentration profile. While the doping experiment at 110^oC appeared to provide sufficient thermal energy to effectively degrade the Cp^*_2Mn precursor, and additional annealing step at temperatures in the range of 150-250^oC should be able to reduce the radial variations in Mn concentration. Bulk phase cluster formation becomes a concern for higher annealing temperatures.[6]

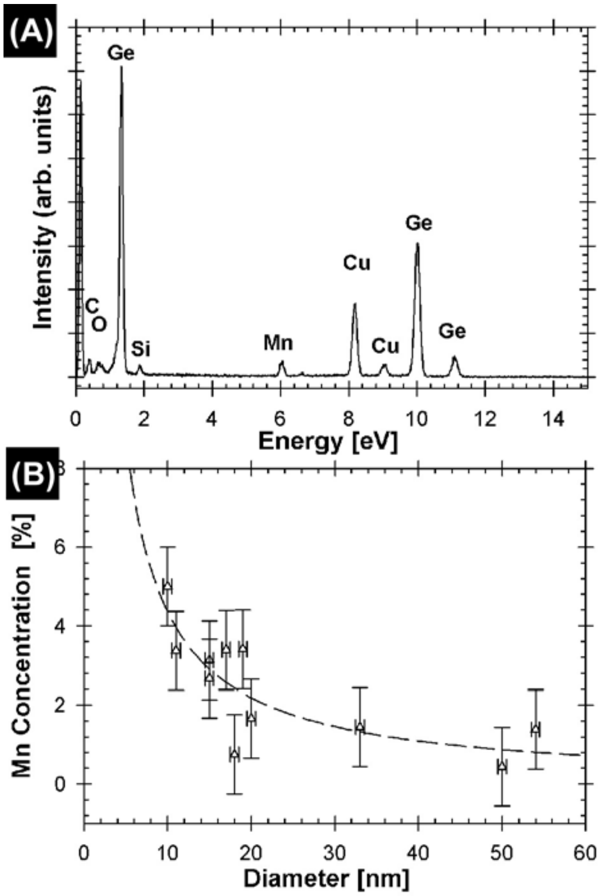

Figure 10.2: EDS analysis of Mn doped Ge nanowires. (A) EDS spectrum of a 20 diameter nanowire and (B) correlation between measured Mn concentration and diameter. The dashed line corresponds to a 1/d fit.

10.4 CHARACTERIZATION OF MAGNETIC PROPERTIES

10.4.1 Temperature-Dependent Magnetization

Temperature-dependent magnetization measurements of the Mn doped and undoped Ge nanowires were performed using a superconducting quantum interference device magnetometer (SQUID, Quantum Design).‡ Ensemble Ge nanowire samples were transferred in to a gelatin capsule (Lilly#4) and packed with cotton to minimize sample movement. Due to the relatively small sample size (~5mg) the background to the weakly diamagnetic gel capsule had to be subtracted.

The temperature dependence of the magnetization of a sample prepared with Mn:Ge ratio 5:95 was measured by cooling the sample from 300 to 4K in a 1000Oe field (see Figure 10.3) The data were fitted to the Curie-Weiss law (see inset) which showed significant deviation at low temperature. Similar deviation has been observed in $Ga_{1-x}Mn_xAs$[12] and Mn_xGe_{1-x} films[7] and was attributed to the presence of multiple exchange interactions. Significantly, the Curie-Weiss fit to the temperature dependence shows that Θ is negative, which suggested ferrimagnetic rather than ferromagnetic ordering in Mn_xGe_{1-x} nanowires. The origin of this magnetic response is not yet understood but may be the results of finite volume effects on the long range and short range magnetic interactions between Mn dopants in the Ge host lattice. In fact, magnetic property calculations by Zhao et al.[13] and Park et al.[7] have shown that the Mn-Mn coupling is strongly antiferromagnetic for nearest neighbor interactions and follows

---

‡ The author gratefully acknowledges Cynthia A. Stowell and Doh C. Lee for helpful discussions and assistance with SQUID measurements.

Ruderman-Kittel-Kasuya-Yosida (RKKY)[§] analytical formula for larger Mn-Mn distances. The magnetic interactions in low-dimensional structures are likely to exhibit significant differences from the interactions in bulk materials with similar compositions; the fundamental origin of the ferrimagnetism observed in the Mn_xGe_{1-x} nanowires studied in this work, could therefore result from either an enhanced antiferromagnetic interaction or a reduced ferromagnetic interaction between the Mn ions in the Ge nanowire lattice.

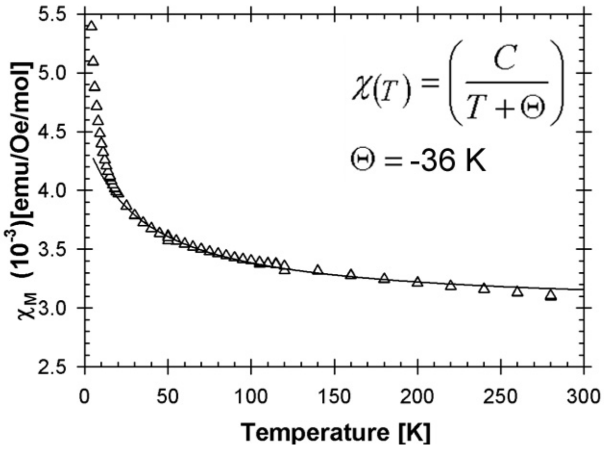

Figure 10.3: Temperature dependence of the magnetization for a Mn doped Ge nanowire sample prepared with Mn:Ge 5:95. Applied field = 1000 Oe. The solid lid shows the Curie Weiss fit for high temperatures with the fitting equation and fitting parameter shown in the inset.

10.4.2 Field-Dependent Magnetization

Figure 10.4 shows magnetization loops of the same sample as in Figure 10.3 measured at 50K, 180K, and 250K. The magnetization loops acquired at

---

[§] The RKKY ferromagnetism describes the oscillations in magnetic ion interactions as a function of the distance between them.

180K and 250K exhibited saturation magnetization of approximately 0.07 emu/g, whereas the field dependent measurement at 50K revealed incomplete saturation magnetization at fields as high at 10000 Oe. These saturation values correspond to a net magnetization of 0.16 Bohr magnetons (μ_B) per Mn atom, or to a magnetically active fraction of 5.5% if every Mn dopant atom has the full theoretical moment of $3\mu_B$. A closer inspection of the magnetization loops revealed hysteresis behavior with coercivity fields of 130 Oe and 70 Oe at 50K and 250K, respectively. The ferrimagnetic Mn_xGe_{1-x} nanowires thus exhibits a coercive field strength and net magnetization per Mn atom approximately an order of magnitude lower than the values reported for bulk ferromagnetic Mn_xGe_{1-x} by Park et al.[7] It is also important to note that the sample still exhibited hysteresis effects at temperatures as high as 250K. This discrepancy with results from bulk phase Mn_xGe_{1-x} could result from surface effects, finite size effects, or different long range and short range Mn-Mn interactions as discussed above. These aspects are currently under intense investigation in the Korgel group and require further experimental and theoretical investigation.

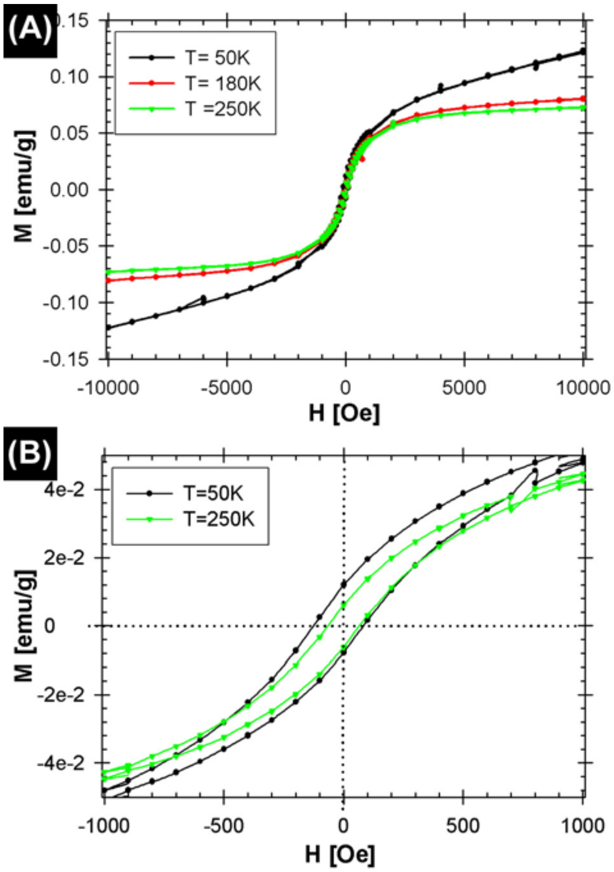

Figure 10.4: Magnetization loops: (A) full field range magnetization loops showing saturation magnetization at 180 and 250K , and (B) hysteresis loop showing remanence magnetization at 80K and 250K.

10.4 OUTLOOK AND CONCLUSIONS

Although certainly not optimized, the synthesis results presented above illustrate a solid foundation for future work on the preparation of Mn doped semiconductor nanostructures. Specifically, annealing processes need to be investigated to address the issue of radial Mn concentration variations indicated by STEM-EDS. The availability of high quality Ge, Si and GaAs nanowires in the Korgel group presents a fertile platform for further Mn doping experiments toward the fabrication of novel dilute magnetic semiconductors nanowires. In context of the results discussed in Chapters 7 and 9, these materials have immense potential for future spin-dependent nanoelectronic devices.

In addition to the improvements and expansions in the synthetic methods, these Mn_xGe_{1-x} nanowires also require significant additional characterization. For example, complimentary electron spin resonance experiments[14] could provide essential information about the coordination of Mn dopants within the Ge lattice and about magnetic behavior or undoped Ge nanowires.[15] In addition to these ensemble measurements, temperature dependent electron transport measurements on individual Mn_xGe_{1-x} nanowire devices in the presence of an external magnetic field would provide invaluable information about the potential application of these materials as building block in nanoscale spintronics. Additionally, transmission electron holography experiments could provide powerful information about the magnetic domain ordering in isolated and ensemble Mn doped Ge nanowires.[16]

10.5 REFERENCES

(1) DiVincenzo, D. P. *Science* **1995**, *270*, 255-261.

(2) Munekata, H.; Ohno, H.; Molnar, S. v.; Segmüller, A.; L. L. Chang; Esaki, L. *Phys. Rev. Lett.* **1989**, *63*, 1849-1852.

(3) Ohno, H. *Science* **1996**, *281*, 951-956.

(4) Ohno, H.; Shen, A.; Matsukura, F.; Oiwa, A.; Endo, A.; Katsumoto, S.; Iye, Y. *Appl. Phys. Lett.* **1996**, *69*, 363-365.

(5) De Boeck, J.; Oesterholt, R.; Esch, A. V.; Bender, H.; Bruynseraede, C.; Hoof, C. V.; Borghs, G. *Appl. Phys. Lett.* **1996**, *68*, 2744-2746.

(6) Park, Y. D.; Wilson, A.; Hanbicki, A. T.; Mattson, J. E.; Ambrose, T.; Spanos, G.; Jonker, B. T. *Appl. Phys. Lett.* **2001**, *78*, 2739-2741.

(7) Park, Y. D.; Hanbicki, A. T.; Erwin, S. C.; Hellberg, C. S.; Sullivan, J. M.; Mattson, J. E.; Ambrose, T. F.; Wilson, A.; Spanos, G.; Jonker, B. T. *Science* **2002**, *295*, 651-654.

(8) Cho, S.; Choi, S.; Hong, S. C.; Kim, Y.; Ketterson, J. B.; Kim, B.-J.; Kim, Y. C.; Jung, J.-H. *Phys. Rev. B.* **2002**, *66*, 033303/033301-033303/033303.

(9) Stowell, C. A.; Wiacek, R. J.; Saunders, A. E.; Korgel, B. A. *Nano Letters* **2003**, *3*, 1441-1447.

(10) Singh, A. K.; Kumar, V.; Kawazoe, Y. *Physical Review B: Condensed Matter and Materials Physics* **2004**, *69*, 233406/233401-233406/233404.

(11) Massalski, T. B.; Murray J.L., B. L. H., Baker H., Ed.; American Society for Metals: Metals Park ,Ohio, 1986.

(12) Van Esch, A.; Bockstal, L. V.; Boeck, J. D.; Verbanck, G.; van Steenbergen, A. S.; Wellmann, P. J.; Grietens, B.; Bogaerts, R.; Herlach, F.; Borghs, G. *Phys. Rev. B* **1996**, *56*, 13103-13112.

(13) Zhao, Y.-J.; Shishidou, T.; Freeman, A. J. *Phys. Rev. Lett.* **2003**, *60*, 047204.

(14) Glaeser, H. J.; Geist, D. *Helvetica Physica Acta* **1968**, *41*, 840-843.

(15) Baumer, A.; Stutzmann, M.; Brandt, M. S.; Au, F. C. K.; Lee, S. T. *Applied Physics Letters* **2004**, *85*, 943-945.

(16) Allard, L. F.; Voelkl, E.; Kalakkad, D. S.; Datye, A. K. *Journal of Materials Science* **1994**, *29*, 5612-5614.

Chapter 11: Conclusions and Future Directions

11.1 CONCLUSIONS

Semiconductor nanowires have been and will likely continue to be one of the most intensely researched nanomaterials. Due to their unique electrical, optical and mechanical properties, they have been proposed as candidates for a broad range of technological applications but also serve as an ideal experimental platform for the study of fundamental quantum mechanical concepts. The first step toward the successful application of these nanowires in future devices is the availability of effective and tunable synthesis methods that enable control over the composition, size, dimensionality, and interface properties. In the past five years, various nanowire synthesis routes have been reported which can be divided into three general categories, (1) CVD based systems, (2) oxide assisted growth, and (3) solution based synthesis. While the high-vacuum CVD-based approaches provide a good system for the study of fundamental nanowire growth factors, the low throughput of these systems poses a principal limitation toward their technological applications. Although the solution-based synthesis methods may be considered ‘dirtier’ than the high-vacuum processes they are equally capable of producing high quality defect free nanowires with controlled surface chemistry and have the significant advantage of being scaleable toward the fabrication of technologically significant quantities of nanowires. The underlying objective of the research presented in this dissertation was therefore the development of effective and controllable nanowire synthesis methods and processes that enable their processing and application in future nanowire-based technologies.

11.1.1 Nanowire Synthesis

The supercritical fluid technologies developed in the early years of collaborative efforts between the Korgel and Johnston groups have provided a solid foundation for further development towards supercritical solution syntheses of various semiconductor materials. In 2000, Holmes et al. first demonstrated the feasibility of growing Si nanowire in the presence of sterically stabilized Au seed nanocrystals in supercritical fluid. The extension of this approach toward the preparation of other semiconductor materials such as Ge or GaAs was the logical next step. Although the preliminary work on the supercritical fluid-liquid-solid (SFLS) by Holmes et al. had identified suitable Si nanowire synthesis conditions, little was known about the effects of fundamental growth parameters such as temperature, pressure, precursor concentration or precursor chemistry.

First step was therefore the identification of a suitable parameter window for the SFLS synthesis of Ge nanowires and the subsequent optimization towards the synthesis of high quality, crystalline nanowires. This work (described in Chapter 2) identified the optimum temperature range for Ge nanowire synthesis in supercritical hexane between 350°C and 400°C, while varying the pressure between 13.8 MPa and 38 MPa did not affect the gross wire morphology. Interestingly, nanowire formation –albeit of poorer quality - was also observed at growth temperatures below the eutectic point of the bulk material (360°C), possibly due to reduced eutectic temperature in nanostructures or the possibility of a solid nucleation particle. The comparison of diphenylgermane (DPG) and tetraethylgermane (TEG) as organogermane precursors showed the quality of Ge nanowires formed from DPG to be superior to those obtained from TEG due to the faster decomposition of the former. This comparison illustrated the importance of the precursor decomposition rate to the morphology of the synthesized nanowires. Initial syntheses showed that aggregated sea urchin nanowire structures formed at low TEG concentrations (5mM), while dense nanowire networks observed in experiments involving the injection of higher concentrations (100-200mM) for both TEG and DPG.

Initial injection-based syntheses revealed that agglomeration of Au nanocrystals or the Au:Ge droplets during the initial stages of the reactions posed significant limitation to the diameter control of the Ge nanowires. A modification to the reactors to enable the continuous flow SFLS synthesis significantly reduced the diameter distribution and at the same time profoundly improved the quality and quantity of the synthesized nanowires. Since the presence of Au in the ensemble Ge nanowire samples is unfavorable toward their integration into current semiconductor processing technologies, alternative metal seed particles including Ag, Al, Mn, and Ni were explored. None of the alternative seed metals were able to match the efficiency of Au as a seed metal either due to unfavorable metal:Ge eutectic phases or to the lack of catalytic properties.

The extension of optimized Ge nanowire synthesis parameters toward the preparation of Si nanowires (see Chapter 3) with similar yield and quality proved considerably more difficult than initially expected. The Si nanowire yield was substantially lower than the yield for Ge nanowires under comparative conditions.

These differences were attributed to the large difference in Ge-Ge and Si-Si bond energies since the Au:Si and Au:Ge eutectic phase diagrams and decomposition rates for the phenyl substituted Si and Ge precursors are similar. The survey of various organosilane precursors illustrated that nanowires could only be formed within a much smaller parameter window compared to Ge nanowires and in most cases, the Si nanowire synthesis products were characterized by high proportions of malformed nanowires or amorphous nanofibers.

More recently, the synthesis capabilities of the supercritical fluid reactor were extended to include the preparation of Ge nanorods (see Chapter 9) Nanorods, which are one-dimensional nanostructures with aspect ratios much smaller than nanowires, have received extensive research interest primarily due to their unique size- and dimensionality-tunable optical properties. The available synthesis methods for Ge and Si nanowires discussed in Chapters 2 and 3 served as a useful starting point toward the preparation of group IV semiconductor nanorods. Initial attempts focused on the top-down destructive sonication of long aspect ratio nanowires. While this approach successfully provided nanorods with average lengths as short as 500 nm, it lacked the desired control and tenability. By combining the SFLS growth method with fundamental aspects from arrested precipitation due to surface bound molecules, the feasibility and initial results of a bottom-up supercritical fluid synthesis of Ge nanorods were demonstrated.

An important aspect of the supercritical fluid reactor discussed in Chapter 2 is its flexibility and adaptability to post-synthesis processes. While Chapter 4 discussed the how surface chemistry modifications were integrated into the reactor system, more recent experiments have demonstrated the reactors adaptability to chemical processes that allowed modification of the chemical composition of the nanowires. In particular, Chapter 10 discussed promising recent experimental results of post-synthesis Mn doping of Ge nanowires. Mn_xGe_{1-x} nanowires with x ranging from 0.01 to 0.06 were prepared and local variations in dopant concentration were probed with STEM-EDS. Temperature- and field-dependent magnetic properties were investigated with superconducting quantum interference device magnetometry. The temperature dependence and remnant magnetization indicated ferrimagnetic behavior, which are currently under still under intense investigation due to the promising technological applications of combined magnetic and semiconducting properties in single crystal nanowires.

11.1.2 Chemical Surface Passivation

Like all nanomaterials, nanowires are characterized by a very high surface-to-volume atomic ratio. The electrical and optical properties are therefore highly sensitive to the chemical surface termination. Furthermore, early work on the processing of Ge nanowires toward electrical devices illustrated the significance of a detailed understanding and control of the Ge nanowire surface chemistry in light of Ge’s infamously electrically and chemically defective oxide termination. The implementation of Ge nanowires as building blocks in device structures consequently required enhanced dispersibility in a variety of solvents as well a chemical passivation layer to protect and control the sensitive nanowire surface. A comprehensive study of Ge nanowire surface chemistry and methods toward the passivation of the surfaces were presented in Chapter 4.

Unpassivated Ge nanowires were readily oxidized to form a suboxide, consisting mostly of Ge^{1+} and some Ge^{2+} species when exposed to air, and mostly Ge^{3+} and Ge^{1+} when immersed in water. Extended exposure to aqueous environments eventually resulted in the complete corrosion of the nanowires toward water soluble $Ge(OH)_4$. HF or HCl acid etching of the nanowires resulted in H- and Cl- terminated surfaces, respectively, with sharp and clean interfaces. However, the etched surfaces were very sensitive to subsequent oxidation, making the use of these species for subsequent surface reactions or device applications difficult. Attempts to passivate the nanowire surface through the formation of a sulfide layer via treatment with $(NH_4)_2S$ did not yield robust well-characterized surface layers since S appeared to penetrate into the Ge nanowire to form a thick GeS_x layer. The formation of a covalent Ge-S bond, via the thiol passivation on HF etched nanowires led to incomplete monolayer coverage, whereas the direct post-synthesis thiol treatment in the reactor formed a well-defined monolayer terminated surface.

The most effective surface treatment used in combination with the SFLS nanowire synthesis was found to be the thermally initiated hydrogermylation approach. Alkenes, alkynes, and dienes were identified as suitable precursors for the formation of covalently bonded organic monolayers rendering abrupt and clean nanowire interfaces. Significantly, the surface passivated nanowires were chemically robust and stable, even when immersed in water. The results presented in Chapter 4 therefore illustrated that rigorous control over organic monolayer chemistry on semiconductor nanowires will be a key requirement for future applications of these materials.

11.1.3 Structural and Crystallographic Characterization

High-resolution transmission electron microscopy (HRTEM) was arguably the most vital tool for the structural characterization of Ge and Si nanowires. Chapter 5 presented essential nanowire properties such as such as growth direction, faceting on the axial and radial surfaces, cross-sectioning, the structure at the Au-Ge interface and crystallographic defects. The Ge nanowires investigated in this work predominantly exhibited the <110> growth direction with isolated occurrences of <211> and <111> oriented nanowires. Fundamental aspects of the VLS growth mechanism were explored in context of the energy minimization of the initial Ge nucleus and the stability of the Au-Ge interface and related to the preferred crystallographic axis occurring under various kinetic and thermodynamic growth conditions.

Cross-sectional imaging revealed that the <110> oriented nanowires are characterized by a hexagonal cross-section low energy {111} and {100} facets, whereas nanowires with the <211> growth axis exhibited rectangular cross-sections with {111} and {110} surface facets. Forbidden reflections observed in electron diffraction patterns were attributed to surface structures with fractional units cells terminating the {111} facets.

In addition to the comprehensive crystallographic characterization, Chapter 5 also discussed recent mechanical property characterization performed with a nanomanipulator. The nanowires exhibited remarkable flexural strength while maintaining their single crystal structure. Intentional fracture of Ge nanowires embedded in a polymer resin demonstrated the {110} facet orthogonal to the long axis of the nanowire as the preferred fracture facet. Additionally, attempts to obtain hexagonal Ge structures via recrystallization under the electron beam were discussed. The intense electron beam irradiation resulted in the amorphization and subsequent recrystallization of the nanowires; however, the unambiguous identification of the hexagonal structure was not possible.

11.1.4 Electron Energy Losses in Ge Nanowires

In addition to the invaluable structural information provided by high-resolution imaging, the combination of scanning transmission electron microscopy and energy loss spectroscopy (STEM-ELS) also provided information about fundamental electronic and optical properties correlated to microscopic details like crystallinity and surface chemistry. Chapter 6 provided accurate measurements of the size-dependent volume plasmon energy, which were decoupled from effects of strain and surface. The volume plasmon energy was found to increase by ~0.8 eV as the diameter decreased from ~25 nm to ~8 nm. In addition to the plasmon spectra, Ge 3d photoemission spectra revealed that at diameters less than ~25 nm, the Ge 3d ionization edge shifted to higher energy with significant changes in the peak fine structure. Complimentary information from Ge 2p core loss spectra would have permitted a complete analysis of the quantum confinement induced changes in the density of states of the conduction band. Unfortunately, the high-energy loss Ge 2p ionization energies were overwhelmed by unfavorably low signal-to-noise ratio.

Complimentary to the surface state dependent electron transport measurements discussed in Chapter 7, the Ge 3d ionization edges presented in chapter 6 were very sensitive to surface chemistry, and oxidized nanowires with poor electrical passivation exhibited up to a ~0.3 eV shift in edge inflection point when the probe was positioned near the surface.

11.1.5 Electron Transport Properties

In addition to the spectroscopic approach discussed above, the electronic properties of isolated Ge nanowires were also probed in measurements of single nanowire field effect devices. The main goal of the device measurements was to elucidate the effects of the nanowire surface chemistry on the electrical characteristics the devices, but first several important device fabrication aspects had to be investigated. In that context, Chapter 7 compared the transport properties of individual Ge nanowires with Au/Cr contacts fabricated using electron-beam lithography methods and Pt contacts deposited by direct-write EA-CVD or IA-CVD methods. In spite of the low-resistance Au electrodes used in EBL-fabrication method, these devices exhibited non-linear Schottky diode behavior and unacceptably high contact resistances. The process reliability was also poor, with a 60% failure rate due to the poor stability of the Au/Ge nanowire contact. In contrast, devices prepared with Pt EA-CVD and IA-CVD exhibited lower contact resistances and could be fabricated with nearly 100% success rate within a timeframe of only a few hours. The IA-CVD devices exhibited the lowest contact resistance for Ge nanowires with untreated surfaces, in the range of 1~10MΩ. In fact, pre-annealed Ge nanowire devices with EA-CVD Pt metal contacts exhibited GΩ contact resistance with nonlinear IV behavior. Annealing the EA-CVD contacts lowered the contact resistance to the range of tens of MΩ. The most effective metal/nanowire electrical contacts were made by EA-CVD Pt deposition on organic monolayer-passivated Ge nanowires, which exhibited reasonably low contact resistance of ~0.8MΩ without the need for thermal annealing. FEB deposited Pt source/drain electrodes on nanowires with organic monolayer surface treatment offered the lowest contact resistance and least amount of nanowire damage in comparison to FIB and EBL.

Field-effect transport measurements conducted in a N_2 environment showed that the intrinsic nanowires exhibit p-type field effect due to an inversion layer formed at the negatively charged nanowire surface. Electron transport through the intrinsic nanowires appeared to be dominated by surface states. The charged nanowire surface was also manifested in the hysteresis observed in gate voltage measurements. Untreated nanowires with an oxide termination exhibited more pronounced hysteresis than nanowires with a hexyl monolayer surface termination. Tunneling currents across a nanowire cross-junction was demonstrated without the need for a high temperature anneal in a device fabricated from isoprene passivated Ge nanowires. Transient behavior observed in field effect measurements were ascribed to the presence of slow surface states on the nanowire surfaces. The density, relative position within the Ge band gap, and the characteristic relaxation times were highly sensitive to the nanowire surface chemistry. Field-effect polarization in oxidized nanowire surfaces occurred over the course of hundred of seconds, whereas monolayer passivated surface exhibited much longer recombination times on the order of 10^4 s. Finally, relaxation time distributions of nanowires with different surface passivation were probed with sinusoidal applied gate voltage measurements.

11.1.6 Nanowire Processing

The device fabrication and electron transport aspects discussed in Chapter 7 provided valuable information about the characteristics of Ge nanowire electrical devices; however, the successful implementation of semiconducting nanowires into large-scale device configurations requires the controlled and precise deposition and alignment of isolated as well as ensemble nanowires. This aspect has long been considered a limiting factor for the broad technological utilization of nanowires and nanotubes and has consequently been under intense research by many groups. Chapter 8 discussed efforts undertaken in the Korgel group toward the controlled and aligned deposition of nanowires onto device substrates. While nanowire alignment in flow fields and on chemically functionalized substrates showed moderate success, the electric field assisted nanowire assembly showed broadest applicability for technological purposes. This approach enabled the same large-scale alignment capability as the Langmuir-

Blodgett film technique, while at the same time providing greater flexibility in the local multidirectional alignment of isolated nanowires.

In addition to isolated nanowire deposits for electronic device applications, Chapter 8 also discussed how the morphology of ensemble Ge nanowire deposits was shaped by multiple factors including the temperature, solubility and mobility in the suspension solvent. Nanowires with chemically passivated surfaces exhibited significantly enhanced solubility and permitted the ensemble samples to undergo phase change into thermodynamically favored nematic-like phases. Unpassivated nanowires on the other had precipitated from the suspension forming randomly oriented agglomerates.

11.2 FUTURE DIRECTIONS

Several aspects of nanowire research discussed in this dissertation offer exciting opportunities for further study. The current SFLS synthesis may be optimized for Au nucleated Ge nanowires, however, the further exploration of alternative seed metals, or processes for the removal of the Au seed crystal at the tip of the nanowires are warranted in context of the incompatibility of Au metal with many current semiconductor processes. The proof of principle nanorod synthesis experiments presented in Chapter 8 illustrated promising opportunities for the future work on group IV nanorods. Better control and tunability of the nanorod dimensions should be explored through a systematic investigation of synthesis parameters growth controlling ligand molecules.

Beyond the synthesis, further modifications to the reactor system to expand the surface passivation or doping processes should be considered. For example, the attachment of bifunctional ligands to the nanowire surface could render a surface termination that provides stability and solubility in aqueous environments, two aspects that are particularly important for the potential application of the nanowires interfaced with biological systems. Furthermore, the surface modifications could be expanded to include the nanowire surface attachment of nanocrystals through covalent bonds or van der Waals forces.

The enhanced nanowire solubility owing to the monolayer passivation has led to the observation of nanowire liquid crystal-like phases, as discussed in Chapter 8. The orientation of observed nematic phase domains appeared to have been determined by the direction of the retreating vapor-liquid interface. Since isolated Ge nanowires aligned in response to an external electric field (see Chapter 8), it should consequently also be possible to influence the alignment of ensemble nanowires. The control over the orientation of the birefringent domains would be a significant step towards nanowire based liquid crystal applications. In addition to the alignment of nematic phases, the improvement of the electric field assisted alignment of individual nanowires deserves further study. The electric field assisted alignment should for example be possible in or on top of thin polymer films providing exciting new opportunities in the fabrication of polymer/nanowire composite flexible electronics. Electronic applications of the nanowires will require improved conductivities, toward that end the introduction of extrinsic carriers is required and is currently still under investigation.

The cross sectional HRTEM study presented in Chapter 5 has illustrated hexagonal or rectangular cross sections for <110> and <211> oriented nanowires, respectively. Nevertheless, the shape of the cross section in relation to the diameter of the nanowire remains an open question that might provide important information toward a better understanding of the factors determining the preferred crystallographic growth orientation. Chapter 5 also discussed preliminary mechanical property measurements conducted in a collaborative effort with Zyvex. Considering the single crystal character of these nanowires, the qualitatively observed mechanical properties are simply amazing and certainly deserve additional study. The Zyvex nanomanipulator system is currently undergoing upgrades to include force-feedback on individual probes, which should eventually permit quantitative mechanical study with corresponding electron transport measurements as a function of stress or strain in the nanowire.

The prospect of combined magnetic and semiconducting properties in single crystal nanowires is very interesting from a fundamental and a technological perspective. The Mn_xGe_{1-x} nanowire fabrication methods discussed in Chapter 10 required significant improvement, specifically in the form of variable temperature annealing studies to minimize the radial Mn concentration profile. Additional SQUID and electron spin resonance experiments would also provide vital information toward the fundamental aspects of the observed magnetic ordering in context of the Mn-Mn interactions and their coordination within the Ge nanowire host lattice. In addition to these fundamental aspects, temperature dependent magnetoresistance are suggested to evaluate potential technological applications of these materials. Finally, the Mn_xGe_{1-x} nanowires would also serve as an exciting experimental platform for transmission electron holography experiments which could identify magnetic domain ordering in isolated or ensemble Mn_xGe_{1-x} nanowires

Appendices

Appendix A: Temperature profile in the continuous flow supercritical fluid reactor

A.1 INTRODUCTION

The continuous flow reactors described in Chapter 2 provides a solid technological platform for the scale-up synthesis of technologically significant quantities of semiconductor nanowires. The batch and injection reactors used in early experiment have the potential disadvantage of local variations in precursors concentration and temperature in the early critical phases of the reaction, which made the reaction product sensitive to minor changes in the injection approach. The flow through reactors was designed to avoid the concentration variations and provide a means for the more consistent and controllable supercritical fluid synthesis of semiconductor nanowires. Furthermore, the continuous flow configuration enabled the investigation of the average reagent residence time inside the reactors as an additional tunable synthesis parameter unavailable to batch and injection methods.

The theoretical analysis of the hydro- and thermodynamic conditions prevailing during the continuous flow synthesis was performed determine the extent of temperature variations along the length of the reactor and to identify suitable parameters for the scale up from the initial 1 ml to a 10 ml reactor cell.

A.2 THEORETICAL MODEL

Variations in the temperature of the reaction solution flowing through the reactor cell were modeled based on fundamental hydro-and thermodynamic concepts.

A.2.1 Physical Model of the 1 ml and 10 ml reactor

The rector configuration of the 1 ml reactor cell was modeled by a 3 cm long section of 0.076 cm i.d. tubing connected to a 5 cm long reactor cell with 0.5 cm i.d. The configuration of the heating block enclosing the reactor cell (see Figure 2.2B) also encloses a segment of tubing leading into the reactor. This inlet tube can therefore be considered as a de facto preheater since the temperature of the inlet tubing connected to the reactor is near the same temperature as the Ti reactor cell itself. The heater configuration for the larger 10 ml reactor cell differs from the one shown in Figure 2.2B, in that the tubing leading to the reactor is not enclosed in the heater block and therefore not preheated. Consequently, the 10 ml reactor could be modeled by a single reactor cell with length and inner diameter of 11 and 1.2 cm, respectively.

A.2.2 Physical Properties of Supercritical Fluid and Basis Conditions

The thermophysical properties, such as density, viscosity, and enthalpy of n-hexane for specific temperatures[**] and pressures were obtained from the NIST chemistry webbook.[1] The properties of the reaction solution were based on hexane alone and the small contributions of diphenylgermane (<1 %v/v) and Au

---

[**] Thermophysical properties up to 600K were available from the NIST webbook. Values in the temperature range of 600 to 673K were obtained by extrapolation.

nanocrystals were neglected. Typical flow-through synthesis conditions with a set point temperature of 380°C a pressure of 7 MPa, and a flow rate of 0.2 ml/min (defined as the liquid flowrate entering the reactor system) were chosen as the basis conditions.

A.2.3 Hydrodynamic Factors

First, the hydrodynamics of the fluid flowing through the reactor were characterized by the Reynolds' number

$$\mathrm{Re} = \frac{\rho D v}{\mu} \tag{1}$$

where ρ, D, υ, and μ are the fluid density, conduit diameter, flow velocity, and viscosity, respectively. For a typical flow-through reaction with a target residence time (τ) near 80 sec this corresponded to fully developed laminar flow (2<Re<29) in the 1 ml cell and developing laminar flow (10<Re<120) in the 10 ml cell. Hydrodynamic conditions were further compared based on the ratio of hydrodynamic entry length to reactor cell length:

$$\left(\frac{x_H}{L}\right) = \left(\frac{D \cdot 0.05\,\mathrm{Re}}{L}\right) \tag{2}$$

An initial comparison of hydrodynamic entry lengths ratios in the 1 ml and 10 ml reactor cells were calculated as 0.075 and 0.27, respectively, indicate significant differences for reactions conducted under similar residence time distributions.

A.2.4 Energy Balance

The heat transfer from the reactor block to the flowing fluid was modeled on the basis of a constant reactor cell temperature assumption. This assumption is supported by a comparison of 'thermal masses' of the ~1 kg brass heating block equipped with two 300 W heating cartridges and small to moderate amounts of hexane (0.1 to 2 g/min) flowing through the block. The temperature of the fluid flowing through the reactor block was obtained from an iterative solution to the energy balance given in equation (3).

For a constant wall temperature assumption, the heat transfer from the reactor block to the fluid is given by:

$$\begin{aligned} q &= \bar{h}\,\pi D(\Delta x)\left[T_s - \frac{T_{x1}+T_{x2}}{2}\right] \\ &= \dot{m}\bar{c}_p(T_{x2}-T_{x1}) \\ &= \dot{m}(H_{x1}-H_{x2}) \end{aligned} \tag{3}$$

where

q = heat transfer from the reactor wall to the fluid [W]

$\Delta x = x_2 - x_1$ = the differences between two positions (x_2) and (x_1) along the length of the reactor cell [cm]

T_s = reactor wall temperature

T_{xi} = temperature of the fluid at position (x_i) along the length of the reactor

$\dot{m}$ = mass flow rate of hexane flowing through the reactor [g/min]

$\bar{c}_p$ = average heat capacity of the fluid, and [J/g/K]

H_{xi} = the fluid enthalpy at position (x_i) along the length of the reactor [J/g]

$\bar{h}$ = the average heat transfer coefficient [W/cm^2/K] given by:

$$\bar{h} = \frac{kNu}{D} \tag{4}$$

with

k = the thermal conductivity of the fluid [W/cm/K]

Nu = Nusselt number, calculated from the appropriate empirical correlation for the prevailing hydrodynamic conditions[2,3]

$$Nu = 0.036\,\mathrm{Re}^{0.8}\,\mathrm{Pr}^{0.33}\left(\frac{D}{L}\right)^{0.055} \tag{5}$$

where

$\mathrm{Pr} = \frac{c_p \mu}{k}$ = Prandtl number

The heat transferred to the fluid flowing through the reactor was calculated from the enthalpy data rather than the product of heat capacity and temperature change since the former easily incorporated the energy changes associated with the liquid-supercritical phase transition.

A.3 RESULTS AND DISCUSSION

The temperature profile for hexane flowing through the reactor cell under the basis conditions (τ =80 sec, $\dot{m}$ = 0.13 g/min, T_{wall}= 390°C, P= 7 MPa) are shown in Figure A.1. The figure illustrates the fundamental differences in the calculated temperature profiles for the 1 ml and 10 ml reactor cell. The temperature profile for the fluid flowing through the 1 ml cell shows that the fluid reaches thermal equilibrium after a few millimeter flowing through the reactor.

The calculated profile including the preheating effects of the inlet tubing[††] show a more rapid equilibration with the reactor wall temperature than the theoretical profile obtained without consideration of the preheating effects. Significantly, the temperature profile for fluid flowing through the 10 ml reactor with an average residence time of 80 sec never reached thermal equilibrium with the wall temperature.

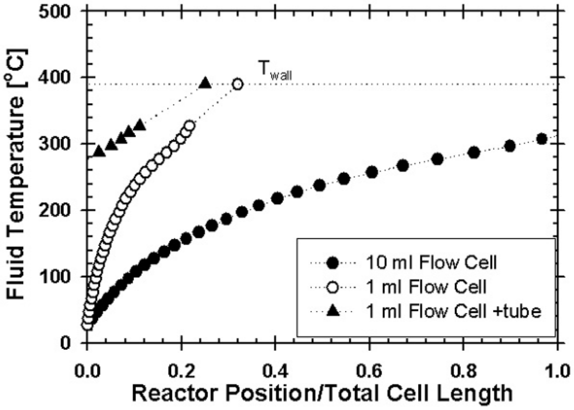

Figure A.1: Temperature profile of hexane flowing through the supercritical fluid reactor with an average residence time of 80 sec. The reactor pressure and wall temperature were 7 MPa and 390°C, respectively.

These theoretical models are in reasonable agreement with preliminary flow-through reactions involving the 10 ml reactor cell. The basis conditions listed above correspond to optimal conditions for the continuous flow synthesis in the 1 ml reactor cell and provide high-quality Ge nanowires with narrow diameter distributions (see Chapter 2). The reaction products under the same conditions in

---

[††] The average temperature of the inlet tubing was based on a conservative estimate of 280°C.

the 10 ml reactor cell on the other hand are reminiscent of malformed Ge nanowires formed at low temperatures (320-350^{o}C) in injection experiments.

A.4 CONCLUSIONS

These theoretical and preliminary experimental results underline the importance of proper considerations for both thermodynamic and hydrodynamic factors in the scale up of the continuous flow supercritical fluid reactor system. Specifically, continues flow reactions with 10 ml reactor cell necessitate the use of a preheater to for the reaction fluid to obtain thermal equilibrium inside the reactor. Furthermore, the theoretical model provides useful insight into the opportunities and limitations of using the reactor for short residence time (~1-10 sec) experiments as are currently under exploration for the supercritical fluid synthesis of semiconductor nanorods.

A.5 REFERENCES

(1) Lemmon, E. W.; McLinden, M. O.; Friend, D. G. *NIST Chemistry WebBook, NIST Standard Reference Database Number 69* **2003**, http://webbook.nist.gov.

(2) Bird, R. B.; Stewart, W. T.; Lightfoot, E. N. *Transport Phenomena*; John Wiley & Sons: New York, 1960.

(3) Holman, J. P. *Heat Transfer*; 8th ed.; McGraw-Hilll: New York, 1997.

Appendix B: Kinetics of nanowire growth

B.1: THE GIBBS-THOMPSON EFFECT

Kinetic studies of crystal growth are usually characterized by a supersaturation or chemical potential difference as the driving force behind the crystallization. Early studies on VLS growth of Si whiskers have demonstrated a direct correlation between the axial growth rate and the whisker diameter and a critical diameter below which whiskers could not be formed.[1] The Gibbs-Thompson effect describes how surface energy terms relate a decrease in alloy droplet diameter to a decrease in Si or Ge effective supersaturation and an increase in solubility. The decrease in effective chemical potential differences at a curves interfaces is given by:

$$\frac{\Delta\mu}{k_B T} = \frac{\Delta\mu_o}{k_B T} - \left(\frac{4\Omega\gamma_{SF-L}}{k_B T}\right)\left(\frac{1}{d}\right) \qquad (1)$$

where $\Delta\mu$ is the effective chemical potential difference between the nutrient phase (degraded Ge in the supercritical fluid) and the liquid alloy droplet, $\Delta\mu_0$ is the same chemical potential difference at a plane interface without surface effects, γ_{SF-L} is the surface energy of the liquid alloy / supercritical fluid interface and Ω is the composite atomic volume of the alloy liquid.

The whisker or nanowire growth rate (V) is related to the effective supersaturation to the nth power through:

$$V = b\left(\frac{\Delta\mu}{k_B T}\right)^n \qquad (2)$$

where b,k_B, and T are an experimentally determined coefficient, the Boltzmann constant and reaction temperature, respectively. Substitution of the Gibbs-Thompson expression (1) then yields

$$V^{\frac{1}{n}} = b^{\frac{1}{n}}\left(\frac{\Delta\mu_o}{k_B T}\right) - b^{\frac{1}{n}}\left(\frac{4\Omega\gamma_{SF-l}}{k_B T}\right)\left(\frac{1}{d}\right) \tag{3}$$

Experimental data for the growth of whiskers,[1] Si/Ge heterostructure nanowires[2] and Si nanowires[3] have validated the linear dependence of V^{-n} and d^{-1} with n=2. In addition to the crystal growth kinetics, equation (3) also predicts a critical alloy diameter below which the VLS growth becomes thermodynamically unfeasible. Setting V=0, the critical diameter is given by

$$d_c = \left(\frac{4\Omega\gamma_{SF-L}}{\Delta\mu_o}\right) \tag{4}$$

The Gibbs-Thompson effect therefore places a lower limit on the nanowire diameter that can be grown under a given set of conditions. This effect also explains how liquid alloy droplets below a certain diameter are unable to nucleate wire growth until they agglomerate and form a single seed with a diameter exceeding the critical size required for nanowire nucleation and growth. (see Chapter 2).

B.2 REFERENCES

(1) Givargizov, E. I. *Journal of Crystal Growth* **1975**, *31*, 20-30.

(2) Wu, Y.; Fan, R.; Yang, P. *Nano Letters* **2002**, *2*, 83-86.

(3) Westwater, J.; Gosain, D. P.; Tomiya, S.; Usui, S.; Ruda, H. *J. Vac. Sci. Tech. B* **1997**, *15*, 554.

Appendix C: Quantum confinement of an electron in cylindrical geometry

C.1 INTRODUCTION

The electron energy loss spectroscopy (EELS) data discussed in Chapter 6 showed a diameter dependent shift in the Ge 3d ionization edge for nanowires with a diameters less than the Bohr exciton diameter for Ge (24 nm). The observed shift was ascribed to a blue shift in the in the conduction band states due to quantum confinement. This appendix discusses the solution to an electron confined to a cylindrical geometry and calculates the kinetic energy of electrons in the conduction band based on a solution to the Schrödinger equation.

C.2 THEORETICAL MODEL

In an effective mass model for the motion of a condition electron in a crystal, the wave function may be represented as a product of crystal Bloch waves with an envelope function ψ.[1] This function is then a solution to the Schrödinger equation with the well known form:

$$\hat{H}\psi(\rho,\theta,z) = E\psi(\rho,\theta,z) \tag{1}$$

Where $\hat{H}$ is the Hamiltonian operator, which for the case of cylindrical coordinates (ρ,θ,z) becomes

$$\begin{aligned}&\left[-\frac{\hbar^2}{2m^*}\left(\frac{\partial^2}{\partial\rho^2}+\frac{1}{\rho}\frac{\partial}{\partial\rho}+\frac{1}{\rho^2}\frac{\partial}{\partial\theta^2}+\frac{\partial}{\partial z^2}\right)+V(\rho,\theta,z)\right]\psi(\rho,\theta,z)\\&=E\psi(\rho,\theta,z)\end{aligned} \tag{2}$$

Since the nanowire is not confined in the axial (z) directions, one can propose a solution with radial and angular components of the form[2]:

$$\psi(\rho,\theta) = R(\rho)A(\theta) = e^{in_A\theta}R(\rho) \tag{3}$$

where n_A is the angular momentum quantum number with values of n_A=0,±1, ±2, … as required by circular geometry. The actual hexagonal or rectangular cross section of the nanowire for <110> and <211> growth direction, respectively, is now simplified by the assumption of a circular cross section. A more detailed theoretical model using the tight-binding method for the electron energy states in Si nanowires with hexagonal cross section was recently reported by Kobayahi.[3] While the results of that work are very intriguing and reported the existence of localized states near the edge of the nanowire, it is beyond the scope of this appendix.

Substitution of (3) into (2) and separation of variables leads to.

$$-\frac{\hbar^2}{2m^*}\left(\frac{\rho^2}{R(\rho)}\right)\left(\frac{d^2R(\rho)}{d\rho^2}+\frac{1}{\rho}\frac{dR(\rho)}{d\rho}\right) = E - V(\rho,\theta) - \frac{\hbar^2 n_A^2}{2m^*} = \mathrm{C} \tag{4}$$

, where C is a separation constant.

To solve the radial part of the above equation the boundary conditions are set with the simplification that the potential is infinite outside the cylinder (with radius r) and zero inside the cylinder. Then,

$$\begin{aligned} V(\rho<r) &= 0 \\ V(\rho=r) &= \infty \end{aligned} \tag{5}$$

and

$$R_{(\rho<r)} = \text{finite} \qquad R_{(\rho=r)} = 0 \tag{6}$$

With these boundary conditions equation (4) becomes

$$\frac{d^2R_{(\rho)}}{d\rho^2} + \frac{1}{\rho}\frac{dR_{(\rho)}}{d\rho} + \left(\frac{2m^*}{\hbar^2}E - n_A^2\right)\frac{1}{\rho^2}R_{(\rho)} = 0 \tag{7}$$

The solutions to this differential equation are in the form of Bessel functions J_n and Y_n with M and N as arbitrary constants.

$$R_{(\rho)} = MJ_n\left(\left(\frac{2m^*}{\hbar^2}E\right)^{\frac{1}{2}}\rho\right) + NY_n\left(\left(\frac{2m^*}{\hbar^2}E\right)^{\frac{1}{2}}\rho\right) \tag{8}$$

Y_n diverges at the nanowire center ($\rho \rightarrow 0$) which is physically impossible based on the first boundary condition in (6), so N=0, and (8) reduces to

$$R_{(\rho)} = MJ_n\left(\left(\frac{2m^*}{\hbar^2}E\right)^{\frac{1}{2}}\rho\right) \tag{9}$$

Invoking the second boundary condition in (6) requires that

$$R_{(\rho=r)} = 0 = MJ_n\left(\left(\frac{2m^*}{\hbar^2}E\right)^{\frac{1}{2}}r\right) = MJ_n\left(S_{nm}\right) \tag{10}$$

The mth zeros of this nth order Bessel function (S_{nm}) are listed in standard mathematical handbooks[4] and the energy is given by

$$E = \frac{\hbar^2}{2m^*}\left(\frac{S_{nm}}{r}\right)^2 \tag{11}$$

Equation (3) therefore predicts the conduction band energy shift resulting from radial electron confinement to scale with the inverse square of the nanowire diameter.

C.3 REFERENCES

(1) Ashcroft, N. W.; Mermin, N. D. *Solid State Physics*; Saunders College Publishing: Fort Worth, 1976.

(2) Proetto, C. R. *Phys. Rev. B* **1992**, *45*, 11911-11917.

(3) Kobayashi, K. *Phys. Rev. B* **2004**, *69*, 115338-118345.

(4) Greenberg, M. D. *Advanced Engineering Mathematics*; 2nd ed.; Prentice Hall: New Jersey, 1998.

Bibliography

Alivisatos, A. P., "Semiconductor clusters, nanocrystals, and quantum dots", *Science* **1996**, *271*, 933-937.

Amjoud, M., Reynes, A., Morancho, R. and Carles, R., "Comparative study of decomposition by metal-organic chemical vapor deposition of tetraethylsilane and tetravinylsilane", *Journal of Materials Chemistry* **1992**, *2*, 1205-1208.

Anderson, G. W., Hanf, M. C., Norton, P. R., Lu, Z. H. and Graham, M. J., "The S- passivation of Ge(100)(1x1)", *Appl. Phys. Lett.* **1995**, *66*, 1123-1125.

Ashcroft, N. W. and Mermin, N. D. *Solid State Physics*; Saunders College Publishing: Fort Worth, **1976**.

Bahr, J. L. Y., J.; Kosynkin, D. V.; Bronikowski, M. J.; Smalley, R. E.; Tour, J. M.;, "Functionalization of Carbon Nanotubes by Electrochemical Reduction of Aryl Diazonium Salts: A Bucky Paper Electrode", *J. Am. Chem. Soc.* **2001**, *123*, 6536-6542.

Bansal, A., Li, X., Lauermann, I., Lewis, N. S., Yi., S. I. and Weinberg, W. H., "Alkylation of Si sirfaces using a two-step halogenation/ Grignard Route", *J. Am. Chem. Soc.* **1996**, *118*, 7225.

Batson, P. E., "Damping of bulk plasmons in small aluminum spheres", *Solid State Commun.* **1980**, *34*, 477-480.

Batson, P. E., "High-energy resolution electron spectrometer for 1-nm spatial analysis." *Rev. of Sci. Instr.* **1986**, *57*, 43-48.

Batson, P. E., "Silicon L 2,3 near-edge fine structure in confined volumes", *Ultramicroscopy* **1993**, *50*, 1.

Batson, P. E. and Heath, J. R., "Electron energy loss spectroscopy of single nanocrystals: The conduction band." *Phys. Rev. Lett.* **1993**, *71*, 911-914.

Baumer, A., Stutzmann, M., Brandt, M. S., Au, F. C. K. and Lee, S. T., "Paramagnetic defects of silicon nanowires", *Applied Physics Letters* **2004**, *85*, 943-945.

Bermudez, V. M., "Study of the initial formation of silicon carbide by reaction of tetraethylsilane with silicon", *Journal of Applied Physics* **1992**, *71*, 5450-5459.

Bird, R. B., Stewart, W. T. and Lightfoot, E. N. *Transport Phenomena*; John Wiley & Sons: New York, **1960**.

Bodlaki, D., Yamamoto, H., Waldeck, D. H. and Borguet, E., "Ambient stability of chemically passivated germanium interfaces", *Surface Science* **2003**, *543*, 63-74.

Bostedt, C. Electronic Structure of germanium Nanocrystal Films probed with Synchrotron Radiation. Hamburg, University of Hamburg.(2002)

Brenner, S. S., "The Growth of Whiskers by the Reduction of Metal Salts", *Acta Metal.* **1956**, *4*, 62-63.

Brust, M., Walker, M., Bethell, D., Schiffrin, D. J. and Whyman, R., "Synthesis of thiol-derivatized gold nanoparticles in a two-phase liquid-liquid system", *Journal of the Chemical Society, Chemical Communications* **1994**, 801-802.

Buhro, W. E. and Colvin, V. L., "Shape Matters", *Nature Materials* **2003**, *2*, 138-139.

Burghard, M., Duesberg, G., Philipp, G., Muster, J. and Roth, S., "Controlled adsorption of carbon nanotubed on chemically modified electrode arrays", *Adv. Mater.* **1998**, *10*, 584-589.

Carter, J. L., "VLS (Vapor-Liquid-Solid): Newly Discovered Growth Mechanism on the Lunar Surface?" *Science* **1973**, *181*, 841-842.

Chakrapani, N., Wei, B., Carrillo, A., Ajayan Pulickel, M. and Kane Ravi, S., "Capillarity-driven assembly of two-dimensional cellular carbon nanotube foams", *Proc. Nat. Acad. of Sciences* **2004**, *101*, 4009-4012.

Chen, C. C., Yeh, C. C., Chen, C. H., Yu, M. Y., Liu, H. L., Wu, J. J., Chen, K. H., Chen, L. C., Peng, J. Y. and Chen, Y. F., "Catalytic growth and characterization of gallium nitride nanowires", *J.Am.Chem.Soc.* **2001**, *123*, 2791.

Chen, J., Hamon, M. A., Hu, H., Chen, Y., Rao, A. M., Eklund, P. C. and Haddon, R. C., "Solution Properties of Single-walled carbon nanotubes", *Science* **1998**, *282*, 95-98.

Cho, S., Choi, S., Hong, S. C., Kim, Y., Ketterson, J. B., Kim, B.-J., Kim, Y. C. and Jung, J.-H., "Ferromagnetism in Mn-doped Ge." *Phys. Rev. B.* **2002**, *66*, 033303/033301-033303/033303.

Choi, K. and Buriak, J. M., "Hydrogermylation of alkenes and alkynes on hydride terminated Ge(100) surfaces", *Langmuir* **2000**, *16*, 7737-7741.

Chung, S.-W., J-Y., Y. and Heath, J. R., "Silicon nanowire devices", *Appl. Phys. Lett.* **2000**, *76*, 2068.

Cicero, R. L., Linford, M. R. and Chidsey, C. E. D., "Photoreactivity of Unsaturated Compounds with Hydrogen-Terminated Silicon(111)", *Langmuir* **2000**, *16*, 5688-5695.

Clark, K. B. and Griller, D., "The Ge-H Bond Dissociation Energies oor Organogermanes. A Laser-Induced Photoacoustic Study." *Organometallics* **1991**, *10*, 746-750.

Coleman, N. R., O'Sullivan, N., Ryan, K. M., Crowley, T. A., Morris, M. A., Spalding, T. R., Steytler, D. C. and Holmes, J. D., "Synthesis and characterization of dimensionally ordered semiconductor nanowires within mesoporous silica", *Journal of the American Chemical Society* **2001**, *123*, 7010-7016.

Coleman, N. R. B., Morris, M. A., Spalding, T. R. and Holmes, J. D., "The formation of dimensionally ordered silicon nanowires within mesoporous silica", *J. Am. Chem. Soc.* **2001**, *123*, 187.

Coutant, R. W. and Levy, A. A kinetic study of the thermal decomposition of selected cyclohexyl and phenylsilanes, Aerospace Research Laboratories United States Air Force. **ARL 69-0213**.(1969)

Cronin, S. B., Lin, Y.-L., Rabin, O., Black, M. R., Ying, J. Y., Dresselhaus, M. S., Gai, P. L., Minet, J.-P. and Issi, J.-P., "making electrical contacts to nanowires with a thick oxide coating", *Nanotechnology* **2002**, *13*, 653-658.

Cui, Y., Lauhon, J., Gudiksen, M. S., Wang, J. and Lieber, C. M., "Diameter-controlled synthesis of single-crystal silicon nanowires", *Appl. Phys. Lett.* **2001**, *78*, 2214.

Cui, Y., Lauhon, L. J., Gudiksen, M. S., Wang, J. and Lieber, C. M., "Diameter-controlled synthesis of single-crystal silicon nanowires", *Applied Physics Letters* **2001**, *78*, 2214-2216.

Cui, Y. and Lieber, C. M., "Functional nanoscale electronic devices assembled using silicon nanowire building blocks", *Science* **2001**, *291*, 851-853.

Cui, Y., Wei, Q., Park, H. and Lieber, C. M., "Nanowire nanosensors for highly sensitive and selective detection of biological and chemical species", *Science* **2001**, *293*, 1289-1292.

Cullen, G. W., Amick, J. A. and Gerlich, D. J., "The stabilization of Germanium Surfaces by Ethylation", *J. Electrochem. Soc.* **1962**, *109*, 124-138.

Dahlhaus, J., Jutzi, P., Frenck, H.-J. and Kulisch, W., "Pentamethylcyclopentadienyl-substituted silanes $(Me_5C_4)SiH_3$ and $(Me_5C_4)_2SiH_2$ as precursors for low-temperature remote plasma-enhanced CVD of thin silicon nitride and silica films." *Adv. Mater.* **1993**, *5*, 377-380.

Davidson III, F. M., Schricker, A. D., Wiacek, R. J. and Korgel, B. A., "Supercritical fluid-liquid-solid synthesis of gallium arsenide nanowires seeded by alkanethiol-stabilized gold nanocrystals", *Advanced Materials* **2004**, *16*, 646-649.

De Boeck, J., Oesterholt, R., Esch, A. V., Bender, H., Bruynseraede, C., Hoof, C. V. and Borghs, G., "Nanometer-scale magnetic MnAs particles in GaAs grown by molecular beam epitaxy", *Appl. Phys. Lett.* **1996**, *68*, 2744-2746.

Dean, J. A., Ed. (1999). Lange's Handbook of Chemistry. New York, McGraw-Hill.

Delerue, C., Lannoo, M. and Allan, G., "Calculations of the electron energy loss spectra of silicon nanostructures and porous silicon", *Phys. Rev. B* **1997**, *56*, 15306-15313.

Ding, Y. and Wang, Z. L., "Structure Analysis of Nanowires and Nanobelts by Transmission Electron Microscopy", *J. Phys. Chem. B* **2004**, *108*, 12280-12291.

Dinger, R., "Carrier mobilities in surface inversion layers on high purity germanium", *Thin Solid Films* **1977**, *43*, 311-318.

DiVincenzo, D. P., "Quantum Computation", *Science* **1995**, *270*, 255-261.

Dixon, D. J. and Johnston, K. P. (1997). Supercritical Fluids. Encyclopedia of Separation. D. M. Ruthven. New York, John Wiley**:** 1544-1569.

Doty, R. C., Bonnecaze Roger, T. and Korgel Brian, A., "Kinetic bottleneck to the self-organization of bidisperse hard disk monolayers formed by random sequential adsorption", *Physical review. E, Statistical* **2002**, *65*, 061503.

Duan, X., Huang, Y., Agarwal, R. and Lieber, C. M., "Single-nanowire electrically driven lasers", *Nature* **2003**, *421*, 241-245.

Duan, X., Huang, Y., Cui, Y., Wang, J. and Lieber, C. M., "Indium phosphide nanowires as building blocks for nanoscale electronic and optoelectronic devices", *Nature* **2001**, *409*, 66-69.

Duan, X., Huang, Y. and Lieber, C. M., "Nonvolatile memory and programmable logic from molecule-gates nanowires", *Nanoletters* **2002**, *2*, 487-490.

Duan, X. and Lieber, C. M., "Laser-assisted catalytic growth of single crystal GaN nanowires", *J. Am. Chem. Soc.* **2000**, *122*, 188-192.

Echenique, P. M., Ritchie, R. H. and Brandt, W., "Spatial excitation patterns induced by swift ions in condensed matter", *Phys. Rev. B.* **1979**, *20*, 2567-2580.

Egerton, R. F. *Electron Energy-Loss Spectroscopy in Electron Microscope*; 2nd ed.; Plenum Press: New York, **1996**.

Erker, L. *Treatise on Ores and Assaying*; 2nd ed.; University of Chicago, **1951**.

Finkelman, R. B., Larson, R. R. and Dwornik, E. J., "Naturally Occuring Vapor-Liquid_Solid (VLS) Whisker Growth of Germanium Sulfide", *Journal of Crystal Growth* **1974**, *22*, 159-160.

García de Abajo, F. J. and Echenique, P. M., "Wake-potential formation in a thin foil", *Phys. Rev. B* **1992**, *45*, 8771-8774.

Geddes, R. L. and Edward Mack, J., "The Thermal Decomposition of Gaseous Germanium Tetraethyl", *J. Am. Chem. Soc.* **1930**, *52*, 4372-4380.

Georgakilas, V., Kordatos, K., Prato, M., Guldi, D. M., Holzinger, M. and Hirsch, A., "Organic Functionalization of Carbon Nanotubes", *J. Am. Chem. Soc.* **2002**, *124*, 760.

Givargizov, E. I., "Fundamental Aspects of VLS Growth", *Journal of Crystal Growth* **1975**, *31*, 20-30.

Glaeser, H. J. and Geist, D., "Electron paramagnetic resonance of manganese in germanium and effect of thermal treatment on the state of the incorporated manganese", *Helvetica Physica Acta* **1968**, *41*, 840-843.

Greenberg, M. D. *Advanced Engineering Mathematics*; 2nd ed.; Prentice Hall: New Jersey, **1998**.

Gregory, O. J., Pruitt, L. A., Crisman, E. E., Roberts, C. and Stiles, P. J., "Native Oxides formed on single-crystal germanium by wet chemical reactions", *J. Electrochem. Soc.* **1988**, *135*, 923-929.

Greytak, A. B., Lauhon, L. J., Gudiksen, M. S. and Lieber, C. M., "Growth and transport properties of complementary germanium nanowire field-effect transistors", *Applied Physics Letters* **2004**, *84*, 4176-4178.

Gu, G., Burghard, M., Kim, G. T., Duesberg, G. S., Chiu, P. W., Krstic, V. and Han, W. Q., "Growth and electical properties of germanium nanowires", *J. Appl. Phys.* **2001**, *90*, 5747-5750.

Gudiksen, M. S., Lauhon, U. J., Wang, J., Smith, D. C. and Lieber, C. M., "Growth of nanowire superlattice structures for nanoscale photonics and electronics", *Nature* **2002**, *415*, 617-620.

Hahm, J.-i. and Lieber, C. M., "Direct ultrasensitive electrical detection of DNA and DNA sequence variations using nanowire nanosensors", *Nano Letters* **2004**, *4*, 51-54.

Han, S. M., Ashurst, R., Carraro, C. and Maboudian, R., "Formation of alkanethiol monolayer on Ge(111)", *J. Am. Chem. Soc.* **2001**, *123*, 2422-2425.

Hanrath, T. and Korgel, B. A., "Nucleation and growth of germanium nanowires seeded by organic monolayer coated gold nanoparticles", *J. Am. Chem. Soc.* **2002**, *124*, 1424-1429.

Hanrath, T. and Korgel, B. A., "Supercritical fluid-liquid-solid (SFLS) synthesis of Si and Ge nanowires seeded by colloidal metal nanocrystals", *Advanced Materials* **2003**, *15*, 437-440.

Hanrath, T., Lu, X., Johnston, K. P. and Korgel, B. A. Growth of Single Crystal Nanowires. USA, Provisional Appl. 60/485,244.(2004)

He, J., Lu, Z. H., Mitchell, S. A. and Wayner, D. D. M., "Self-assembly of alkyl monolayers on Ge (111)", *J. Am. Chem. Soc.* **1998**, *120*, 2660-2661.

Heath, J. R. and LeGoues, F. K., "A Liquid Solution Synthesis of Single Crystal Germanium Quantum Wires", *Chem. Phys. Lett.* **1993**, *208*, 263-266.

Hinz, H. J., "The influence of crystal orientation on the volumen plasmon of germanium", *Zeitschift fuer Physik* **1980**, *38*, 111.

Hinz, H. J. and Raether, H., "Lineshape of the volume plasmons of silicon and germanium", *Thin Solid Films* **1979**, *58*, 281-284.

Holman, J. P. *Heat Transfer*; 8th ed.; McGraw-Hilll: New York, **1997**.

Holmes, J. D., Johnston, K. P., Doty, R. C. and Korgel, B. A., "Control of thickness and orientation of solution-grown silicon nanowires", *Science* **2000**, *287*, 1471-1473.

Holmes, J. D., Lyons, D. M. and Ziegler, K. J., "Supercritical Fluid Synthesis of Metal and Semiconductor Nanomaterials", *Chem. Eur. J.* **2003**, *9*, 2144-2156.

Holzinger, M., Vostrowsky, O., Hirsch, A., Hennrich, F., Kappes, M., Weiss, R. and Jellen, F., "Sidewall Functionalization of Carbon Nanotubes", *Angew. Chem. Int. Ed.* **2001**, *40*, 4002-4005.

Hu, J., Odom, T. W. and Lieber, C. M., "Chemistry and Physics in one dimension: synthesis and properties of nanowires and nanotubes", *Acc. Chem. Res.* **1999**, *32*, 435-445.

Huang, M. H., Wu, Y., Feick, H., Tran, N., Weber, E. and Yang, P., "Catalytic growth of zinc oxide nanowires by vapor transport", *Advanced Materials* **2001**, *13*, 113-116.

Huang, Y., Duan, X., Cui, Y., Lauhon, L. J., Kim, K. H. and Lieber, C. M., "Logic Gates and Computation from Assembled Nanowire building blocks", *Science* **2001**, *294*, 1313-1317.

Huang, Y., Duan, X., Wei, Q. and Lieber, C. M., "Directed assembly of one-dimensional nanostructures into functional networks", *Science* **2001**, *291,* 630-633.

Huang, Y., Duan, X., Wei, Q. and Lieber, C. M., "One-dimensional nanostructures into functional networks", *Science* **2001**, *291*, 630-633.

Jana, N. R., Gearheart, L. A., Obare, S. O., Johnson, C. J., Edler, K. J., Mann, S. and Murphy, C. J., "Liquid crystalline assemblies of ordered gold nanorods", *J. Mater. Chem* **2002**, *12*, 2909-2912.

Jin, S., Whang, D., McAlpine, M. C., Friedman, R. S., Wu, Y. and Lieber, C. M., "Scaleable interconnection in aintegration of nanowiure devices without registration", *NanoLetters* **2004**, *4*, 915-919.

Johnson, C. E., "Characterization of magnetic materials by Mössbauer spectroscopy", *Journal of Physics D: Applied Physics* **1996**, *29*, 2266-2274.

Johnson, E. R. and Amick, J. A., "Formation of single crystal silicon fibers", *J. Appl. Phys.* **1954**, *25*, 1204-1208.

Johnson, J. C., Yan, H., Schaller, R. D., Haber, L. H., Saykally, R. J. and Yang, P., "Single Nanowire Lasers", *J. Phys. Chem. B.* **2001**, *105*, 11387-11390.

Johnson, J. R. T. and Panas, I., "Structure, bonding and formation of molecular germanium oxides, hydroxides and oxyhydroxides." *Chem. Phys.* **1999**, *249*, 273-278.

Kamins, T. I., Li, X., Williams, R. S. and Liu, X., "Growth and structure of chemically vapor deposited Ge nanowires on Si substrates", *Nano Letters* **2004**, *4*, 503-506.

Kamins, T. I., Williams, R. S., Basile, D. P., T., H. and Harris, J. S., "Ti-catalyzed Si nanowires by chemical vapor deposition: microscopy and growth mechanisms", *J. Appl. Phys.* **2001**, *89*, 1008.

Kamins, T. I., Williams, R. S., Chen, Y., Chang, Y. L. and Chang, Y. A., "Chemical vapor deposition of Si nanowires nucleated by TiS2 islands on Si", *Appl. Phys. Lett.* **2000**, *76*, 562-566.

Kim, F., Kwan, S., Akana, J. and Yang, P., "Langmuir-Blodgett nanorod assembly", *Journal of the American Chemical Society* **2001**, *123*, 4360-4361.

Kingston, R. H., "Water-vapor-induced n-type surface conductivity on p-type germanium", *Phys. Rev.* **1955**, *98*, 1766-1775.

Kingston, R. H., "Review of germanium surface phenomena", *J. Appl. Phys.* **1956**, *27*, 101-114.

Kingston, R. H. and McWhorter, A. L., "Relaxation time of Surface States on Germanium", *Phys. Rev.* **1956**, *103*, 534-540.

Klipp, A., Petri, S. H. A., Hammelmann, F., Jutzi, P. and Heinzmann, U. *Organosilicon Chemistry - From Molecules to Materials*; Wiley-VCH: Weinheim, Germany, **2000**.

Kobayashi, K., "Surface-state conduction in medium sized nanowires", *Phys. Rev. B* **2004**, *69*, 115338-118345.

Koc, S., "New Interpretation of Slow Surface Relaxations on Germanium", *Phys. Stat. Sol.* **1962**, *2*, 1304-1311.

Kolmakov, A., Zhang, Y., Cheng, G. and Moskovits, M., "Detection of CO and O2 using tin oxide nanowire sensors", *Adv. Mater.* **2003**, *15*, 997-1000.

Korgel, B. A. and Fitzmaurice, D., "Condensation of Ordered Nanocrystal Thin Films", *Physical Review Letters* **1998**, *80*, 3531-3534.

Kosuri, M. R., Cone, R., Li, Q. and Han, S. M., "Adsorption kinetics of 1-alkanethiols on hydrogenated Ge(111)", *Langmuir* **2003**, *20*, 835-840.

Kuykendall, T., Pauzauskie, P., Lee, S., Zhang, Y., Goldberger, J. and Yang, P., "Metalorganic Chemical Vapor Deposition Route to GaN Nanowires with Triangular Cross Sections", *Nano Letters* **2003**, *3*, 1063-1066.

Lee, S. W., Nelen, L. N., Ihm, H., Scoggins, T. and Greenlief, C. M., "Reaction of 1,3-cyclohexadiene with the Ge(100) surface", *Surface Science* **1998**, *410*, L773-778.

Lemmon, E. W., McLinden, M. O. and Friend, D. G., "Thermophysical Properties of Fluid Systems", *NIST Chemistry WebBook, NIST Standard Reference Database Number 69* **2003**, http://webbook.nist.gov.

Levy, A., Coutant, R. W., Merryman, E. L. and Trent, D. E. The thermal stability of some arylsilanes, Aerospace Research Laboratory United States Airforce.(1965)

Li, C. P., Lee, C. S., Ma, X. L., Wang, N., Zhang, R. Q. and Lee, S. T., "Growth direction and cross sectional area study of Si nanowires", *Adv. Mater.* **2003**, *15*, 607-609.

Li, L.-S. and Alivisatos, A. P., "Semiconductor Nanorod liquid crystals and their assembly on a substrate", *Adv. Mater.* **2003**, *15*, 408-411.

Li, L.-s., Marjanska, M., Park, G. H. J., Pines, A. and Alivisatos, A. P., "Isotropic-liquid crystalline phase diagram of a CdSe nanorod solution", *J. Chem. Phys.* **2004**, *120*, 1149-1152.

Li, L. S., Walda, J., Manna, L. and Alivisatos, A. P., "Semiconductor nanorod liquid crystals", *Nanoletters* **2002**, *2*, 557-560.

Li, W. Z., Xie, S. S., Qian, L. X., Chang, B. H., Zou, B. S., Zhou, W. Y., Zhao, R. A. and Wang, G., "Large-Scale Synthesis of Aligned Carbon Nanotubes", *Science* **1996**, *274*, 1701-1703.

Linde, D. R., Ed. (2000). CRC Handbook of Chemistry and Physics. Boca Raton, Fl, CRC Press.

Linford, M. R. and Chidsey;, C. E. D., "Alkyl monolayers covalently bonded to silicon surfaces", *J. Am. Chem. Soc.* **1993**, *115*, 12631-12632.

Liu, J., Casavant, J., Cox, M., Walters, D. A., Boul, P., Lu, W., Rimberg, A. J., Smith, K. A., Colbert, D. T. and Smalley, R. E., "Controlled deposition of individuyal single-walled carbon nanotubes on chemically functionalized templates", *Chem. Phys. Lett.* **1999**, *303*, 125-129.

Loo, Y.-L. W., R. L.; Baldwin, K. W.; Rogers, J. A.;, "Interfacial Chemistries for Nanoscale Transfer Printing", *J. Am. Chem. Soc.* **2002**, *124*, 7654-7755.

Lu, X., Hanrath, T., Johnston, K. P. and Korgel, B. A., "Growth of single-crystal silicon nanowires in supercritical solution from tethered gold particles on a silicon substrate", *Nano Letters* **2003**, *3*, 93-99.

Lu, X., Ziegler, K. J., Ghezelbash, A., Johnston, K. P. and Korgel, B. A., "Synthesis of Germanium Nanocrystals in High Temperature Supercritical Fluid Solvents", *Nano Letters* **2004**, *4*, 969-974.

Lu, Z. H., "Air-stable Cl-terminated Ge(111)", *Appl. Phys. Lett.* **1996**, *68*, 520-522.

Lyman, P. F., Marasco, D. L., Walko, D. A. and Bedzyk, M. J., "Multiple bonding configurations for Te adsorbed on the Ge(001) surface", *Phys. Rev. B.* **1999**, *60*, 8704-8712.

Lyman, P. F., Sakata, O., Marasco, D. L., Lee, T. L., Breneman, K. D., Keane, D. T. and Bedzyk, M. J., "Structure of a passivated Ge surface prepared from aqeous solution", *Surface Science* **2000**, *462*, L594-L598.

Lynch, D. F., "Out-of-zone effects in dynamic electron diffraction intensities from gold." *Acta Crystal.* **1971**, *27*, 399-407.

Ma, D. D. D., Lee, C. S., Au, F. C. K., Tong, S. Y. and Lee, S. T., "Small-diameter silicon nanowire surfaces", *Science* **2003**, *299*, 1874-1877.

Maeda, Y., "Quantum size effect of bulk plasmon energy observed in Ge quantum dots", *Phys. Low-Dim. Struct.* **1997**, *10*, 23-25.

Martins, J. L. and Cohen, M. L., "Superconductivity in primitive hexagonal germanium", *Phys. Rev. B* **1988**, *37*, 3304-3307.

Massalski, T. B. (1986). Binary Alloy Phase Diagrams. B. L. H. Murray J.L., Baker H. Metals Park ,Ohio, American Society for Metals.

Maury, F., Mestari, A. and Morancho, R., "Organometallic chemical vapor deposition of silicon-rich amorphous silicon carbide (SixC1-x) refractory layers using tetraethylsilane as a single source", *Materials Science & Engineering, A: Structural Materials: Properties, Microstructure and Processing* **1989**, *A109*, 69-75.

Melnikov, D. V. and Chelikowsky, J. R., "Absoprtion spectra of germanium nanocrystals", *Solid State Commun.* **2003**, *127*, 361-365.

Mitome, M., Yamazaki, Y., Takagi, H. and Nakagiri, T., "Size dependence of plasmon energy in Si clusters." *J. Appl. Phys.* **1992**, *72*, 812-814.

Morales, A. M. and Lieber, C. M., "A laser ablation method for the synthesis of crystalline semiconductor nanowires", *Science* **1998**, *279*, 208-211.

Moriarty, P., Taylor, M. D. R. and Brust, M., "Nanostructured Cellular Networks", *Phys. Rev. Lett.* **2002**, *89*, 248303.

Morrison, S. R., "Slow Surface Reaction on Germanium", *Phys. Rev.* **1956**, *102*, 1297-1301.

Muller, D. A., Sorsch, T., Moccio, S., F. H. Baumann, Evans-Lutterodt, K. and Timp, G., "The electronic structure at the atomic scale of ultrathin gate oxides", *Nature* **1999**, *399*, 758-761.

Munekata, H., Ohno, H., Molnar, S. v., Segmüller, A., L. L. Chang and Esaki, L., "Diluted magnetic III-V semiconductors", *Phys. Rev. Lett.* **1989**, *63*, 1849-1852.

Nakashime, P. N. H., Tsuzuki, T. and Johnson, A. W. S., "Particle size dependence of the volume plasmon energy in cadmium sulphide quantum dots by electron energy loss spectroscopy", *J. Appl. Phys.* **1999**, *85*, 1556-1559.

Ng, H. T., Han, J., Yamada, T., Nguyen, P., Chen, Y. P. and Meyyappan, M., "Single Crystal Nanowire Vertical Surround-Gate Field-Effect Transistor", *Nano Letters* **2004**, *4*, 1247-1252.

Niwano, M., Kageyama, J., K.Kurita, Kinashi, K., Takahashi, I. and Miyamoto, N., "Infrared spectroscopy study of initial stages of oxidation of hydrogen-terminated Si surfaces stored in air", *J. Appl. Phys.* **1994**, *76*, 2157-2163.

O'Connell, M. J., Boul, P., Ericson, L. M., Huffman, C., Wang, Y., Haroz, E., Kuper, C., Tour, J., Ausman, K. D. and Smalley, R. E., "Reversible water-solubilization of single-wrapped carbon nanotubes by polymer wrapping", *Chem. Phys. Lett.* **2001**, *342*, 265-271.

Ohno, H., "Making Nonmagnetic Semiconductors Ferromagnetic", *Science* **1996**, *281*, 951-956.

Ohno, H., Shen, A., Matsukura, F., Oiwa, A., Endo, A., Katsumoto, S. and Iye, Y., "(Ga,Mn)As: A new diluted magnetic semiconductor based on GaAs", *Appl. Phys. Lett.* **1996**, *69*, 363-365.

Parabhakaran, K. and Ogino, T., "Oxidation of Ge(100) and Ge(111) surfaces: an UPS and XPS study", *Surface Science* **1995**, *325*, 263-271.

Park, Y. D., Hanbicki, A. T., Erwin, S. C., Hellberg, C. S., Sullivan, J. M., Mattson, J. E., Ambrose, T. F., Wilson, A., Spanos, G. and Jonker, B. T., "A Group IV ferromagentic semiconductor; MnxGe1-x", *Science* **2002**, *295*, 651-654.

Park, Y. D., Wilson, A., Hanbicki, A. T., Mattson, J. E., Ambrose, T., Spanos, G. and Jonker, B. T., "Magnetoresistance of Mn:Ge ferromagnetic nanoclusters in a diluted magnetic semiconductor matrix", *Appl. Phys. Lett.* **2001**, *78*, 2739-2741.

Parsons, J. R. and Hoelke, C. W., "Crystallography of hexagonal germanium", *Nature* **1983**, *301*, 591-592.

Parsons, J. R. and Hoelke, C. W., "Hexagonal germanium and high-resolution electron microscopy", *Philosophical Magazine A: Physics of Condensed Matter: Structure, Defects and Mechanical Properties* **1984**, *50*, 329-337.

Peng, H. Y., Wang, N., Zhou, X. T., Zheng, Y. F., Lee, C. S. and Lee, S. T., "Control of growth orientation of GaN nanowires", *Chem. Phys. Lett.* **2002**, *359*, 241-245.

Pines, D., "Collective energy losses in solids", *Rev. Mod. Phys.* **1956**, *28*, 184-198.

Pokrovski, G. S. S., Jacques, "Thermodynamic properties of aqueous Ge(IV) hydroxide complexes from 25 to 350°C: Implications for the behavior of germanium and the Ge/Si ratio in hydrothermal fluids." *Geochimica et Cosmochimica Acta* **1998**, *62*, 1631-1633.

Prasad, B., Stoeva, S., Sorensen, C., Zalkovski, V. and Klabunde, K., "Gold Nanoparticles as Catalysts for Polymerization of Alkylsilanes to Siloxane Nanowires, Filaments, and Tubes", *J. Am. Chem. Soc.* **2003**, *125*, 10488.

Proetto, C. R., "Self-consistent structure of a cylindrical quantum wire", *Phys. Rev. B* **1992**, *45*, 11911-11917.

Raether, H. *Springer Tracts in Modern Physics*; Springer Verlag: New York, **1980**; Vol. 88.

Reboredo, F. A. and Zunger, A., "Surface-passivation-induced optical changes in Ge quantum dots", *Phys. Rev. B* **2001**, *63*, 235314.

Ren, Z. F., Huang, Z. P., Xu, J. W., Wang, J. H., Bush, P., Siegal, M. P. and Provencio, P. N., "Synthesis of Large Arrays of Well-Aligned Carbon Nanotubes on Glass", *Science* **1998**, *282*, 1105-1107.

Rotkina, L., Lin, J.-F. and Bird, J. P., "Nonlinear current-voltage characteristics of Pt nanowires and nanowire transistors fabricated by electron-beam deposition", *Appl. Phys. Lett.* **2003**, *83*, 4426-4428.

Sanchez, A., Abbet, S., Heiz, U., Schneider, W.-D., Häkkinen, H., Barnett, R. N. and Landman, U., "When Gold Is Not Noble: Nanoscale Gold Catalysts", *J. Phys. Chem. A.* **1999**, *103*, 9573.

Sander, M. S., Gronsky, G., Lin, Y. M. and Dresselhaus, M. S., "Plasmon excitation modes in nanowire arrays", *J. Appl. Phys.* **2001**, *89*, 2733-2736.

Savage, P. E., Goplan, S., Mizan, T. I., Martino, C. J. and Brock, E. E., *AIChE Journal* **1995**, *41*, 1723-1778.

Schaich, W. L. and MacDonald, A. H., "Confined plasmons", *Solid State Commun.* **1992**, *83*, 779.

Scheu, C., Gao, M., Benthem, K. V., Tsukimoto, S., Schmidt, S., Sigle, W., Richter, G. and Thomas, J., "Advances in EELS spectroscopy by using new detector and new specimen preparation technologies", *J. Microscopy* **2003**, *210*, 16-24.

Schlittler, R. R., Seo, J. W., Gimzewski, J. K., Durkan, C., Saifullah, M. S. M. and Welland, M. E., "Single Crystals of Single-Walled Carbon Nanotubes Formed by Self-Assembly", *Science* **2001**, *292*, 1136-1139.

Schluckebier, G. and Predel, B., "Investigations on the structure of metastable phases in the gold-germanium system", *Z. Metallkd.* **1980**, *71*, 535.

Schrieffer, J. R., "Effective Carrier Mobility in Surface-space charge layers", *Phys. Rev.* **1955**, *97*, 641-646.

Sears, G. W., "A mechanism of whisker growth", *Acta Metal.* **1955**, *3*, 367-369.

Singh, A. K., Kumar, V. and Kawazoe, Y., "Ferromagnetism and piezomagnetic behavior in Mn-doped germanium nanotubes", *Physical Review B: Condensed Matter and Materials Physics* **2004**, *69*, 233406/233401-233406/233404.

Smith, P. A., Nordquist, C. D., Jackson, T. N., Mayer, T. S., Martin, B. R., Mbindyo, J. and Mallouk, T. E., "Electric-field assisted assembly and alignment of metallic nanowires", *Appl. Phys. Lett.* **2000**, *77*, 1399-1401.

Span, R. (2000). Multiparameter Equations of State - An Accurate Source of Thermodynamic Property Data. Berlin, Springer**:** 367.

Stowell, C. and Korgel, B. A., "Self-Assembled Honeycomb Networks of Gold Nanocrystals", *Nano Letters* **2001**, *1*, 595-600.

Stowell, C. A., Wiacek, R. J., Saunders, A. E. and Korgel, B. A., "Synthesis and Characterization of Dilute Magnetic Semiconductor Manganese-Doped Indium Arsenide Nanocrystals", *Nano Letters* **2003**, *3*, 1441-1447.

Streetman, B. G. and Banerjee, S. *Solid State Electronic Devices*; 5th ed.; Prentice Hall: Upper Saddle River, **2000**.

Strobl, C. J., Schaflein, C., Beierlein, U., Ebbecke, J. and Wixforth, A., "Carbon nanotube alignment by surface acoustic waves", *Applied Physics Letters* **2004**, *85*, 1427-1429.

Sturm, K., "Local-field effects in the plasmon line shape of semiconductors of the diamond and zinc-blende structures", *Phys. Rev. Lett.* **1978**, *40*, 1599-1602.

Sueoka, O., "Plasma Oscillation of Electrons in Be, Mg, Al, Si, Ge, Sn, Sb, and Bi." *J. Phys. Soc. of Japan* **1965**, *20*, 2203.

Sundarram, V. S. and Mitzel, A., "Surface effects on nanowire transport: a numerical investigaton using Boltzmann equation", *Jounral of Physics: Condensed Matter* **2004**, *16*, 4697-4709.

Surnev, L., "Oxygen adsorption on germanium(111) surface. I. Atomic clean surface", *Surface Science* **1981**, *110*, 439-457.

Surnev, L. and Tikhov, M., "Oxygen adsorption on a germanium(100) surface. I. Clean surfaces", *Surface Science* **1982**, *123*, 505-518.

Sze, S. M. *Physics of Semiconductor Devices*; 2nd ed.; Wiley: New York, **1981**.

Telari, K. A., Rogers, B. R., Fang, H., Shen, L., Weller, R. A. and Baski, D. N., "Characterization of platinum films deposited by focused ion beam-assisted chemical vapor deposition", *J. Vac. Sci. Technol. B* **2002**, *20*, 590-595.

Terrones, M., Grobert, N., Olivares, J., Zhang, J. P., Terrones, H., Kordatos, K., Hsu, W. K., Hare, J. P., Townsend, P. D., Prassides, K., Cheetham, A. K., Kroto, H. W. and Walton, D. R. M., "Controlled production of aligned-nanotube bundles", *Nature* **1997**, *388*, 52-55.

Trent, D. E., Levy, A., Coutant, R. W. and Merryman, E. L., "The thermal stability of some arylsilanes", *Aerospace Research Laboratories* **1965**, *ARL 65-64*.

Trentler, T. J., Hickman, K. M., Goel, S. C., Viano, A. M., Gibbons, P. C. and Buhro, W. E., "Solution-Liquid-Solid growth of crystalline III-V semiconductors: an analogy to vapor-liquid-solid growth", *Science* **1995**, *270*, 1791-1796.

Van Esch, A., Bockstal, L. V., Boeck, J. D., Verbanck, G., van Steenbergen, A. S., Wellmann, P. J., Grietens, B., Bogaerts, R., Herlach, F. and Borghs, G., "Interplay between the magnetic and transport properties in the III-V diluted magnetic semiconductor Ga1-xMnxAs", *Phys. Rev. B* **1996**, *56*, 13103-13112.

Wagner, R. S. *Whisker Technology*; Wiley: New York, **1970**.

Wagner, R. S. and Ellis, W. C., "Vapor-liquid-solid mechanism of single crystal growth", *Appl. Phys. Lett.* **1964**, *4*, 89-90.

Wagner, R. S., Ellis, W. C., Jackson, K. A. and Arnold, S. M., "Filamentary growth of silicon crystals from the vapor", *J. Appl. Phys.* **1964**, *35*, 2993-2995.

Wang, D., Chang, Y.-L., Wang, Q., Cao, J., Farmer, D., Gordon, R. and Dai, H., "Surface Chemistry and Electrical Properties of Germanium Nanowires", *Condensed Matter - preprints* **2004**.

Wang, D. and Dai, H., "Low-temperature synthesis of single-crystal germanium nanowires by chemical vapor deposition", *Angewandte Chemie, International Edition* **2002**, *41*, 4783-4786.

Wang, D., Wang, Q., Javey, A., Tu, R., Dai, H., Kim, H., McIntyre, P. C., Krishnamohan, T. and Saraswat, K. C., "Germanium nanowire field-effect transistors with SiO2 and high-k HfO2 gate dielectrics", *Appl. Phys. Lett.* **2003**, *82*, 232-2434.

Wang, J., Gudiksen, M. S., Duan, X., Cui, Y. and Lieber, C. M., "Highly polarized photoluminescence and photodetection from single indium phosphide nanowires", *Science* **2001**, *293*, 1455-1457.

Wang, N., Zhang, Y. F., Tang, Y. H., Lee, C. S. and Lee, S. T., "SiO2-enhanced synthesis of Si nanowires by laser ablation", *Applied Physics Letters* **1998**, *73*, 3902-3904.

Westwater, J., Gosain, D. P., Tomiya, S., Usui, S. and Ruda, H., "Growth of Silicon nanowires via gold/silane vapor-liquid-solid reaction", *J. Vac. Sci. Tech. B* **1997**, *15*, 554.

Whang, D., Jin, S., Wu, Y. and Lieber, C. M., "Large-Scale Hierarchical Organization of Nanowire Arrays for Integrated Nanosystems", *Nano Letters* **2003**, *3*, 1255-1259.

Wu, Y., Cui, Y., Huynh, L., Barrelet, C. J., Bell, D. C. and Lieber, C. M., "Controlled Growth and Structures of Molecular-Scale Silicon Nanowires", *Nano Letters* **2004**, *4*, 433-436.

Wu, Y., Fan, R. and Yang, P., "Block-by-Block Growth of Single-Crystalline Si/Si-Ge Superlattice Nanowires", *Nano Letters* **2002**, *2*, 83-86.

Wu, Y. and Yang, P., "Germanium nanowire growth via simple vapor transport", *Chemistry of Materials* **2000**, *12*, 605-607.

Wu, Y. and Yang, P., "Direct observation of vapor-liquid-solid nanowire growth", *Journal of the American Chemical Society* **2001**, *123*, 3165-3166.

Wu, Y. and Yang, P., "Melting and welding semiconductor nanowires in nanotubes", *Advanced Materials* **2001**, *13*, 520-523.

Yorikawa, H., Uchida, H. and Muramatsu, S., "Energy gap of nanoscale Si rods", *J. Appl. Phys.* **1996**, *79 (7)*, 3619-3621.

Yu, D. P., Bai, Z. G., Ding, Y., Hang, Q. L., Zhang, H. Z., Wang, J. J., Zou, Y. H., Qian, W., Xiong, G. C., Zhou, H. T. and Feng, S. Q., "Nanoscale silicon wires synthesized using simple physical evaporation", *Applied Physics Letters* **1998**, *72*, 3458-3460.

Yu, H. and Buhro, W. E., "Solution-liquid-solid growth of soluble GaAs nanowires", *Adv. Mater.* **2003**, *15*, 416-420.

Yu, H., Li, J., Looms, R. A., Wang, L.-W. and Buhro, W. E., "Two-versus three-dimensional quantum confinement in indiium phosphide wires and dots", *Nature Materials* **2003**, *2*, 517-520.

Yu, J.-Y., Chung, S.-W. and Heath, J. R., "Silicon Nanowires: preparation, device fabrication and transport properties", *J. Phys. Chem. B.* **2000**, *104*, 11864-11870.

Zabala, N., Ogando, E., Rivacoba, A. and Abajo, F. J. G. d., "Inelastic scattering of fast electons in nanowires: A dielectric formalism approach", *Phys. Rev. B* **2001**, *64*, 205410.

Zeppenfeld, K. and Raether, H., "Energy losses of 50-kev. electrons in Ge and Si", *Zeitschift fuer Physik* **1966**, *193*, 471-477.

Zhang, Y., Iqbal, Z., Vijayalakshmi, S., Qadri, S. and Grebel, H., "Formation of hexagonal-wurtzite germanium by pulsed laser ablation", *Solid State Communications* **2000**, *115*, 657-660.

Zhang, Y. F., Tang, Y. H., Lam, C., Wang, N., Lee, C. S., Bello, I. and Lee, S. T., "Bulk-quantity Si nanowires synthesized by SiO sublimation", *J. Cryst. Growth* **2000**, *212*, 115.

Zhang, Y. F., Tang, Y. H., Wang, N., Lee, C. S., Bello, I. and Lee, S. T., "Germanium nanowires sheathed with an oxide layer", *Phys. Rev. B* **2000**, *61*, 4518-4521.

Zhao, Y.-J., Shishidou, T. and Freeman, A. J., "Ruderman-Kittel-Kasuya-Yosida–like Ferromagnetism in MnxGe1–x", *Phys. Rev. Lett.* **2003**, *60*, 047204.

Zhu, Y. Q., Hsu, W. K., Terrones, M., Grobert, N., Terrones, H., Hare, J. P., Kroto, H. K. and Walton, D. R. M., "3D silicon oxide nanostructures: from nanoflowers to radiolaria", *Adv. Mater* **1998**, *8*, 1859-1862.

Ziegler, K. J., Doty, R. C., Johnston, K. P. and Korgel, B. A., "Synthesis of Organic Monolayer-Stabilized Copper Nanocrystals in Supercritical Water", *J. Am. Chem. Soc.* **2001**, *123*, 7797-7803.

Vita

Tobias Hanrath, the second child of Wilhelm and Marlene Hanrath, was born on January 31, 1977 in Bad Pyrmont, Germany. From 1987-1993 and 1994-1995 he pursed pursued upper secondary education at the S*tädtische Gymnasium* in Blomberg, Germany and attended High School in Hallsville, Texas from 1993-1994. In 1995 he returned to the United States in pursuit of his undergraduate education and graduated, summa cum laude, with dual B.S. degrees in Chemical Engineering and Chemistry in 2000. During his undergraduate tenure at the University of Tulsa, he began his research career working on interfaces of lithium-polymer batteries under the supervision of Dr. Dale Teeters and later worked with Dr. Saibal Mitra on the growth of ultrahard carbon nitride films. In 2000, he entered graduate school at the University of Texas at Austin in the Department of Chemical engineering and pursued his Ph.D. under the supervision of Dr. Brian A. Korgel researching germanium nanowires.

Permanent address: Auf der Klus 2A,
32676 Lügde, Germany

This dissertation was typed by the author.